UNIVERSIDAD NACIONAL AUTÓNOMA DE MÉXICO

PROGRAMA DE MAESTRÍA Y DOCTORADO EN INGENIERÍA
ELÉCTRICA-INTRUMENTACIÓN

DEVELOPMENT AND CONSTRUCTION OF A MUELLER MATRIX POLARIMETER FOR THE STUDY OF STRUCTURED SURFACES USING FOCUSED ILLUMINATION

TESIS

QUE PARA OPTAR POR EL GRADO DE:
DOCTOR EN INGENIERÍA

PRESENTA:
OMAR RODRÍGUEZ NÚÑEZ

TUTOR PRINCIPAL:
DR. NEIL CHARLES BRUCE DAVIDSON, ICAT-UNAM
COMITÉ TUTOR:
DR. MAXIMINO AVENDAÑO ALEJO, ICAT-UNAM
DR. AUGUSTO GARCÍA VALENZUELA, ICAT-UNAM

CIUDAD UNIVERSITARIA, CD. MX. MAYO 2019

Jurado Asignado

Presidente: Dr. García Valenzuela Augusto

Secretario: Dr. Rodríguez Herrera Oscar G.

1er. Vocal: Dr. Bruce Davidson Neil Charles

2do. Vocal: Dr. Avendaño Alejo Maximino

3er. Vocal: Dr. Hautefeuille Mathieu Christian A.

Lugar donde se realizó la tesis: CIUDAD UNIVERSITARIA, UNAM

TUTOR DE TESIS:
DR. NEIL CHARLES BRUCE DAVIDSON

________________________-
FIRMA

Abstract

We present a method to measure the polarization of scattered light on structured surfaces, through the implementation of an angle-resolved Mueller matrix polarimeter, using focused illumination. Typically the scattered light has been measured using an incident beam with a diameter on the order of a few cm for surfaces with scales of the order of microns, mainly to avoid problems with the speckle pattern of light, however in this way it is not possible to obtain information on local variations in the polarization effects present on the surface. Therefore, we use an incident spot size of a few microns to illuminate and analyze the local variations in the polarization state produced by the sample. First, we will begin by describing the instrumentation of the angle-resolved polarimeter, which uses Liquid Crystal Variable Retarders (LCVRs) to control the incident and detected polarization states. Our device implements a calibration and novel data extraction method, which allows us to reduce the experimental error in the instrument to obtain precise measurements. We use as a sample square structures of height and width equal to 15 mm and we use an incident beam size of 5 microns to compare results of experimental cases with results of numerical calculations based on the Kirchhoff Approximation of light scattering, including polarization effects. The simulation has been verified previously with other methods and has been shown to give correct results. Finally, we conclude on the advantages of measuring the polarization effect in the scattering pattern from one point to another in the studied sample, and we present a potential application of the system.

Resumen

Presentamos un método para medir la polarización de luz esparcida en superficies estructuradas, a través de la implementación de un polarímetro de matriz de Mueller con resolución angular, utilizando iluminación enfocada. Usualmente, la luz esparcida se ha medido utilizando un haz incidente del orden de unos cuantos centímetros para superficies con escalas del orden de micras, principalmente para evitar problemas con el patrón de speckle, pero de esta manera no es posible obtener información sobre las variaciones locales en los efectos de polarización, presentes en la superficie. Así, utilizamos un tamaño de haz incidente de unas cuantas micras para iluminar y analizar las variaciones locales en el estado de polarización producido por la muestra. Primero, comenzamos describiendo la instrumentación del polarímetro, el cual utiliza Retardadores Variables de Cristal Líquido (RVCL) para controlar los estados de polarización incidentes y detectados. Nuestro dispositivo implementa un método de calibración y extracción de datos novedoso, que nos permite reducir el error experimental en el instrumento para obtener mediciones precisas. Usamos como muestra un cuadrado de altura y ancho de 15 micras y un tamaño de haz incidente de 5 micras, para comparar resultados de casos experimentales con resultados de cálculo numérico basado en la aproximación de Kirchhoff para esparcimiento de luz, la cual incluye efectos de polarización. La simulación ha sido verificada previamente con otros métodos mostrando resultados consistentes. Finalmente, concluimos sobre las ventajas de medir el efecto de polarización en el patrón de esparcimiento de un punto a otro en la muestra estudiada, y presentamos una potencial aplicación del sistema.

A mi esposa Karina, el amor de mi vida. Porque a tu lado todo es posible.

Acknowledgement

Primeramente quiero agradecer profundamente a mi tutor, Dr. Neil Bruce, gracias por la disposición, el apoyo, la orientación y sobre todo la paciencia que me ha tenido estos años.

Al Dr. Maximino Avendaño por sus valiosos comentarios, al Dr. Augusto García por las interesantes discusiones, al Dr Mathieu Hautefeuille por darse el tiempo para revisar y hacer comentarios clave en el trabajo, así como por la flexibilidad y apoyo para micro-fabricar las superficies de este trabajo y al Dr. Oscar Rodríguez quien con su claridad, conocimiento y disposición aportó ideas importantes al trabajo.

Al Mtro. Guadalupe Bañuelos por las facilidades para analizar muestras en el LUCE, ICAT. Al Mtro. Alejandro Esparza por la deposición de películas delgadas en nuestras superficies. Por último al Fis. Aaron Cruz por su gran soporte en el LaNSbioDyT para la fabricación de estructuras.

A CONACYT que me proporcionó la beca de doctorado de tiempo completo.

A DGAPA-UNAM por el financiamiento a través de los proyectos PAPIIT IT100114 y IT100417).

Al Posgrado de Ingeniería por los apoyos para congresos y estancias de investigación que ayudaron a complementar mi formación doctoral.

A mi esposa Karina, porque gran parte de este trabajo fue gracias a tu apoyo incondicional.

A mi familia por siempre apoyarme y a mis amigos y compañeros de la universidad, por las discusiones, el apoyo y sobre todo por siempre estar ahí con una taza de café.

Finalmente quiero agradecer a mi Alma Mater, la Universidad Nacional Autónoma de México, que a través del ahora Instituto de Ciencias Aplicadas y Tecnología, me permite obtener un nuevo grado académico y que complemento mi formación profesional y personal.

Contents

List of Figures

Chapter 1

Introduction

Light scattering has been used as a method of characterizing materials or surface roughness in different areas. In particular, it has been reported for applications in remote sensing, printed circuit testing and measuring surface patterns for growth of nanometric structures [1]-[7]. In the literature, theoretical studies [8]-[18] and experimental studies [19, 28] have been reported. There is experimental work on measurements of light scattering from this type of surfaces, and in reference [29] calculations are performed to study the angular distribution of the scattered light from a one-dimensional rough surface. The direct problem is studied, calculating the angular distribution of light scattered, and also the inverse problem, where the RMS[1] of the roughness and the auto-correlation function are obtained by a least squares fit to measurements of the angular distribution. In general, there are a large number of studies that probe the effect of incident angle, the geometrical shape, and the optical properties of the surface by different materials, by measuring the relationship between the shape and the intensity of light scattering.

Theoretical work of scattering has been centred on the problem of the calculation of scattering patterns given by the form and the material of the surface, using the approximation of scalar diffraction (without changes in the polarization for one dimensional surfaces) [30]. There are very few works on inverse methods (to calculate the surface when the pattern of scattering is known) due to the complex mathematics involved. A lot of methods have been used to calculate the diffraction pattern, including perturbation methods [12]-[15], integral methods [11], modal methods for periodic surfaces [4],[8]-[10] and the Kirchhoff Approximation [16]-[18]. It is important to highlight that because of the complexity of the problem, in general, the results reported in the literature are the results of numerical calculations, because it is not possible to resolve the equations involved analytically.

---

[1] The root-mean-square (RMS).

In the literature the size of the illumination spot is larger than the spatial variation size, therefore it is not possible to obtain information about the local variations of structure point to point on the sample. The illumination over a large area means that the pattern of scattered light is an average over all of the surface. In the reported works the beam of illumination over an area bigger than the scale of the structure or roughness of the surface, is used to avoid problems with the speckle in the pattern of the light scattering and to have an average over the surface structure. For example, when we illuminate a printed circuit over an area which includes structure together with a flat area, it gives us a pattern of scattering that depends on both areas and that could be insensitive to variations of the structure of the first area [31]. Also, there are reports of measurements for specific applications using points of illumination, for example in [32] the size of the spot illumination is important for the scattering from a scale of the wing of a butterfly to investigate the structural colouration of biological tissue. A scale has a size of 100 microns, which gives us the size of illumination required.

In many research areas there is particular interest in surfaces with infinite surface slopes. This kind of surface involves rectangular structures, for example, as we mentioned before, printed cirucuits or pattern surfaces used for growing nanostructures [33, 34]. Different methods have been used to calculate the scattering from this type of surface. Results of calculating the light scattered from 1D surfaces with infinite slopes using modal methods, rigorous coupled-wave analysis and integral equation methods are computationally difficult to generalize to 2D surfaces. Geometrical optics methods (ray-tracing or specular point theory) have also been presented for other 2D surface scattering problems, but they are limited in their range of application and, of course, do not include diffraction effects. In [35] the application of the Kirchhoff approximation to calculate the scattering of light from 2D rough surfaces with infinite slopes was presented as a previous step to give an insight into the physical basis of a method which is a formulation of the 3D Kirchhoff approximation that allows calculation for surfaces with infinite slopes [16].

On the other hand, the polarization properties of the light scattered from surfaces contains information about the properties of the sample. The complete polarization properties of the surface scattering process are contained in the Mueller matrix [36]. The Mueller matrix has been measured or calculated for the scattering of light from 1D surfaces, with the calculations performed using the diffraction theory [2]-[19]. There have been very few vector-diffraction calculations performed for the Mueller matrix for scattering from a 2D surface because of the numerical difficulties involved and the complicated surface structures [20]. In [17] a numerical method is used to calculate the double-scattered Mueller matrices for scattering of vector-electromagnetic waves form rough surfaces, where the method is based on a modified version of the Kirchhoff approximation and is valid for surfaces with vertical walls and for any surface material. Calculations were performed for the case of ribs on silicon and gold surfaces, and the results are compared with experimental measurements. The calculated results of the 16 elements of the Mueller matrix as function of the scatter angle show good qualitative agreement with the experimental results for the groove cases. Mueller matrix polarimetry has also shown great potential in this field, this thesis is focused on the polarization point of view, studying the polarization of light scattered by periodic structured surfaces, using an analysis based on a numerical simulation with the Kirchhoff approximation that will allow us to compare theoretical and experimental results. Thus, the following section presents a review of the current status of the instruments to measure the full 4 x 4 Mueller Matrix (MM).

1.1 An overview of instruments for measuring the 4 x 4 Mueller matrix

The state of polarization (SOP) of light (the transversal vibration of its electric vector) emitted by various sources, or scattered (reflected, transmitted, or diffracted) by different objects, provides essential information about the emitting sources and scattering objects. Its measurement, i.e., optical polarimetry, has contributed fundamental advances in the physical, chemical, and biological sciences, and has provided essential sensing, diagnostic, analytical, and metrology tools in numerous applications. This includes the chemical, pharmaceutical, biomedical, metal, and semiconductor integrated-circuit industries [37]. Ellipsometry, which is reflection polarimetry for the characterization of surfaces, interfaces, and thin films, has witnessed rapid growth since the 1970s, and has found many applications in virtually every branch of science and technology [37]-[45]. Atmospheric, astonomical, and astrophysical polarimetry is another significant broad area of research [46]-[53]. Passive Stokes-vector imagining polarimetry for remote sensing applications is reviewed by Tyo *et al.* [54]. Active optical polarimetry (which requires polarization state generation and detection) for biomedical applications is reviewed by Tuchin *et al.* [55] and Ghosh and Vitkin [56]. A review of instrumentation in ellipsometry and polarimetry up to 1980 is that of Hauge [57]. More detailed recent reviews of Mueller matrices and polarimetry are provided by Chipman [58].

Recently, studies in ellipsometry-based scatterometry (or spectral ellipsometry) has been introduced to monitor the critical dimension (CD) and overlay of grating structures in semiconductor manufacturing [59]-[61]. Among the various types of ellipsometry, Mueller matrix polarimetry (MMP), can obtain all 16 quantities of a 4x4 Mueller matrix. Consequently, MMP-based scatterometry can acquire much more useful information about the sample and thereby can achieve better measurement sensitivity and accuracy than the conventional ellipsometric scatterometry [62]-[64]. MMP is thus expected to provide a powerful tool [36].

Stokes vectors and Mueller matrices

The polarization properties of an object, as well as the polarization state of a light beam, can be described in different ways. One possibility is to represent the object with a matrix and the beam with a vector. The interaction of the light beam with the object is then represented by the product of the matrix and the vector. Jones formalism [65] is a suitable tool to describe this interaction as long as the object is non-depolarising. Thus, Jones formalism is limited in the range of objects and light beams that can be described. A more general formalism is given by the combination of the Mueller matrix and the Stokes vectors.
The Stokes parameters, i.e. the elements of the Stokes vectors, were introduced by Sir George Stokes as a set of measurable quantities that describe the polarization state of a light beam for completely polarized, partially polarised and unpolarized light. The definition of the Stokes vector, for quasi-monochromatic light, is [66].

$$S = \begin{bmatrix} \langle E_x E_x^* + E_y E_y^* \rangle \\ \langle E_x E_x^* - E_y E_y^* \rangle \\ \langle E_x E_y^* + E_y E_x^* \rangle \\ i\langle E_x E_y^* - E_y E_x^* \rangle \end{bmatrix}, \tag{1.1}$$

where E_x and E_y are the components of the electric field in the x- and y-direction, respectively. The symbol $\langle\rangle$ indicates that the quantities are ensemble averages but, assuming stationary and ergodicity, they can be replaced by time averages with the same result. The first element of the Stokes vector is the total irradiance the second one is the fraction of light linearly polarized in the horizontal and/or vertical direction, the third element is the fraction linearly polarized at ±45° and the fourth one is the fraction of light circularly polarized with right and/or left handedness.

The Mueller matrix is a 4x4 real matrix of the form:

$$\mathbf{M} = \begin{bmatrix} M_{11} & M_{12} & M_{13} & M_{14} \\ M_{21} & M_{22} & M_{23} & M_{24} \\ M_{31} & M_{32} & M_{33} & M_{34} \\ M_{41} & M_{42} & M_{43} & M_{44} \end{bmatrix}, \tag{1.2}$$

that contains all the information concerning the linear polarization properties of the object that it represents. Depending on the polarization properties of the object, there may be symmetries between elements of the Mueller matrix. However, in the most general case, all the elements of the matrix are different [67].

An important property of the Mueller matrix representation of polarization is linearity. That is, the total effect over the polarization of a light beam due to a series of N optical elements, each one represented by a Mueller matrix M_i, $i = 1, ..., N$, is given by

$$\mathbf{M} = \mathbf{M}_N \cdots \mathbf{M}_2 \mathbf{M}_1. \tag{1.3}$$

In Eq.1.3 $\mathbf{M}_1$ is the Mueller matrix of the first-to-be-encountered optical element along the light-beam path.

A Mueller matrix polarimeter is always composed of a polarization-state generator (PSG), which generates at least four linearly independent basis states $\mathbf{S}_{in}$, and a polarization state analyzer (PSA) which measures $\mathbf{S}_{out}$ by measuring its projections over at least another four linearly independent basis states. Here we consider a single-channel system with a PSG generating exactly four Stokes vectors $\mathbf{S}_{in}$, which are the column vectors of the modulation matrix, $\mathbf{W}$. Similarly, the PSA is assumed to project S_{out} over exactly four Stokes vectors, which are the row vectors of the analyzer matrix, $\mathbf{A}$. Then, a complete set of 16 measurements on a sample characterized by a Mueller matrix $\mathbf{M}$ can be written in matrix form:

$$\mathbf{B} = \mathbf{AMW}, \tag{1.4}$$

and $\mathbf{M}$ can be extracted readily from the raw data matrix, $\mathbf{B}$, provided that $\mathbf{A}$ and $\mathbf{W}$ are known, i.e., if the system is calibrated [58]. Light polarization can be modulated and analyzed by a variety of approaches: rotating retardation plates [21]-[37], rotating compensators [68], Pockels cells [24], photoelastic modulators [69]-[70], or liquid-crystal(LC) variable retarders [71]-[72].

In our laboratory of Light Scattering at ICAT, UNAM[2] studies have been carried out on the measurement of light scattering on rough surfaces, for which theoretical and numerical studies have been developed including scattering of vector-electromagnetic waves. Surfaces with 1 and 2 dimensional structures have been studied and consistent results based on numerical simulations verified by comparison with other calculation methods have been obtained. The measurement of the light in the full hemisphere can be achieved by using a mirror to collect the scattered light and direct it to a detector, but with this method the polarization of the scattered light is affected by the optical system and it is very difficult to compensate the effects of all the optical components to separate only the polarization of the scattering process [6]. So, it is necessary to explore other methods to perform the polarization measurement of scattered light. One way is to implement measurements of the polarization through a scanning scatterometer which

---

[2] Institute of Applied Sciences and Technology of the National Autonomous University of Mexico.

uses two rotational movements to scan and detect light over the hemisphere of interest, details of the mechanical construction for the scatterometer can be seen in [73]. However, this method presents mechanical complications that could affect the polarization measurements. Therefore, a third method that will help us to compensate the complications of the other methods, it is to use a linear positioning system to scan a sample bidimensionally and then measure the polarization of light scattered point to point with a beam size of illumination of the same order (microns) as the spatial variations of the surface, to be able to study the effects on the polarization of local shape variations.

In this thesis the polarization will be measured by using a system of Liquid Crystal Variable Retarders (LCVR), this system has some limitations, in particular, the accessible spectral range, but also significant advantages, such as the absence of moving parts or high driving voltages. As we mentioned before to measure a Mueller matrix, at least 16 intensities must be measured, the Mueller matrix must be reconstructed, and finally a calibration step [81] should be performed to remove errors and polarization effects of other optical components in the polarimeter (for example, lenses or beam splitters). The errors in the final Mueller matrix can be caused by noise in the intensity measurements or by errors in the experimental set-up of the polarimeter, which could be, for example, errors in the angular positions of the axes of the retarders, polarizers or errors in the retardances. This means that a stable and accurate method for extraction and calibration data for polarimeters is required, and in this thesis we will propose a method for that.

In this context we present a novel method to measure the polarization of light scattered on structured surfaces through the implementation of an angle-resolved Mueller-matrix polarimeter, using focused illumination. We use an incident spot size of a few microns to illuminate and analyze the local variations in the polarization state produced by a sample. First, we will describe the instrumentation of the polarimeter, which uses liquid crystal variable retarders to control the incident and detected polarization states. Our device implements a calibration and data extraction method, which allows us to reduce the experimental error in the instrument to obtain efficient measurements. We use as a sample a reflective structured surface with different dimensions (5-15 microns) and we use an incident beam size of 5 microns to compare results of experimental cases with results of numerical calculation based on the Kirchhoff Approximation of light scattering, including polarization effects. The simulation has been previously verified with other methods [16]-[18],[35],[73]. The calculating cases will allow us to restrict the problem due to the large number of variables involved in the system, thus, we will work with the most representative variables in the experimental case preserving the relevance of having a very-well calibrated system to make measurements with liquid crystals and the problems associated with these instruments. We will include an application of the polarimeter on surfaces and its potential implementation. Finally, we conclude on the advantages of measuring the polarization effect in the scattering pattern from one point to another in the studied sample.

1.2 Objectives

The specific objectives of this work are:

- Design, build and optimize a Mueller-matrix polarimeter to measure the polarization state of light scattered on structured surfaces using a focused beam as a source of illumination.
- Develop an automatized control system to perform a two-dimensional sweep of illumination point on the surface, to measure the variations in the polarization state point-to-point over the illuminated area. It is necessary to include the data extraction in the system.
- Develop a method to analyze and compare the experimental data obtained with results of numerical calculations with the Kirchhoff approximation method.
- Describe advantages and limits of the method and application to validate the instrument.

To achieve the proposed objectives, this work is organized as follows:

Chapter 1 presents the general problem that gives origin to the project, here the motivation is presented for the development a Mueller-matrix Polarimeter to study changes in the polarization state of scattered light, and we describe the context to study structured surfaces, measuring changes in the polarization state through the Mueller matrix.

Chapter 2 contains the fundamental principles of the behaviour of light and the interaction with matter. We introduce the basic concepts of polarization and its study using the Mueller matrices. It is important to define a formal treatment of the Mueller matrix and the scope of it.

Chapter 3 is to discuss Mueller-matrix polarimetry and how it should be applied experimentally to achieve a polarimeter with a very good performance, and how we achieve that through the use of a new calibration method for polarimeters.

In Chapter 4 the details of the experiment are presented, from design, construction and automation to the calibration and optimization of the system to obtain better results. The last part of the chapter addresses the experimental measurements using our Mueller matrix polarimeter for known samples.

Chapter 5 presents our proposal of numerical fitting for calibration of non-optimized polarimeters, which is a very significant previous step to the development of precise Mueller matrix polarimeters.

Chapter 6 presents numerical calculation based on the Kirchhoff approximation to restrict the variables in the system. Experimental and theoretical cases for structured surfaces are compared. We also present the principles of fabrication of the samples used in this dissertation.

Finally we present a summary of the results to specify the contributions and conclusions of the present dissertation.

1.3 Conferences and publications

Results of the method developed in this thesis has been presented for discussion with the community in a number of international conferences, workshops and papers. We will continue working in a paper describing the implementation of the method.

- O. Rodríguez-Núñez and Neil Bruce, *Comparison of the pattern of light scattering from one-dimensional rough surfaces using focused illumination*, Light in Science, Light in Life (Li-Sci), Tequisquiapan, Queretaro, México.

- O. Rodríguez-Núñez and Neil Bruce, *Esparcimiento de luz en superficies rugosas unidimensionales utilizando iluminación enfocada*, LVII Congreso Nacional de Física y Congreso LAtinoamericano de Física 2015, Mérida, Yucatán, México. (2015)

- O. Rodríguez-Núñez and Neil Bruce, *Measurement of defects by measuring of light scattering from surfaces using focused illumination*, Proc. SPIE 9890, Optical Mircro- and Nanometrology VI, 989012, (2016).

- O. Rodríguez-Núñez, Juan Manuel López-Téllez, Oscar G. Rodríguez-Herrera, Neil C. Bruce, *Calibration and data extraction in non-optimized Mueller matrix polarimeters*, Applied Optics, Vol. 56, No.15, (2017).

- O. Rodríguez-Núñez and Neil C. Bruce, *Implementation of a System to Measure Polarization and Light Scattering on Structured Surfaces Using Focused Illumination*, Optical Metrology, The 24th Congress of the International Commission for Optics (ICO-24), Tokyo, Japon, (2017).
- Neil C. Bruce, Juan Manuel Lopez-Tellez, Omar Rodríguez-Núñez, and Oscar G. Rodríguez-Herrera, *Permitted experimental errors for optimized variable-retarder Mueller-matrix polarimeters*, Optics Express, Vol. 26, No.11, (2018).
- Neil C. Bruce, Oscar G. Rodríguez-Herrera, Juan Manuel López-Tellez, Omar Rodríguez-Núñez, *Experimental limits for Eigenvalue Calibration in Liquid-Crystal Mueller-Matrix Polarimeters*, Optics Letters, Vol.43, No.11, (2018).
- O. Rodríguez-Núñez, Ivan Montes-Gonzalez and Neil C. Bruce, *Measurement of scattered light polarization on surfaces using focused illumination*, SPIE Optical Engineering+Applications, Polarization Science and Remote Sensing IX(accepted), (2019).
- O. Rodríguez-Núñez and Neil C. Bruce, *Instrumentation of a Mueller-matrix polarimeter with LCVR using focused illumination*, paper in preparation.

Chapter 2

Light propagation fundamentals

With the formulation of electromagnetic theory by James Clerk Maxwell in 1865 it was shown that light is an electromagnetic wave with a frequency within a particular range. At that time it was already known from previous work on optics that when light propagates through an optical medium it shows rather complicated behaviour due to refraction and absorption phenomena[66]. The electromagnetic theory has permitted the development of a rigorous theoretical framework for the successful analysis of the optical properties of a wide range of media. Nowadays, the interest in this topic has not decreased because this is not a finished research, particularly for anisotropic and/or inhomogeneous media.

In this chapter we give a short theoretical background on the propagation of light in a medium and we review some basics topics about polarization optics. This revision focuses on the presentation of Maxwell's equations and the constitutive relations for different types of media and on the different vector representations for polarized light.

2.1 The Wave Equation

Maxwell's equations can be written in terms of the electric field amplitude **E**, the electric displacement vector **D**, the magnetic flux density **B**, and the magnetic field amplitude **H** as

$$\nabla \times \mathbf{E}(\mathbf{r},t) = -\frac{\partial \mathbf{B}(\mathbf{r},t)}{\partial t} = -\mu \frac{\partial \mathbf{H}(\mathbf{r},t)}{\partial t}, \tag{2.1}$$

$$\nabla \times \mu \mathbf{H}(\mathbf{r},t) = \nabla \times \mathbf{B}(\mathbf{r},t) = \mu\sigma \mathbf{E}(\mathbf{r},t) + \frac{\mu\varepsilon \partial \mathbf{E}(\mathbf{r},t)}{\partial t}, \tag{2.2}$$

$$\nabla \cdot \mathbf{D}(\mathbf{r},t) = \nabla \cdot \varepsilon \mathbf{E}(\mathbf{r},t) = \rho(\mathbf{r},t), \tag{2.3}$$

$$\nabla \cdot \mathbf{B}(\mathbf{r},t) = 0. \tag{2.4}$$

D, **E**, **B** and **H** are in bold to indicate that they are vector quantities and ρ is the free charge density. The symbols μ, σ, and ε represent the medium permeability, conductivity, and dielectric constants, respectively.
Relations between the physical quantities appearing in Eqs.[2.1−2.4] (between **E** and **D** and between **H** and **B**) are required to solve the Maxwell equations. They are known as constitutive relations, and they are established by the physical properties of the medium in which light propagates. Maxwell's equations are generally held to be inviolable and, therefore, the properties of matter enter solely through the constitutive equations. In free space the constitutive relations are:

$$\mathbf{D} = \varepsilon_0 \mathbf{E}, \tag{2.5}$$

$$\mathbf{B} = \mu_0 \mathbf{H}, \tag{2.6}$$

where ε_0 and μ_0 are the permittivity and the permeability of vacuum, respectively. In general, the constitutive relations in regions filled by matter have the form

$$\mathbf{D} = \varepsilon_0 \mathbf{E} + \mathbf{P}, \tag{2.7}$$

$$\mathbf{B} = \mu_0 (\mathbf{H} + \mathbf{M}), \tag{2.8}$$

where **P** and **M** are, respectively, the electric and the magnetic polarizations and they can be interpreted as the average electric and magnetic dipole moment per unit volume. In a homogeneous linear isotropic dielectric medium, the electric polarization is parallel and proportional to the electric field:

$$\mathbf{P} = \varepsilon_0 \chi_e \mathbf{E}, \tag{2.9}$$

so that

$$\mathbf{D} = \varepsilon_0 (1 + \chi_e) \mathbf{E} = \varepsilon \mathbf{E}, \tag{2.10}$$

where χ_e is the electric susceptibility that is always positive and ε, the permittivity. Similarly, in isotropic homogeneous linear magnetic media, the magnetic polarization is parallel and proportional to the magnetic field

$$\mathbf{M} = \chi_m \mathbf{H}, \tag{2.11}$$

so that

$$\mathbf{B} = \mu_0(1 + \chi_m)\mathbf{H} = \mu\mathbf{H}, \tag{2.12}$$

where χ_m is the magnetic susceptibility that can be positive or negative; and μ is the permeability.

In an anisotropic material, the polarization and the electric field are not necessarily in the same direction. For these materials the electric and magnetic susceptibilities are in general tensors, which means that the permittivity ε and the permeability μ are tensors:

$$\mathbf{D} = \varepsilon\mathbf{E}, \tag{2.13}$$

$$\mathbf{B} = \mu\mathbf{H}. \tag{2.14}$$

Along with the Eqs. 2.13 and 2.14, there is one more *constitutive equation*,

$$\mathbf{J} = \sigma\mathbf{E}, \tag{2.15}$$

known as Ohm's Law, it is a statement of an experimentally determined rule that holds for conductors at constant temperatures. The electric field amplitude, and therefore the force acting on each electron in a conductor, determines the flow of charge. The constant of proportionality relating **E** and **J** is the conductivity of the particular medium.

Taking the curl of Eq. 2.1 and substituting Eq. 2.2 to eliminate **B** (or **H**) gives

$$\nabla \times (\nabla \times \mathbf{E}) = -\frac{d(\nabla \times B)}{dt}. \tag{2.16}$$

Using the identity

$$\nabla \times (\nabla \times \mathbf{E}) = \nabla(\nabla \cdot \mathbf{E}) - \nabla^2\mathbf{E} = -\nabla^2\mathbf{E}, \tag{2.17}$$

gives the differential relationship

$$\nabla^2\mathbf{E} = \mu\sigma\frac{d\mathbf{E}}{dt} + \mu\varepsilon\frac{d^2\mathbf{E}}{dt^2}, \tag{2.18}$$

which is known as the wave equation. An identical equation can be found for **B** by eliminating **E**.

2.1.1 Electromagnetic Plane Waves in Free Space

In this section we will restrict our attention to the study of Maxwell's equations with linear isotropic constitutive relations (Eqs. 2.13 and 2.14). Maxwell's equations 2.1 with these constitutive relations and in a source-free space (without current or charge densities $\mu = \mu_0, E = E_0, \sigma = 0.$) can be written as

$$\nabla \times \mathbf{E}(\mathbf{r}, t) = -\mu \frac{\partial \mathbf{H}(\mathbf{r}, t)}{\partial t}, \tag{2.19}$$

$$\nabla \times \mu \mathbf{H}(\mathbf{r}, t) = \frac{\varepsilon \partial \mathbf{E}(\mathbf{r}, t)}{\partial t}, \tag{2.20}$$

$$\nabla \cdot \mathbf{E}(\mathbf{r}, t) = 0, \tag{2.21}$$

$$\nabla \cdot \mathbf{H}(\mathbf{r}, t) = 0. \tag{2.22}$$

Taking the curl of both sides of Eq. 2.19 and substituting Eq. 2.20 we get

$$\nabla \times (\nabla \times \mathbf{E}) = -\mu\varepsilon \frac{\partial^2 \mathbf{E}}{\partial t^2}. \tag{2.23}$$

Applying the identity $[\nabla \times \nabla \times = \nabla(\nabla \cdot) - \nabla^2]$ and using Eq. 2.21 we obtain the wave equation:

$$\nabla^2 \mathbf{E} - \mu^2 \varepsilon^2 \frac{\partial^2 \mathbf{E}}{\partial t^2} = 0, \tag{2.24}$$

where $u = 1/\sqrt{\mu\varepsilon}$ is the phase velocity of light propagating in the medium, in vacuum $c = 1/\sqrt{\mu_0 \varepsilon_0}$. $n = \frac{c}{u}$ is referred to as the index of refraction. For a monochromatic wave the time variation of the electric field vector is sinusoidal and one possible solution to Eq. 2.18 can be shown to take the form of

$$\mathbf{E} = \mathbf{E}_0 e^{j(2\pi\nu\sqrt{\mu_0\varepsilon_0}z - 2\pi\nu t)}, \tag{2.25}$$

where $\mathbf{E}_0$ is a constant vector that determines the electric field amplitude and polarization direction. The parameter ν is the frequency of the sinusoidal wave. The usual convention of writing the solution in terms of a phasor, but recognizing that only the real part is of interest, has been used. The specific solution shown in Eq. 2.25 is a plane wave propagating in the z direction. The more-general solution is given in terms of the wave-number, which is the phase increase per unit propagation distance and is defined as

$$k = 2\pi\nu/c = 2\pi/\lambda. \tag{2.26}$$

The propagation constant is also defined as a vector $\mathbf{k}$ of magnitude k in the direction perpendicular to surfaces of constant phase. Then, we get

$$\nabla^2\mathbf{E}(\mathbf{r}) + k^2\mathbf{E}(\mathbf{r}) = 0, \tag{2.27}$$

which is known as the Helmholtz equation.

and we can write

$$\mathbf{E}(\mathbf{r}) = \mathbf{E}_0 e^{j(\mathbf{k}\cdot\mathbf{r}-2\pi\nu t)}. \tag{2.28}$$

The full solution to Eq. 2.27 is actually the summation of many waves of the form of Eq.2.28 plus their complex conjugates. If $k < 0$, then the wave travels in the opposite direction. Some texts define plane waves with the negative of the exponent shown in Eq 2.28. An identical solution set exists for $\mathbf{B}$. The two field vectors can be shown to be perpendicular to each other and to $\mathbf{k}$, making the solution a transverse wave. Figure 2.1 shows the relative directions of $\mathbf{E}$, $\mathbf{B}$, $\mathbf{k}$ (which is in the $\mathbf{z}$ direction) for the solution.

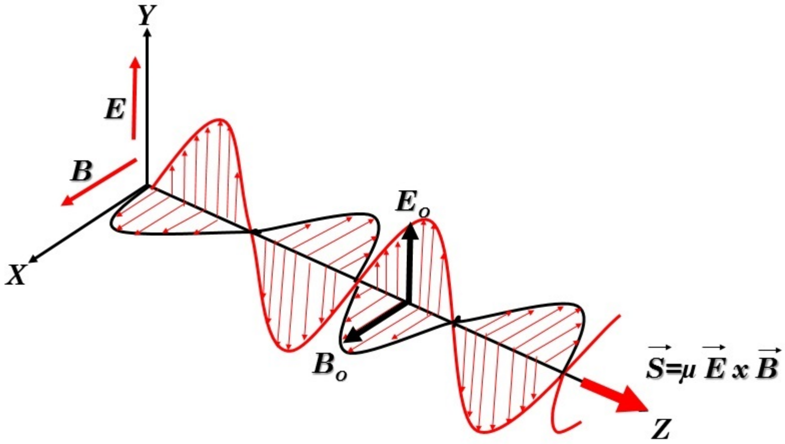

Figure 2.1: The transverse nature of the Electromagnetic wave. The wave is plotted in space for an instant of time.

Substituting the plane-wave solution into Maxwell's equations and manipulating them gives a relationship for η_0, the impedance of free space. This expression can be used for other media by substituting the appropriate material constants [74]:

$$\eta_0 = \frac{|\mathbf{E}|}{|\mathbf{H}|} = \frac{2\pi\nu\mu_0}{k} = \frac{k}{2\pi\nu\varepsilon_0} = \sqrt{\frac{\mu_0}{\varepsilon_0}} \cong 377 ohms. \tag{2.29}$$

The Poynting vector **S** gives the instantaneous power density (watts per unit area) associated with the wave[65], [75]. For isotropic media, it has the same direction as **k**. Usually, the time-average power density is expressed as the scalar *I*. For sinusoidal fields, the time average introduces a factor of 1/2. The resulting equation are analogous to power calculations based on Ohm's law:

$$\mathbf{S} = \mathbf{E} \times \mathbf{H}^{*} \tag{2.30}$$

$$I = \frac{1}{2}|\mathbf{E} \times \mathbf{H}| = \frac{1}{2}\frac{|\mathbf{E}|^2}{\eta_0} = \frac{P}{A}. \tag{2.31}$$

The $*$ indicates taking the complex conjugate and P is the power measured over cross sectional area A.

A true plane wave has an infinite transverse width and no beam divergence (angle spread). This makes sense because with infinite width, there is no room for divergence. However, beams of finite width do diverge. As presented in Chapter 1 of this dissertation, we focus our attention on a common situation of a finite-width laser beam with a Gaussian electric field cross section, we study this case because the results are useful for developing the practical measurement application that we will present in Chapter 4. Gaussian beams have an electric-field cross section described by

$$E = E_0 \frac{\omega_0}{\omega(z)} e^{-[r/\omega(z)]^2} e^{j[kz - tan^{-1}(z/z_0) + kr/2R(z) - 2\pi\nu t]}. \tag{2.32}$$

where

$$\omega^2(z) = \omega_0^2 \left[1 + \left(\tfrac{z}{z_0}\right)^2\right]$$
$$\omega_0 \equiv e^{-1} \text{ beam radius at } z = 0 (e^{-2} \text{ intensity radius}),$$
$$\omega(z) \equiv e^{-1} \text{ beam radius at } z (e^{-2} \text{ intensity radius}),$$
$$R(z) = z\left[1 + \left(\tfrac{z}{z_0}\right)^2\right] \equiv \text{characteristic length.}$$

The geometry, shown in Fig.2.2 is for a beam propagating in the z direction. The beam has an e^{-1} field radius of $w(z)$ that has a minimum width ω_0 located at $z = 0$. The *beam radius* expands to $2\omega_0$ after travelling a distance z_0. Cross-sectional amplitude variations are described by the first three term in Eq.2.32. The second exponential term contains the phase information. At $z = 0, R(z) = 4$, the phase radius of curvature $R(z)$ becomes infinite and the phase exponential terms looks like the phase description of a plane wave. Notice that knowledge of the wavelength and either ω_0 or z_0 is enough to define Θ_{div}, as shown in Fig. 2.2.

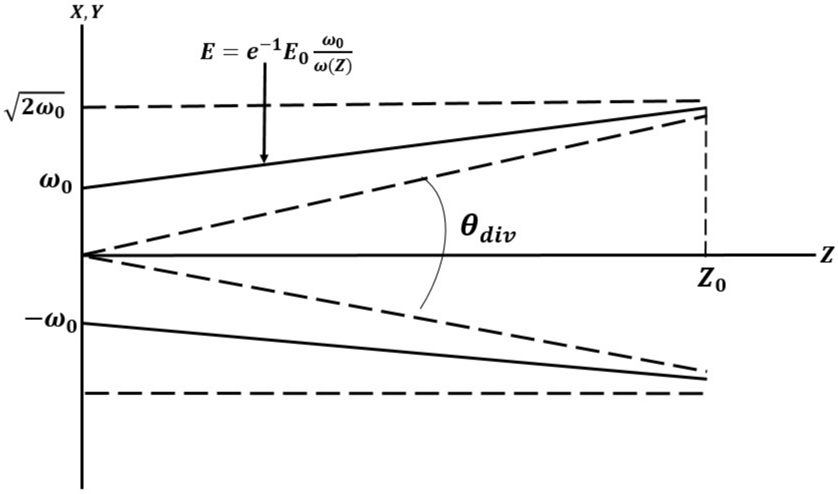

Figure 2.2: Divergence of a Gaussian beam.

For visible wavelengths, divergences are small (approximately a milliradian for a conventional HeNe laser). The minimum focused spot size can be calculated, as shown in Fig. 2.3. A broad (slowly diverging) Gaussian beam $[\omega(z) = \omega_{01}]$ is focused by a thin lens to a diffraction-limited spot diameter of $2\omega_{02}$ located approximately one focal length from the lens.

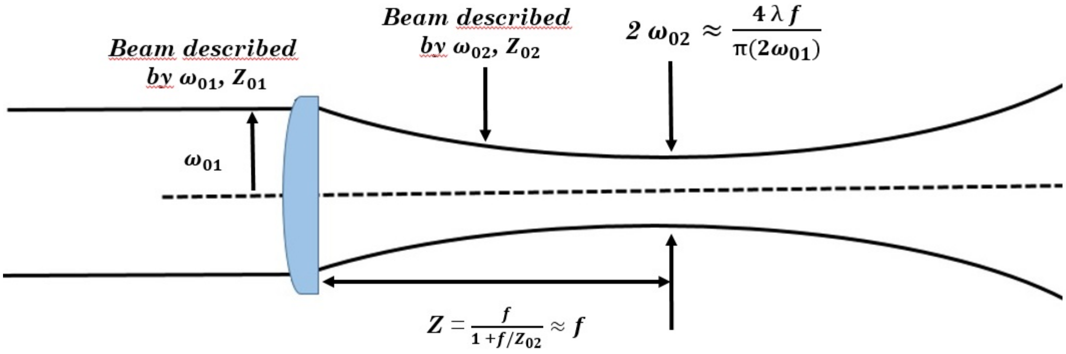

Figure 2.3: Divergence beam focused by a lens.

Beam divergence and minimum spot size are realities that will be dealt with in the design of the optical instrumentation for our polarimeter. As we will present in Chapters 4 and 5, the width of the focused source beam in a polarimetric scatterometer limits the largest measurable value of the instrument, and divergence limits the ability to work with long thin beams. However, the plane-wave approach to analysing wave behaviour is a useful tool in this work.

2.2 Formalism of polarized light

At the beginning of the nineteenth century Young and Fresnel demonstrated the transverse vibration of light and the concept of polarization wave with the development of electromagnetism. Two formalisms were used for this description, that of Jones and that of Stokes. However, nowadays one of the most used techniques to describe the polarizing properties of objects is the method of Stokes vectors and Mueller matrices, which we describe briefly in this section. This technique is advantageous over similar ones (such as that of the Jones vectors and matrices) because completely polarized states as well as unpolarized and partially polarized states can be described [65],[37].

An advantage of the matrix methods for this type of studies is that, with a beam of light that passes through different optical elements, the study of the total effect of the elements in the polarization of the beam can be obtained directly by multiplying the Stokes vector incident on each optical element by the corresponding Mueller matrix, simplifying the calculation of the final state of polarization.

2.2.1 Polarization of light

We are only interested here in the case of monochromatic plane waves. By convention, the polarization of an electromagnetic wave describes the evolution of the electric field **E** at a given point of space, the evolution of the magnetic field **H** can be deduced using Maxwell's equations.

The electric field **E** is perpendicular to the direction of propagation. If its behaviour is totally disordered, the wave will be called depolarized. If it is ordered, the figure that it describes defines the state of polarization, which may be elliptical or linear, Fig. 2.4. In general, a wave may be partially polarized which is the superposition of a depolarized contribution and a polarized contribution.

Electric field

Given a plane wave with a direction of propagation **k**, Maxwell's equations impose that the electric and magnetic field should be perpendicular to the direction of propagation and to each other. Conventionally, when considering polarization, only the electric field vector is described, since the magnetic field is perpendicular to the electric field and proportional to it. In a properly chosen orthogonal coordinate system, the electric field vector of a plane wave propagating along the z-axis ($\mathbf{k} \equiv \mathbf{z}$) can be written in the form

$$\mathbf{E}(z,t) = \begin{bmatrix} E_x \\ E_y \\ 0 \end{bmatrix} = \begin{bmatrix} E_{x,0} cos(\omega t - kz + \varphi_x) \\ E_{y,0} cos(\omega t - kz + \varphi_x) \\ 0 \end{bmatrix}, \tag{2.33}$$

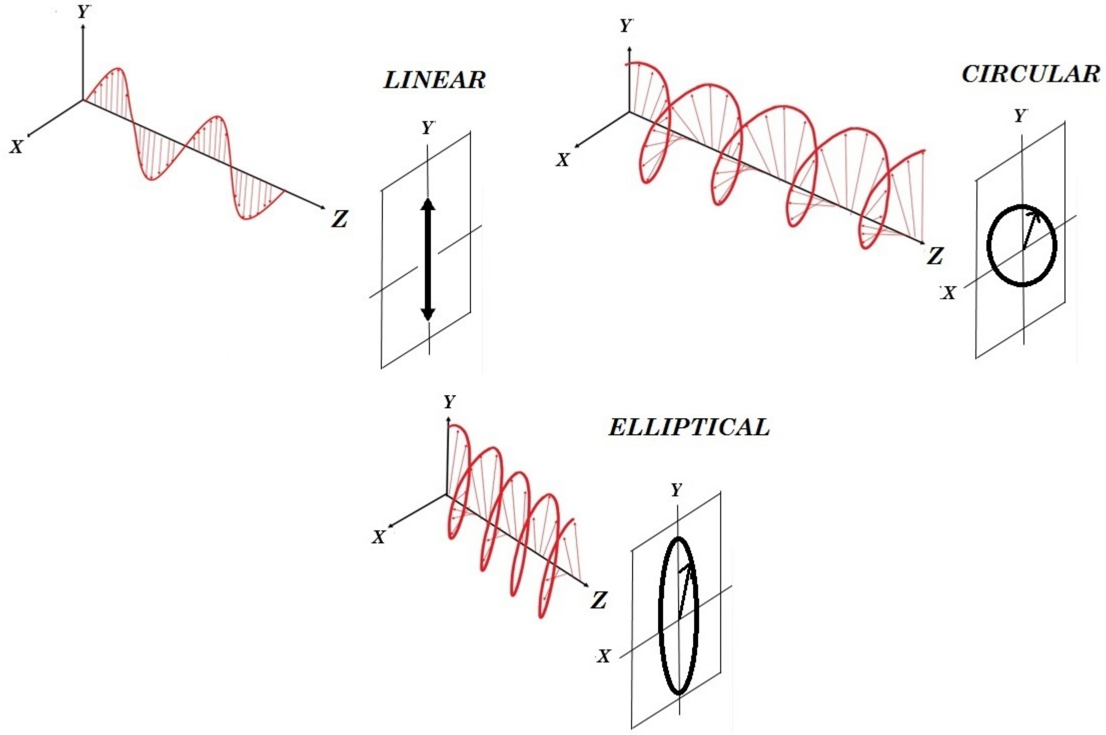

Figure 2.4: Polarization states for totally polarized light.

where the amplitudes E_{x0} and E_{y0} are real numbers. The polarization state is given by the relative difference in magnitude and phase between these components. If we consider the electric field at a certain point z as a function of time, Eq. 2.33 with a fixed value we obtain the representation of an ellipse in the plane xy Fig. 2.5. The parameters that describe the ellipse are the azimuth $\theta \in [-\frac{\pi}{2}, \frac{\pi}{2}]$ and the ellipticity[1] $\epsilon \in [-\frac{\pi}{4}, \frac{\pi}{4}]$. For a vanishing ellipticity the two components of the electric field are in phase and the light wave is linearly polarized. When $\epsilon \pm \frac{\pi}{4}$ the polarization is circular. When ϵ does not satisfy any of the above conditions the light wave is elliptically polarized.

The handedness of the ellipse of polarization determines the sense in which the ellipse is described. The polarization is *right-handed* if the field vector rotates clockwise when looking against the direction of $\mathbf{k}$ (i.e. looking "into the beam" for a travelling wave). Similarly, the polarization is *left-handed* for a counter clockwise rotation sense.

---

[1] Usually the ellipticity is given as $e = \pm tan(\epsilon)$ where the + and - signs correspond to right- and left-handed polarizations, respectively. In these cases ϵ is referred to as *ellipticity angle.*

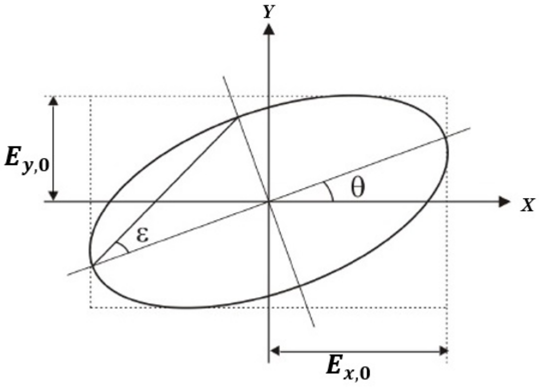

Figure 2.5: Polarization Ellipse.

2.2.2 Derivation of the Stokes polarization parameters and Mueller matrices

We consider a pair of plane waves that are orthogonal to each other at a point in space, conveniently taken to be $z = 0$, and not necessarily monochromatic, to be represented by the equations:

$$E_x(t) = E_{0x}(t) cos[\omega t + \varphi_x(t)], \tag{2.34}$$

$$E_y(t) = E_{0y}(t) cos[\omega t + \varphi_y(t)], \tag{2.35}$$

where E_{0x} and E_{0y} are the instantaneous amplitudes, ω is the instantaneous angular frequency, and $\varphi_x(t)$ and $\varphi_y(t)$ are the instantaneous phase factors. At all times the amplitudes and phase factors fluctuate slowly compared to the rapid vibrations of the cosinusoids. It is possible to obtain the polarization ellipse for an electromagnetic wave. To do that, we multiply equation 2.34 by the factor $E_{0y}(t) sin\varphi_y(t)$, and obtain

$$E_x(t)E_{0y}(t) sin\varphi_y(t) = E_{0x}(t)E_{0y}(t) cos(\omega t + \varphi_x(t)) sin\varphi_y(t). \tag{2.36}$$

Then, Eq. 2.35 is multiplied by the factor $E_{0x}(t) sin\varphi_x(t)$, we have

$$E_y(t)E_{0x}(t) sin\varphi_x(t) = E_{0x}(t)E_{0y}(t) cos(\omega t + \varphi_y(t)) sin\varphi_x(t). \tag{2.37}$$

Once this is done, the cosines of the sums are expanded in each of the previous equations and we take the difference between them, the result is squared and simplified to obtain

$$E_x^2(t)E_{0y}^2(t) sin^2\varphi_y(t) + E_y^2(t)E_{0x}^2(t) sin^2\varphi_x(t) - 2E_x(t)E_y(t)E_{0x}(t)E_{oy}(t) sin\varphi_x(t) sin\varphi_y(t) =$$

$$E_{0x}^2(t)E_{0y}^2(t)cos^2\omega t sin^2(\varphi_y(t)-\varphi_x(t)). \tag{2.38}$$

On the other hand, if we now multiply equation 2.34 by $E_{0y}(t)cos\varphi_y(t)$ and Eq. 2.35 by $E_{0x}(t)cos\varphi_x(t)$ we obtain:

$$E_x(t)E_{0y}(t)cos\varphi_y(t) = E_{0x}(t)E_{oy}(t)cos(\omega t+\varphi_x(t))cos\varphi_y(t), \tag{2.39}$$

$$E_x(t)E_{0x}(t)cos\varphi_x(t) = E_{0x}(t)E_{0y}(t)cos(\omega t+\varphi_y(t))cos\varphi_x(t). \tag{2.40}$$

Similar to the previous case, we expand the cosines of the sums and we take the difference between the resulting equations, the result is squared and simplified to obtain

$$E_x^2(t)E_{0y}^2(t)cos^2\varphi_y(t)+E_y^2(t)E_{0x}^2(t)cos^2\varphi_x(t)-2E_x(t)E_y(t)E_{0x}(t)E_{0y}(t)cos\varphi_x(t)cos\varphi_y(t) =$$

$$E_{0x}^2(t)E_{0y}^2(t)sin^2\omega t sin^2(\varphi_y(t)-\varphi_x(t)). \tag{2.41}$$

From the sum of Eqs. 2.38 and 2.41 we obtain

$$E_x^2(t)E_{0y}^2(t)+E_y^2(t)E_{0x}^2(t)-2E_x(t)E_y(t)E_{0x}(t)E_{0y}(t)cos(\varphi_y(t)-\varphi_x(t)) =$$

$$E_{0x}^2(t)E_{0y}^2(t)sin^2(\varphi_y(t)-\varphi_x(t))). \tag{2.42}$$

Finally, dividing Eq. 2.42 by $(E_{0x})^2(E_{0y)^2}$, we get

$$\frac{E_x^2(t)}{E_{0x}^2(t)}+\frac{E_y^2(t)}{E_{0y}^2(t)}-\frac{2E_x(t)E_y(t)}{E_{0x}(t)E_{0y}(t)}cos\varphi(t) = sin^2\varphi(t), \tag{2.43}$$

where $\varphi(t)=\varphi_y(t)-\varphi_x(t)$. Eq. 2.43 is valid for a moment of time and is known as the polarization ellipse. We need to notice that the polarization ellipse was obtained by getting rid of the explicit dependence in equation 2.34 and 2.35 on ω. This ellipse tells us the state of vibration of the electric field of an electromagnetic wave as a function of the phase difference between x and y.

For monochromatic radiation, the amplitudes and phases differences are constant for all time, so 2.43 reduces to

$$\frac{E_x^2(t)}{E_{0x}^2}+\frac{E_y^2(t)}{E_{0y}^2}-\frac{2E_x(t)E_y(t)}{E_{0x}E_{0y}}cos\varphi(t) = sin^2\varphi. \tag{2.44}$$

While E_{0x}, E_{0y}, and φ are constants, E_x and Ey continue to be implicitly dependent on time, as we see from Eqs. 2.34 and 2.35. We want to write this equation in terms of physical observables, and no detector measures instantaneous values of the field in an electromagnetic wave, so a temporary average of the previous equation must be made. The time average is represented by the symbol $\langle ... \rangle$ and so we write the Eq. 2.44 as

$$\frac{\langle E_x^2(t)\rangle}{E_{0x}^2}+\frac{\langle E_y^2(t)\rangle}{E_{0y}^2}-\frac{\langle 2E_x(t)E_y(t)\rangle}{E_{0x}E_{0y}}cos\varphi(t)=sin^2\varphi(2.45)$$

where

$$\langle E_i(t)E_j(t)\rangle=\lim_{T\to\infty}\frac{1}{T}\int_0^T E_i(t)E_j(t)dt \qquad i,j=x,y \tag{2.46}$$

which is an average over the time of observation. In view of the periodicity of $E_x(t)$ and $E_y(t)$, we need average Eq. 2.44 only over a single period of oscillation. Multiplying Eq. 2.45 by $4E_{0x}^2E_{0y}^2$, we see that

$$4E_{0y}^2\langle E_x^2(t)\rangle+4E_{0x}^2\langle E_y^2(t)\rangle-8E_{0x}E_{0y}\langle E_{x(}(t)E_y(t)\rangle cos\varphi=(2E_{0x}E_{0y}sin\varphi)^2 \tag{2.47}$$

From Eqs. 2.34 and 2.35, we then find that the average values of Eq. 2.47 using Eq. 2.46 are

$$\langle E_x^2(t)\rangle=\frac{1}{2}E_{0x}^2, \tag{2.48}$$

$$\langle E_y^2(t)\rangle=\frac{1}{2}E_{0y}^2, \tag{2.49}$$

$$\langle E_x^2(t)E_y^2(t)\rangle=\frac{1}{2}E_{0x}^2E_{0y}^2cos\varphi. \tag{2.50}$$

Substituting Eqs. 2.48, 2.49 and 2.50 into Eq. 2.47 yields

$$2E_{0x}^2E_{0y}^2+2E_{0x}^2E_{0y}^2-(2E_{0x}E_{0y}cos\varphi)^2=(2E_{0x}E_{0y}sin\varphi)^2. \tag{2.51}$$

Since we wish to express the final result in terms of intensity, which is proportional to the square of the field, we complete the squares in Eq. 2.51. Then, we add the quantity $E_{0x}^4+E_{0y}^4$ to both sides of the Eq. 2.51 and we have

$$E_{0x}^4+E_{0y}^4+2E_{0x}^2E_{0y}^2+2E_{0x}^2E_{0y}^2-(2E_{0x}E_{0y}cos\varphi)^2=(2E_{0x}E_{0y}sin\varphi)^2+E_{0x}^4+E_{0y}^4, \tag{2.52}$$

from where

$$(E_{0x}^2+E_{0y}^2)^2-(E_{0x}^2-E_{0y}^2)^2-(2E_{0x}E_{0y}cos\varphi)^2=(2E_{0x}E_{0y}sin\varphi)^2. \tag{2.53}$$

We now write the quantities inside the parentheses as

$$S_0 = E_{0x}^2 + E_{0y}^2, \tag{2.54}$$

$$S_1 = E_{0x}^2 - E_{0y}^2, \tag{2.55}$$

$$S_2 = 2E_{0x}E_{0y}cos\varphi, \tag{2.56}$$

$$S_3 = 2E_{0x}E_{0y}sin\varphi. \tag{2.57}$$

Eqs. 2.54-2.57 define the Stokes parameters and using Eq. 2.53 we express

$$S_0^2 = S_1^2 + S_2^2 + S_3^2. \tag{2.58}$$

We see that Stokes' parameters are real quantities, and they are simply the observables of the polarization ellipse and, hence, the optical field. The first Stokes parameter S_0 is the total intensity of the light. The parameter S_1 describes the amount of liner horizontal or vertical polarization, S_2 describes the amount of linear $+45\circ$ or $-45°$ polarization, and the parameter S_3 describes the amount of right or left circular polarization contained within the beam; this correspondence will be shown shortly. We note that the four Stokes parameters are expressed in terms of intensities, and we again emphasize that the Stokes parameters are *real measurable* quantities.

If we now have partially polarized light, then we see that the relations given by Eqs. 2.54 to 2.57 continue to be valid for very short time intervals, since the amplitudes and phases fluctuate slowly. Using Schwarz's inequality[80],

$$|\int_a^b f^*(x)g(x)dx|^2 \leq \int_a^b f^*(x)f(x)dx \int_a^b g^*(x)g(x)dx, \tag{2.59}$$

it can be shown that for any state of polarized light the Stokes parameters always satisfy the relation:

$$S_0^2 \geq S_1^2 + S_2^2 + S_3^2. \tag{2.60}$$

The equality sign applies when we have completely polarized light, and the inequality sign when we have partially polarized light or unpolarized light. The orientation angle θ of the polarization ellipse [66] is given by

$$tan2\theta = \frac{2E_{0x}E_{0y}cos\varphi}{E_{0x}^2 - E_{0y}^2}. \tag{2.61}$$

Inspecting Eqs. 2.54 to 2.57 we see that if we divide Eq. 2.56 by Eq.2.55, θ can be expressed in terms of the Stokes parameters:

$$tan2\theta = \frac{S_2}{S_1}. \tag{2.62}$$

Similarly, the ellipticity angle ϵ is given by [66]

$$tan2\epsilon = \frac{2E_{0x}E_{0y}sin\varphi}{E_{0x}^2 + E_{0y}^2}. \tag{2.63}$$

Again, inspecting Eqs. 2.54 to 2.57 and dividing Eq. 2.56 by Eq.2.55, we can see that we can expressed in terms of the Stokes parameters:

$$sin2\epsilon = \frac{S_3}{S_0}. \tag{2.64}$$

The Stokes parameters enable us to describe the degree of polarization P for any state of polarization. By definition,

$$P = \frac{I_{pol}}{I_{tot}} = \frac{(S_1^2 + S_2^2 + S_3^2)^{1/2}}{S_0}, \qquad 0 \leq P \leq 1, \tag{2.65}$$

where I_{pol} is the intensity of the sum of the polarization components and I_{tot} is the total intensity of the beam. The value of $P = 1$ corresponds to completely polarized light, $P = 0$ corresponds to unpolarized light, and $0 < P < 1$ corresponds to partially polarized light.

To obtain the Stokes parameters of an optical beam, one must always take a time average of the polarization ellipse. However, the time-averaging process can be formally bypassed by representing the (real) optical amplitudes, Eqs. 2.34 and 2.35, in terms of complex amplitudes:

$$E_x(t) = E_{0x}e^{i(\omega t + \varphi_x)} = E_x e^{(i\omega t)}, \tag{2.66}$$

$$E_y(t) = E_{0y}e^{i(\omega t + \varphi_y)} = E_y e^{(i\omega t)}, \tag{2.67}$$

where

$$E_x = E_{0x}e^{i(\varphi_x)}, \tag{2.68}$$

and

$$E_y = E_{0y}e^{i(\varphi_y)}, \tag{2.69}$$

are complex amplitudes. The Stokes parameters for a plane wave are now obtained from the formulas:

$$S_0 = E_x E_x^* + E_y E_y^*, \tag{2.70}$$

$$S_1 = E_x E_x^* - E_y E_y^*, \tag{2.71}$$

$$S_2 = E_x E_y^* + E_y E_x^*, \tag{2.72}$$

$$S_3 = i(E_x E_y^* - E_y E_x^*). \tag{2.73}$$

We shall use Eqs.2.70-2.73, the complex representation, henceforth, as the defining equations for the Stokes parameters. Substituting Eq. 2.68 and 2.69 into the Stokes parameters S_0, S_1, S_2 and S_3 gives

$$S_0 = E_{0x}^2 + E_{0y}^2, \tag{2.74}$$

$$S_1 = E_{0x}^2 - E_{0y}^2, \tag{2.75}$$

$$S_2 = 2E_{0x}E_{0y}cos\varphi, \tag{2.76}$$

$$S_3 = 2E_{0x}E_{0y}sin\varphi, \tag{2.77}$$

which are the Stokes parameters obtained formally from the polarization ellipse. As examples of the representation of polarized light in terms of the Stokes parameters, we consider linear horizontal and linear vertical polarized light, linear +45° and linear −45° polarized light, and right and left circularly polarized light.

Linear Horizontally Polarized Light. For this case $E_{0y} = 0$. Then, from Eq. 2.74 we have

$$S_0 = E_{0x}^2, \tag{2.78}$$

$$S_1 = E_{0x}^2, \tag{2.79}$$

$$S_2 = 0, \tag{2.80}$$

$$S_3 = 0. \tag{2.81}$$

Linear Vertically Polarized Light. For this case $E_{0x} = 0$. Then, from Eq. 2.75 we have

$$S_0 = E_{0y}^2, \tag{2.82}$$

$$S_1 = -E_{0y}^2, \tag{2.83}$$

$$S_2 = 0, \tag{2.84}$$

$$S_3 = 0. \tag{2.85}$$

Linear +45° Polarized Light. For this case $E_{0x} = E_{0y} = E_0$ and $\varphi = 0$. Using the Eqs. 2.74-2.77, we find that

$$S_0 = 2E_0^2, \tag{2.86}$$

$$S_1 = 0, \tag{2.87}$$

$$S_2 = 2E_0^2, \tag{2.88}$$

$$S_3 = 0. \tag{2.89}$$

Linear −45° Polarized Light. The conditions on the amplitude are the same as for the case +45, but the phase difference is $\varphi = 180°$. Then, from Eqs. 2.74-2.77, we find that

$$S_0 = 2E_0^2, \tag{2.90}$$

$$S_1 = 0, \tag{2.91}$$

$$S_2 = -2E_0^2, \tag{2.92}$$

$$S_3 = 0. \tag{2.93}$$

Right Circularly Polarized Light. The conditions in this case are $E_{0x} = E_{0y} = E_0$ and $\varphi = 90°$. From Eqs. 2.74-2.77 the Stokes parameters are then

$$S_0 = 2E_0^2, \tag{2.94}$$

$$S_1 = 0, \tag{2.95}$$

$$S_2 = 0, \tag{2.96}$$

$$S_3 = 2E_0^2. \tag{2.97}$$

Left Circularly Polarized Light. For this case the amplitudes are again equal, but the phase shift between the orthogonal, transverse components is $\varphi = -90°$. The Stokes parameters from Eqs. 2.74-2.77 are then

$$S_0 = 2E_0^2, \tag{2.98}$$

$$S_1 = 0, \tag{2.99}$$

$$S_2 = 0, \tag{2.100}$$

$$S_3 = -2E_0^2. \tag{2.101}$$

Finally, the Stokes parameters for elliptically polarized light are, of course, given by Eqs. 2.74-2.77. Inspection of the four Stokes parameters suggests that they can be arranged in the form of a column matrix. This column matrix is called the Stokes vector. This step, while simple, provides a formal method for treating numerous complicated problems involving polarized light. We define

$$S = \begin{bmatrix} S_0 \\ S_1 \\ S_2 \\ S_3 \end{bmatrix} = \begin{bmatrix} I \\ Q \\ U \\ V \end{bmatrix}, \tag{2.102}$$

where S_1, S_2, S_3 and S_4 are the four Stokes parameters and we rename these as I, Q, U and V. Using Eq. 2.60 and 2.102 we can write

$$I^2 \geq Q^2 + U^2 + V^2. \tag{2.103}$$

Also, the degree of polarization can be write as

$$P = \frac{\sqrt{Q^2 + U^2 + V^2}}{I}. \tag{2.104}$$

According to Eq. 2.60, $0 \leq P \leq 1$, P is equal to 0 for a totally depolarized wave and 1 for a totally polarized wave. The Stokes vector for elliptically polarized light is then written from Eqs. 2.74-2.77 as

$$S = \begin{bmatrix} E_{0x}^2 + E_{0y}^2 \\ E_{0x}^2 - E_{0y}^2 \\ 2E_{0x}E_{0y}cos\varphi \\ 2E_{0x}E_{0y}sin\varphi \end{bmatrix}. \tag{2.105}$$

Equation 2.105 is also called the Stokes vector for a plane wave [66]. It can be expressed in terms of measurable quantities, namely the intensities in different directions of linear and circular polarization:

$$S = \begin{bmatrix} I \\ Q \\ U \\ V \end{bmatrix} = \begin{bmatrix} I_{0^\circ} + I_{90^\circ} \\ I_{0^\circ} - I_{90^\circ} \\ I_{+45^\circ} + I_{-45^\circ} \\ I_L + I_R \end{bmatrix} = \begin{bmatrix} I_H + I_V \\ I_H - I_V \\ I_{+45^\circ} + I_{-45^\circ} \\ I_L + I_R \end{bmatrix}. \tag{2.106}$$

Table 2.1 presents Stokes vectors for polarization states which are frequently used.

2.3 Mueller matrices

In the general case, we can describe the transformation of any polarization state by a real 4x4 matrix called the Mueller matrix. The modification of an incident wave of Stokes vector $\mathbf{S}$ into a wave with Stokes vector $\mathbf{S}'$ can be described by

$$\mathbf{S}' = \mathbf{M} \cdot \mathbf{S}, \tag{2.107}$$

H	V	+45	-45	Right	Left
$\begin{bmatrix}1\\1\\0\\0\end{bmatrix}$	$\begin{bmatrix}1\\-1\\0\\0\end{bmatrix}$	$\begin{bmatrix}1\\0\\1\\0\end{bmatrix}$	$\begin{bmatrix}1\\0\\-1\\0\end{bmatrix}$	$\begin{bmatrix}1\\0\\0\\1\end{bmatrix}$	$\begin{bmatrix}1\\0\\0\\-1\end{bmatrix}$

Table 2.1: Stokes vectors of degenerate polarization states. From left to right:linear horizontal (0°), linear vertical (90°), linear +45°, linear −45°, Right Circular (Right) and Left Circular (Left).

$$\begin{bmatrix}S_0'\\S_1'\\S_2'\\S_3'\end{bmatrix} = \begin{bmatrix}M_{11} & M_{12} & M_{13} & M_{14}\\M_{21} & M_{22} & M_{23} & M_{44}\\M_{31} & M_{32} & M_{33} & M_{34}\\M_{41} & M_{42} & M_{43} & M_{44}\end{bmatrix}\begin{bmatrix}S_0\\S_1\\S_2\\S_3\end{bmatrix}. \tag{2.108}$$

In this work, the Mueller matrices will always, unless explicitly stated otherwise, be normalized by the term M_{11}.

$$\begin{bmatrix}1 & M_{12}/M_{11} & M_{13}/M_{11} & M_{14}/M_{11}\\M_{21}/M_{11} & M_{22}/M_{11} & M_{23}/M_{11} & M_{24}/M_{11}\\M_{31}/M_{11} & M_{32}/M_{11} & M_{33}/M_{11} & M_{34}/M_{11}\\M_{41}/M_{11} & M_{42}/M_{11} & M_{43}/M_{11} & M_{44}/M_{11}\end{bmatrix}. \tag{2.109}$$

The first element M_{11} represents the intensity modification of a totally depolarized beam after interaction with the system. Following the inequality of Eq. 2.103, a Mueller matrix must obey the relationships $M_{11} \geq 0$ and $|M_{ij}| \leq M_{11}$, $\forall i, j$, which implies in particular that the elements of the normalized Mueller matrix will be between -1 and 1.

2.3.1 Polarimetry properties

We will focus on different basic properties that allow us to analyse and to characterize Mueller matrices. Physically, a non-depolarizing optical element modifies the polarization of light by changing the amplitudes or phases of the components of the electric field vector. Two basic properties then appear naturally. A *diattenuator* (also called a dichroic, we will use these two terms indifferently) modifies the amplitudes of the components of the electric field vector differently. A *retarder* only changes the phases of these components [66],[76]-[77].

Diattenuation (or dichroism)

The *Diattenuation* D (or dichroism) of a polarizing element is defined as [66]

$$D \equiv \frac{T_{max} - T_{min}}{T_{max} + T_{min}}, \tag{2.110}$$

where T_{max} and T_{min} are respectively the maximum and minimum transmission rates. Diattenuation characterizes the dependence of the transmission as a function of the incident polarization state. As different diattenuators can have the same scalar diattenuation, it is necessary to define vector dichroism. The direction is defined as that of the polarization state at the highest transmission rate[2]. Let $(1, d_1, d_2, d_3)^t$ be the Stokes vector of such an eigenvector. We define $\mathbf{D}$ as

$$\mathbf{D} \equiv D \begin{bmatrix} d_1 \\ d_2 \\ d_3 \end{bmatrix} = \begin{bmatrix} D_H \\ D_{45^\circ} \\ D_C \\ 0 \end{bmatrix}, \tag{2.111}$$

The 3 components are horizontal, 45 and circular diattenuation respectively. The linear diattenuation can be defined by $D_L = \sqrt{D_H^2 + D_{45^\circ}^2}$. As the diattenuation is given by the relation between the intensity of the outgoing beam depending on the components of the incident polarization state, it can be read directly on the Mueller matrix and is fully defined by its first row:

$$\mathbf{D} = \frac{1}{M_{11}} \begin{bmatrix} M_{12} \\ M_{13} \\ M_{14} \end{bmatrix}. \tag{2.112}$$

The Mueller matrix of a pure diattenuator is

$$\mathbf{M}_D = T_u \begin{bmatrix} 1 & \mathbf{D}^t \\ \mathbf{D} & \mathbf{m}_D \end{bmatrix}, \tag{2.113}$$

where $\mathbf{D}$ is the 3 x 1 diattenuation vector and m_D is a 3 x 3 symmetric submatrix (i.e., superscript "t" denoting a vector or matrix transpose). The latter can be obtained from $\mathbf{D}$ as

$$\mathbf{m}_D = \sqrt{1 - D^2}\mathbf{Id} + (1 - \sqrt{1 - D^2})\frac{\mathbf{D}\mathbf{D}^t}{D^2}, \tag{2.114}$$

with $D = \parallel D \parallel$ ($\parallel \cdot \parallel$ denotes Euclidean vector norm), and where $\mathbf{Id}$ is the 3 x 3 identity matrix and T_u is the transmission rate for for a non-polarized incident

---

[2] For a homogeneous optical element, this direction is that of a natural state of polarization, and T_{max} and T_{min} in 2.110 are the transmission rates of the eigenstates. These properties are not true for an inhomogeneous element.

state. This matrix is symmetrical and it has 4 degrees of freedom: the 3 components of the diattenuation vector and the transmission rate for unpolarized light. The maximum and minimum transmission rates can also be written according to elements of the Mueller matrix

$$T_{max} = M_{11} + \sqrt{M_{12}^2 + M_{13}^2 + M_{14}^2} = M_{11}(1 + D), \tag{2.115}$$

$$T_{min} = M_{11} - \sqrt{M_{12}^2 + M_{13}^2 + M_{14}^2} = M_{11}(1 - D). \tag{2.116}$$

There are also incident polarization states associated with these transmission rates, $\mathbf{S}_{max} = (1, \mathbf{s}_{max})^t$ and $\mathbf{S}_{min} = (1, \mathbf{s}_{min})^t$

$$\mathbf{s}_{max} = \frac{1}{\sqrt{M_{12}^2 + M_{13}^2 + M_{14}^2}} \begin{bmatrix} M_{12} \\ M_{13} \\ M_{14} \end{bmatrix} = \frac{1}{M_{11}D} \begin{bmatrix} M_{12} \\ M_{13} \\ M_{14} \end{bmatrix} \tag{2.117}$$

$$\mathbf{s}_{min} = -\mathbf{s}_{max} \tag{2.118}$$

Note that $\mathbf{S}_{max}$ and $\mathbf{S}_{min}$ are orthogonal states.

2.3.2 Polarizance

We consider an entirely unpolarized incident polarization state $\mathbf{S}_i = (1, 0, 0, 0)^t$. The outgoing polarization state is entirely defined by the first column of the Mueller matrix. Its degree of polarization, called *polarizance* is defined as

$$P = \frac{1}{M_{11}} \sqrt{M_{21}^2 + M_{31}^2 + M_{41}^2}. \tag{2.119}$$

The vector polarizance can be defined as

$$\mathbf{P} = \frac{1}{M_{11}} \begin{bmatrix} M_{21} \\ M_{31} \\ M_{41} \end{bmatrix} = \begin{bmatrix} P_H \\ P_{45^\circ} \\ P_C \end{bmatrix}. \tag{2.120}$$

The outgoing polarization state is $M_{11}(1, \mathbf{P})^t$. It is also the state of average outgoing polarization if one integrates on the Poincaré sphere for the polarization state of the incident beam. For a non-depolarizing element, we can show that $D = P$ [78] and that we therefore have the relationship

$$M_{12}^2 + M_{13}^2 + M_{14}^2 = M_{21}^2 + M_{31}^2 + M_{41}^2. \tag{2.121}$$

It is also shown that a non-depolarizing Mueller matrix is homogeneous if and only if $\mathbf{D} = \mathbf{P}$.

2.3.3 Retardance (or birefringence)

A retarder modifies the phases of its own polarization states differently, but not their amplitudes, thus introducing a phase shift. The transmission rate does not depend on the incident wave. For a homogeneous optical element, we can define the scalar delay as

$$R \equiv |\delta_q - \delta_r|, \qquad 0 \leq R \leq \pi \tag{2.122}$$

where δ_{ij} are the phase changes of its eigenstates. The fast axis of the retarder is defined as the direction of the eigenstate that first emerges from the retarder, which is forward in phase. Let $(1, r_1, r_2, r_3)^t$ be the Stokes vector of this eigenvector, with $\sqrt{r_1^2 + r_2^2 + r_3^2} = 1$. We can define the *retardance vector* **R**

$$\mathbf{R} \equiv R \begin{bmatrix} r_1 \\ r_2 \\ r_3 \end{bmatrix} = \begin{bmatrix} R_H \\ R_{45} \\ R_C \end{bmatrix}. \tag{2.123}$$

The *linear* retardance can be defined by $R_L = \sqrt{R_H^2 + R_{45}^2}$.

The matrix of a retarder is unitary. It is fully described by the retardance vector **R**. Its effect is a rotation in the Poincare sphere. It is given by [79]

$$\mathbf{M}_R = \begin{bmatrix} 1 & \mathbf{0}^t \\ \mathbf{0} & \mathbf{m}_R \end{bmatrix}, \tag{2.124}$$

$$(\mathbf{m}_R)_{ij} = \delta_{ij} cosR + r_i rj(1 - cosR) + \sum_{k=1}^{3} \epsilon_{ijk} r_k sinR, \tag{2.125}$$

where δ_{ij} is the Kronecker symbol and ϵ_{ijk} the permutation symbol of Levi-Civita [80]. It can be noted that m_R is a rotation matrix in $\mathbb{R}^3$. The matrix of the retarder has 3 degrees of freedom, which are given by its retardance vector **R**. We can determine the retardance vector from the Mueller matrix $\mathbf{M}_R$ by

$$R = arcos\left[\frac{tr(\mathbf{M}_R)}{2} - 1\right], \tag{2.126}$$

$$r_i = \frac{1}{2sinR} \sum_{j,k=1}^{3} \epsilon_{ijk} (\mathbf{m}_R)_{jk}. \tag{2.127}$$

2.3.4 Depolarization

An optical element may have depolarization, due to a lack of coherence, it can be spatial, temporal or spectral. We define several indicators or properties to characterize it. In the same way that polarization represented the average polarization state at the output, the quadratic depolarization

$$\Delta_m = 1 - \sqrt{\frac{Tr(\mathbf{M}^t\mathbf{M}) - M_{11}^2}{3M_{11}^2}} \tag{2.128}$$

of any Mueller matrix $\mathbf{M}$, represents the average value of depolarization when integrated over the entire Poincaré sphere for incident polarization states. Δ_m varies between 0 for a non-depolarizing matrix to 1 for a totally depolarizing matrix. The condition

$$Tr(\mathbf{M}^t\mathbf{M}) = 4M_{11}^2 \tag{2.129}$$

gives $\Delta_m = 0$ which is necessary and sufficient for the Mueller matrix to be perfectly non-depolarizing and is equivalent to a Jones matrix[3] [81], [82], [83]. A pure depolarizer can be written as [79]

$$\mathbf{M}_\Delta = \begin{bmatrix} 1 & \mathbf{0}^t \\ \mathbf{0} & \mathbf{m}_\Delta \end{bmatrix}, \tag{2.130}$$

where m_Δ is a 3x3 symmetrical matrix, so is diagonalizable in a orthonormal base. This matrix has 6 degrees of freedom. We can represent $\mathbf{M}_\Delta$ after a base change by

$$\mathbf{M}_\Delta = \begin{bmatrix} 1 & 0 & 0 & 0 \\ 0 & a & 0 & 0 \\ 0 & 0 & b & 0 \\ 0 & 0 & 0 & c \end{bmatrix}, \qquad a, b, c \quad \in \quad [-1, 1]. \tag{2.131}$$

a, b and *c* determine the depolarization along the 3 proper axes. We then define the main depolarization.

$$\rho^{dep} = 1 - \frac{|a| + |b| + |c|}{3} \tag{2.132}$$

or in form more generally

$$\rho^{dep} = 1 - \frac{Tr(|\mathbf{M}_\Delta|) - M_{11}}{3M_{11}(2.133)}$$

---

[3] This condition is only enough if the matrix $\mathbf{M}$ is physically feasible. Otherwise, it is only necessary [84],[85], [86].

and we find a formula similar to that of the quadratic depolarization.

2.3.5 Typical matrices

In Tables 2.3.5 to 2.6 some Mueller matrices of typical elements [77] are presented. The matrices of a linear diattenuator and a retarder are of particular importance, as they allow us to describe many matrices and will be used frequently during the calibration procedure.

Air/vacuum	**Absorber**
$\begin{bmatrix}1&0&0&0\\0&1&0&0\\0&0&1&0\\0&0&0&1\end{bmatrix}$	$\begin{bmatrix}a&0&0&0\\0&a&0&0\\0&0&a&0\\0&0&0&a\end{bmatrix}$

Table 2.2: Elementary Mueller Matrices.

Linear polarizer oriented at $0°$	**Linear polarizer oriented at** $90°$
$\frac{\tau}{2}\begin{bmatrix}1 & 1 & 0 & 0\\ 1 & 1 & 0 & 0\\ 0 & 0 & 0 & 0\\ 0 & 0 & 0 & 0\end{bmatrix}$	$\frac{\tau}{2}\begin{bmatrix}1 & -1 & 0 & 0\\ -1 & 1 & 0 & 0\\ 0 & 0 & 0 & 0\\ 0 & 0 & 0 & 0\end{bmatrix}$
Linear polarizer oriented at $45°$	**Circular polarizer**
$\frac{\tau}{2}\begin{bmatrix}1 & 0 & 1 & 0\\ 0 & 0 & 0 & 0\\ 1 & 0 & 1 & 0\\ 0 & 0 & 0 & 0\end{bmatrix}$	$\frac{\tau}{2}\begin{bmatrix}1 & 0 & 0 & \pm 1\\ 0 & 0 & 0 & 0\\ 0 & 0 & 0 & 0\\ \pm 1 & 0 & 0 & 1\end{bmatrix}$
Linear Diattenuator at $0°$	**Linear Diattenuator at** $45°$
$\frac{1}{2}\begin{bmatrix}q{+}r & q\text{-}r & 0 & 0\\ q\text{-}r & q{+}r & 0 & 0\\ 0 & 0 & 2\sqrt{qr} & 0\\ 0 & 0 & 0 & 2\sqrt{qr}\end{bmatrix}$	$\frac{1}{2}\begin{bmatrix}q{+}r & 0 & q\text{-}r & 0\\ 0 & 2\sqrt{qr} & 0 & 0\\ q\text{-}r & 0 & q{+}r & 0\\ 0 & 0 & 0 & 2\sqrt{qr}\end{bmatrix}$
Linear Diattenuator at θ**, Transmission rate** q, r	
$\frac{1}{2}\begin{bmatrix}q{+}r & (q{-}r)\cos 2\theta & (q{-}r)\sin 2\theta & 0\\ (q{-}r)\cos 2\theta & (q{+}r)\cos^2 2\theta + 2\sqrt{qr}\ sin^2 2\theta & (q{+}r{-}2\sqrt{qr}) sin 2\theta cos 2\theta & 0\\ (q{-}r)\sin 2\theta & (q{+}r{-}2\sqrt{qr}) sin 2\theta cos 2\theta & (q{+}r)\sin^2 2\theta + 2\sqrt{qr}\ cos^2 2\theta & 0\\ 0 & 0 & 0 & 2\sqrt{qr}\end{bmatrix}$	

Table 2.3: Diattenuators. τ is the transmission rate for a particular case

Ideal Depolarizer	**Partial Depolarizer**
$\begin{bmatrix}1 & 0 & 0 & 0\\ 0 & 0 & 0 & 0\\ 0 & 0 & 0 & 0\\ 0 & 0 & 0 & 0\end{bmatrix}$	$\begin{bmatrix}1 & 0 & 0 & 0\\ 0 & a & 0 & 0\\ 0 & 0 & b & 0\\ 0 & 0 & 0 & c\end{bmatrix}$

Table 2.4: Depolarizers.

Ideal Mirror or half-wave plate at 45°	**Quarter wave plate at 0°**
$\begin{bmatrix}1 & 0 & 0 & 0\\ 0 & 1 & 0 & 0\\ 0 & 0 & -1 & 0\\ 0 & 0 & 0 & -1\end{bmatrix}$	$\begin{bmatrix}1 & 0 & 0 & 0\\ 0 & 1 & 0 & 0\\ 0 & 0 & 0 & 1\\ 0 & 0 & -1 & 0\end{bmatrix}$
Linear birefringent oriented at 0°	Linear birefringent oriented at 90°
$\begin{bmatrix}1 & 0 & 0 & 0\\ 0 & 1 & 0 & 0\\ 0 & 0 & \mathrm{cos}\Delta & \mathrm{sin}\Delta\\ 0 & 0 & \text{-}\mathrm{sin}\Delta & \mathrm{cos}\Delta\end{bmatrix}$	$\begin{bmatrix}1 & 0 & 0 & 0\\ 0 & 1 & 0 & 0\\ 0 & 0 & \mathrm{cos}\Delta & \text{-}\mathrm{sin}\Delta\\ 0 & 0 & \mathrm{sin}\Delta & \mathrm{cos}\Delta\end{bmatrix}$
Birefringent linear oriented at 45°	**Birefringent circular**
$\begin{bmatrix}1 & 0 & 0 & 0\\ 0 & \mathrm{cos}\Delta & 0 & \text{-}\mathrm{sin}\Delta\\ 0 & 0 & 1 & 0\\ 0 & \mathrm{sin}\Delta & 0 & \mathrm{cos}\Delta\end{bmatrix}$	$\begin{bmatrix}1 & 0 & 0 & 0\\ 0 & \mathrm{cos}\Delta & \pm sin\Delta & 0\\ 0 & \mp sin\Delta & \mathrm{cos}\Delta\ 0 & \\ 0 & 0 & 0 & 1\end{bmatrix}$
Linear Birefringent oriented at θ	
$\frac{1}{2}\begin{bmatrix}1 & 0 & 0 & 0\\ 0 & \mathrm{cos}^2 2\theta + sin^2 2\theta cos\Delta & \mathrm{sin}2\theta cos\theta(1-cos\Delta) & \text{-}\mathrm{sin}2\theta sin\Delta\\ 0 & \mathrm{sin}2\theta cos2\theta(1-cos\Delta) & \mathrm{sin}^2 2\theta + cos^2 2\theta cos\Delta & \mathrm{cos}2\theta sin\Delta\\ 0 & \mathrm{sin}2\theta sin\Delta & \text{-}\ \mathrm{cos}2\theta sin\Delta & \mathrm{cos}\Delta\end{bmatrix}$	
Birefringent elliptical oriented at θ and the ellipticity $tan\varepsilon$	
$\frac{1}{2}\begin{bmatrix}1 & 0 & 0 & 0\\ 0 & \mathrm{D}^2 - E^2 - F^2 + G^2 & 2(\mathrm{DE} + \mathrm{FG}) & 2(\mathrm{DF}-\mathrm{EG})\\ 0 & 2(\mathrm{DE}-\mathrm{FG}) & \text{-}\ \mathrm{D}^2 + E^2 - F^2 + G^2 & 2(\mathrm{EF}+\mathrm{DG})\\ 0 & 2(\mathrm{DF} + \mathrm{EG}) & 2(\mathrm{EF} - \mathrm{DG}) & \text{-}\ \mathrm{D}^2 - E^2 + F^2 + G^2\end{bmatrix}$ $\mathrm{D} = \mathrm{cos}2\varepsilon\ cos2\theta\ sin\Delta/2$ $\mathrm{E} = \mathrm{cos}2\varepsilon\ sin2\theta\ sin\Delta/2$ $\mathrm{F} = \mathrm{sin}2\varepsilon\ sin2\Delta/2$ $\mathrm{G} = \mathrm{cos}\ \Delta/2$	

Table 2.5: Retarders.

Homogeneous Linear Dichroic Retarder, oriented at 0°
$\begin{bmatrix} 1 & -\mathrm{cos}2\Psi & 0 & 0 \\ \mathrm{cos}2\Psi & 1 & 0 & 0 \\ 0 & 0 & \mathrm{sin}2\Psi\ cos\Delta & \mathrm{sin}2\Psi\ sin\Delta \\ 0 & 0 & -\mathrm{sin}2\Psi\ sin\Delta & \mathrm{sin}2\Psi\ cos\Delta \end{bmatrix}$
Homogeneous Linear Dichroic Retarder, oriented at θ
$\begin{bmatrix} 1 & -\mathrm{C}_\theta\ cos2\Psi & -\mathrm{S}_\theta\ cos2\Psi & 0 \\ \mathrm{C}_\theta cos2\Psi & \mathrm{C}_\theta^2 + S_\theta^2 sin2\Psi cos\Delta & \mathrm{C}_\theta S_\theta(1 - sin2\Psi cos\Delta) & -\mathrm{S}_\theta sin2\Psi sin\Delta \\ -\mathrm{S}_\theta cos2\Psi & \mathrm{C}_\theta S_\theta(1 - sin2\Psi cos\Delta) & \mathrm{S}_\theta^2 + C_\theta^2 sin2\Psi cos\Delta) & \mathrm{C}_\theta sin2\Psi sin\Delta \\ 0 & \mathrm{S}_\theta sin2\Psi sin\Delta & -\mathrm{C}_\theta sin2\Psi sin\Delta & \mathrm{sin}2\Psi cos\Delta \end{bmatrix}$ $\mathrm{C}_\theta = \mathrm{cos}2\theta$ $\mathrm{S}_\theta = \mathrm{sin}2\theta$

Table 2.6: Homogeneous linear retarders (axis of retardance and dichroism combined).

Chapter 3

Polarimetry

As we have seen, the polarization state of light varies after interaction with an optical system and this variation can be characterized by the Jones matrix or in a more general setting by the Mueller matrix. The measurement of these variations constitutes polarimetry.

The implementation of a polarimeter involves a controlled modulation of input polarization states, states which are modified during the passage through the system, then analyzed, to extract the Mueller matrix of the sample studied from these measurements.

3.1 Mueller Matrix Polarimetry

In general, a Mueller matrix polarimeter consists first of all of a light source. This source can be monochromatic or broadband according to the applications and instrument specifications. The source is followed by a polarization state generator (PSG), wich modulates the polarization of the light and provides the initial polarization states. In order to be able to measure a complete Mueller matrix, these states have to be composed of at least four independent polarization states. It is well known that a minimum of 16 independent combinations of input and output Stokes vectors is required to calculate the 16 elements of the Mueller matrix of a general sample (four incident independent Stokes vectors and four detected independent Stokes vectors)[66],[87].

The controlled input polarization interacts with the studied sample, which can be, according to the configuration, by transmission, reflection, diffraction, scattering, etc. The modified polarization states are then projected on a known state basis, provided by the polarization state analyzer (PSA), before measuring the intensity using a detector.

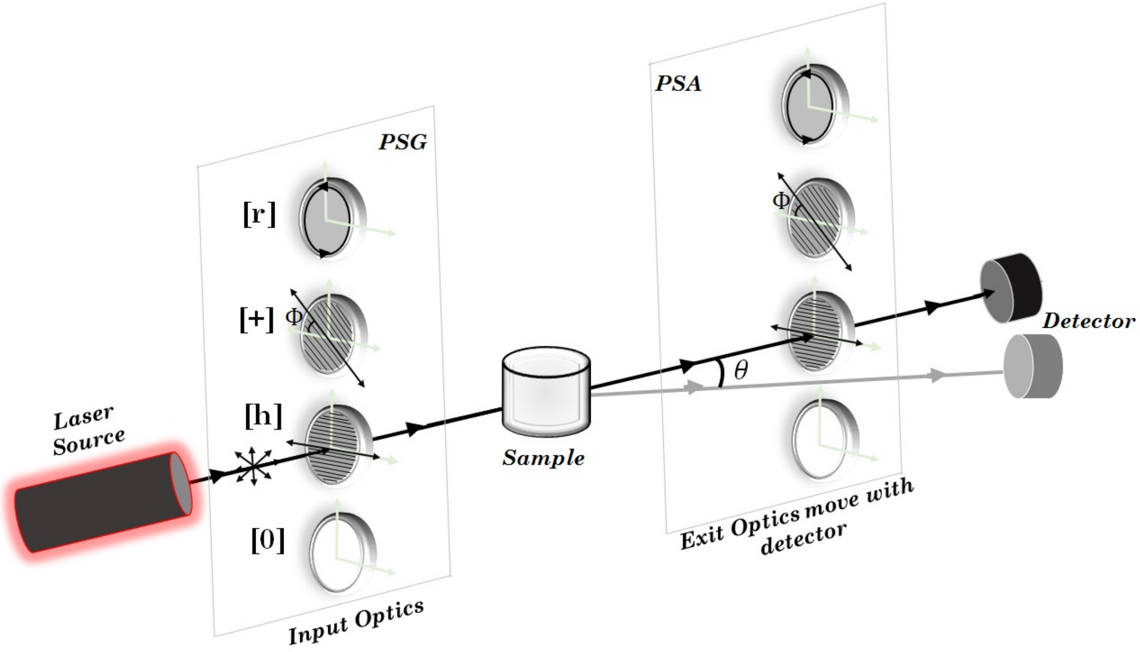

Figure 3.1: The experimental optical system used to measure all elements of the scattering matrix and polarization states. The detector can be rotated through angle $\theta = 180°$.

A typical Mueller matrix polarimeter which requires 4 independent incident polarization states and 4 independent analyzers, is shown schematically in Fig. 3.1 [87]. To obtain the complete Mueller matrix of a general sample, we present in Fig. 3.2, a diagram of the combinations polarizer-analizer used in the measurement of each element of the Mueller matrix for the polarimeter in Fig. 3.1. Depending on the polarization properties of a particular sample, and on the possible symmetries between its Mueller matrix elements, fewer measurements may be required.

Light polarization can be modulated and analyzed by a variety of approaches: rotating retardation plates [38, 66], rotating compensators [68], Pockels cells [24, 67, 88], photoelastic modulators[69, 89], or liquid-crystal variable retarders (LCVRs) [71, 72]. In this work we present a device based on the LCVR approach that has some limitations, in particular, the accessible spectral range, but also significant advantages, such as the absence of moving parts or high driving voltages. As we mentioned in the introduction, it is sometimes important to have an optimized system to obtain polarimetric measurements of a given sample. We will demonstrate that in some cases it may be better, or easier, to work with polarimeters that are not optimized. For example, working with liquid crystal variable retarders, the dead time, between changes of voltage or retardance values, is smaller when smaller voltage or retardance changes are introduced, so that the full measure-

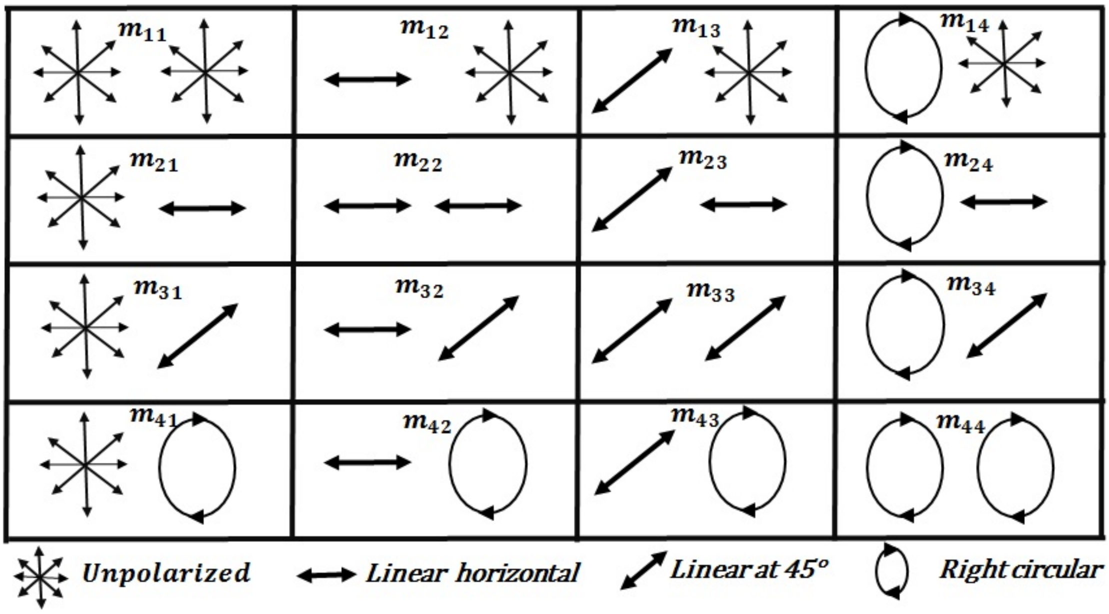

Figure 3.2: Diagram of the combinations polarizer-analizer, for the polarimeter in Fig. 3.1, used in the measurement of each element of the Mueller matrix.

ment can be faster for non-optimized, closer voltage or retardance values. We will discuss more on the optimization and calibration processes that are necessary to have a polarimeter with a consistent performance, in next Chapter.

3.2 Modulation of the Liquid Crystal Variable Retarders

In this work, although the retardance values were chosen to give the values of the incident and detected polarization states required by the method of Bickel and Bailey[87], it is possible to use other methods to extract the sample Mueller matrix from the measured intensities. To change the condition number[1] in the experiment, the number of independent polarization states was changed. For an optimized system six incident Stokes vectors and six detected Stokes vectors were used; these were linearly horizontal (H), linear vertical(V), linear at +45°(+), linear at −45°(-), right circular(R), and left circular(L) polarized light. This meant that there were 36 intensity measurements made. The characteristic matrix for the PSG and the PSA is in this case:

---

[1] The condition number is defined as the ratio of largest singular value of the measurement matrix divide by the smalles singular value of the measurement matrix[90].

$$P_6 = \begin{bmatrix} 1 & 1 & 1 & 1 & 1 & 1 \\ 1 & -1 & 0 & 0 & 0 & 0 \\ 0 & 0 & 1 & -1 & 0 & 0 \\ 0 & 0 & 0 & 0 & 1 & -1 \end{bmatrix}, \tag{3.1}$$

and the condition number for this matrix is $\kappa_6 = 1.7321$, the optimized value. For the non-optimized case we used only four incident Stokes vectors and four detected Stokes vectors; linearly horizontal, vertical, at +45° and right circular polarized light. This requires 16 intensity measurements and has a PSG and PSA characteristic matrix given by:

$$P_4 = \begin{bmatrix} 1 & 1 & 1 & 1 \\ 1 & -1 & 0 & 0 \\ 0 & 0 & 1 & 0 \\ 0 & 0 & 0 & 1 \end{bmatrix}, \tag{3.2}$$

with a condition number of $\kappa_4 = 3.2255$, which indicates that the system is not optimized [90].

3.3 Theoretical modelling of the Polarization State Generator (PSG)

In this thesis the state of polarization of light incident on the sample was modulated using two electro-optical Liquid Crystal Variable Retarders (LCVR) which we consider behave as ideal linear retarders with variable retardance. Therefore, the retardance of a linear retarder with the fast axis at 0° is a function of time $\Delta(t)$ given by

$$\mathbf{R}_{0^\circ}(\tau, \Delta(t)) = \tau \begin{bmatrix} 1 & 0 & 0 & 0 \\ 0 & 1 & 0 & 0 \\ 0 & 0 & \cos\Delta(t) & \sin\Delta(t) \\ 0 & 0 & -\sin\Delta(t) & \cos\Delta(t) \end{bmatrix}, \tag{3.3}$$

where τ is the transmittance for unpolarized light and $\Delta(t)$ is the variable retardance.

The Mueller matrix of a polarizer (or a retarder) with the transmission axis (or fast) oriented at an azimuth angle θ, M_θ must be [58]

$$\mathbf{M}_\theta = \mathbf{Rot}(\theta)\mathbf{M}_{0^\circ}\mathbf{Rot}(-\theta), \tag{3.4}$$

where $\mathbf{M}_{0^\circ}$ is the Mueller matrix of the optical element with its axis (the transmission axis or the fast axis) parallel to the horizontal direction and $\mathbf{Rot}(\theta)$ is the rotation matrix given by

$$\mathbf{Rot}(\theta) = \begin{bmatrix} 1 & 0 & 0 & 0 \\ 0 & \cos 2\theta & -\sin 2\theta & 0 \\ 0 & \sin 2\theta & \cos 2\theta & 0 \\ 0 & 0 & 0 & 1 \end{bmatrix}. \tag{3.5}$$

Then, the Mueller matrix for a linear variable retarder with the fast axis oriented at an azimuth angle θ must be

$$\mathbf{R}_{0^\circ}(\tau, \Delta(t), \theta) = \tau \cdot \mathbf{Rot}(\theta) \cdot \begin{bmatrix} 1 & 0 & 0 & 0 \\ 0 & \cos 2\theta & -\sin 2\theta & 0 \\ 0 & \sin 2\theta & \cos 2\theta & 0 \\ 0 & 0 & 0 & 1 \end{bmatrix} \cdot \mathbf{Rot}(-\theta). \tag{3.6}$$

From Eq. 3.3 and Eq. 3.5, the Mueller matrix of the first LCVR1, with its fast axis at +45° from the horizontal, is given by

$$\mathbf{R}_{+45^\circ}(\tau_1, \Delta_1(t), \theta) = \tau_1 \begin{bmatrix} 1 & 0 & 0 & 0 \\ 0 & \cos\Delta_1(t) & 0 & -\sin\Delta_1(t) \\ 0 & 0 & 1 & 0 \\ 0 & \sin\Delta_1(t) & 0 & \cos\Delta_1(t) \end{bmatrix}, \tag{3.7}$$

where the variable retardance, $\Delta_1(t)$, and the transmittance, τ_1, have a subscript to indicate that they correspond to the first retarder, LCVR1.
The fast axis of the second Liquid Crystal Variable Retarder is oriented at 0°, LCVR2, then its Mueller matrix is given by

$$\mathbf{R}_{0^\circ}(\tau_2, \Delta_2(t)) = \tau_2 \begin{bmatrix} 1 & 0 & 0 & 0 \\ 0 & 1 & 0 & 0 \\ 0 & 0 & \cos\Delta_2(t) & \sin\Delta_2(t) \\ 0 & 0 & -\sin\Delta_2(t) & \cos\Delta_2(t) \end{bmatrix}, \tag{3.8}$$

where the variable retardance, $\Delta_2(t)$, and the transmittance, τ_2, have a subscript to indicate that they correspond to the second retarder LCVR2.

If we have a Polarization State Generator (PSG), as is depicted in Fig. 3.3, with incident light linearly polarized in the horizontal direction and whose Stokes vector is given by

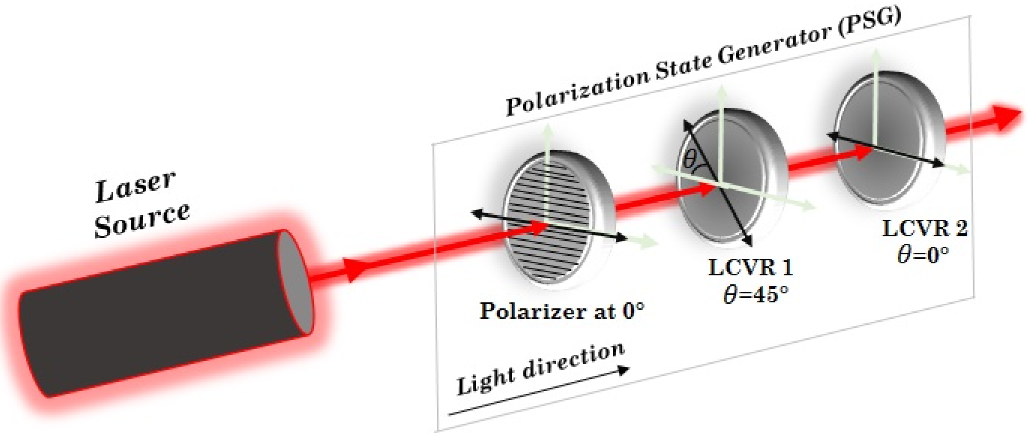

Figure 3.3: Polarizing elements of the PSG which define $S_{PSG}(t)$.

$$\mathbf{S}_i = \begin{bmatrix} 1 \\ 1 \\ 0 \\ 0 \end{bmatrix}, \tag{3.9}$$

combining Eq. 3.7, Eq. 3.8 and Eq. 3.9, the polarization state of the light after LCVR2, as a function of the two variable retardances, for light that passed through the PSG, resulted in

$$\mathbf{S}_{PSG}(t) = \mathbf{R}_2(\tau_2, \Delta_2(t)) \cdot \mathbf{R}_1(\tau_1, \Delta_1(t)) \cdot \mathbf{S}_i = \tau_1\tau_2 \begin{bmatrix} 1 \\ \cos\Delta_1(t) \\ \sin\Delta_1(t)\sin\Delta_2(t) \\ \sin\Delta_1(t)\cos\Delta_2(t) \end{bmatrix} \tag{3.10}$$

The proper choice of the modulation parameters for the retardances $\Delta_1(t)$ and $\Delta_2(t)$ ensures that at least 4 linearly independent states of polarization are generated to obtain a complete polarimetry measurement. The last three elements of the Stokes vector $\mathbf{S}_{PSG}(t)$ in Eq. 3.10 can be interpreted as a transformation from spherical to rectangular coordinates of points on the surface of the Poincaré sphere [88]. In this work, only six linearly independent polarization states were used in the measurements, the implementation of this will be discussed in detail later. For now we present, in Table 3.1, the pairs of retardances used, in wavelengths. We present the variable retardances, Δ_1 and Δ_2 without time dependence to emphasize that their values were kept constant during the time taken for the measurements with a given incident polarization state.

Polarization state	Δ_1 $[\lambda' s]$	Δ_2 $[\lambda' s]$
H	0	0
V	$\frac{1}{2}$	$\frac{1}{4}$
$+$	$\frac{1}{4}$	$\frac{1}{4}$
$-$	$\frac{1}{4}$	$\frac{3}{4}$
R	$\frac{1}{4}$	0
L	$\frac{1}{4}$	$\frac{1}{2}$

Table 3.1: Retardances Values for the Polarization States Generator.

3.4 Theoretical modelling of the Polarization State Analizer (PSA)

As for the discussion for the PSG, we can analyze the system for the Polarization State Analyzer (PSA), and for every state of polarization that is incident on the sample, it is possible to relate the Stokes parameters to the measurable intensities. In Chapter 2 we showed that the Stokes parameters are related to measurable intensities, the S_0 or I is the total intensity and we can write or measure it in different ways [66]

$$S_0 = I = I_H + I_V = I_+ + I_- = I_L + I_R \tag{3.11}$$

$$S_1 = Q = I_H - I_V \tag{3.12}$$

$$S_2 = U = I_+ - I_- \tag{3.13}$$

$$S_1 = V = I_R - I_L \tag{3.14}$$

where H, V, $+$, and $-$ are linear polarization horizontal, vertical, +45 and -45, respectively, and R and L are circular polarization right and left, respectively.

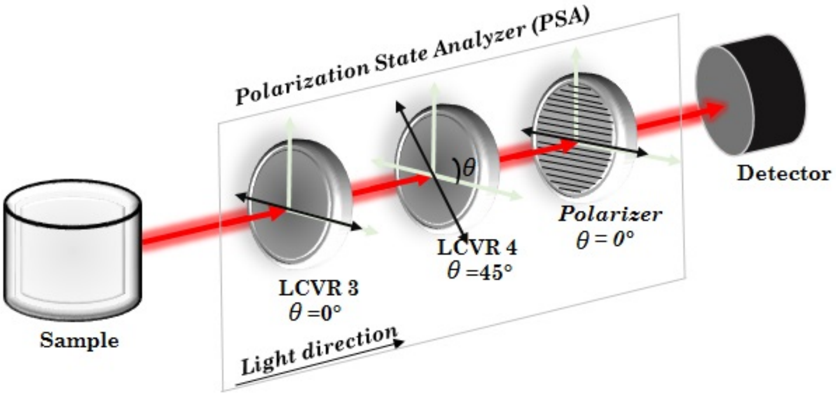

Figure 3.4: Polarization State Analizer.

If we consider the system in Fig. 3.4, with a Stokes vector leaving the sample S_{out}, the Stokes vector reaching the detector after the linear polarizer is

$$\mathbf{S}_{PSA} = \mathbf{M}_{P0^\circ}\mathbf{R}_4(\tau_4, \Delta_4(t))\mathbf{R}_3(\tau_3, \Delta_1(t))\mathbf{S}_{out}. \tag{3.15}$$

Writing the values of the matrices $\mathbf{R}_3$ at 0° and $\mathbf{R}_4$ at 45°, LCVR3 and LCVR4 respectively, we obtain

$$\mathbf{S}_{PSA} = \frac{1}{2}\begin{bmatrix} 1 & 1 & 0 & 0 \\ 1 & 1 & 0 & 0 \\ 0 & 0 & 0 & 0 \\ 0 & 0 & 0 & 0 \end{bmatrix} \begin{bmatrix} 1 & 0 & 0 & 0 \\ 1 & cos\Delta_4 & 0 & -sin\Delta_4 \\ 0 & 0 & 0 & 0 \\ 0 & sin\Delta_4 & 0 & cos\Delta_4 \end{bmatrix} \begin{bmatrix} 1 & 0 & 0 & 0 \\ 0 & 1 & 0 & 0 \\ 0 & 0 & cos\Delta_3 & sin\Delta_3 \\ 0 & 0 & -sin\Delta_3 & cos\Delta_3 \end{bmatrix} \mathbf{S}_{out} \tag{3.16}$$

and thus

$$\begin{bmatrix} S_{PSA0} \\ S_{PSA1} \\ S_{PSA2} \\ S_{PSA3} \end{bmatrix} = \frac{1}{2}\begin{bmatrix} 1 & cos\Delta_4 & sin\Delta_3 sin\Delta_4 & -cos\Delta_3 sin\Delta_4 \\ 1 & cos\Delta_4 & sin\Delta_3 sin\Delta_4 & -cos\Delta_3 sin\Delta_4 \\ 0 & 0 & 0 & 0 \\ 0 & sin\Delta_4 & 0 & cos\Delta_4 \end{bmatrix} \begin{bmatrix} S_{out0} \\ S_{out1} \\ S_{out2} \\ S_{out3} \end{bmatrix}. \tag{3.17}$$

The intensity detected is the first element of the final Stokes vector, S_{PSA0},

$$S_{PSA0} = \frac{1}{2}(1 + cos\Delta_4 + sin\Delta_3 sin\Delta_4 - cos\Delta_3 sin\Delta_4). \tag{3.18}$$

So, if we want to detect the component of S_{out} in H polarized (linear horizontally polarized light), we need

$$\begin{gathered}\cos\Delta_4 = 1, sin\Delta_4 = 0 \\ \Delta_4 = 0, 2\pi, 4\pi,... \\ \Delta_3 = \bigstar\ ^{2}\end{gathered} \tag{3.19}$$

In this case

$$S_{I0} = \frac{1}{2}(S_{out0} + S_{out1}) = \frac{1}{2}([I_H + I_V] + [I_H - I_V]) = I_H. \tag{3.20}$$

If we want to detect the component of S_{out} in V polarized (linear vertically polarized light), we need

$$\begin{gathered}\cos\Delta_4 = -1, sin\Delta_4 = 0 \\ \Delta_4 = \pi, 3\pi, 5\pi,... \\ \Delta_3 = \bigstar\end{gathered} \tag{3.21}$$

In this case

$$S_{I0} = \frac{1}{2}(S_{out0} - S_{out1}) = \frac{1}{2}([I_H + I_V] - [I_H - I_V]) = I_V. \tag{3.22}$$

If we want to detect the component of S_{out} in +45 polarized (linear +45° polarized light), we need

$$\begin{gathered}\cos\Delta_4 = 0, sin\Delta_4 = 1 \\ \cos\Delta_3 = 0, sin\Delta_3 = 1 \\ \Delta_4 = \tfrac{\pi}{2}, \tfrac{5\pi}{2},... \\ \Delta_3 = \tfrac{\pi}{2}, \tfrac{5\pi}{2},...\end{gathered} \tag{3.23}$$

In this case

$$S_{I0} = \frac{1}{2}(S_{out0} + S_{out2}) = \frac{1}{2}([I_+ + I_-] + [I_+ - I_-]) = I_+. \tag{3.24}$$

---

[2] Notice that the symbol $\bigstar$ here represent that the value of Δ_3 does not affect the measured intensity.

If we want to detect the component of S_{out} in -45 polarized (linear $-45°$ polarized light), we need

$$\begin{gathered}\cos\Delta_4 = 0, sin\Delta_4 = 1 \\ \cos\Delta_3 = 0, sin\Delta_3 = -1 \\ \Delta_4 = \tfrac{\pi}{2}, \tfrac{5\pi}{2}, ... \\ \Delta_3 = \tfrac{3\pi}{2}, \tfrac{7\pi}{2}, ...\end{gathered} \tag{3.25}$$

In this case

$$S_{I0} = \frac{1}{2}(S_{out0} - S_{out2}) = \frac{1}{2}([I_+ + I_-] - [I_+ - I_-]) = I_-. \tag{3.26}$$

If we want to detect the component of S_{out} in R polarized (right circularly polarized light), we need

$$\begin{gathered}\cos\Delta_4 = 0, sin\Delta_4 = 1 \\ \cos\Delta_3 = -1, sin\Delta_3 = 0 \\ \Delta_4 = \tfrac{\pi}{2}, \tfrac{5\pi}{2}, ... \\ \Delta_3 = \pi, 3\pi, 5\pi, ...\end{gathered} \tag{3.27}$$

In this case

$$S_{I0} = \frac{1}{2}(S_{out0} + S_{out3}) = \frac{1}{2}([I_R + I_L] + [I_R - I_L]) = I_R. \tag{3.28}$$

If we want to detect the component of S_{out} in L polarized (left circularly polarized light), we need

$$\begin{gathered}\cos\Delta_4 = 0, sin\Delta_4 = 1 \\ \cos\Delta_3 = 1, sin\Delta_3 = 0 \\ \Delta_4 = \tfrac{\pi}{2}, \tfrac{5\pi}{2}, ... \\ \Delta_3 = 0, 2\pi, 4\pi, ...\end{gathered}$$

(3.29)

In this case

$$S_{I0} = \frac{1}{2}(S_{out0} - S_{out3}) = \frac{1}{2}([I_R + I_L] - [I_R - I_L]) = I_L. \tag{3.30}$$

Again we can choose the modulation parameters for the retardances $\Delta_3(t)$ and $\Delta_4(t)$ to obtain the relationship between the Stokes parameters and the measurable intensities for the Polarization State Analyzer (PSA).

3.5 Calculation of the Mueller matrix

The calculation of the Mueller matrix from the experimental intensities data depends on the nature of the measurment technique. For instance, the Mueller matrix can be obtained from the spectral analysis of the polarimetric measurements [24] or from direct algebraic relations between the measurements [87].
It is possible to calculate the Mueller matrix of a sample through a Polarimetric Data Reduction Matrix method. For now we present the calculation method which is suitable for the experimental data obtained with the polarimeter that we describe in the next Chapter. This method was presented by Bickel and Bailey [87], and establishes four properties of the experimental data and their relation with the elements of the Mueller matrix:

- The kind of polarized light (incident and detected) used in a particular measurement establishes uniquely the matrix elements that will be mixed by that measurement.

- Various complimentary orientations of any polarizer configuration give matrix element combinations that differ only in the sign of the elements mixed.

- Each matrix element has a unique location in the matrix. S_{11} occurs in every location, S_{ij} (i=j) occurs only along the diagonal.

- The matrix elements S_{ij} where i and/or $j = 4$ contain information about circularly polarized light.

For our analysis the first 2 properties are the most relevant. The analytic relations describing the irradiance measured for a particular combination polarizer-analizer are used to determine what set of measurements is necessary to obtain each element of the Mueller matrix, it can be seen in Fig. 3.5.

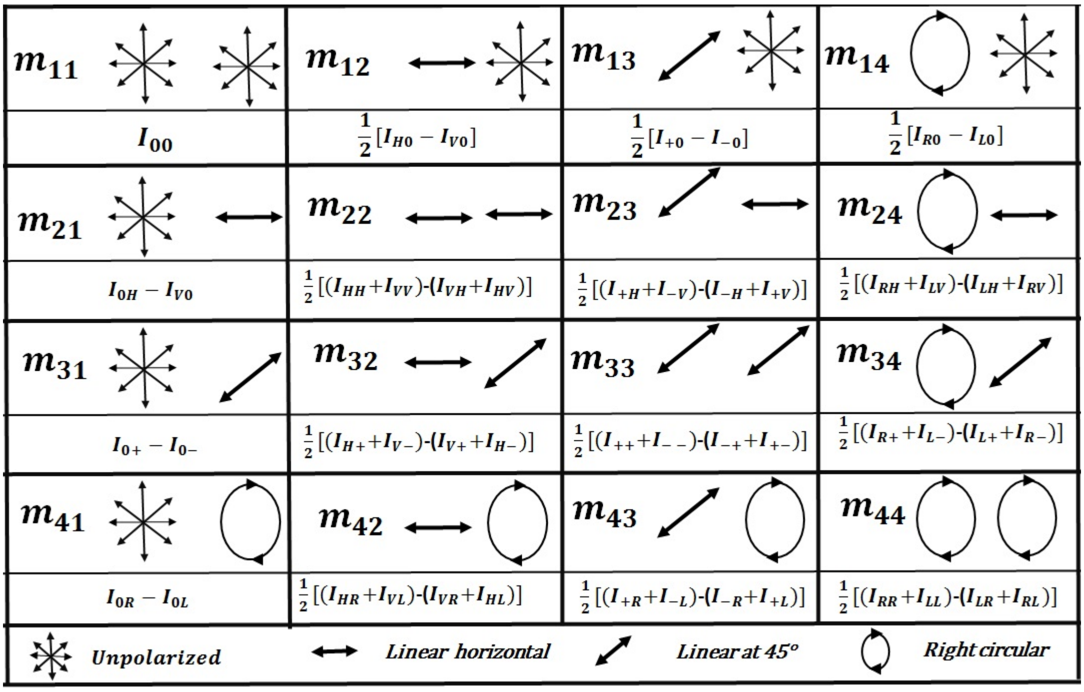

m_{11} ✳ ✳	m_{12} ↔ ✳	m_{13} ↗ ✳	m_{14} ↻ ✳
I_{00}	$\frac{1}{2}[I_{H0} - I_{V0}]$	$\frac{1}{2}[I_{+0} - I_{-0}]$	$\frac{1}{2}[I_{R0} - I_{L0}]$
m_{21} ✳ ↔	m_{22} ↔ ↔	m_{23} ↗ ↔	m_{24} ↻ ↔
$I_{0H} - I_{V0}$	$\frac{1}{2}[(I_{HH}+I_{VV})\text{-}(I_{VH}+I_{HV})]$	$\frac{1}{2}[(I_{+H}+I_{-V})\text{-}(I_{-H}+I_{+V})]$	$\frac{1}{2}[(I_{RH}+I_{LV})\text{-}(I_{LH}+I_{RV})]$
m_{31} ✳ ↗	m_{32} ↔ ↗	m_{33} ↗ ↗	m_{34} ↻ ↗
$I_{0+} - I_{0-}$	$\frac{1}{2}[(I_{H+}+I_{V-})\text{-}(I_{V+}+I_{H-})]$	$\frac{1}{2}[(I_{++}+I_{--})\text{-}(I_{-+}+I_{+-})]$	$\frac{1}{2}[(I_{R+}+I_{L-})\text{-}(I_{L+}+I_{R-})]$
m_{41} ✳ ↻	m_{42} ↔ ↻	m_{43} ↗ ↻	m_{44} ↻ ↻
$I_{0R} - I_{0L}$	$\frac{1}{2}[(I_{HR}+I_{VL})\text{-}(I_{VR}+I_{HL})]$	$\frac{1}{2}[(I_{+R}+I_{-L})\text{-}(I_{-R}+I_{+L})]$	$\frac{1}{2}[(I_{RR}+I_{LL})\text{-}(I_{LR}+I_{RL})]$
✳ **Unpolarized**	↔ **Linear horizontal**	↗ **Linear at 45°**	↻ **Right circular**

Figure 3.5: Measurements and operations necessary to compute each of the 16 elements of the Mueller matrix [87]. The first symbol, and subscript of I, represents the polarization state of the incident light whereas the second symbol, and subscript, represents the analyzer used in the corresponding measurement. The convention followed for the subscripts is the same as in Chapter 2 with the extra '0' indicating unpolarized light, for the incident light, or total irradiance, for the analyzer [67].

For instance, m_{12} can be obtained as:

$$m_{12} = \frac{1}{2}(I_{H0} - I_{V0}). \tag{3.31}$$

That is, we can obtain m_{12} as the difference between the total scattered irradiance for incident light polarized in the horizontal direction and the total scattered irradiance for incident light polarized in the vertical direction. The sum of the horizontal and vertical irradiances gives the total irradiance and, thus, this quantity is obtained indirectly as the incoherent superposition of the horizontal and vertical components. Therefore, m_{12} for our polarimeter is obtained as:

$$m_{12} = \frac{1}{2}[(I_{HH} + I_{HV}) - (I_{VH} + I_{VV})]. \tag{3.32}$$

Similar expressions can be found for the rest of the elements. Fig. 3.5 shows the measurements and operations necessary to calculate the complete Mueller matrix of a sample.

We can write most elements of the Mueller matrix, except m_{11} in terms of other elements previously calculated. As an example, let us consider again the element given by Eq. 3.32.

The first element of the Mueller matrix in the polarimeter is given by

$$m_{11} = \frac{1}{2}[(I_{HH} + I_{HV}) + (I_{VH} + I_{VV})]. \tag{3.33}$$

Therefore,

$$m_{11} + m_{12} = I_{HH} + I_{HV}, \tag{3.34}$$

from which

$$m_{12} = I_{HH} + I_{HV} - m_{11}. \tag{3.35}$$

Thus, m_{12} is given in terms of a pair of measurements and m_{11}. Again, similar relations can be found for the rest of the elements of the Mueller matrix [67, 87].

For the case of 36 intensity measurements, the relationship between the detected intensities[3] of light and the Mueller-matrix components are given by

$$\begin{array}{c}
m_{11} = I_{H0} + I_{V0} = I_{HH} + I_{HV} + I_{VH} + I_{VV} \\
m_{12} = \frac{1}{2}[I_{H0} - I_{V0}] = \frac{1}{2}[I_{HH} + I_{HV} - I_{VH} - I_{VV}] \\
m_{13} = \frac{1}{2}[I_{+0} - I_{-0}] = \frac{1}{2}[I_{+H} + I_{+V} - I_{-H} - I_{-V}] \\
m_{14} = \frac{1}{2}[I_{R0} - I_{L0}] = \frac{1}{2}[I_{LH} + I_{LV} - I_{RH} - I_{RV}] \\
m_{21} = I_{0H} - I_{0V} = I_{HH} + I_{VH} - I_{HV} - I_{VV} \\
m_{22} = \frac{1}{2}[I_{HH} + I_{VV} - I_{VH} - I_{HV}] \\
m_{23} = \frac{1}{2}[I_{+H} + I_{-V} - I_{-H} - I_{+V}] \\
m_{24} = \frac{1}{2}[I_{RH} + I_{LV} - I_{LH} - I_{RV}] \\
m_{31} = I_{0+} - I_{0-} = I_{H+} + I_{V+} - I_{H-} - I_{V-} \\
m_{32} = \frac{1}{2}[I_{H+} + I_{H-} - I_{V+} - I_{H-}] \\
m_{33} = \frac{1}{2}[I_{++} + I_{--} - I_{-+} - I_{+-}] \\
m_{34} = \frac{1}{2}[I_{R+} + I_{L-} - I_{L+} - I_{R-}] \\
m_{41} = I_{0R} + I_{0L} = I_{HR} + I_{VR} - I_{HL} - I_{VL} \\
m_{42} = \frac{1}{2}[I_{HR} + I_{VL} - I_{VR} - I_{HL}] \\
m_{43} = \frac{1}{2}[I_{+R} + I_{-L} - I_{-R} - I_{+L}] \\
m_{44} = \frac{1}{2}[I_{RR} + I_{LL} - I_{LR} - I_{RL}]
\end{array} . \tag{3.36}$$

---

[3] The notation I_{ab} is the detected intensity with polarization a incident and polarization b detected from the sample.

For the case of 16 intensity measurements, we used H, V, + and R and the equations for the Mueller matrix are:

$$\begin{aligned}
m_{11} &= \tfrac{1}{2}[I_{H0} + I_{V0}] = \tfrac{1}{2}[I_{HH} + I_{HV} + I_{VH} + I_{VV}] \\
m_{12} &= I_{H0} - m_{11} = I_{HH} + I_{HV} - m_{11} \\
m_{13} &= I_{+0} - m_{11} = I_{+H} + I_{+V} - m_{11} \\
m_{14} &= I_{R0} - m_{11} = I_{RH} + I_{RV} - m_{11} \\
m_{21} &= I_{HH} + I_{VH} - m_{11} \\
m_{22} &= 2I_{HH} - m_{11} - m_{12} - m_{21} \\
m_{23} &= 2I_{+H} - m_{11} - m_{13} - m_{21} \\
m_{24} &= 2I_{RH} - m_{11} - m_{14} - m_{21} \\
m_{31} &= I_{H+} + I_{V+} - m_{11} \\
m_{32} &= 2I_{H+} - m_{11} - m_{12} - m_{31} \\
m_{33} &= 2I_{++} - m_{11} - m_{13} - m_{31} \\
m_{34} &= 2I_{R+} - m_{11} - m_{14} - m_{31} \\
m_{41} &= I_{HR} + I_{VR} - m_{11} \\
m_{42} &= 2I_{HR} - m_{11} - m_{12} - m_{41} \\
m_{43} &= 2I_{+R} - m_{11} - m_{13} - m_{41} \\
m_{44} &= 2I_{RR} - m_{11} - m_{14} - m_{41}
\end{aligned} \tag{3.37}$$

In practise we measured only for the case of 36 measured intensities, that is with six incident Stokes vectors and six detected Stokes vectors, it is the overdetermined and the optimized case. We present other two cases, for 24 and 16 measurements, the last one is a non-optimized case, which is the most important case in our work because we present in Chapter 5 a method for calibration and data-extraction for a non-optimized Mueller matrix polarimeter. The case for 24 measurements is a intermediate step only to validate the method. The retardance values used are shown in Table 3.2, for each of the 36 values of the intensity. The results for the cases of 24 and 16 measurements are obtained using only the appropriate values of the measured intensities from the same data set. This is to remove any effects due to variations in the measured values and only to study the variations due to the different analyses of the data.

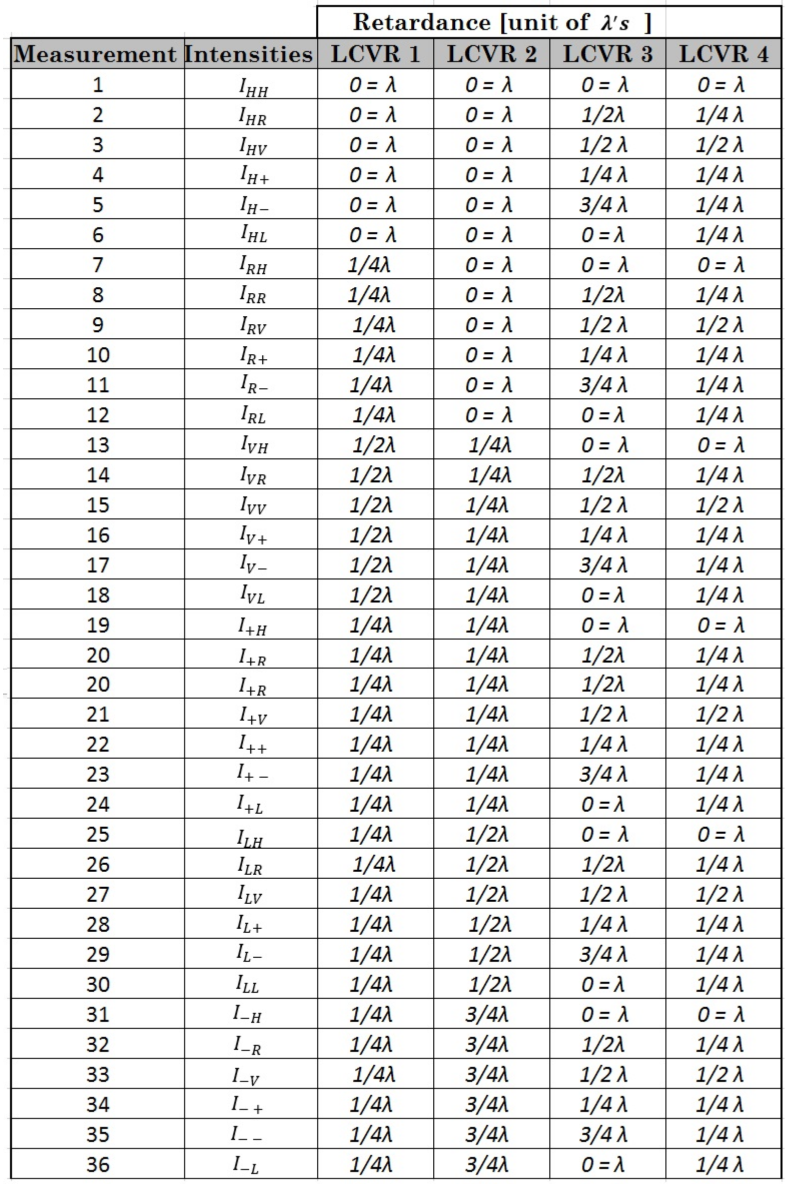

		Retardance [unit of λ's]			
Measurement	**Intensities**	**LCVR 1**	**LCVR 2**	**LCVR 3**	**LCVR 4**
1	I_{HH}	0 = λ	0 = λ	0 = λ	0 = λ
2	I_{HR}	0 = λ	0 = λ	1/2λ	1/4 λ
3	I_{HV}	0 = λ	0 = λ	1/2 λ	1/2 λ
4	I_{H+}	0 = λ	0 = λ	1/4 λ	1/4 λ
5	I_{H-}	0 = λ	0 = λ	3/4 λ	1/4 λ
6	I_{HL}	0 = λ	0 = λ	0 =λ	1/4 λ
7	I_{RH}	1/4λ	0 = λ	0 = λ	0 = λ
8	I_{RR}	1/4λ	0 = λ	1/2λ	1/4 λ
9	I_{RV}	1/4λ	0 = λ	1/2 λ	1/2 λ
10	I_{R+}	1/4λ	0 = λ	1/4 λ	1/4 λ
11	I_{R-}	1/4λ	0 = λ	3/4 λ	1/4 λ
12	I_{RL}	1/4λ	0 = λ	0 =λ	1/4 λ
13	I_{VH}	1/2λ	1/4λ	0 = λ	0 = λ
14	I_{VR}	1/2λ	1/4λ	1/2λ	1/4 λ
15	I_{VV}	1/2λ	1/4λ	1/2 λ	1/2 λ
16	I_{V+}	1/2λ	1/4λ	1/4 λ	1/4 λ
17	I_{V-}	1/2λ	1/4λ	3/4 λ	1/4 λ
18	I_{VL}	1/2λ	1/4λ	0 =λ	1/4 λ
19	I_{+H}	1/4λ	1/4λ	0 = λ	0 = λ
20	I_{+R}	1/4λ	1/4λ	1/2λ	1/4 λ
20	I_{+R}	1/4λ	1/4λ	1/2λ	1/4 λ
21	I_{+V}	1/4λ	1/4λ	1/2 λ	1/2 λ
22	I_{++}	1/4λ	1/4λ	1/4 λ	1/4 λ
23	I_{+-}	1/4λ	1/4λ	3/4 λ	1/4 λ
24	I_{+L}	1/4λ	1/4λ	0 =λ	1/4 λ
25	I_{LH}	1/4λ	1/2λ	0 = λ	0 = λ
26	I_{LR}	1/4λ	1/2λ	1/2λ	1/4 λ
27	I_{LV}	1/4λ	1/2λ	1/2 λ	1/2 λ
28	I_{L+}	1/4λ	1/2λ	1/4 λ	1/4 λ
29	I_{L-}	1/4λ	1/2λ	3/4 λ	1/4 λ
30	I_{LL}	1/4λ	1/2λ	0 =λ	1/4 λ
31	I_{-H}	1/4λ	3/4λ	0 = λ	0 = λ
32	I_{-R}	1/4λ	3/4λ	1/2λ	1/4 λ
33	I_{-V}	1/4λ	3/4λ	1/2 λ	1/2 λ
34	I_{-+}	1/4λ	3/4λ	1/4 λ	1/4 λ
35	I_{--}	1/4λ	3/4λ	3/4 λ	1/4 λ
36	I_{-L}	1/4λ	3/4λ	0 =λ	1/4 λ

Table 3.2: Values of the retardances in each LCVR for each of the 36 measurements. The used polarization states are as follows: H, linear horizontal; V, linear vertical; L, left circular; +, linear at +45°; −, −45°, R, right circular; L, left circular.

Chapter 4

Experimental device

4.1 Instrument description

The motivation behind the development of this device is related to the metrology of periodic structures and scattering from rough surfaces. There are several applications of these systems, in particular for the control of processes in microelectronics [91]-[95].

There are different ways of approaching this problem, for example, through ellipsometric spectroscopy (or reflectometry) that almost always measures at normal incidence. As we have mentioned in Chapter 1, we are interested in measuring the Mueller matrix at a fixed wavelength and angle of incidence. In addition, the system can detect angular changes in the state of polarization produced by the sample. It is possible to take a wide range of polar and azimuthal angles, however in this work we will not move the sample or the instrument angularly, due to the fact that in a previous work [96] a detailed characterization of the angularly resolved scattering of light for rough surfaces was carried out. From the results presented in that work, we selected a fixed detection angle and performed a micrometric spot scan on the sample, then the Mueller matrix of the sample is obtained at each scanned point.
An important restriction for metrology in microelectonics is the size of the point that illuminates the sample. The diffraction gratings engraved on wafers for optical metrology are of the order of 50μm x 50μm [77]. The main idea of this work, is to illuminate with a spot size on the order of 5μm, with this we are sure that we can study local effects in samples which allows us to perform polarimetric analysis of them basen on a simulation using Kirchhoff approximation [16]-[18],[97].

4.2 Elements of experimental assembly[1]

4.2.1 Source

We use a 633 nm wavelength laser diode as a light source[2]. The beam is spatially filtered, suppressing intensity changes due to imperfections (dirt, scratches, etc.) in the optics. We present in Fig 4.1 the optical power measurement to verify its stability over a long period of time (we did one measurement every 30 seconds for 8.5 hours, each value was obtained by averaging 250 values of optical power, with an error of $\pm 0.0006\mu$W). The detector was placed after the spatial filter to ensure that the filtered light beam was stable. As we can see in Fig. 4.1 the optical power has some variations (the maximum variation is 0.22%) with time. To avoid effects of these small variations of optical power on the final polarimetric measurements, we place a beam splitter exactly at the laser output, so that the reflected beam incident on the second detector is synchronized to normalize the polarization measurements. With this we assure that any possible variations of the intensity in the source will be corrected and not affect the final results of the experiment.

4.2.2 Collimating lens

We implement two collimating lenses in the system, the first lens is to collimate the light spatially filtered, (CL1) and the other lens is used to collect the light (CL2) after it interacts with the sample. The lens CL2 projects a collimated beam on the PSA, to analyze its polarization state. The lenses used are achromatic doublets, designed to limit the effects of chromatic and spherical aberrations present in single lenses. Each doublet is composed of two lenses of different materials and refractive index, which makes it possible to focus different wavelengths at the same point. They also correct spherical aberration on the optical axis.

For all experiments presented in this work, the entire optical window of the LCVRs (9.5 mm) was used for the measurements; uniform illumination was applied by expanding the light beam at the output of the source with the spatial filter, followed by the collimating lens that selects and collimates only the central and homogeneous intensity region of the expanded beam.

---

[1] In Appendix A are presented complementary experimental details, for example all data of the experimental graphs presented in this chapter with their associated error.

[2] In Appendix C are presented the data-sheet with all details

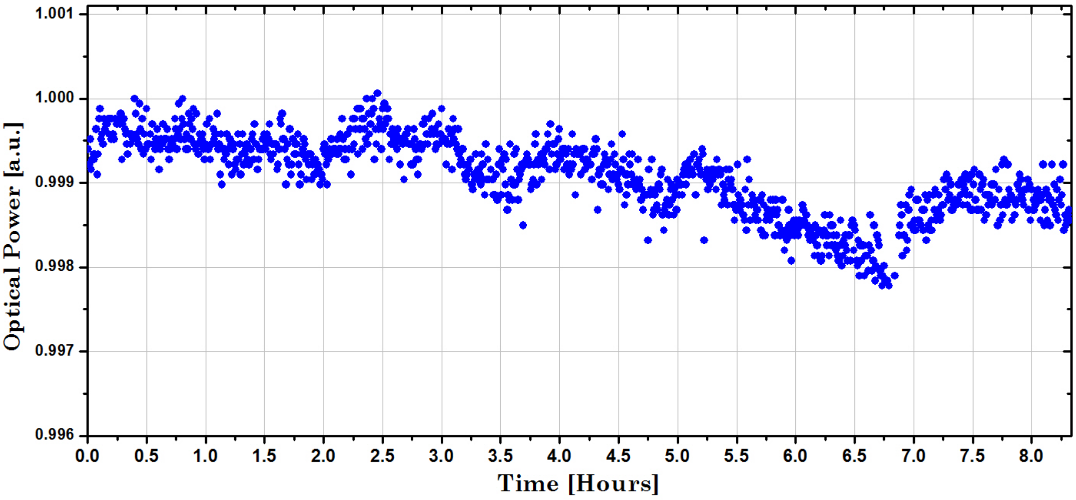

Figure 4.1: Measurements of the Optical Power VS Time for a laser diode IIIb Class, He-Ne, Uniphase of 20mW and a wavelength of 633 nm. We did one measurement every 30 seconds for 8.5 hours, each value was obtained by averaging 250 values of optical power, with a standard deviation of $\pm 0.0006 \mu$W)

4.2.3 Polarization State Generator (PSG)

The configuration of the polarimeter PSG is the following (see Fig. 4.2): the linearly polarized laser beam of wavelength 633 nm is incident on the PSG after being spatially filtered and collimated. Then, a linear horizontal polarizer, P1, increases the purity of the incident polarization state. Two liquid crystal variable retarders with their fast axis at 45° and 0° from the horizontal, LCVR1 and LCVR2 respectively, are modulated to convert the linearly polarized incident light into the required polarization states over the Poincaré sphere. We will present details about the modulation of the LCVRs in Section 1.3. The light transmitted by the LCVR2 reaches the focusing system described in 4.2.4. The light is then directed onto the sample with a specific polarization state determined by the theoretical calculation for the PSG presented in Chapter 3.

We have the possibility to work with a polarimeter in reflection or transmission mode, as can be seen in Fig. 4.2. In both types of polarimeter, lens CL2 collects and collimates the light scattered by the sample and sends it to the PSA, as we will describe in section 4.2.6. That gives us the opportunity to perform the calibration in the transmission mode and make measurements by reflection or transmission depending on the sample. In this work we focus on reflective samples but the whole calibration process was performed in transmission mode.

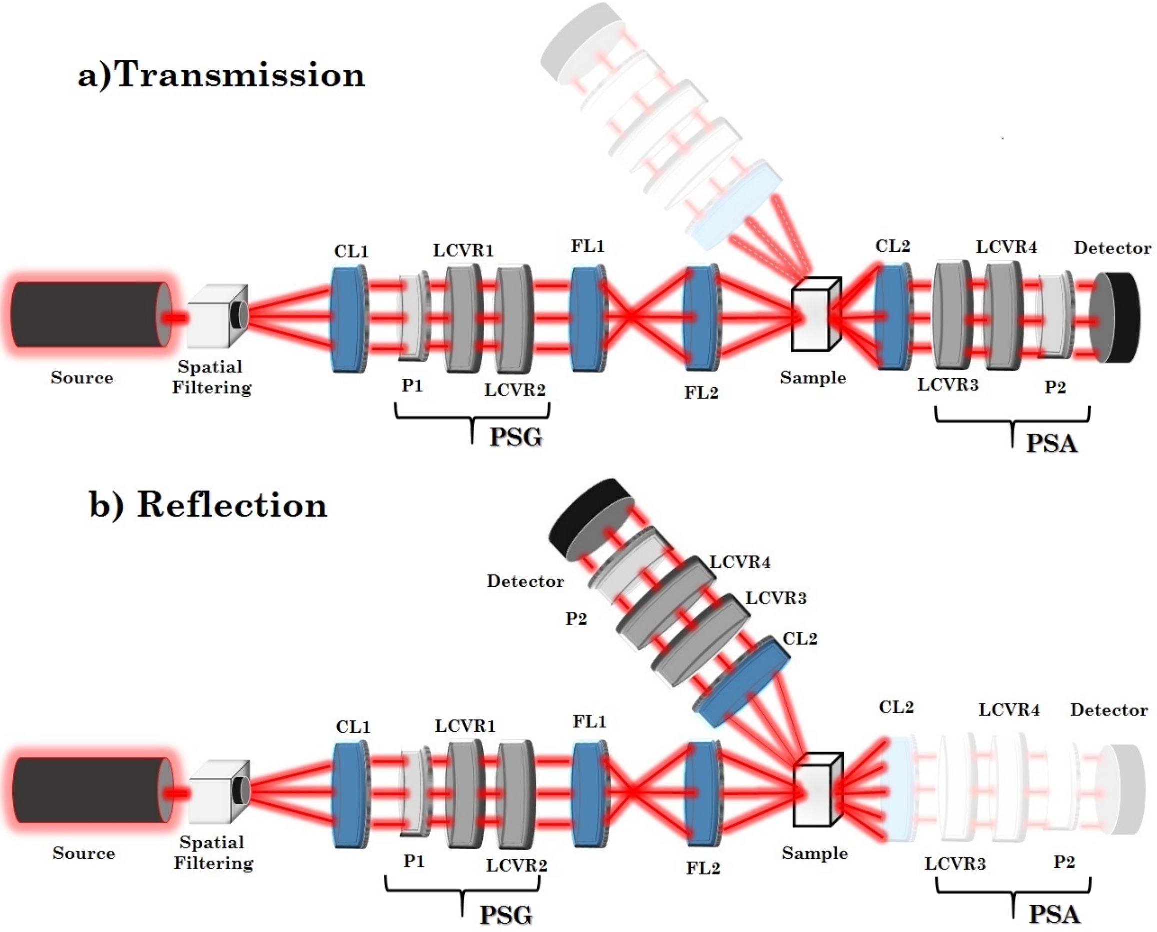

Figure 4.2: Set-up of the Mueller matrix polarimeter a)Transmission and b) Reflection mode. We present schematically the light rays to understand how the optical system works.

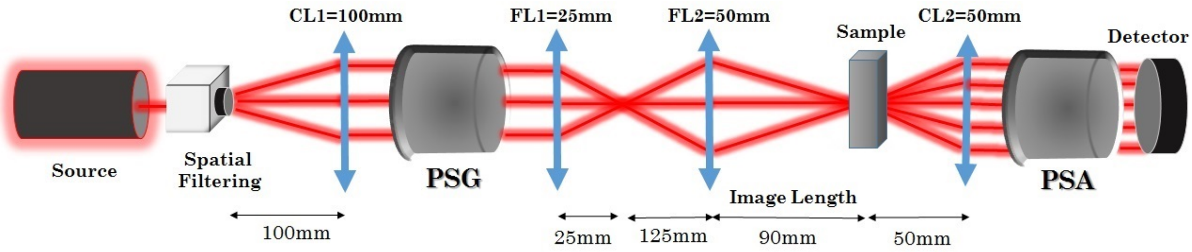

Figure 4.3: Focus system to obtain a spot size of a few microns.

4.2.4 Focus system

One of the main ideas in this work is to use focused illumination and to measure the polarization state of the scattering pattern produced by each point of the studied sample. After the light goes through the PSG, it is possible to use an aspheric lens to focus the light on the sample. This lens allows spot-sizes of the order of microns[3] (for example: 3μm, 5μm or 10μm), however, aspheric lenses typically have a focal length of $\approx 50mm$ maximum. (Due to space constraints we needed to design an optical system that allows us to obtain an illumination beam smaller than 10μm, but that allowed us to use an image length around of $100mm$). It is important to point out that the simulation with which we compare the experimental results in our experiment uses a Gaussian beam as a source of illumination[16]-[18]. So, we need to use the least number of optical components, so as to reduce the aberrations introduced to the beam.

Calculations were made in an optical design program to optimize our system and find what lenses should be used to obtain the desired parameters for the illumination spot. We obtained an optical system that uses only 2 lenses, the optical system is presented in Fig. 4.3. A fused silica aspheric lens (FL1) with a focal length of $25mm$ and a numerical aperture of 0.50 was used to collect the collimated light that comes out of the PSG and focuses it on a point, which is then the object for the second focus lens (FL2, which is an aspherized achromatic lens of 50 mm focal length). The object length for the lens FL2 is 125 mm, which allows the system to increase the image length and in turn maintains the spot size in the order of a few microns, as required.

The spot was measured using the traditional method of the knife-edge [75, 98, 99]. The knife-edge technique was used to measuring the minimum size of the focused spot formed by our lens system. The relationship of the measured spot-size is shown in Fig. 4.4 as a function of the focus depth, note that the minimal

---

[3] In appendix A.3 we present de complete data of spot-size obtained with the optical system used in this work.

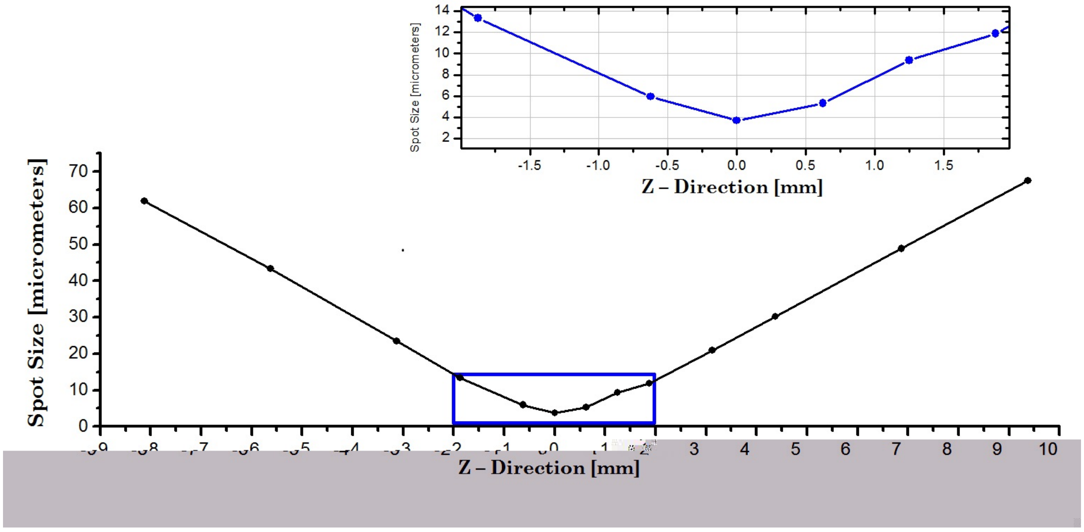

Figure 4.4: The graph shows the size of the beam as a function of the focus depth, using the knife-edge test to estimate the spot-size. For the test automated linear positioning plates with resolution of one micrometer were used to perform the scan of the knife and with this measure the optical power that comes to the photodetector accurately. An error function was obtained from the intensity measurements as a function of the position and the derivative of that function is a Gaussian function. In this work is consider the width of that Gaussian beam to $1/e$, as the spot-size.

spot-size measured was $3.7 \pm 0.06\mu$m, with an image length of 90 ± 0.025mm. An important fact is that the spot-size stays under 10μm approximately in a focus depth of 3 mm, which is required for the experiment. A table with the precise values of the spot-size is presented in Appendix A.3.

However as we can see in Fig. 4.4 the spot-size changes when we take different focus depths. It is important to note that the curve presented is totally experimental, because we need to know precisely the size of the spot and the position where it is minimal to be able to guarantee that the sample is illuminated with known parameters.

4.2.5 Sample positioning system

The study surface is mounted on a pair of linear motorized control plates, which allow us to move the sample to scan it two-dimensionally point to point[4]. The

---

[4] Each point with precision of a micron.

two-dimensional movement of the linear plates to move the sample is done by a pair of TDC001 T-Cube^{TM} DC Servo Motor Driver[100]. These are very compact individual channel controllers which have a manual and automatic control of the direct current servomotors, they also have an USB connectivity to operate through the PC. The cube has a graphical interface with the user which provides extensive software functions. In our particular case we used LabVIEW to add the control of the plates stages to the whole automation system of the experiment.

4.2.6 Polarization State Analyzer (PSA)

The experimental system for the polarization state analyzer, which is after a lens, CL2 that collects and collimates the light backscattered by the sample, is formed by two liquid crystal variable retarders LCVR3 and LCVR4 with axes at 45° and 0°, respectively, followed by a linear horizontal polarizer, P2 at 0°, after them. The PSA in the polarimeter measure the polarization state of the collected light, through the combination of the LCVR3 and LCVR4 at 45° and 0° using the retardances of the Table 3.2 to generate a set of polarization states to allow us to construct the Mueller matrix of the sample.

The PSA, the collector lens and the detector are placed on a mechanical arm, which can move angularly to have a configuration by transmission or reflection, by means of a rotatory plate[5]. The device used to move the mechanical arm was a Universal Motion Controller (Driver Model ESP300 of Newport). The controller coupled to a rotating plate provides an automatic or manual control system, as required. The angular plate used provides a precision in the angular movement of a thousandth of a degree. The rotatory positioning system is controllable through the PC with RS232-C connection allowing us to use again LabVIEW programming for the automated control of the system.

4.2.7 Detector

The detector used in our polarimeter[6] was a Dual Channel Optical Power and Energy Meter ($PM320E$), with its corresponding Power sensor Photodiode ($S120C$) [101]. One of the advantages of this detector is the wide range of optical power ($50nW - 50mW$) and wavelength ($400 - 1100$) that it detects. The photo-diode in conjunction with the power meter has two channels that allow differential, radiometric and simultaneous measurements using the input aperture of $9.5mm$. The instrument has compatibility with LabVIEW to perform manual or automated operation through the computer.

---

[5] In the Appendix C we present the data-sheet with the specification of the rotatory plate

[6] This detector was used in all experiments of this work.

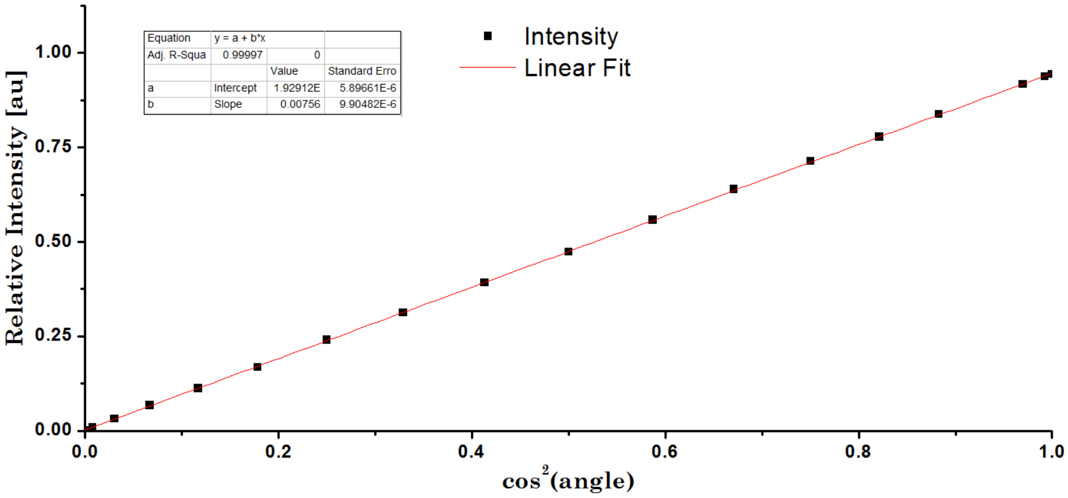

Equation	y = a + b*x		
Adj. R-Squa	0.99997	0	
		Value	Standard Erro
a	Intercept	1.92912E	5.89661E-6
b	Slope	0.00756	9.90482E-6

Figure 4.5: Intensity variation due to the detector as a function of the angle between the two polarizers.

An important parameter to consider is the linearity of the detector to the wavelength that we used[7]. To test the linearity we used a setup with two linear polarizers in front of the detector. Gradually varying the angle between the two polarizers varies the intensity observed on the detector, and this should be proportional to $cos^2(angle)$, the angle is taken between the two polarizers (Malus's law) [75], Figure Fig. 4.5 shows the results obtained, with excellent precision (correlation coefficient $R = 0.99997$).

4.2.8 Automated control system

The program used to perform the automation of the experimental system was LabVIEW, using a specific program to control the experimental set-up and allow the control, acquisition and analysis of the Mueller matrices obtained. With the program we have easy integration with the hardware used, specifically with the device controllers. Another very important part is that it allows the user a simple interaction with the interface. We will explain the functionalities in Appendix B. In Fig. 4.6 the block diagram of the algorithm used for the automation of our experiment is presented.

First we must define all of the initial parameters (two-dimensional motion range and step size in the horizontal and vertical direction, step size of stages,

---

[7] Details presented in Appendix C.

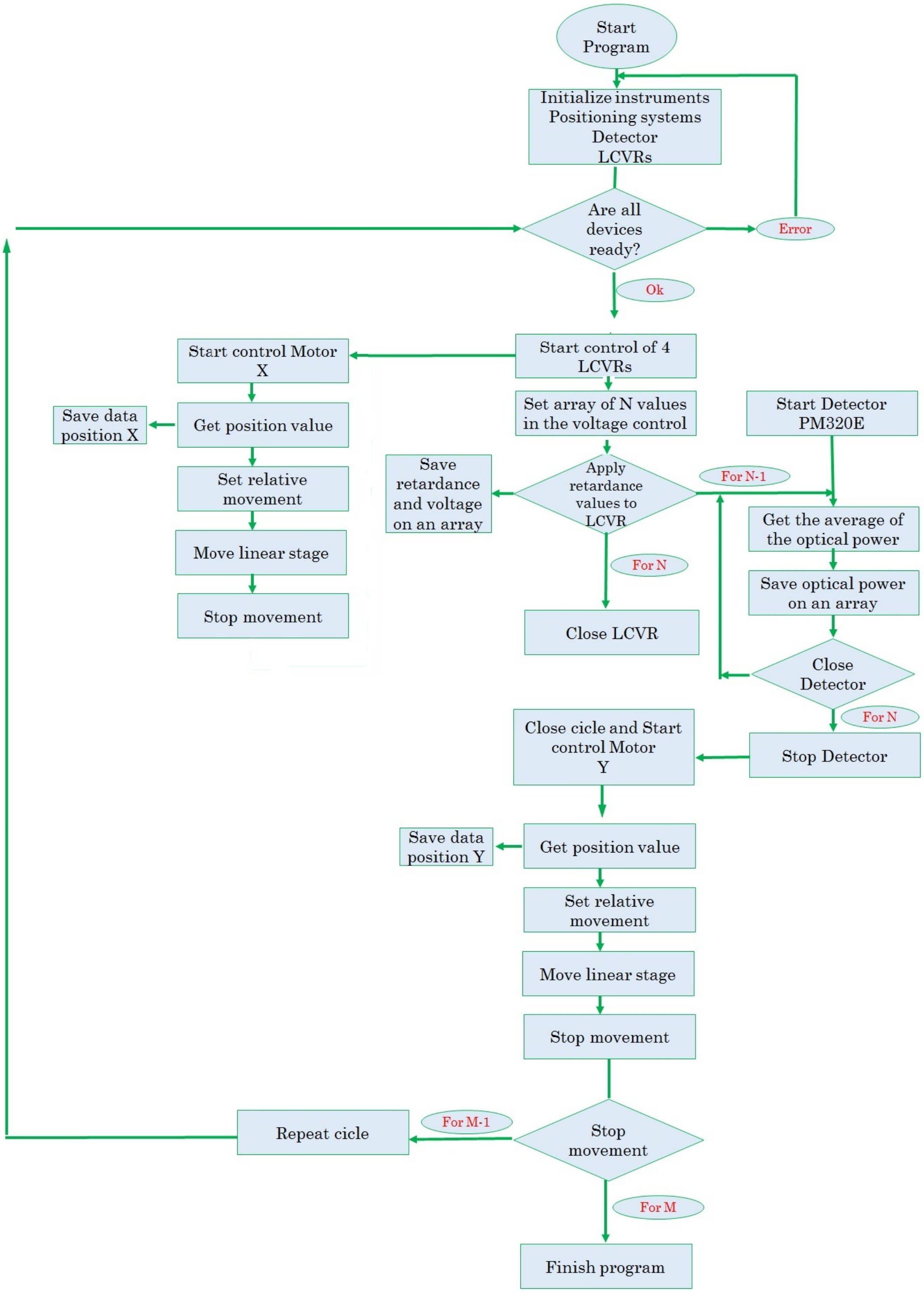

Figure 4.6: Block diagram of the program to automate the polarimeter with the most basic aspects of the operation of all devices. In Appendix B, the complete description of the program is presented.

detector sampling and the set of voltage-retardance values). After setting the parameters, all devices are initialized, the instrument connections are checked, and the program's logical procedure is initialized. The horizontal linear stage moves to the starting position, after which the LCVR sets the delay values and then the detector measures the optical power values and all data is saved. This procedure is performed iteratively for each position of the horizontal stage and the set of retardances that have been defined. Once the first cycle is complete, the second linear stage moves in the vertical direction, the value is saved and the previous cycle is repeated until it complies with the previously set parameters.

The Mueller matrices for each position are stored in a file that we can use to analyze the behaviour of the sample studied. With this program it is possible to scan the sample bi-dimensionally point to point with resolution up to 1 micrometer, and we can scan an area of 25mm. Obviously if we scan a sample bigger it will take more time to acquire the data, but we can maintain the resolution in the measurements.

4.3 An overview of the liquid crystal variable retarders

4.3. An overview of the liquid crystal variable retarders

Liquid crystal (LC) are optically anisotropic media that act locally as a uniaxial retardation plate and exhibit optical birefringence [69]. They produce different polarization states depending on the external applied voltage and therefore can also be used in polarimeters [70, 71, 89]. These voltage-controlled LC devices are being used in many different applications ranging from optical rotators or protection sensors, to wavefront corrector devices. In this work the theoretical basis of a polarimeter using a set of LC variable retarders (LCVR), all of them in the input and output optical paths is presented. As we described before in this work, the first two LCVRs are combined to act as the polarization-state generator with the second two forming the polarization-state analyzer. In this way, 16 intensities are recorded, each corresponding to a different independent combination of states PSG-PSA. With this set of intensities the Mueller matrix of the sample and its polarization properties can be computed.

In a nematic liquid crystal the molecules are distributed randomly as in a liquid but orient themselves in the same direction. In their nematic phase, liquid crystal molecules have an ordered orientation, which together with the stretched shape of the molecules creates an optical anisotropy. When an electric field is applied, the molecules align to the field and the level of birefringence is controlled by the tilting of the LC molecules, as can be seen in Fig. 4.7

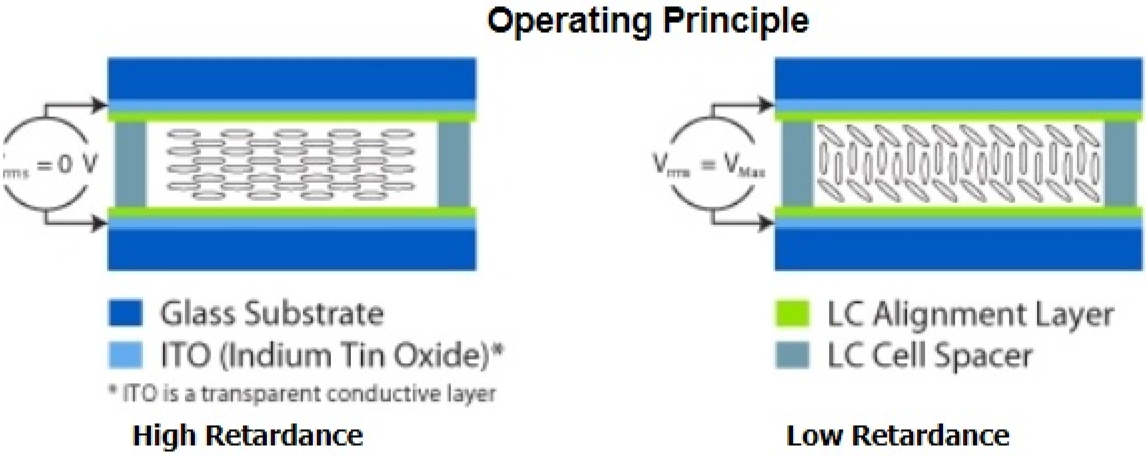

Figure 4.7: We present the diagram of operation from the LCVR implemented in this work, [102].

We use the Full Wave Liquid Crystal Variable Retarder LCC1223 from Thorlabs, this uses a nematic liquid crystal cell to function as a variable wave plate. The absence of moving parts provides quick switching times on the order of milliseconds. This retarder is used directly with the LCC25 liquid crystal controller also from Thorlabs. The LCC1223 has anti-reflection(AR) coating for visible light from 350 to 700 nm. The retarder features a 10mm clear aperture. Each of the liquid crystal variable retarders consists of a transparent cell filled with a solution of Liquid Crystal molecules. The orientation of the LC molecules is determined by the alignment layer in the absence of an applied voltage. The alignment layer is composed of an organic polymide (PI) coating whose molecules are aligned in the rubbing direction during manufacturing. Due to the birefringence of the LC material, this LC retarder acts as an optically anisotropic wave plate, with its slow axis, marked on the mechanical housing, parallel to the surface of the retarder. Two parallel inner faces of the cell wall are coated with a transparent conductive film so that a voltage can be applied across the cell. When an AC voltage is applied, the LC molecules will reorient from their default alignment according to the applied V_{rms}[8].

LCVR Characterization

We characterized the relationship between the observed retardance and the applied voltage in order to verify the manufacturer's characterization and to be able to produce a set of polarization states with high precision. Here we focus on the

---

[8] In the Appendix C is include the data sheet of the LCVRs used.

most significant properties involved in the operation of the LCVRs for optical applications: the optical axes position, retardance and transmittance.

4.3.1 Measuring the optical axis position

In order to characterize the retarders, we need to find their fast axes. The experimental determination of the orientation of this axis can be performed by placing the retarder between two linear polarizers. The first polarizer is used to generate the linearly polarized light that will pass through the retarder and the second to analyze the light transmitted by it. The polarizers must be oriented so that the polarization direction of one of them is orthogonal to that of the other. By rotating the retarder until the transmitted intensity (or power according to what our detector measures) is minimal, the orientation of the retarder axis can be located, since the lack of detected light will indicate that one of the axes of the retarder is parallel to the direction of the incident polarization. Although this technique allows us to find the orientation of the axis, it does not distinguish between the two axis, then, it will be necessary to determine which axis it is (fast or slow), using known information of the optical elements or information provided by the manufacturer. Using that method, in Fig. 4.8 it is shown that for the first voltages (0-6 Volts) of each LCVR, the relative fast axes position presented a variation of less than 0.5°.

4.3.2 Measuring the retardance-voltage relationship

Fig.4.9, shows a schematic diagram of the typical set-up used to characterize the retardance function of the variable retarders. The light to be analyzed passes through a linear polarizer, then through a variable retarder with its optical fast axis at 45° to the linear polarizer axis. Then, the light passes through a linear polarizer with its tranmission axis perpendicular to the axis of the first polarizer. Finally, the intensity of the light transmitted by the optical system is measured. The detected light intensity depends on the retardance, which also depends on the birefringence of the variable retarder [103].

Theoretical modelling of the LCVR characterization

Analogously to the theoretical calculation made for the PSG and PSA in Chapter 3, we can make the calculation for the system presented in Figure 4.9. By using a combination of Stoke vectors and Mueller matrices, the optical system affects the Stokes vector of the light through the following relation:

$$\mathbf{S}^{out} = \mathbf{M}_{sys}\mathbf{S}^{in}, \tag{4.1}$$

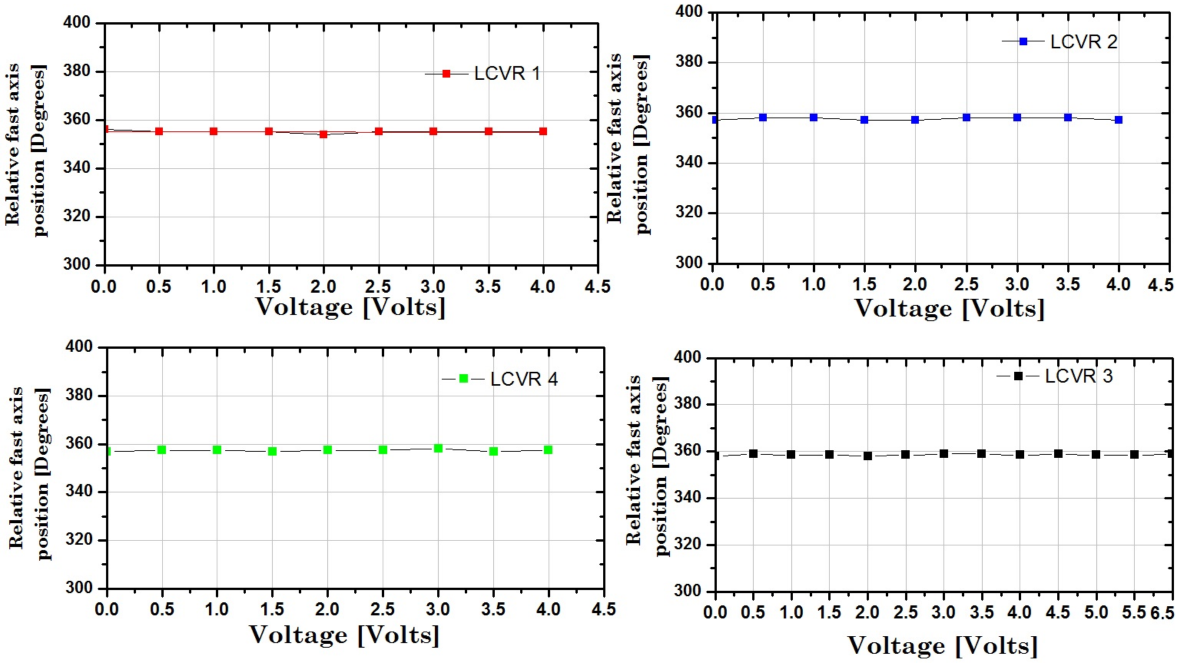

Figure 4.8: Optical axes position for liquid crystal variable retarders. The resultant error bar for each measurement is smaller than its distinct symbol. If we average the relative axis position of each LCVR, we obtain $LCVR1 = 355° \pm 0.5°$, $LCVR2 = 357.5° \pm 0.5°$, $LCVR3 = 358.62° \pm 0.36°$, $LCVR4 = 357.38° \pm 0.33°$.

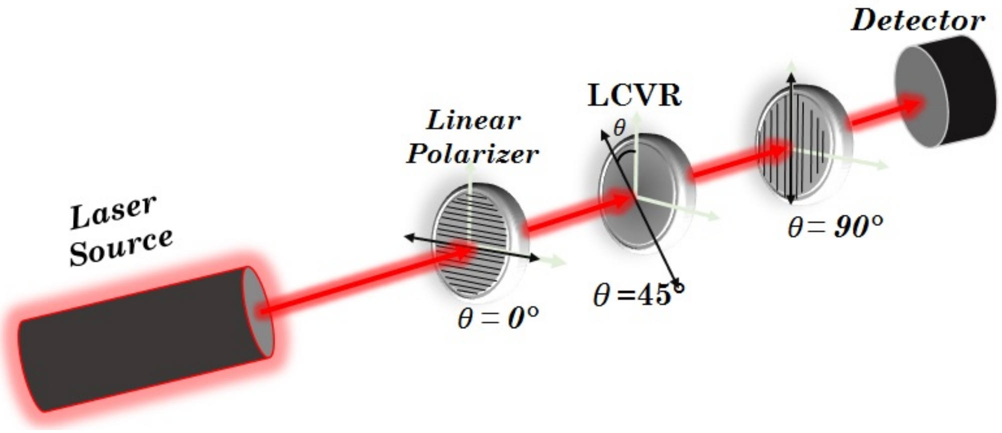

Figure 4.9: Set-up used to characterize the Liquid Crystal Variable Retarders.

where $\mathbf{S}^{in}$ is the Stokes vector of the light coming out of the source, $\mathbf{S}^{out}$ is the Stokes vector of the light at the detector. The detected intensity I is the first term of the Stokes vector $\mathbf{S}^{out}$, which is

$$I = S^{out0}. \tag{4.2}$$

The term $\mathbf{M}_{sys}$ in Eq. 4.3 is the Mueller matrix of the system and can be written in terms of the Mueller matrices of each of the components in the system; namely,

$$\mathbf{M}_{sys} = \mathbf{M}_{P2}(90°)\mathbf{M}_{R}(\delta, 45°)\mathbf{M}_{P1}(0°), \tag{4.3}$$

where $\mathbf{M}_{P2}(90°)$ and $\mathbf{M}_{P1}(0°)$ are the Mueller matrices of the linear polarizer with its transmission axis at 90° and 0°, respectively. $M_R(\Delta, 45°)$ is the Mueller matrix of a retarder of retardance Δ with its fast axis at 45°. Then, the Mueller matrix for the system becomes

$$\mathbf{M}_{sys} = \frac{1}{4}\begin{bmatrix} 1 & -1 & 0 & 0 \\ -1 & 1 & 0 & 0 \\ 0 & 0 & 0 & 0 \\ 0 & 0 & 0 & 0 \end{bmatrix} \begin{bmatrix} 1 & 0 & 0 & 0 \\ 0 & \cos\Delta & 0 & -\sin\Delta \\ 0 & 0 & 1 & 0 \\ 0 & \sin\Delta & 0 & \cos\Delta \end{bmatrix} \begin{bmatrix} 1 & 1 & 0 & 0 \\ 1 & 1 & 0 & 0 \\ 0 & 0 & 0 & 0 \\ 0 & 0 & 0 & 0 \end{bmatrix}$$

$$= \begin{bmatrix} 1-\cos\Delta & 1-\cos\Delta & 0 & 0 \\ -1+\cos\Delta & -1+\cos\Delta & 0 & 0 \\ 0 & 0 & 0 & 0 \\ 0 & 0 & 0 & 0 \end{bmatrix}$$

. (4.4)

To perform the calculation of the output Stokes vector of the light in the detector, after passing through the second polarizer, we need a particular value of the input Stokes vector(for the light arriving at the first polarizer). We assume the incident light to be unpolarized. Substituting Eq. 4.2 into Eq. 4.3 with the Stokes vector of the incident light given by

$$S^{in} = \begin{bmatrix} 1 \\ 0 \\ 0 \\ 0 \end{bmatrix}, \tag{4.5}$$

and the detected intensity I becomes

$$I = A(1 - cos\Delta), \tag{4.6}$$

where Δ is the retardance of the liquid-crystal cell and A is a constant that depends on the experimental parameters such as the absorption and extinction ratio of the poalrizers and the incident intensity. The maximum intensity I_{max}, is achieved when $cos\Delta = -1$. Thus, substituting this value in Eq. 4.6 we obtain

$$I_{max} = A(1 + 1) = 2A, \tag{4.7}$$

so that in this case

$$A = \frac{I_{max}}{2}, \tag{4.8}$$

and, Eq. 4.6 becomes

$$I = \frac{I_{max}}{2}(1 - cos\Delta). \tag{4.9}$$

Therefore, the retardance of a LCVR as function of the detected intensity is given by

$$\Delta = cos^{-1}(1 - \frac{2I}{I_{max}}). \tag{4.10}$$

Experimental characterization and phase unwrapping procedure

We present in Fig. 4.10 the relationship between detected light intensity and the voltage applied to the liquid crystal variable retarder 1, for a wavelength of 633 nm. The error associated to each measurement is about $\pm 0.0006\mu$W which represents the standard deviation of a set of 100 optical power measurements performed for each applied voltage value. The measurement time was 0.001 seconds. Then, for each value of optical power measured by the system in Fig. 4.9 presented in Fig. 4.10 we can apply Eq. 4.10 to obtain the retardance in degrees as a function of the applied voltage to the LCVR1.

In Fig. 4.11, the variation of the retardance curve (in degrees) with the applied voltage is shown, but this phase is "*wrapped*" into a range from 0° to 180°. This range is due to the application of Eq. 4.10, where the inverse cosine is limited to values between 0 and π. Because the actual retardance values cannot be extracted directly form the physical signal, it is necessary to perform a phase unwrapping.

Phase unwrapping procedure

The experimental procedure described above generates data in the range between 0° and 180°. Due to the trigonometric functions that are used in the analysis procedure an analysis known as "*phase unwrapping*" must be performed on the experimental data to indirectly obtain the original, continuous function of the applied voltage to retardance relationship by removing discontinuities known as "*phase jumps*" (as can be seen in Fig. 4.11). This problem can be solved for

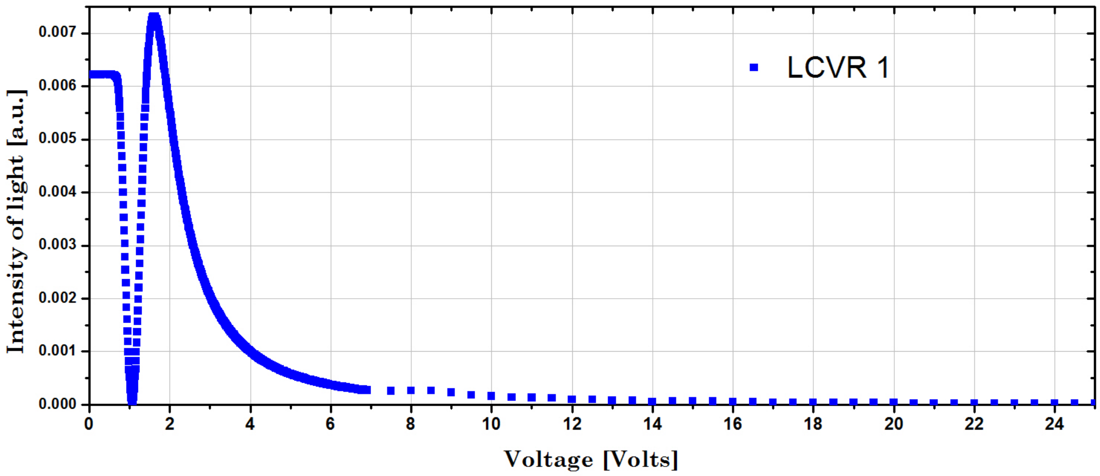

Figure 4.10: Intensity of Light VS. Applied voltage to the liquid crystal variable retarder 1 (the same process was implemented to all LCVRs) using a wavelength of 633nm at $T = 22°C$. Measurements were made in steps of 0.01V, from 0 to 25 V.

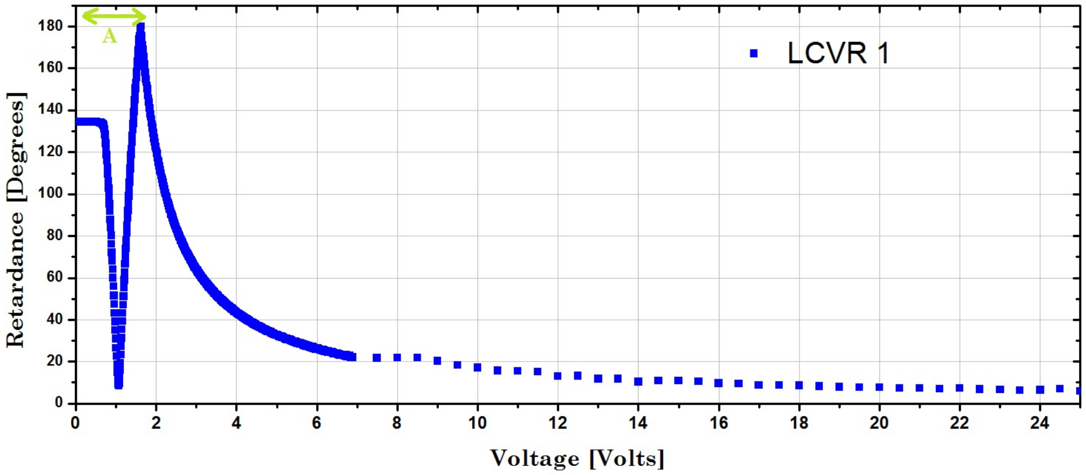

Figure 4.11: Optical retardance as a function of the voltage applied to the LCVR1 for a wavelength of 633 nm at $T = 22°C$. The section labelled A need to be corrected using the phase unwrapping procedure.

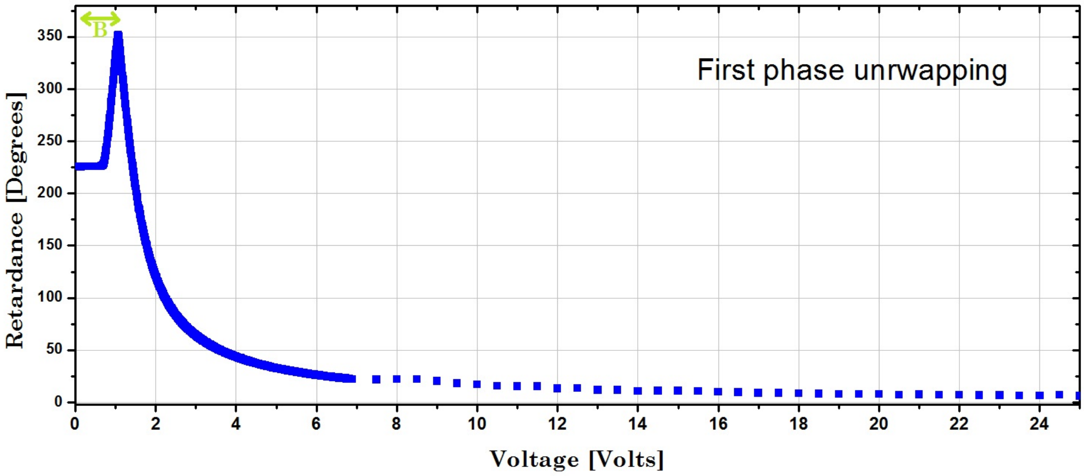

Figure 4.12: Curve resulting from the first phase unwrapping procedure. It is necessary to repeat step 4 of the phase unwrapping in the section labeled B.

low-noise data by integrating the wrapped phase over the full domain of voltage values [104]-[107]. The final result is a continuous curve that shows the full range of variation of the optical retardance with applied voltage, which usually spans more than a wavelength ($0° - 360°$).
To perform the phase unwrapping on our experimental results, the following steps are used. First, it is necessary that the final shape of the experimental curve be smooth, with no discontinuities or sudden changes in the slope. Second, sections of the curve that need to be corrected (for phase jumps) must be identified. For Example, Fig. 4.11 shows section A on the curve of the experimental results that need to be corrected. Third, one must identify sections of the curve where the phase can be smoothed by multiplying the values of the phase by -1(if it is the case). Fourth, in the sections where the phase exceeds the values of 180°, the curve can be corrected by correcting the phase using

$$\Delta^{'} = 2\Delta_{max} - \Delta, \tag{4.11}$$

where Δ_{max} is the largest value of the retardance on the current version of the curve. For example, in Fig. 4.11 the highest value is seen to be $\Delta_{max} = 180°$. Here, Δ is the value of retardance that needs to be corrected and $\Delta^{'}$ is the corrected retardance value. Section A on Fig. 4.11 was corrected following steps 3 and 4, respectively, and the result is shown in Fig. 4.12. As can be seen, there is another section that needs to be corrected (section B). Thus, it is necessary to repeat step 4 (now with Δ_{max} equal to 360°) to obtain the experimental curve given by Fig. 4.13. Each time the fourth step is repeated the value of Δ_{max} is readjusted.

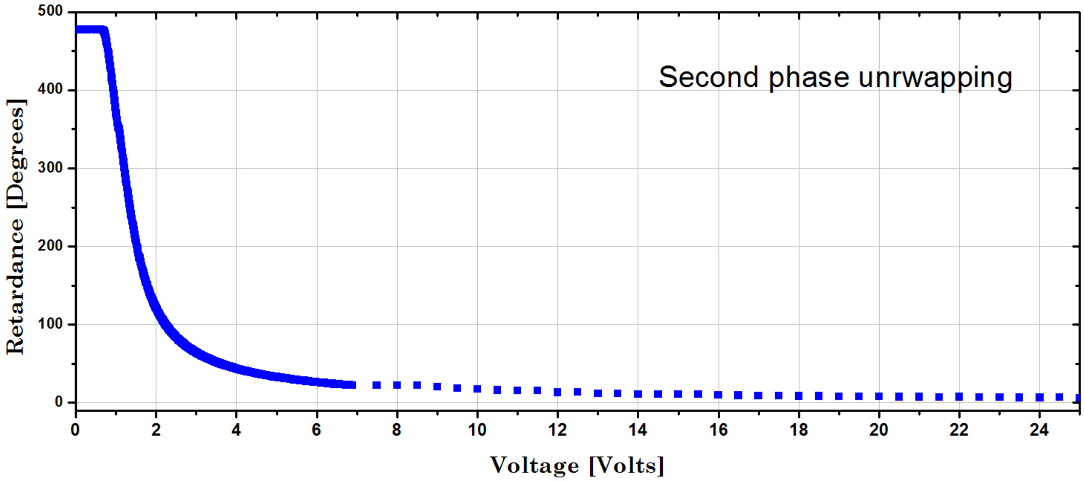

Figure 4.13: Curve resulting from the second phase unwrapping procedure.

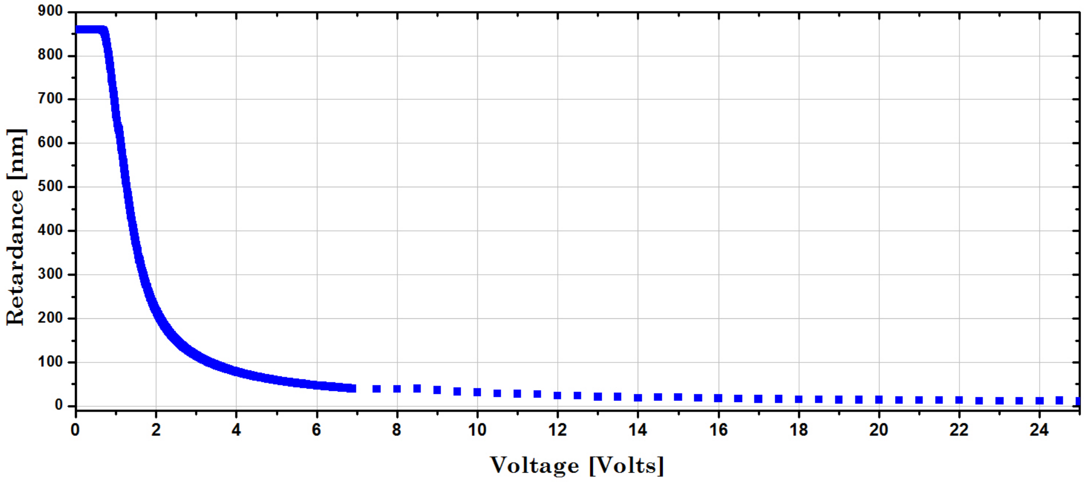

Figure 4.14: Final characterization curve for the LCVR1 in nanometers, which was obtained applying the phase unwrapping procedure twice. The resulting curve has the same behaviour as the curve of the manufacturer.

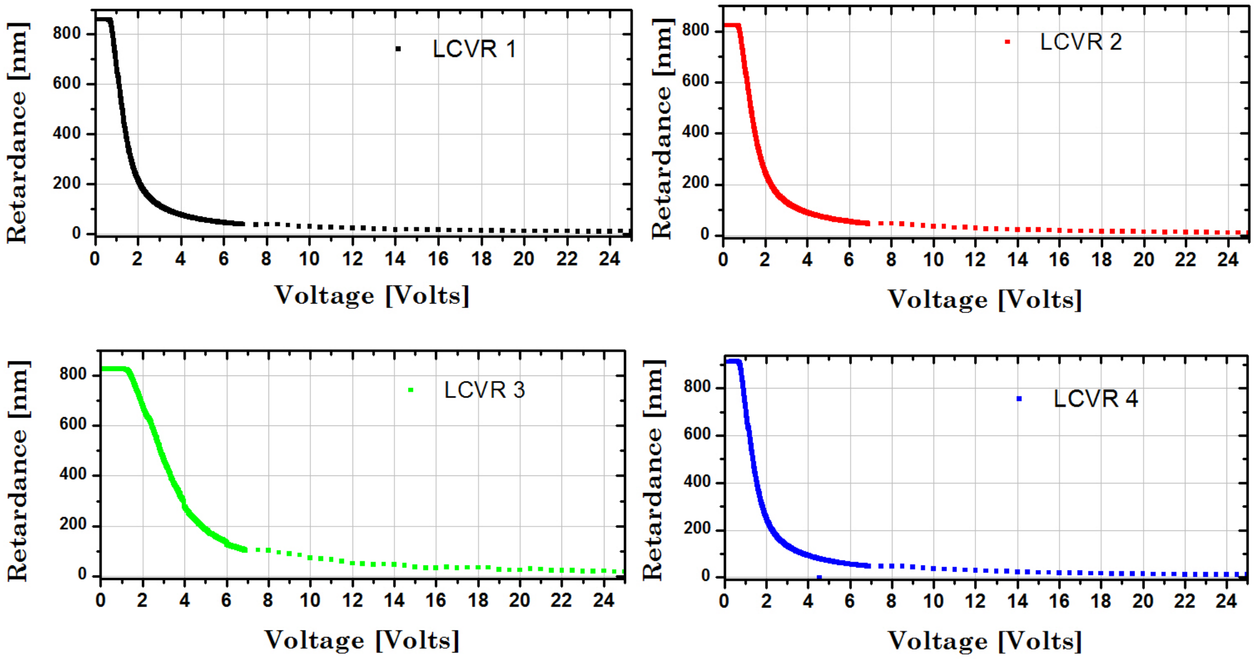

Figure 4.15: Curves of the final characterization for the Liquid Crystal Variable Retarders used in the PSG and PSA of our polarimeter. We used the same procedure described by Fig. 4.10 - 4.14 for al LCVRs

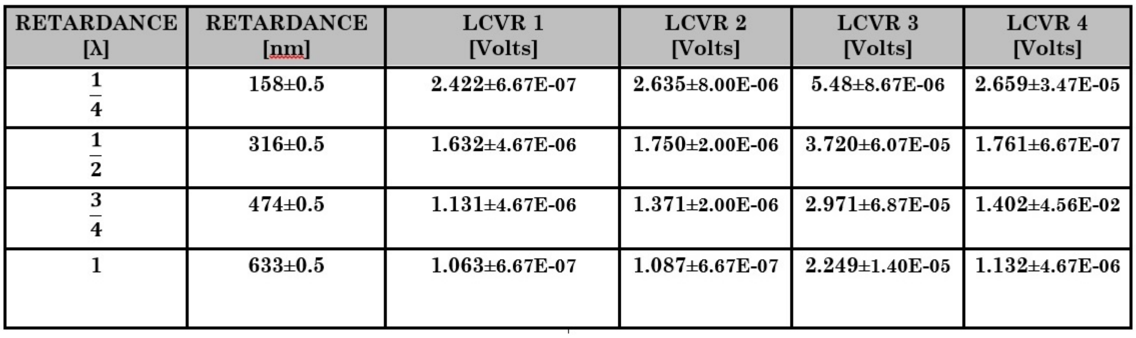

RETARDANCE [λ]	RETARDANCE [nm]	LCVR 1 [Volts]	LCVR 2 [Volts]	LCVR 3 [Volts]	LCVR 4 [Volts]
$\frac{1}{4}$	158±0.5	2.422±6.67E-07	2.635±8.00E-06	5.48±8.67E-06	2.659±3.47E-05
$\frac{1}{2}$	316±0.5	1.632±4.67E-06	1.750±2.00E-06	3.720±6.07E-05	1.761±6.67E-07
$\frac{3}{4}$	474±0.5	1.131±4.67E-06	1.371±2.00E-06	2.971±6.87E-05	1.402±4.56E-02
1	633±0.5	1.063±6.67E-07	1.087±6.67E-07	2.249±1.40E-05	1.132±4.67E-06

Table 4.1: Experimental values of the relationship retardance-voltage. These values were obtained using the characterization curves presented in Fig.4.15. The associated error is calculated considering the standard deviation of the average of voltage values chosen in the characterization curves, according to the retardance value required.

Therefore, by solving the phase unwrapping problem, we get a continuous curve that shows the full range of variation of the optical retardance with the applied voltage, as seen in Fig. 4.14. This curve presented in nanometers has the same behaviour as the curve presented by the manufacturer [102].

Fig. 4.15 presents the characterization curves of the four liquid crystal variable retarders, these curves were used to choose the voltage and then the retardance applied to the PSG and PSA in our polarimeter, as shown in Table 4.1.

4.3.3 Optical transmittance behaviour of the LCVRs

The operational definition of the optical transmittance is given by[75]

$$T = \frac{I_t}{I_i}, \tag{4.12}$$

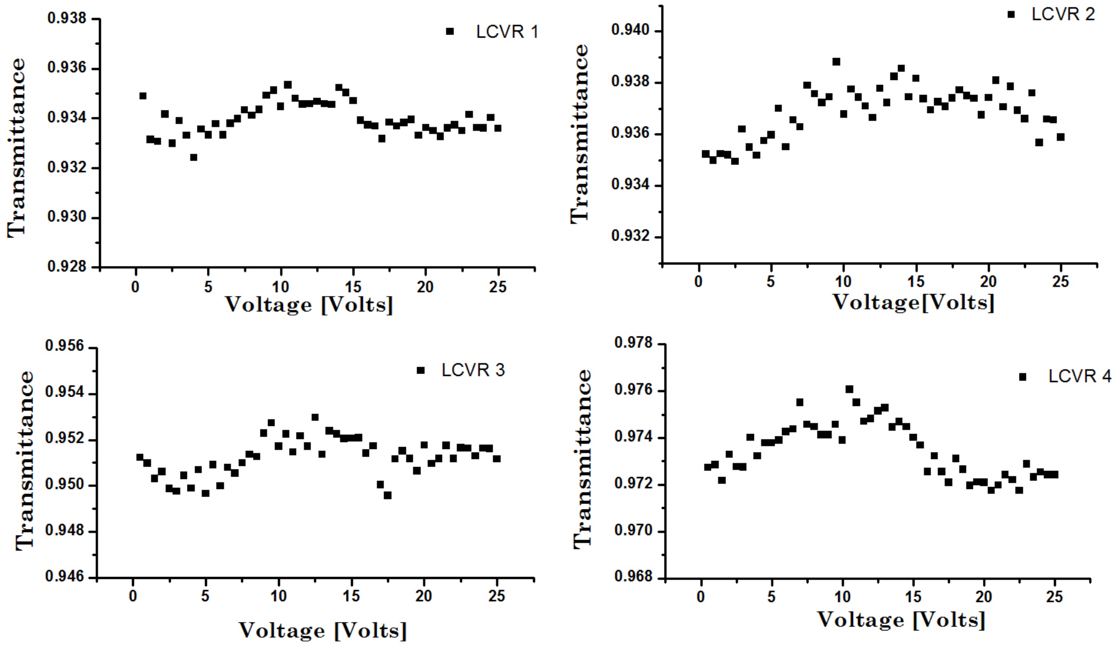

Figure 4.16: Voltage dependence of the optical transmittance in the LCVRs for a wavelength of 633 nm. The associated error for each measurement is presented in Appendix G.

where I_t is the irradiance transmitted by a sample (LCVR) and I_i is the incident irradiance on the sample. This definition is only valid for light at normal incidence angle on the surface of a material. Hence, for a constant I_i, I_t was measured for each applied voltage value as shown in Fig. 4.16. In this case, the lowest measured value corresponds to a transmittance reduction between 2.5% to 7% and the maximum

POLARIZING ELEMENT	TRANSMISSION COEFFICIENT
Quarter-wave Plate λ/4	$0.9334 \pm 8.7785x10^{-6}$
Nanoparticle Linear Film Polarizer (P1)	$0.7901 \pm 2.7976x10^{-6}$
Nanoparticle Linear Film Polarizer (P2)	$0.7581 \pm 3.1815x10^{-6}$
Glan Thompson Polarizer (Calibration element)	$0.9190 \pm 4.4679x10^{-6}$

Table 4.2: Transmission coefficients of the polarizing optical elements in the polarimeter built in this work. Although the nanoparicle linear polarizers have a lower transmission than the Glan Thompson polarizers, they are more compact for the implementation inside the polarimeter, besides that we only have a Glan Thompson polarimeter.

variation with the applied voltage represents a change of 0.6%. This variation should produce a negligible effect on the results of the polarimetric measurement methods proposed in Chapter 2 and 3. This procedure was repeated on four LCVRs obtaining the results shown in Fig.4.16. On the other hand, measurements of the transmission coefficient for the rest of the optical elements of our polarimeter are presented in Table 4.2.

4.4 Mueller matrices of known samples

4.4. Mueller matrices of known samples

The experimental procedure to perform the measurement of the experimental Mueller matrix is as follows.

- We need to establish the parameters in the experimental set-up, for example the size of the movements in the linear stage.

- For known samples that are composed of transmitting materials, the number of measurements that will be made (for example 16, 24 or 36 intensity measurements), is chosen in the program, according to the Table 3.2.

- The measurement time is established (each measurement takes 1 ms) in the program and is not modified unless variations are required to perform specific time-related tests.

- The angle of the polarimeter arm is set to fix the position at lens CL2, the PSA and the detector are placed. The default value is 45°, although it is possible to change it, if it is required. We should only consider that this angle is limited by the dimensions of the mounts, and is valid in the range of 30°-90°. There are some works [96] where studies are carried out focusing on the variations of this angle, here we focus only on the effect on polarization changes when the light interacts with the sample at a fixed angle.

- The spot-size can be changed with the displacement of the surface and detection arm with a micrometric positioning linear stage (resolution 25μm), using the characterization curve presented in Fig. 4.4. We use a fixed spot of 3.7μm and a image length of $90mm$, which allows us to concentrate our attention on the effects of the polarization changes produced by the surface when it is illuminated point to point with a focused beam.

- When we analyze unknown reflecting samples, it is necessary to include in the program the scan parameters of the sample, typically we are going to use a scan of 30μm x 30μm with step of 1μm.

- The experimental data of the Mueller matrices are ordered and stored in a text file which we can easily analyze.

In Fig. 4.17 we present the experimental set-up of the final polarimeter. The measurements to calibrate the system and the measurement of the known samples are performed in transmission mode, because the samples used are made of transmitting materials. In Fig. 4.17 we also present the polarimeter in reflection mode, this configuration allows us to carry out the measurements of unknown samples in Chapter 5.

Before making measurements of the Mueller matrix of any unknown optical sample, it is advisable to first measure that of some element with known matrix, such as vaccum(air), a polarizer(with optical axes at $0°, 45°, 90°$ and $-45°$), a retarder (with optical axis at 30°), etc. In this way it is possible to make an assessment of the reliability of the method and the components of the system, as well as comparing the results that are obtained experimentally with the theoretical results reported in the literature [66].

In Eq. 4.13 to Eq. 4.17 we present the experimental Mueller matrices obtained with our polarimetric device, which are known matrices of the known samples.

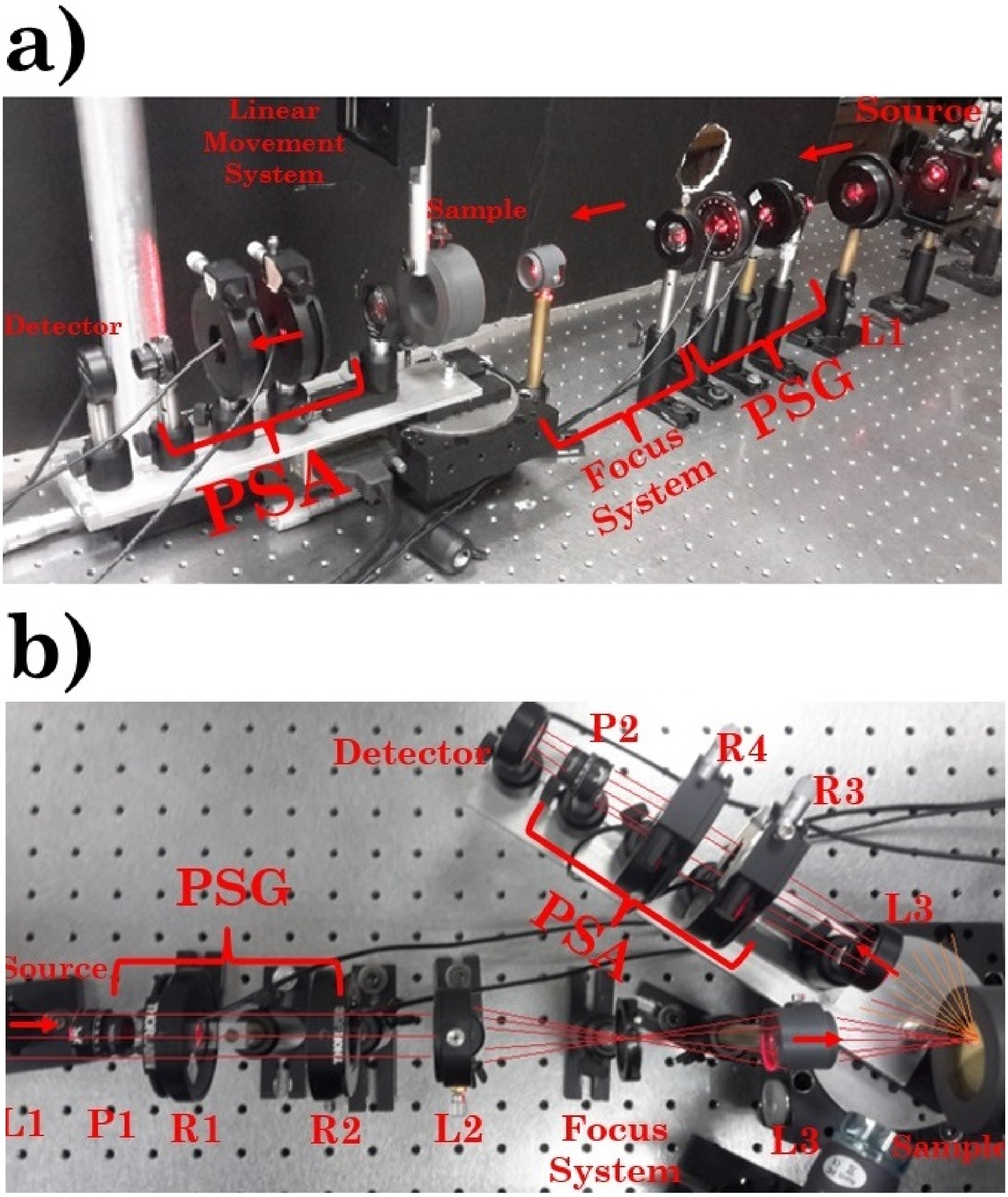

Figure 4.17: Experimental device of the polarimeter design and built in the present dissertation. a) Polarimeter in transmission mode and b) Polarimeter in reflection mode.

$$\mathbf{M}_{air} = \begin{bmatrix} 0.9997 & -0.0039 & -0.2492 & 0.2430 \\ -0.0383 & 0.9539 & 0.2910 & 0.1997 \\ 0.1754 & -0.0088 & 0.8689 & -0.0160 \\ -0.0616 & -0.1997 & 0.0542 & 0.9181 \end{bmatrix} \pm \begin{bmatrix} 0.001 & 0.001 & 0.145 & 0.003 \\ 0.001 & 0.001 & 0.193 & 0.002 \\ 0.227 & 0.005 & 0.010 & 0.010 \\ 0.001 & 0.004 & 0.001 & 0.001 \end{bmatrix} \tag{4.13}$$

$$\mathbf{M}_{Pol.0^\circ} = \begin{bmatrix} 1.0000 & 0.9210 & 0.2618 & 0.2613 \\ 0.9597 & 0.8852 & 0.2521 & 0.2517 \\ -0.2051 & -0.1863 & -0.0620 & -0.0604 \\ 0.0226 & 0.0230 & -0.0006 & 0.0014 \end{bmatrix} \pm \begin{bmatrix} 0.001 & 0.0008 & 0.0083 & 0.0062 \\ 0.0003 & 0.0010 & 0.0081 & 0.0062 \\ 0.0026 & 0.0028 & 0.0065 & 0.0048 \\ 0.0045 & 0.0045 & 0.0055 & 0.0043 \end{bmatrix} \tag{4.14}$$

$$\mathbf{M}_{Pol.45^\circ} = \begin{bmatrix} 1.0000 & -0.0440 & 0.9308 & 0.1712 \\ -0.0401 & -0.0021 & -0.0125 & 0.0061 \\ 0.8672 & -0.0016 & 0.9749 & -0.0162 \\ 0.2100 & 0.0597 & -0.0410 & -0.0897 \end{bmatrix} \pm \begin{bmatrix} 0.0001 & 0.0078 & 0.0436 & 0.2349 \\ 0.0086 & 0.0081 & 0.0417 & 0.0084 \\ 0.0160 & 0.0674 & 0.0212 & 0.3534 \\ 0.0703 & 0.1243 & 0.5494 & 0.1337 \end{bmatrix} \tag{4.15}$$

$$\mathbf{M}_{Pol.90^\circ} = \begin{bmatrix} 1.0000 & -0.8450 & -0.2410 & -0.2099 \\ -0.9556 & 0.8100 & 0.2307 & 0.2009 \\ 0.1834 & -0.1590 & -0.0419 & -0.0340 \\ -0.0283 & 0.0293 & 0.0068 & 0.0068 \end{bmatrix} \pm \begin{bmatrix} 0.0001 & 0.0035 & 0.0013 & 0.0020 \\ 0.0001 & 0.0033 & 0.0013 & 0.0019 \\ 0.0004 & 0.0004 & 0.0025 & 0.0007 \\ 0.0001 & 0.0001 & 0.0008 & 0.0007 \end{bmatrix} \tag{4.16}$$

$$\mathbf{M}_{Pol.135^\circ} = \begin{bmatrix} 0.9596 & 0.1052 & -0.9535 & 0.1586 \\ 0.0165 & 0.0023 & -0.0947 & 0.0205 \\ -0.9547 & -0.0467 & 0.8245 & -0.0908 \\ -0.2708 & -0.0497 & 0.1811 & -0.1917 \end{bmatrix} \pm \begin{bmatrix} 0.0700 & 0.0592 & 0.0007 & 0.0121 \\ 0.0102 & 0.0007 & 0.1259 & 0.1259 \\ 0.3419 & 0.0581 & 0.4984 & 0.0942 \\ 0.1802 & 0.0010 & 0.3065 & 0.0856 \end{bmatrix} \tag{4.17}$$

As we can see from Fig. 4.18, the Mueller matrices are not exaclty the expected matrices. The differences between the experimental matrices and the theoretical matrices [66] are mainly due to errors in the angles of the fast axes of the retarders, errors in the values of the retardances used in the variable retarders to produce the required incident and detected Stokes vectors used, and it may be that, to a lesser extent, the quality of each polarizing element.

These differences between the theoretical Mueller matrices and the Mueller matrices measurements of our known samples, suggest that the precision of the polarimeter for known samples will be reliable only up to the first significant figure, reaching errors of up to 22%. To reduce the errors of our instrument, and improve the accuracy of the polarimeter it is possible to approach the problem in two different ways: manual adjustments can be made in the experiment, however there will always be systematics errors; the other option is to work with a calibration and data extraction program that considers the errors present in the instrument in such a way that accuracy of the instrument is improved. Details about the data extraction program will be presented in Chapter 5.

Figure 4.18: Mueller matrices of a known samples, blue lines show the experimental results and the orange lines the theoretical values for air, horizontal polarizer(0°), polarizer at 45°, vertical polarizer (90°) and polarizer at 135°, respectively.

Chapter 5

Calibration and data extraction method

In this Chapter we present a method for calibration and data-extraction for non-optimized Mueller matrix polarimeters. The advantage of this method is that it is a very precise method to estimate the Mueller matrix, and allows a reduction in measurement time to compensate the time used by our polarimeter presented in Chapter 4, which is a scanning polarimeter. The calibration process requires the measurement of four known polarization devices. Here we use free-space transmission, a horizontal and a vertical linear polarizer, and a quarter-wave retarder with its fast axis at 30° to the horizontal. Experimental measurements of rotating quarter-wave, half-wave retarders and a linear polarizer show that very good results can be obtained with the proposed fitting optimization method.

5.1 Fitting Optimization Method

The method proposed here does not require exact optimization of the experimental system to reduce the condition number, and uses calibration samples to calculate the errors in the experimental system. These errors include the experimental alignment errors, experimental errors in the retardance values in the variable retarders, and also the errors introduced in the calculation method. During calibration, all of these errors are calculated assuming that the data-extraction algorithm is perfect and introduces no errors, and that the only errors are alignment and retardance errors in the experimental system. Because of this, the calculated errors obtained in actual measurements for a fixed experimental system, but with different calculation methods, are different, reflecting the different error propagation for different calculation strategies.

In this work, although the retardance values were chosen to give the values of the incident and detected polarization states required by the method of Bickel and Bailey [87], it is possible to use other methods to extract the sample Mueller matrix from the measured intensities. The Bickel and Bailey method was used so that the optimized and non-optimized cases could be studied with the same data set, only changing the calculation method.

In our system for measuring the polarization of scattered light, we are interested in measuring the Mueller matrix from one point to another in the studied sample. This means that a stable and accurate method for extraction of polarimetric data from non-optimized polarimeter must be implemented. As we presented in Chapter 3, to change the condition number in the experiment, the number of independent polarization states should be changed. For an optimized system six incident Stokes vectors and six detected Stokes vectors were used; these were linear horizontal (H), linear vertical (V), linear at +45°(+), linear at −45°(−), right circular (R), and left circular (L) polarized light. This meant that there were 36 intensity measurements made. The characteristic matrix for the PSG and the PSA in this case is given again by Eq. 3.1 and the condition number for this matrix is $\kappa_6 = 1.7321$, the optimized value.

For the non-optimized case we used only four incident Stokes vectors and four detected Stokes vectors; linearly horizontal, vertical, at +45° and right circular polarized light. This requires 16 intensity measurements and has a PSG and PSA characteristic matrix given by Eq. 3.2, with a condition number of $\kappa_4 = 3.2255$, wich indicates that the system is not optimized [90].

The relation between the measured intensity values and the unknown sample Mueller matrix values was given in Table 3.2. In practice we measured only for the case of 36 measured intensities, and then selected the appropriate data for the case of 16 (four incident and four detected Stokes vectors, see Fig. 5.1), to use the same dataset for each case and ensure that any variations in the results were due to the calculation method.

The experimental system shown in Fig. 5.2 was modeled using the Mueller matrix formalism presented in Chapter 3.3 and 3.4, where we developed the model of the polarization state generator and analyzer. So, we can write the Mueller matrix of the complete system as:

$$\mathbf{M} = \mathbf{M}_{(P2,0^\circ)}\mathbf{R}_4(\Delta_4,\theta_4)\mathbf{R}_3(\Delta_3,\theta_3)\mathbf{M}_S\mathbf{R}_2(\Delta_2,\theta_2)\mathbf{R}_1(\Delta_1,\theta_1)\mathbf{M}_{(P1,0^\circ)}, \tag{5.1}$$

where $\mathbf{M}_{(P,0^\circ)}$ is the Mueller matrix of a polarizer with the transmission axis at an angle $\theta_P = 0^\circ$, and $\mathbf{R}_i(\Delta_i,\theta_i)$ is the Mueller matrix of a retarder with retardance Δ and angular position of the fast axis θ_i. $\mathbf{M}_S$ is the Mueller matrix of the sample. The proposed method involves two steps: a calibration step, and the data-extraction step to obtain the sample Mueller matrix. In the calibration step,

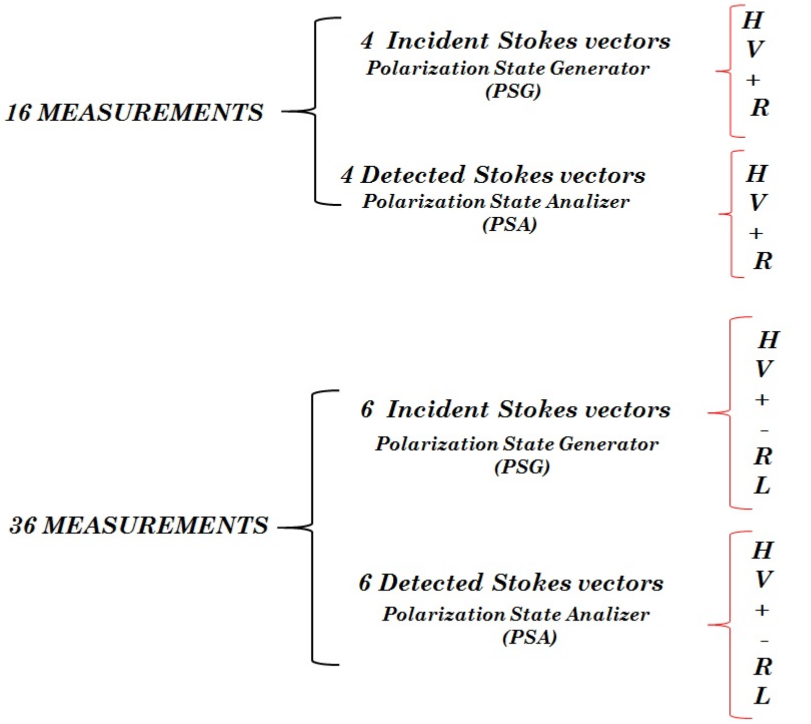

Figure 5.1: Set of retardances for 16 and 36 measurements. The used polarization states are the same presented before: H, linear horizontal; V, linear vertical; +, linear at +45°; −, linear at −45° ; R, right circular; L, left circular.

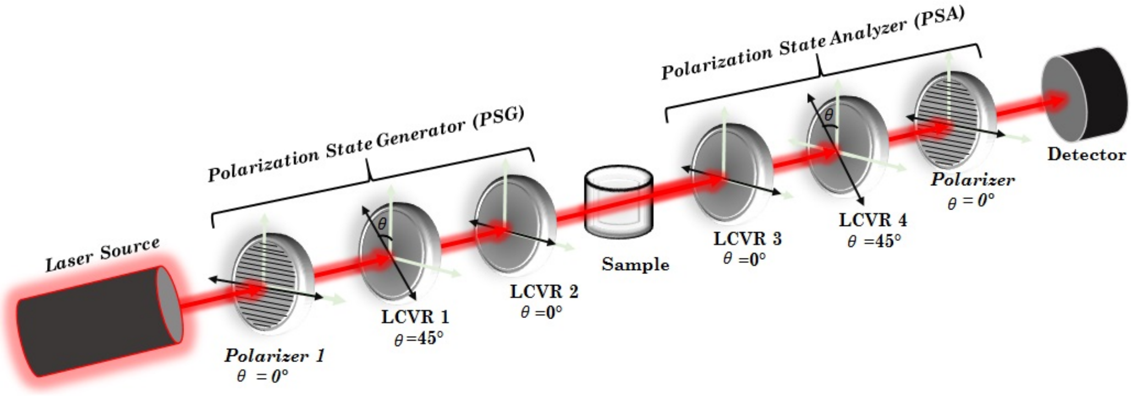

Figure 5.2: Experimental setup for a Mueller-matrix polarimeter. The angles associated with each component refer to the relative angle of the optical axis of that component with respect to the horizontal plane.

four known samples were used: no sample (transmission in air), a horizontal linear polarizer, a linear polarizer at 45°, and a quarter wave retarder with its fast axis at 30°, Fig. 5.3. These were used as they are the samples often used for calibration with other methods. This gives four sets of intensity measurements obtained with known samples.

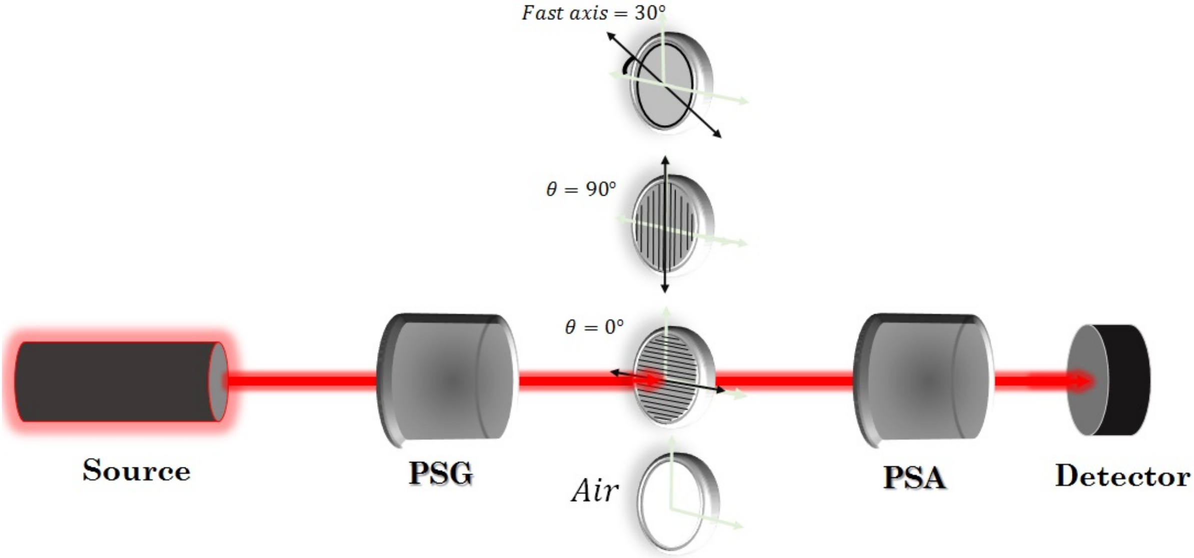

Figure 5.3: Schematic diagram of the four calibration samples used in the method.

The intensities will not be exactly the same as the ideal system model because of errors in the angles of the fast axes of the retarders (four error parameters, one for each variable retarder), and errors in the values of the retardances used in the variable retarders to produce the required incident and detected Stokes vectors. This second error source requires one error parameter for each different retardance value in the variable retarders, and depends on the particular combinations of retardance values and the number of incident and detected Stokes vectors used. In our case, we had 12 retardance values for 16 intensity measurements, and 15 retardance values for 36 intensity measurements. We also included errors in the angles of the two polarizers in Fig. 5.2 (two error parameters) and errors in the position of the transmission axis of the sample polarizer for the calibration samples (two error parameters) and in the fast axis angle and the retardance value of the sample retarder plate (two error parameters). This gives a total of 22 error parameters for the case of 16 intensity measurements, with a total 64 intensity measurements for the four calibration samples; and 25 error parameters for the case of 36 intensity measurements, with a total of 144 intensities for the four calibration samples. Then the model intensities were fitted to the measured experimental intensity values using the error parameters described above as fitting parameters, using a standard non-linear fitting procedure, such as the "Powell" algorithm from Numerical Recipes in C, which we used. While it is true that the non-linear fitting algorithms can be unstable for large numbers of fitting parameters, we have found that, for the cases presented here, the algorithm was very stable and very fast (a few seconds on a 2.70 GHz PC). We found that we required a double fitting procedure to have accurate results; the fitting algorithm was performed for a given tolerance parameter, then the optimization directions were reset to the unit vectors and the fitting algorithm was run again. This procedure was found to give better results than simply reducing the tolerance parameter, probably because of numerical errors in the calculations. Another important point for these algorithms is the proposed starting solution for the fitting process. In all cases here, we used the ideal designed experimental system as the starting solution.

The second step is the calculation of the Mueller matrix of an unknown sample. In this step the error parameters calculated in the previous step are assumed as known, fixed errors, so that we know the system parameters exactly, and the sixteen elements of the unknown Mueller matrix, $M_{S'}$, are now the unknown parameters to be fitted. Again, we fit the model intensity values for the unknown sample, using M_S as the fitting parameters. Notice that in the worst case we have 16 parameters with 16 measurement values, but again the "Powell" algorithm from Numerical Recipes in C [108] was very stable and fast, less than 5 seconds running time on a 2.70 GHz PC. The starting solution in all cases presented here was the unitary matrix, and was reset to the same matrix for each angle of the rotating samples presented in the results section.

5.1.1 Experiment details for calibration

Fig. 5.2 shows the configuration of the polarimeter with no focus system, however we are interested in calibrating the complete system described extensively in Chapter 4. The diagram in Fig. 5.4 implements a system which focuses the light beam on the study sample to be analyzed point by point. We use the transmission polarimeter to perform the calibration through the fitting method. We present results of the calibration and data extraction for this system, as well as the advantages and scopes of the calibration method that we are proposing. Thus a complete calibration of our polarimeter is obtained to measure polarization of scattered light of different samples in the next Chapter.

The calibration procedure consisted of measuring 36 consecutive intensities for a predefined set of voltages applied to the LCVR's for each orientation of the standard optical component used as calibration sample, we measured only for the case of 36 intensity values, that is with six incident Stokes vectors and six detected Stokes vectors. The retardance values used are shown in Table 3.2, for each of the

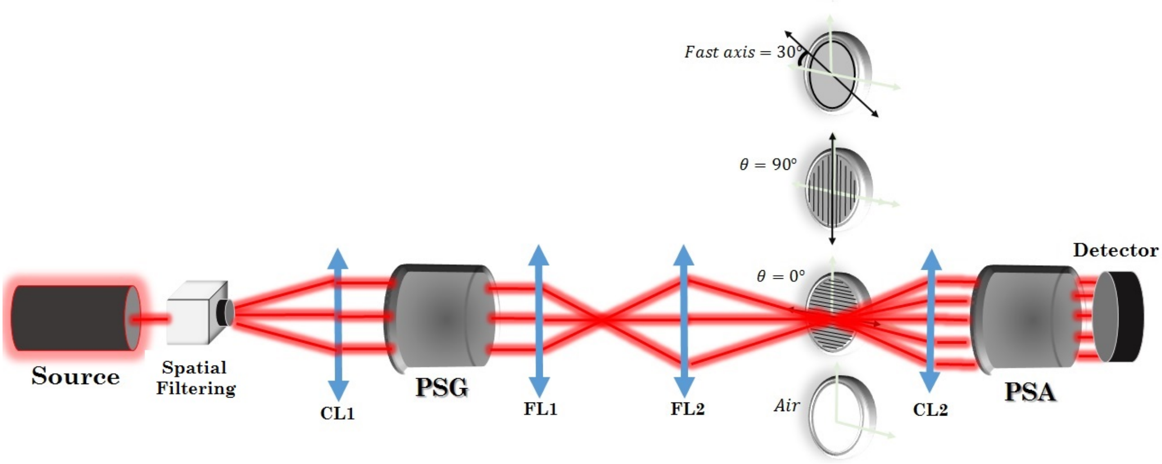

Figure 5.4: Schematic diagram of the four calibration samples used in the fitting method including the focusing system.

36 values of the intensity. The results for the case of 16 measurements (four incident and four detected Stokes vectors), were obtained using only the appropriate values of the measured intensities from the same data set. This was to remove any effects due to variations in the measured values and only study the variations due to the different analysis of the data.

The optical components were then rotated in steps of 10° from 0° to 180°. As we mentioned previously, we used as calibration samples known optical components, then we obtained data for simple transmission without any sample for which the expected Mueller matrix is the identity matrix. The data corresponding to the polarizer, quarter waveplate and no sample where then processed as the four sets of measurement samples required by the fitting method proposed in this chapter.

In order to reduce random errors and noise, each value of the intensity was averaged over 10 individual measurements, with each measurement taking $10ms$, that is a total of $100ms$ per measurement but with a dead time due to the changes of retardance and the response time of the LCVRs of around $100ms$.

5.1.2 Results of the calibration

We implemented a quarter-wave plate (QWP), a half-wave plate (HWP) and a linear polarizer, all of them rotating over a range of 0° to 180°. These samples have been used as standard, known, samples in the literature [109],[110]. The results are presented in Fig. 5.5 to Fig. 5.10. The blue colour shows the ideal theoretical curves for the Mueller matrix element for a QWP (Fig. 5.5 and Fig. 5.6), a HWP (Fig. 5.7 and Fig. 5.8) and a Linear Polarizer (Fig. 5.9 and Fig. 5.10).

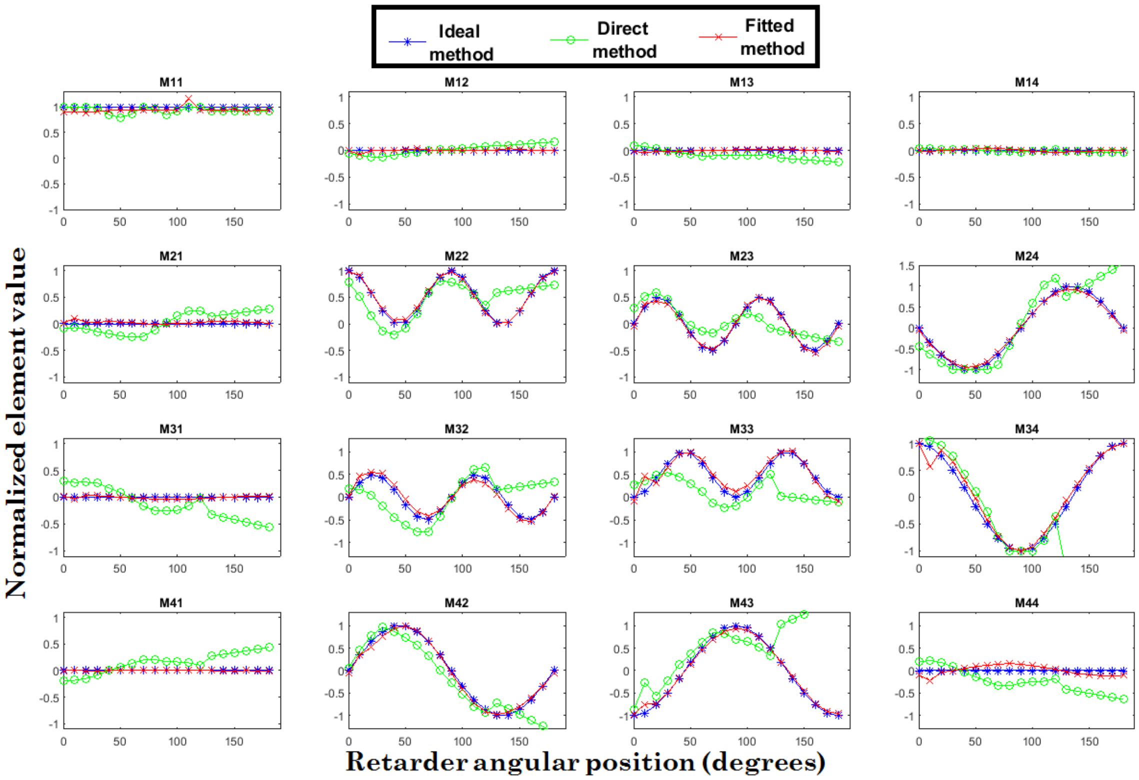

Figure 5.5: The ideal theoretical curves for the Mueller matrix element values(blue), the experimental results of the Mueller matrix element values calculated using the direct (Bickel and Bailey) method (green) and using the fitting method (red) for a rotating QWP, for the case of 16 intensity measurements.

Also in these figures we present the experimental results of the Mueller matrix element values calculated using the direct (Bickel and Bailey) method in green and using the fitting calibration method proposed here in red for the same samples (QWP, HWP and a Linear Polarizer). We present the results for both an optimized system (36 intensities) and the non-optimized case (16 intensities).

The first case we will analyze is the case of 16 intensity values, which is the non-optimized case for the QWP. Fig. 5.5 shows the results of the direct calculation of the unknown Mueller matrices using the Bickel and Bailey equations presented in Eq.3.37, and the results of the fitting method proposed here. The ideal theoretical values of the Mueller matrix elements for the rotating QWP are presented as the blue points. Figure 5.6 shows the same results as Fig. 5.5, but using the optimized case, that is the case of 36 intensity values. It can be seen that for the non-optimized case, the values of Mueller matrix elements using the fitting method are nearer to the theoretical case than the results presented using the direct method.

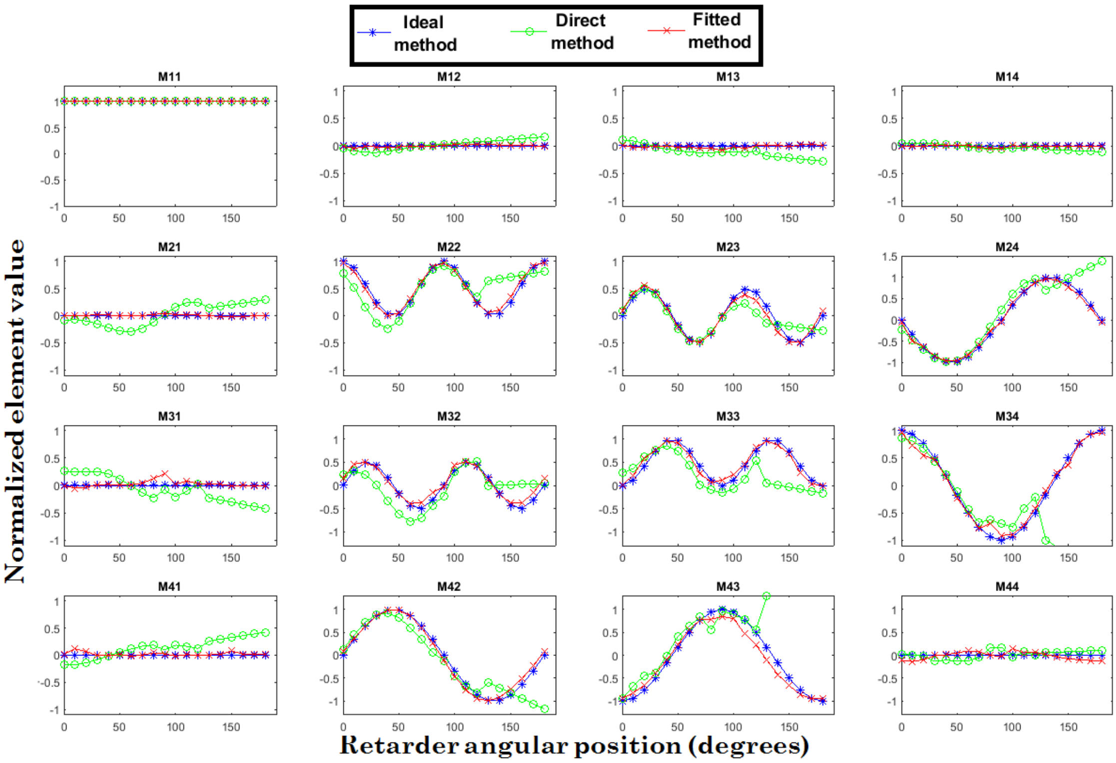

Figure 5.6: The ideal theoretical curves for the Mueller matrix element values (blue), the experimental results of the Mueller matrix element values calculated using the direct (Bickel and Bailey) method (green) and using the fitting method (red) for a rotating QWP, for the case of 36 intensity measurements.

The optimized case (see Fig. 5.6) presents the same results as for the case of 16 intensity values, i.e. the values of the Mueller matrix with the fitting method and closer to the theoretical values than the results using the direct calculation. Because we have an optimized system, the results presented using the direct calculation (Bickel and Bailey) present an improvement compared to the non-optimized case, however the fitting procedure continues to show a better behaviour when we make the element-by-element comparison of the Mueller matrix for the QWP. Thus, the calibration procedure using the fitting method presents very good results for a quarter-wave plate.

For the HWP we find the same performance in the results as those presented for the QWP. As can be seen in Figures 5.7 and 5.8 using the fitting method to calibrate the Mueller matrix of the half-wave plate, it is possible to obtain better results when we compare the Mueller elements of the matrix with the ideal theoretical case, than when we make the comparison of the Mueller matrix elements using the direct method. The results show the same behaviour for both the optimized and non-optimized cases. It is very clear in Fig. 5.7 that the non-optimized case presents very poor results, and the Mueller matrix elements are very different from the theoretical case when the matrix elements are calculated using the direct method. The optimized case can improve these results, however they are not as good as when we use the fitting method to calibrate (see Fig. 5.8). Again, the calibration procedure using the fitting method presents very good results, in this case of a half-wave plate.

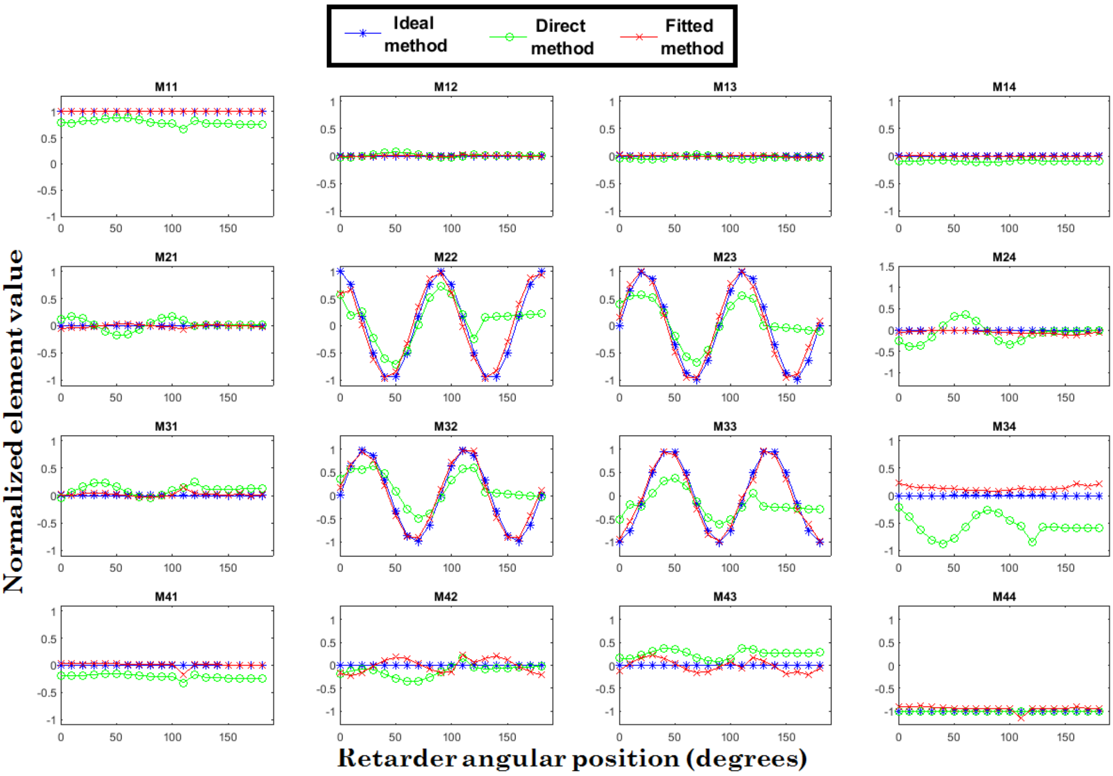

Figure 5.7: The ideal theoretical curves for the Mueller matrix element values (blue), the experimental results of the Mueller matrix element values calculated using the direct (Bickel and Bailey) method (green) and using the fitting method (red) for a rotating HWP, for the case of 16 intensity measurements.

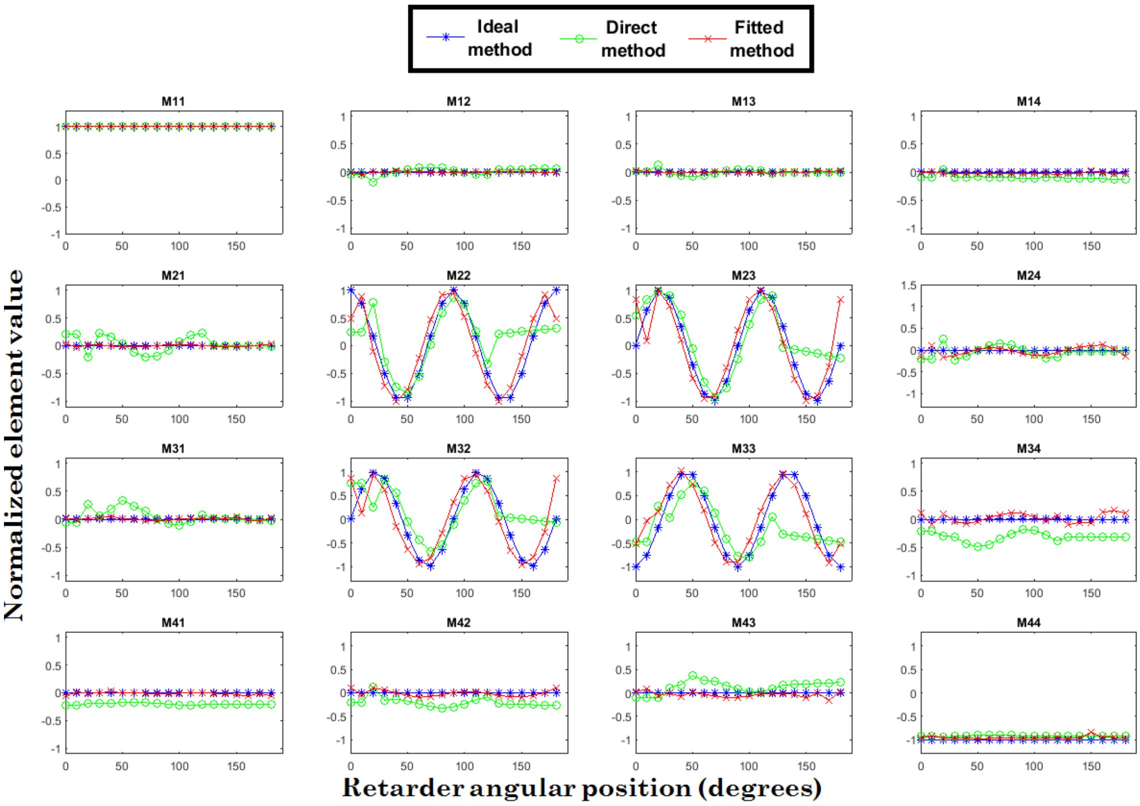

Figure 5.8: The ideal theoretical curves for the Mueller matrix element values(blue), the experimental results of the Mueller matrix element values calculated using the direct (Bickel and Bailey) method (green) and using the fitting method (red) for a rotating HWP, for the case of 36 intensity measurements.

Analogous to the analysis carried out in previous paragraphs for the QWP and HWP, we can analyze the results for the Linear Polarizer rotating from 0° to 180°. It can be seen in figures 5.9 and 5.10 that again the fitting method shows very good results when we do the element-by-element comparison of the Mueller matrix with the ideal theoretical case. In optimized and non-optimized cases, it is possible to observe the same behaviour. When performing the calculation with 36 intensity values for the direct method, we observe that the results improve considerably, however, we observe that the results are closer to the ideal theoretical case when we use the fitting method.

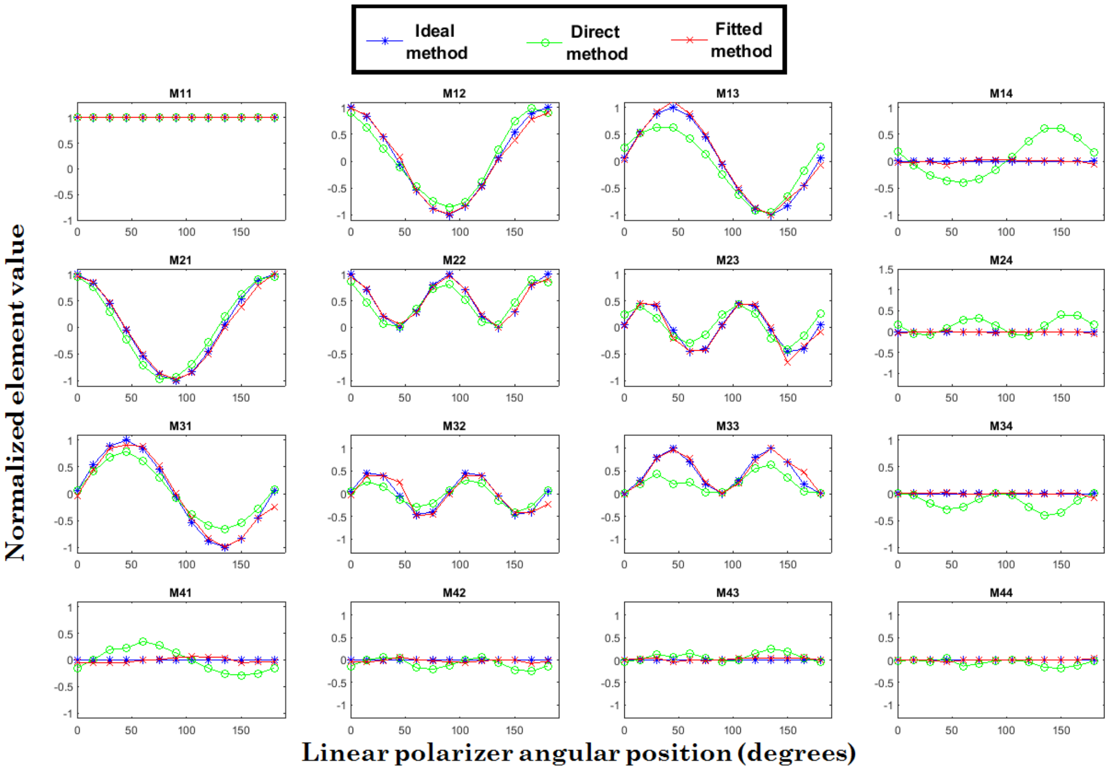

Figure 5.9: The ideal theoretical curves for the Mueller matrix element values (blue), the experimental results of the Mueller matrix element values calculated using the direct (Bickel and Bailey) method (green) and using the fitting method (red) for a rotating linear polarizer, for the case of 16 intensity measurements.

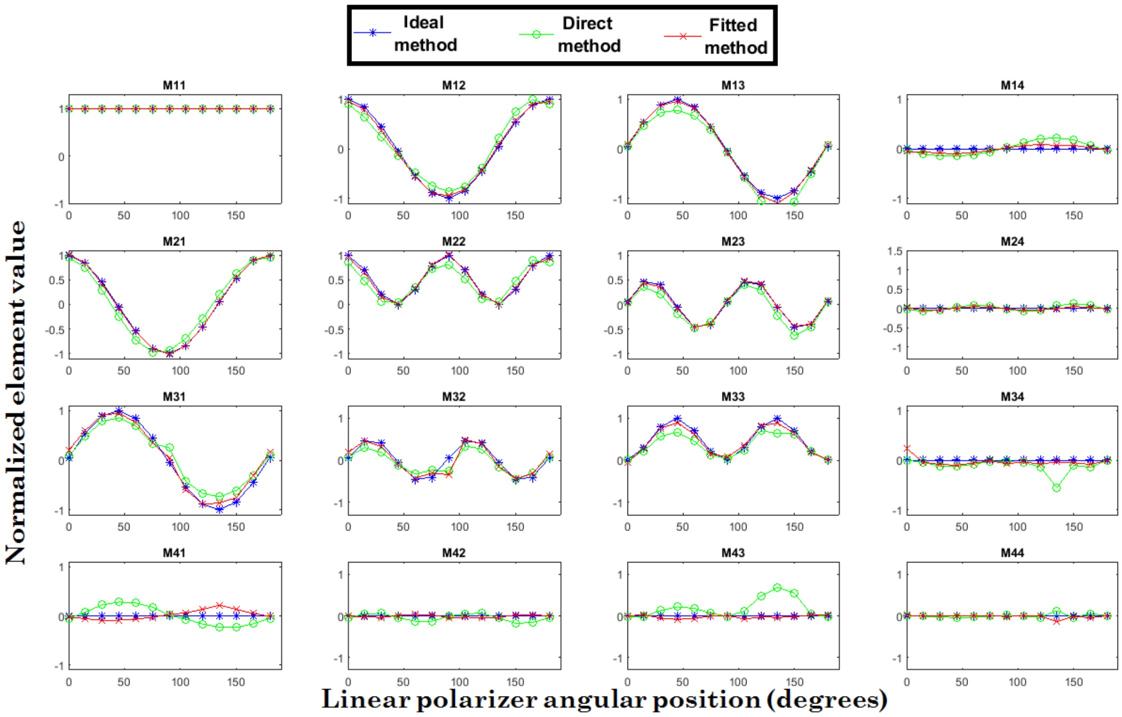

Figure 5.10: The ideal theoretical curves for the Mueller matrix element values (blue), the experimental results of the Mueller matrix element values calculated using the direct (Bickel and Bailey) method (green) and using the fitting method (red) for a rotating linear polarizer, for the case of 36 intensity measurements.

The errors between the calculated Mueller values and the theoretical values are given in Figures 5.11, 5.12 and 5.13, for a QWP, a HWP and a Linear Polarizer, respectively. We present the error in terms of the root mean square error (RMS[1]) differences between the calculated cases and the theoretical values, for each Mueller matrix element. For each sample we present the RMS error for the direct method and the fitting method, for both optimized a non-optimized cases. It can be seen that the fitting method proposed in this work has a smaller total RMS error than the direct method in all cases.

If we analyze Fig. 5.11, it can be seen that for the non-optimized case the RMS is reduced for each element between 12.91% to 97.04%, with an average reduction of the RMS error of 77.08%, when we do the calibration using our fitting

---

[1] The RMS is defined $RMS = \sqrt{\frac{1}{N}\sum_{n=1}^{N}(M_i^{exp} - M_i^{theo})^2}$ where the subindex i indicates one particular Mueller matrix element, the subindex n indicates the angle at which the Mueller matrix is calculated, and N is the number of rotation angles in the measurement of each Mueller matrix.

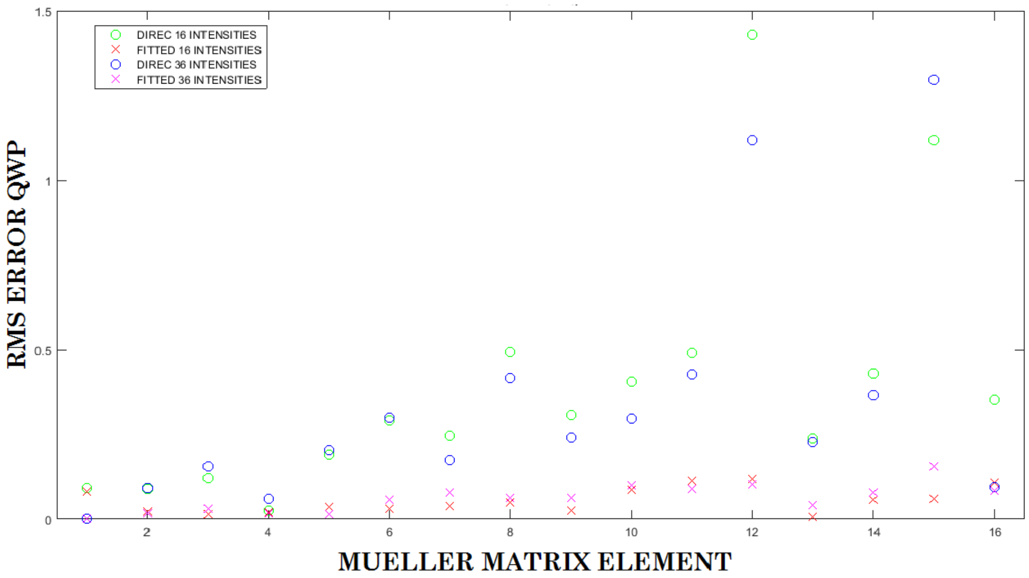

Figure 5.11: Values of the RMS differences between the calculated values an the theoretical values for the direct and fitting calculation methods, for non-optimized and optimized polarimeters, using a rotating QWP as a sample. The X-axis represent each of the sixteen Mueller matrix elements.

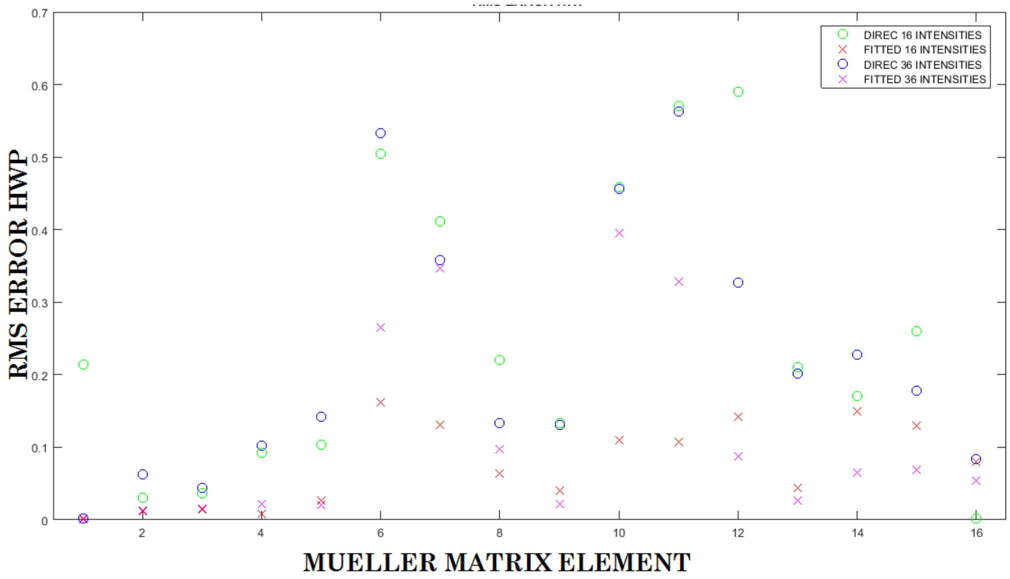

Figure 5.12: Values of the RMS differences between the calculated values an the theoretical values for the direct and fitting calculation —methods, for non-optimized and optimized polarimeters, using a rotating HWP as a sample. The X-axis represent each one of the sixteen Mueller matrix element.

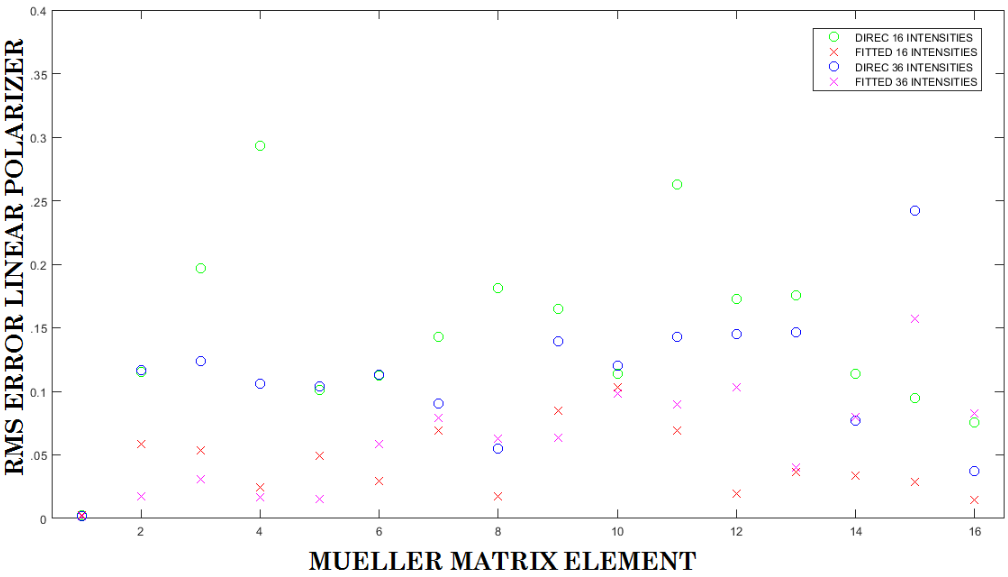

Figure 5.13: Values of the RMS differences between the calculated values an the theoretical values for the direct and fitting calculation methods, for non-optimized and optimized polarimeters, using a rotating Linear Polarizer as a sample. The X-axis represent each one of the sixteen Mueller matrix element.

	RMS AVERAGE REDUCTION [%]	MINIMAL RMS [%]	MAXIMUM RMS [%]
RMS 16 INTENSITIES-QWP	77.08	12.91	97.04
RMS 36 INTENSITIES-QWP	69.78	11.58	92.51
RMS 16 INTENSITIES-HWP	62.65	12.67	91.79
RMS 36 INTENSITIES-HWP	53.41	2.90	87.10
RMS 16 INTENSITIES-LP	62.64	9.36	91.77
RMS 36 INTENSITIES-LP	53.75	8.34	85.19

Figure 5.14: Percentage values of the total RMS differences between the calculated values and the theoretical values for the different calculation methods after the calibration procedure.

method. For the case the QWP using 36 intensity values we obtain that the RMS error is reduced by the calibration between 11.58% and 92.51%, with an average reduction of the RMS error for all cases of 69.78%. For completeness in Fig. 5.14 the percent RMS error between the calculated Mueller values and the theoretical values for a QWP, a HWP and a Linear Polarizer are presented, and which show consistent performance. The RMS average reduction is bigger for the 16 intensity values than the case of the 36 intensity values in all samples studied, because the optimized cases should be better than the non-optimized cases, which is true in our experiment.

Finally we can conclude this chapter highlighting the advantage of having developed a calibration system through a nonlinear fitting algorithms to find the real parameters of an experimental polarimeter with four known calibration samples. The calibration samples used were free-space propagation, a horizontal and a vertical linear polarizer, and a quarter-wave retarder with its fast axis at 30° to the horizontal direction. Then the errors in the polarimeter are assumed fixed and a new adjustment is made to find the 16 elements of an unknown sample Mueller matrix. Experimental data for a rotating quarter-wave, half-wave and a linear polarizer showed very good results. The results presented show that the RMS is even smaller for the case of a non-optimized system using our fitting method, than when an optimized polarimeter is implemented using the direct method of Bickel and Bailey to measure the Mueller matrix of the measured intensities. We found that the average reduction of the RMS when calibrating a polarimeter using our fitting method is up to 77.08 percent, which is an extremely important result in this thesis because it will allow us to measure very accurately the Mueller matrix of a structured surfaces in the next Chapter, this will allow us to reduce the time used for the measurements of the Mueller matrix on a sample point-to-point.

Chapter 6

Polarimetry Application

Through the implementation of the polarimeter developed in this work, an application for the study of structured surfaces is presented. Firstly, the present work will be put into context within the techniques of optical microscopy, describing the most used techniques and the implementation of Mueller polarimetry for the characterization of surfaces. The principles of the Kirchhoff approximation will be described and numerical results presented for the restriction of variables for our system. The manufacturing methods of the surfaces will be presented to be able to make the comparison of the theory and the experiment, concluding with the validity and scope of the system.

6.1 Overview of Metrology and Polarization

Polarized light micro-imaging that combines optical microscopy with polarization modulation techniques plays an important role in various research fields, such as optical mineralogy [111], optical crystallography [112], biomedicine [113]-[115] and metrology [116]–[119]. To acquire more details of spatially distributed information of a sample, a high-numerical-aperture (high-NA) objective lens (OL) is often employed for a high lateral resolution [67, 120]. Another point of view is of a diffuser system illuminated by a beam of determined wavelength, the Mueller matrix (MM) is a polarimetric result as it contains all the information on the intensity and state of polarization of the emerging light. This implies that the measure of the MM of a system is a tool to characterize the behaviour of that system, while it may not be unique, it can be part of the solution of the inverse problem. The are numerous works that address the connections between the MM of a system and its properties, both optical and geometric [30, 121, 122].

The semiconductor industry continues to drive pattering solutions that enable devices with higher memory storage capacity, faster computing performance, and lower cost per transistor. These developments in the field of semiconductor manufacturing along with the overall minimization of the size of transistor require continuous development of metrology tools used for characterization of these complex three-dimensional device architectures [91].

Ellipsometry-based scatterometry has been introduced to monitor the critical dimension (CD) and overlay of grating structures in semiconductor manufacturing. It measures the change of ellipsometric angles in the zeroth-order difracting beam that is scattered from the periodic structure. Among the various types of ellipsometry, Mueller matrix polarimetry (MMP), can obtain up to 16 quantities of a 4x4 Mueller matrix. Consequently, MMP-based scatterometry can acquire much more useful information about the sample and thereby can achieve better measurement sentitivity and accuracy than the conventional ellipsometric scaterometry [62]-[64]. MMP is thus expected to provide a powerful tool for metrology in high-volume manufacturing [36].

In [36] Liu *et. al.* implement Mueller matrix imagining ellipsometry for nanostructure metrology, in order to achieve effective process control. Fast, inexpensive, non-destructive and reliable nanometre scale feature measurements are extremely useful in high-volume nano-manufacturing. Among the possible techniques, optical scatterometry is ideal due to its high throughput, low cost, and minimal sample damage. However, this technique is inherently limited by the illumination spot size of the instrument and the low efficiency in construction of a map of the sample over a wide area. In order to attack these issues, it is possible to combine conventional imagining techniques and optical scatterometry based on ellipsometry of the Mueller-matrix, the combination of these techniques is expected to be a powerful tool for measuring nanostructures in the future of high volume nano-fabrication. In this work we are not seeking to achieve spatial resolution of nanometres. We uses a beam of light of a few microns spot size to illuminate surfaces with spatial variations of the same order and study the effects produced in the polarization state by the surface, through the Mueller matrix formalism, which has been described extensively in this thesis. In this way, a quantitative method is proposed that could allow the study of spatial variations in structured surfaces. Then, in this chapter, we present the comparison of numerical and experimental results for a structured surface and verify the potential of the proposed method.

6.2 Overview of Microscopy Techniques

Traditional techniques based on electron microscopy exist for routinely measuring sub-micron dimensions but these techniques have some limitations, for example, it is difficult to extract from this type of image, reliable information of the slopes and height, for which sophisticated simulations of the propagation of the electrons in the material are required. It is possible to use electron microscopy for very thin sections of a sample, but it is a very expensive and limited sampling technique. In response to this, a new interest in diffraction based optical methods has arisen. The determination of important, critical dimensions via optical techniques is appealing for several reasons: The sample is exposed to only visible light and is not susceptible to charging effects. The technique is capable of measuring the critical dimensions of grating structures down to approximately 40 nm. Minimal facilities are required for installation (no high vacuum, cooling or shielding of electromagnetic fields). Like optical thin film metrology, the optical critical dimension technology can be integrated into process tools enabling advanced process control.

There are techniques with the advantage of being able to directly visualize structured or rough surfaces, but they have several limitations: on the one hand, the images are not free of artefacts and their quantitative interpretation can be complicated. On the other hand, for a large number of techniques, the measurement time can be too long for real-time quality control. The next section presents advantages and disadvantages of electronic techniques and optical techniques

6.2.1 Electronic Techniques

Electron microscopy tools have naturally taken over optical microscopy as soon as the patterns become too small to be properly resolved in optical wavelengths. From an instrumental point of view, electron microscopy can be implemented in two ways:

-Scanning electron microscopy (SEM): The beam is focused on the sample, the focal point is scanned spatially and the secondary electrons emitted by the studied object are used to make the image.

-Transmission microscopy or (TEM): the beam passes through the sample and the image is formed with the beam transmitted.

Scanning microscopy can be used nondestructively in a view from above (technique called CDSEM). This technique, relatively fast to implement, is certainly the most widespread and has long been considered as the reference technique. In practice, we have a good estimate of the width of the pattern and its roughness, but it is difficult to extract from this kind of image reliable information on the slopes and on the height: for this it is necessary to implement sophisticated simulations of the propagation of electrons in the material. These simulations are also essential to have a good absolute accuracy. To overcome CDSEM limitations, electron microscopy can be used for a range of ad hoc specimens. In addition, scanning microscopy (this is called XSEM for SEM Cross-section) or Transmission microscopy (TEM) can be performed. In both cases, these are destructive techniques that are costly and allow for limited sampling. This is particularly true for TEM, which requires not only to divide, but also to dilute the sample studied to allow good beam transmission. This technique is still used because of its ability to characterize complex structures and its resolution, which allows the visualize of the atomic planes and, therefore, provide a very reliable absolute scale for the characterization of dimensional standars [123].

Atomic force microscopy

This is the most recent technique, and probably the most functional for images in real space. The principle of operation is based on scanning mechanically, by means of piezoelectric elements, a point along the structure to be characterized, and the profile is reconstructed from the movement of the point. The point is guided by its interaction with the material, which causes a force measured in general by changing the frequency of a resonant system. Like the CDSEM, the AFM has the essential advantage of being non-destructive. Its main limitations are related to the shape of the tip on the one hand, and on the other hand the measurement time [124].

These two limitations are continuously being reduced: today there are points with the shape of an $elephant's foot$ to describe the slopes, or carbon nanotubes, very suitable for the characterization of narrow grooves. The useful life of these tips also increases constantly. The latest generation of AFM, once calibrated by ad hoc standards, are probably the reference instruments for other metrological techniques [123]. However, this device can only characterize the external profile of the structure studied, and is totally insensitive, for example, to the presence of internal layers.

6.2.2 Optical techniques

Since they are based on the exploitation of optical measurements, these techniques have the advantage of being non-destructive. In addition, the measurement itself can be rapid (in the order of one second) and does not require a vacuum as in electron microscopy. This advantage of speed, if retained by a sufficiently efficient digital data processing scheme, makes these techniques very competitive for the control of online processes, possibly even on all wafers and not just in a small sample.

However, unlike image techniques in real space that can be implemented practically anywhere in the wafer, given their lack of spatial resolution, optical techniques cannot work on some particular structures, which are sometimes a representative structures of the shape of the lithographed lines.

In general, the techniques of optical metrology consists of making one or more measurements in the structure to be characterized, and then in solving the inverse diffraction problem by adjusting the measurements to the simulations provided by a model that is supposed to correctly describe the structure and includes adjustable parameters. However, the resolution of the inverse problem is notoriously difficult. For example, if we try to characterize a one-dimensional network with a known period, we can assume that the feature of the profile is rectangular: the parameters to be determined are simply the height H and the width L (also called CD for critical dimension) of the lines. If we assumed symmetric trapezoidal: it is necessary to add a parameter to describe the difference between the width in the upper part and in the lower part of the lines. For an asymmetric trapezoidal shape: in comparison with the previous case, we still need an additional parameter to describe the asymmetry [77].

This brief enumeration shows the difficulties that are normally encountered in this type of problem: the data must be sufficiently numerous and not redundant so that it is possible to unequivocally separate the different models, choose "the correct one" and refine the relevant parameters. It is easy to believe that the quality of the adjustment is sufficient; if the adjustment is good, the model must be adequate. We can be sure there is a problem when the adjustment is bad, but on the other hand, if the adjustment is good, the model still may not be "correct", for example, because it includes "too many" parameters: these parameters show strong correlations, which means that if we change one of them, we can find the same answer by appropriately modifying the others. Then it is impossible to choose, among all the set of parameters that give the same answer, the one that really corresponds to the profile. It is therefore essential for the effective use of these methods, to expand as much as possible all the measures to restrict the choice of the model and the values of the relevant parameters, as much as possible.

Spectroscopic techniques

We now briefly describe two spectroscopic techniques: Spectroscopic refractometry, almost always implemented under normal incidence, which is easy to implement from a practical point of view [126]. Spectroscopic ellipsometry, at an angle of 70°, near the angle of Brewster for silicon, which for studies of thin films on Si [37], offers the best sensitivity [127]-[132]. These techniques do not require beam movement during the measurement, which is a significant advantage given the small size of the targets (50μm squares).

Goniometric techniques

These techniques are based on the measurement of the optical response, not as a function of the wavelength, but of the polar and/or azimuthal angles. An instrument of this type has been marketed, which measures the reflectivity in the incidence variable [133]. Other techniques that use measurements of the variable azimuthal angle, such as scatterometry [134] or reflectivity of the Fourier transform [135], have also been studied. This last technique uses a principle similar to that of the polarimeter developed during this work, but with optics designed specifically to allow measurements in a very wide angular range for a particular angle of the reflectivity in the intensity of the object studied. Compared to our method, this instrument is complementary, in the same way that an ellipsometer differs from a reflectometer.

Mueller Matrix Polarimetry

As we have seen, metrology through optical measurements is linked to the resolution of an inverse problem, it is advantageous to gather as much information as possible to better limit the choice of model and the value of the parameters. From this point of view, Mueller polarimetry seems *a priori* particularly interesting, since it provides fifteen quantities (for the matrix normalized by m11) instead of two for the other techniques: R_p and R_s for the reflectometry at normal incidence [75], α and β or Δ and Ψ for classical ellipsometry in flat diffraction geometry (with the plane of incidence perpendicular to the lines) [77].

We will use properties of symmetry of the Mueller matrices to validate the results. And from the measurement of the Mueller matrix, we will try to obtain information from the surface. From the information presented in previous paragraphs on the different methods of microscopy and using a numerical simulation based on the Kirchhoff approximation, we will limit the variables of our problem presenting some theoretical cases to establish the parameters that according to the simulation could give us more information from the measurements of the experimental Mueller matrix.

6.3 Kirchhoff Approximation Simulation

One of the most used theories for calculating the scattering of light from rough surfaces is the Kirchhoff approximation [1],[136]-[142]. With this theory it is assumed that the local curvatures of rough surfaces are small enough to approximate (locally) the reflection of light as the reflection of a plane wave from a flat surface, i.e., the Fresnel reflection coefficients can be used. Assuming that the surface curvature condition is satisfied, it is possible to use the Kirchhoff approximation to calculate scattering from smooth surfaces with small surface solpes. In this case the reflected light is mostly directed away from the surface, so the surface itself does not intercept any of the light and there is no shadowing or multiple scattering. Increasing the slopes increases the range of angles with which the light is reflected from the surface and shadowing and multiple scattering become more important. At this point the normal (single-scatter) Kirchhoff approximation is inaccurate. However, multiple-scattering methods based on the Kirchhoff approximation have been developed to extend the range of applicability of the method [136, 137, 140, 141].

Therefore there appears to be no limit on the surface slopes for the Kirchhoff approximation if shadowing and multiple scattering are taken into account. However, in practice, there is a problem with surface sampling. The usual implementation of the Kirchhoff approximation for numerical calculation requires a discretization in the x direction, which means that for steeper solpes more points are required to have a reasonable sampling of the field distribution on that part of the surface. This problem becomes worse for surface with infinite slopes, such as surfaces with rectangular grooves. Since the equation for the Kirchhoff approximation contain a term that includes the surface slope, when the slope is infinite, the equations cannot be resolved, i.e., the Kirchhoff approximation cannot be used in its usual formulation for rectangular surfaces. This type of surface shape has importance as we mentioned before. In [16] Bruce presented a simple reformulation of the usual Kirchhoff approximation equations to allow the calculation of single- and double-scatter intensity distributions of surfaces with high or even infinite slopes. Therefore, in this work we implement a simulation on the Kirchhoff approximation, firstly to restrict the problem and then to validate our experimental results [16]-[18],[35].

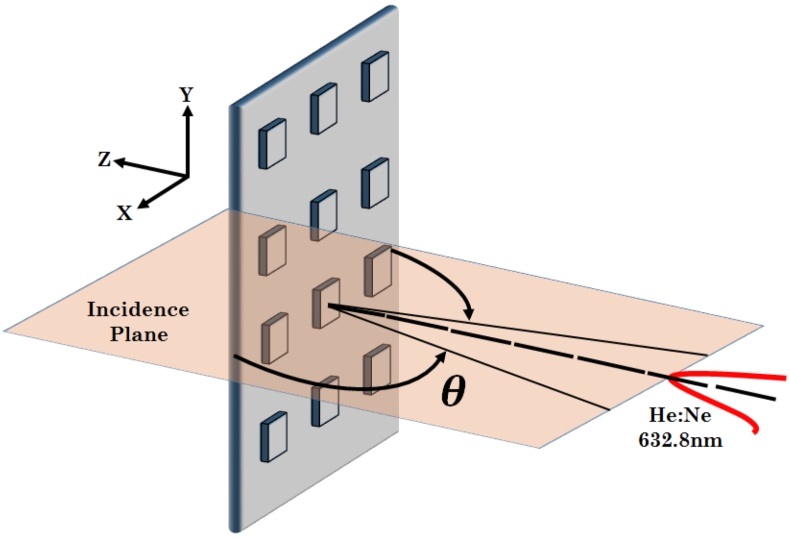

Figure 6.1: Schematic system for a structured sample.

To restric the problem using the Kirchhoff approximation we need to define some variables. We use the same parameters and calculate the variation of the detected intensity with the position of the illumination beam. We present the system schematically in Fig. 6.1, where a Gaussian beam of 632.8 nm is used as a source of illumination, both in the simulations and in the experimental cases. The system works in the plane of incidence, so that both the PSG and the PSA are located in this plane. The PSG is normal to the surface and the angle theta in the figure represents the angular variation of the PSA as has been described throughout this work, however, using the fact that in [96] an analysis was performed for this system using only intensity measurements and for practical reasons, we used $\theta = 45°$. Using other design in our instrument we could increase this angle by around 5 degrees, which does not change the scattered light patterns significantly.

Fig. 6.2 describes the parameters used to generate the simulated surface, which consists of rectangular structures (we will refer to these structures as ribs or steps). The design of the surfaces obeys the need to generate deterministic profiles defined in 1D or 2D that present, to a greater or lesser degree, changes in the polarization state. The range of structures studied includes those with a two or three ribs with a height *ht*, a width *wd*, and a separation *sep*, all these parameters varying between 7, 10 and 15 microns. Since the surfaces are studied by reflection, it is necessary to introduce the metallic character in them through the index of refraction of the material, which for this study were aluminium (Al), silver (Ag) and gold (Au).

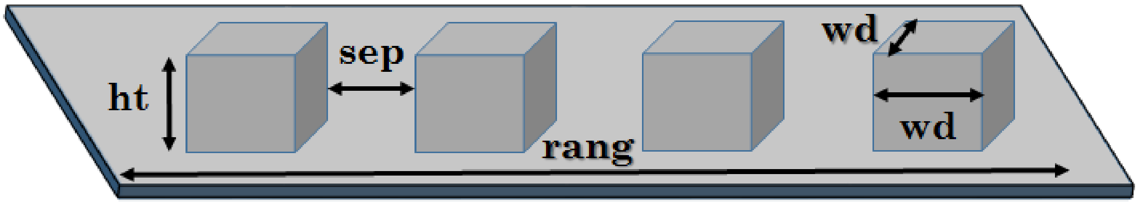

Figure 6.2: Parameters used in the Kirchhoff simulation to construct the surface.

In Figures 6.3 and 6.4, examples are shown of simulated surfaces for which the scattered signal variation is calculated. It is important to note that the modification of the number of ribs, the width or the separation, for example, requires a modification in a variable that is defined in Fig. 6.2 as a range (*rang*), this variable basically gives us the total length of the surface, a quantity that must be modified if any of the other parameters is modified.

So, the length of the surface is given in wavelengths depending on the parameters defined, and it is necessary to discretize the surface. The variation of the scattered signal is calculated as a function of the position of the incident beam. The calculation takes between 2 and 5 minutes depending on the surface on a 2.7GHz speed PC. It is important to remember that results include the changes in the polarization state produced by the sample present in the system, these polarization effects are represented in terms of the calculation of the Mueller matrix point to point in the particular area of the surface.

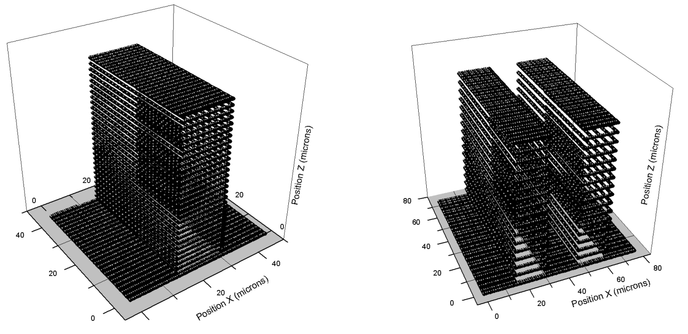

Figure 6.3: Structure with 1 and 2 blocks and same size of block, i.e., $ht = 15\mu$m, $sep = 15\mu$m and. $wd = 15\mu$m.

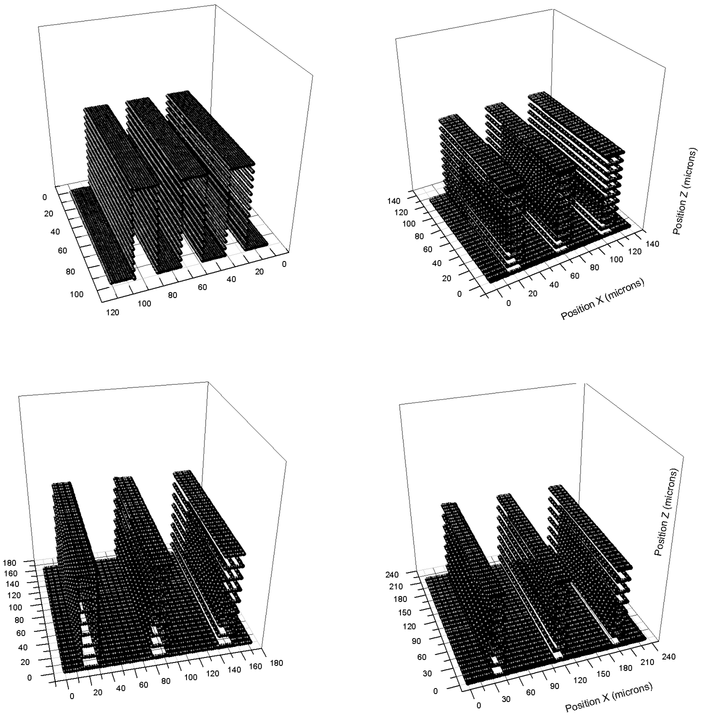

Figure 6.4: Structure with 3 steps and different separation between blocks. $sep1 = 10\mu$m, $sep2 = 20\mu$m, $sep3 = 30\mu$m, $sep4 = 40\mu$m.

6.3.1 Mueller Matrix Numerical Results

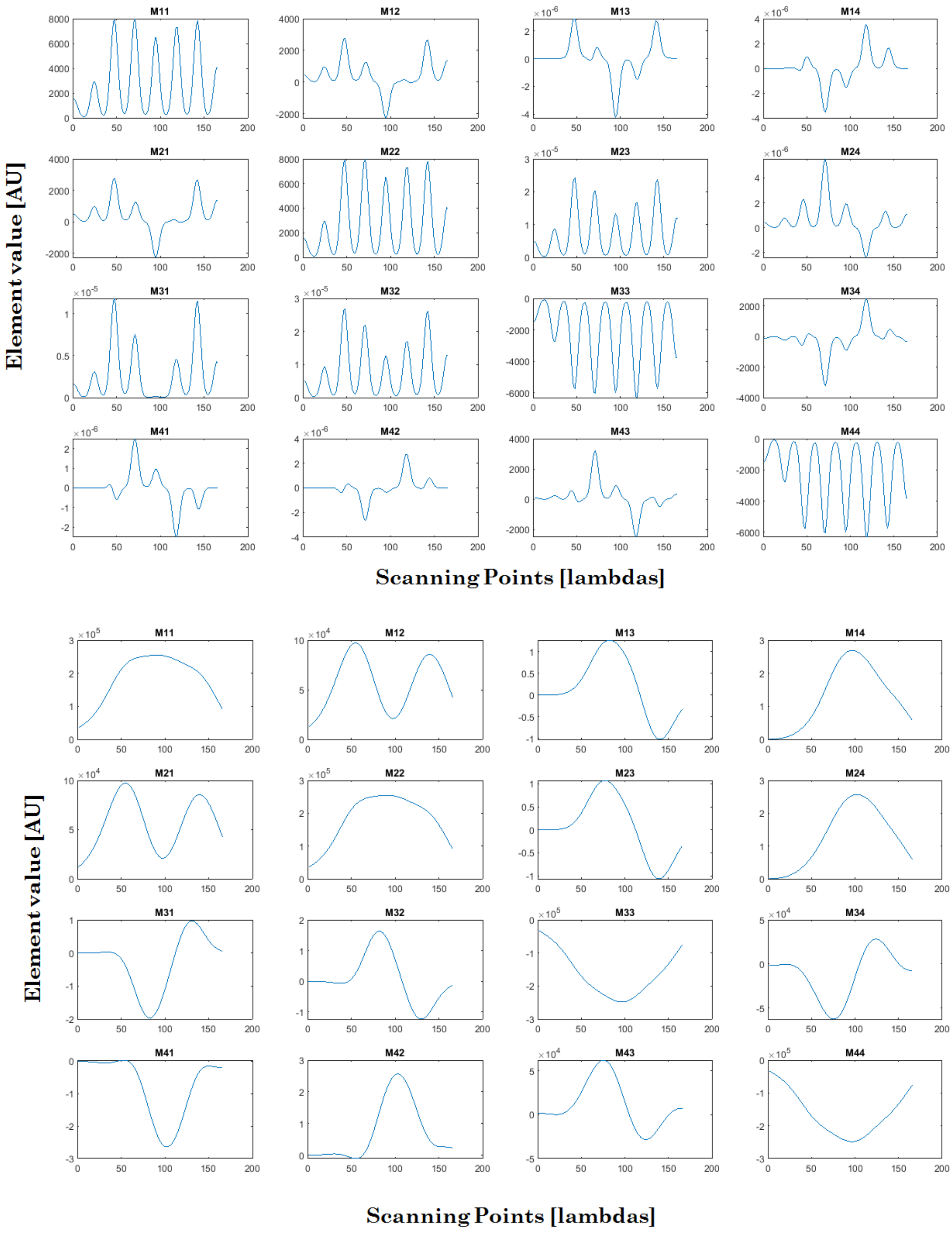

Figure 6.5: Structure with 3 ribs with $sep = 7\mu$m, $wd = 7\mu$m, $ht = 7\mu$m. An illumination beam of a) $spotsize = 5\mu$m and b) $spotsize = 40\mu$m. The material used for the simulation was Aluminium.

In Fig. 6.5, we present the Mueller matrix (MM) for a structured surface with 3 steps, with dimensions of *sep* x *wd* x *ht* = 7μm x 7μm x 7μm and an illumination beam spot size of 5μm and 40μm. It can be seen clearly that when the illumination spot is smaller, the Mueller matrix shows well-defined intensity variations in all its elements, and when the spot is larger compared to the size of the structure, the MM shows some variations in intensity but practically does not present significant changes related to the structure. This result demonstrates our initial hypothesis that using a small illumination beam it is possible obtain more information about the sample in terms of the changes in the polarization state.

When we change the number of ribs for fixed geometric parameters as in Fig.6.6, we note that the variation of intensity in the elements of the MM depends on the number of ribs in the sample, if the number of ribs grows, then the number of maxima and minima of intensities increases in the signal for each one of the MM elements.

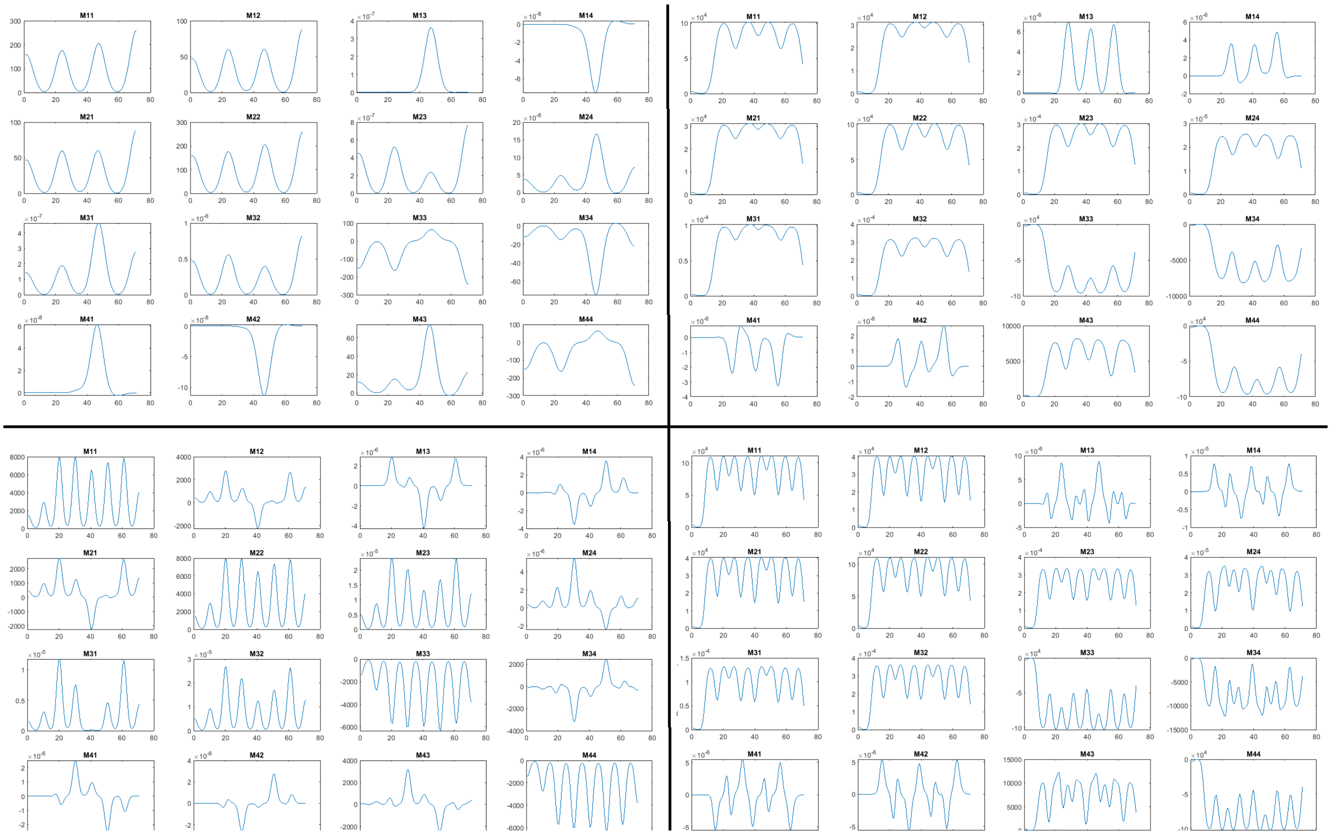

Figure 6.6: MM for structures with different number of ribs, a) 1, b) 2, c) 3 and d) 4 respectively and with dimensions of *sep* = 7μm, *wd* = 7μm, *ht* = 7μm. For an illumination beam of 5 microns. The material used for the simulation was Aluminium.

In Figures 6.7 and 6.8, we show the Mueller matrices for a surface of 21x7x7 and 45x15x15 (*sep* x *wd* x *ht*) micrometers which have the parameter *sep* 3 times larger than the parameter *wd*, with three ribs each one. In both figures it can be seen that the magnitude in each MM element is associated with the changes in the spatial form of the surface, since there are flat areas and structured areas which have well-defined intensity changes. Comparing element by element in the matrix it is clear in Fig. 6.7 that maximum and minimum magnitude are not defined with high precision, this is because when scanning the illumination beam on the sample, it is not possible to define the maximum and minimum as in the case of the figure for 15 microns which has longer flat sections and this allows us to define the elements of the MM with more resolution. Although in Fig. 6.7, the surface does not show a perfectly defined behaviour as in the case of Fig. 6.8, it can be seen that there are changes in the polarization state due to the spatial structure of the sample.

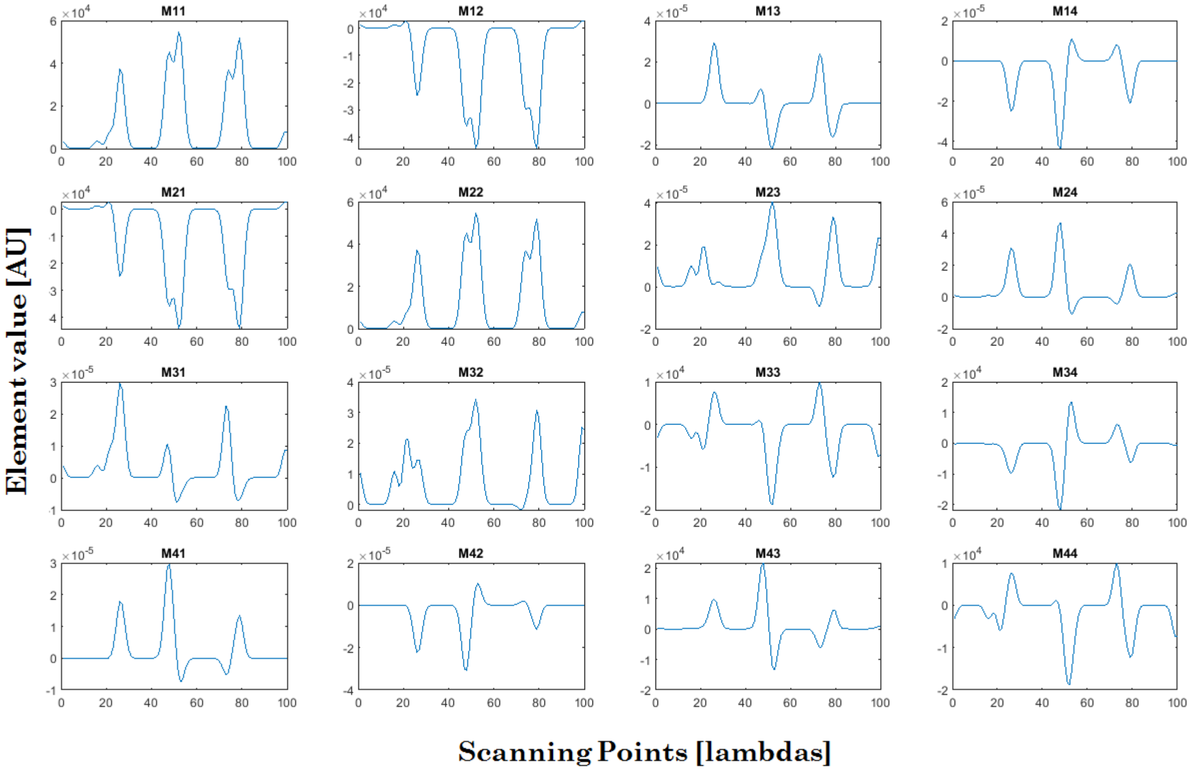

Figure 6.7: MM for a structure of 3 steps with 21x7x7 micrometers.

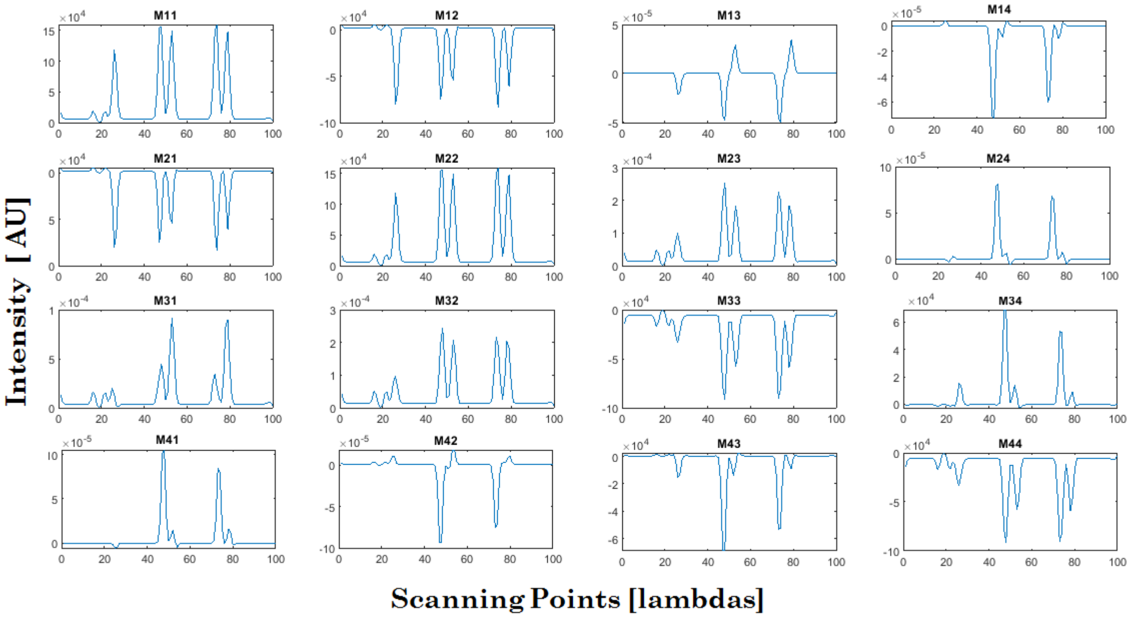

Figure 6.8: MM for a structure of 3 steps with 45x15x15 micrometers.

Fig. 6.9 shows the graph for each of the 16 elements of the Mueller matrix, as in the previous figures the scan is over the point-to-point structure. As can be seen in the different elements of the Mueller matrix, the intensity of the light depends on the section of the structure that we are illuminating. Therefore, it provides intensity changes depending on the position in which the illumination beam interacts with the surface. In Fig. 6.9 the results are presented for a surface with different materials: aluminium, gold and or silver. With dimensions of 45x15x15 micrometres and a spot size of 5 micrometer. The magnitude in each element is consistent and regular for all the elements of the Matrix, the simulation's results do not present significant changes in the polarization state for different materials.

The general behaviour of the MM elements also allows us to realize that there is a symmetrical behaviour with respect to other components of the matrix, as should be expected from the independent elements of the Mueller matrix of a one-dimensional surface.

Based on the numerical results presented in Figures 6.5 to 6.9, it is possible to reduce the parameters in the polarimeter for the experimental measurement of the MM of a structured surface with known dimensions and parameters. To determine the validity of the measurement and therefore the validity of the instrument, the experimental results are compared with the Mueller matrix obtained with the same parameters through the numerical calculation using the Kirchhoff approximation.

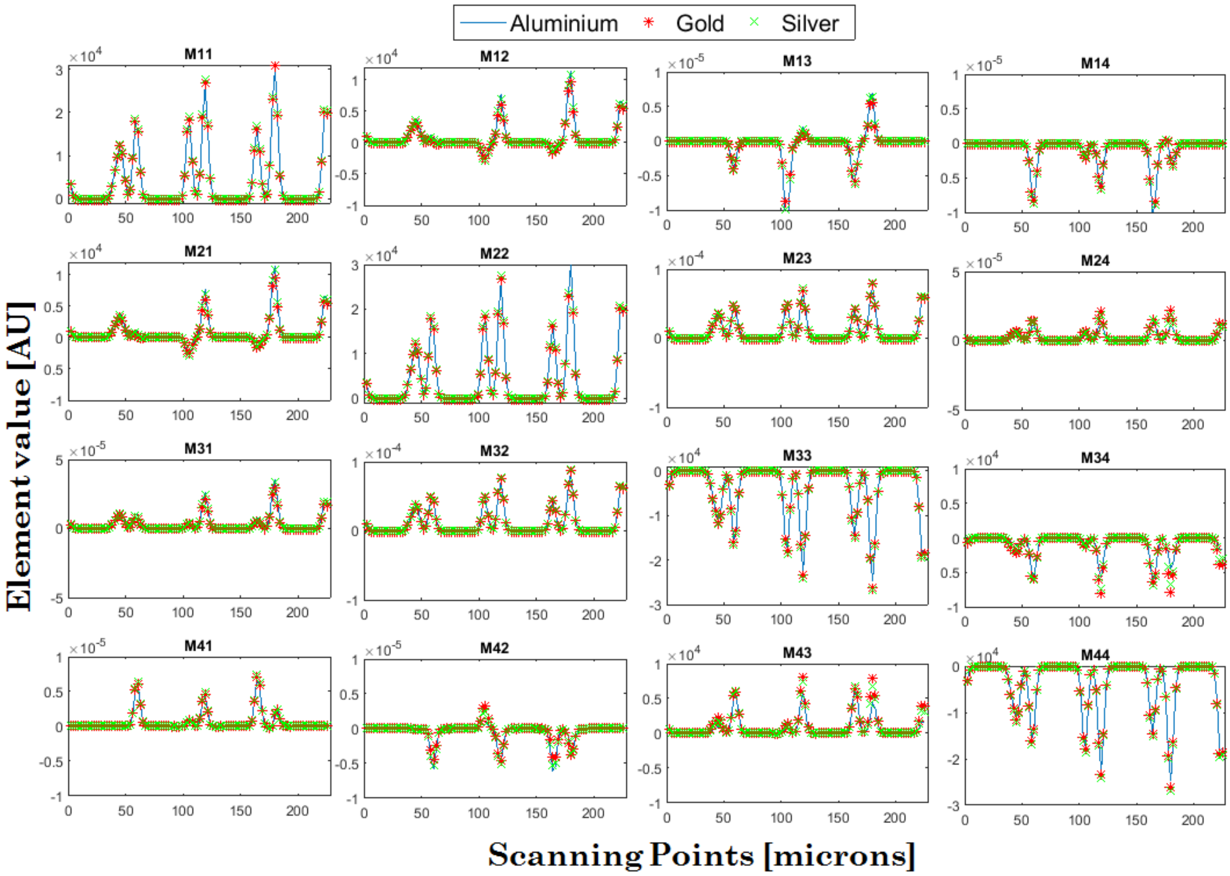

Figure 6.9: Comparison of the MM of a surface with different materials, aluminium, silver and gold, with 3 ribs of 15x15x15 microns and spot-size illumination of 5 microns.

6.4 Fabrication Method of Structured Surface

The flat samples studied in this work consist of structures on a square profile substrate (ribs or steps), the design of these is with the idea of studying well-defined patterns that have structures of the order of the size of the beam of illumination to be able to measure changes produced by the spatial variation of the sample. It is possible to fabricate structures that includes those that have different ribs, for example between 1 and 6 ribs with a height (*ht*), height (*ht*), width (*wd*) and separation (*sep*), varying from 5, 7, 10 and 15 microns, all those parameters as those defined in the theoretical case. The samples are surfaces with micrometric structures, which were manufactured in the The National Laboratory of Biomimetic Solutions for Diagnosis and Therapy (LaNSBioDyT for its acronym in Spanish), of the Faculty of Sciences of the National Autonomous University of Mexico (UNAM).

The structures were manufactured by a process that uses the new generation of Nanoscribes 3D laser lithography systems, Photonic Professional GT [143], which provides a fast and powerful platform for micro- and nano-fabrication up to the third dimension. Almost arbitrarily complex shaped polymer structures with finest feature sizes in the sub-micrometer range are achieved by means of two-photon polymerization [145]-[147]. A speed-up of the writing process is driven by an embedded ultra-high precision galvo technology, which laterally deflects the laser focus position by use of a galvanic mirror system. Thus, the fabrication of large area 3D micro- and nano-structures is feasible in short times. In addition to rapid x-y-beam-scanning, a piezoelectric scanning stage provides ultra-precise x-y-z-movements of the substrate relative to the laser focus position. The table-top laser lithography systems are fully automated. Structures were designed in 3D printer compatible CAD software programs.

Surfaces were printed in configuration Dipin Laser Lithography (DiLL) on a 20x20 mm glass substrate. IP-Dip serves as immersion and photosensitive material at the same time by dipping the microscope objetive into this liquid photoresist. Due to its refractive index matched to the focusing optics IP-Dip gurantees ideal focusing hence the highest resolution technology in DiLL [144].

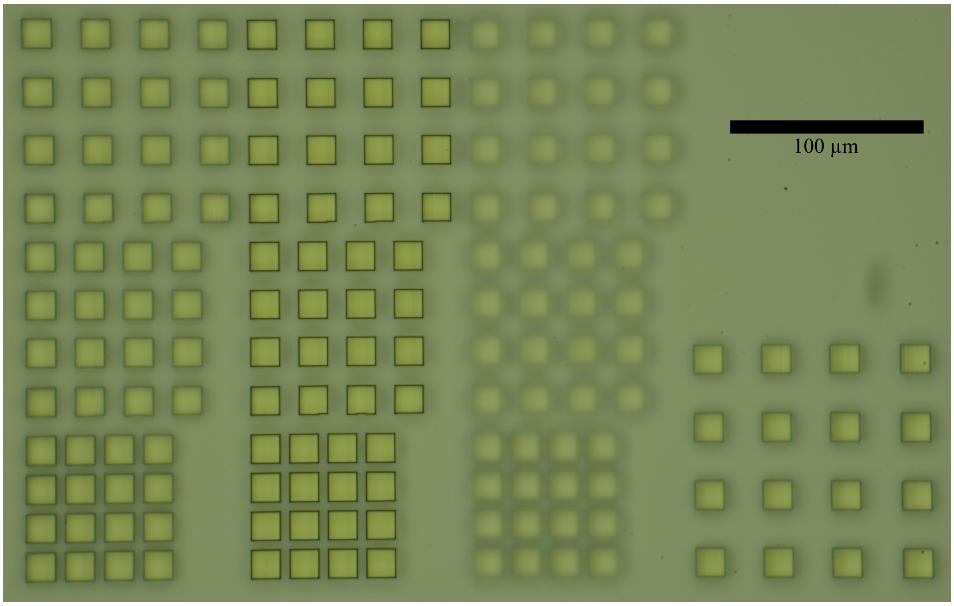

Figure 6.10: Microfabricated surface with dimensions of 15x15xh and $h = 5, 10, 15$ micrometers.

The structures were verified by optical microscopy(Fig. 6.10) and were analyzed also by scanning microscopy (SEM) to review the depth or height parameter, as can be seen in Fig. 6.11, the sample was coated with a layer of gold not greater than 400 nm thick for the analysis by SEM microscopy. The difference in dimensions in the structures between the ideal and experimental cases were below the tolerable value (5%) [148].

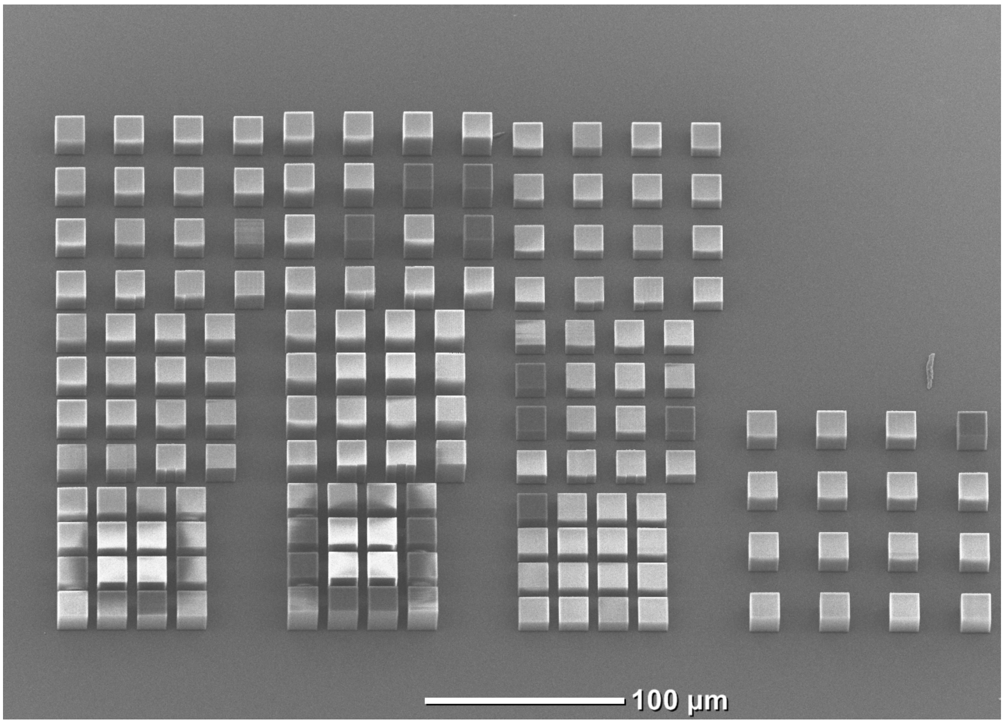

Figure 6.11: Micro-fabricated surface with dimensions of 15x15xh and $h = 5, 10,$ 15 micrometers.

On the structured substrate another nanometer-controlled thin film was deposited of gold (Au)[1], silver (Ag) or aluminium[2], introducing the metallic characteristic in them by means of two techniques:

- Thermal evaporation; this technique works through the heating of the material until melting is carried out by an electrical current through a filament or metal plate on which the material is deposited (Joule effect). The material in the form of vapor is then condensed on the substrate. The assembly of the technique is simple, and is very appropriate for depositing metals and

---

[1] The deposition of the thin film of gold was made in the Photonics of Microwaves Laboratory at ICAT, Mexico [149].

[2] Sputtering deposition was made in the Thin Film Laboratory at ICAT, Mexico.

some compounds with low melting point (Al, Ag, Au, SiO, etc.), details of the process used can be found in [149].

- Sputtering deposition; the samples of aluminium and silver were thin films grown onto the micro-manufactured surface, using the DC-sputtering technique with an aluminium/silver target in argon, respectively. The film thickness was approximately 200nm, corresponding to a deposition time of 5 min, at a pressure of 22 mbar and a discharge power of 10W. This film thickness does not affect the shape of our samples.

6.4.1 Surface profile

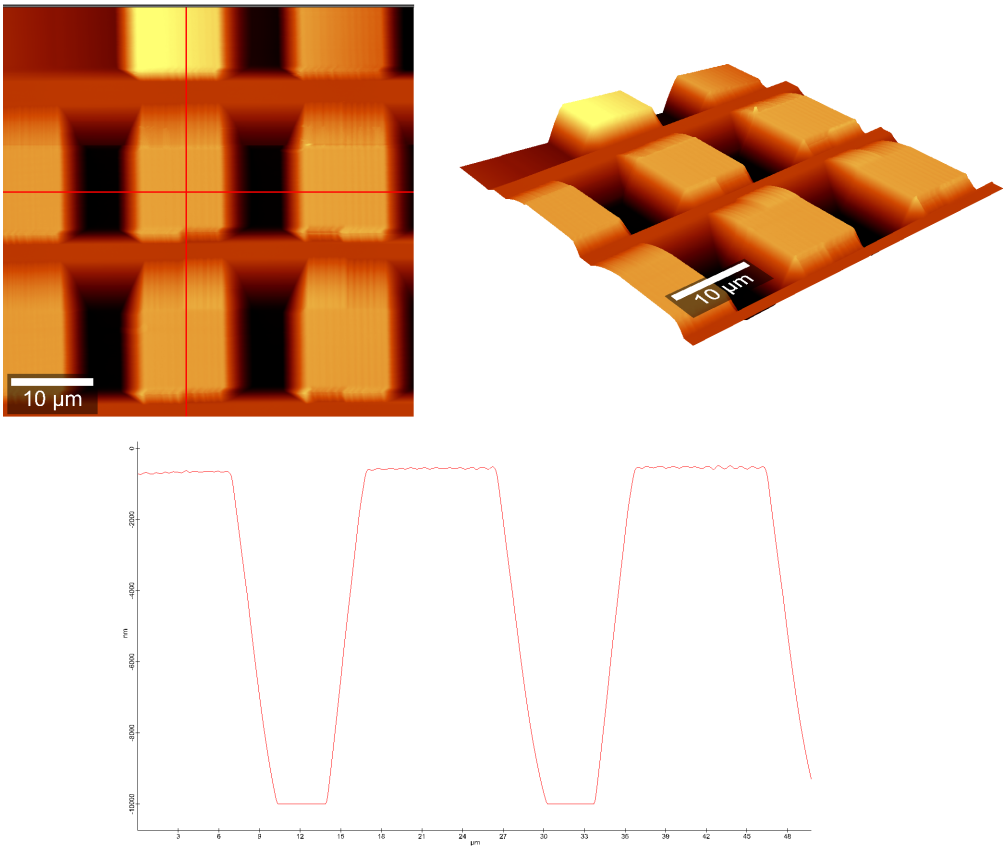

Figure 6.12: Section Image of a microfabricated surface using AFM microscope Witec[4].

Although with SEM microscopy it is possible to observe the depth uniformity of our surfaces, atomic force microscopy was used to guarantee that the study surface really has the desired depth. As an example we take the surface profile of 10x10x10 micrometers, in Fig. 6.12 can be seen a section of the surface, with the 3D image and the profile for a cross section of the structure. From Fig. 6.12 c) we can verify that the depth has a difference with respect to the ideal value of less than 5%, showing a consistency of all the parameters of the surface.

6.5 Experimental VS Theory results

Based on the restriction of variables presented in Section 6.3, which is based on numerical simulation using the Kirchhoff approximation and the fact that surfaces were micro-manufactured with the same characteristics as the simulations, a comparison of the experimental and simulated Mueller matrix is presented.

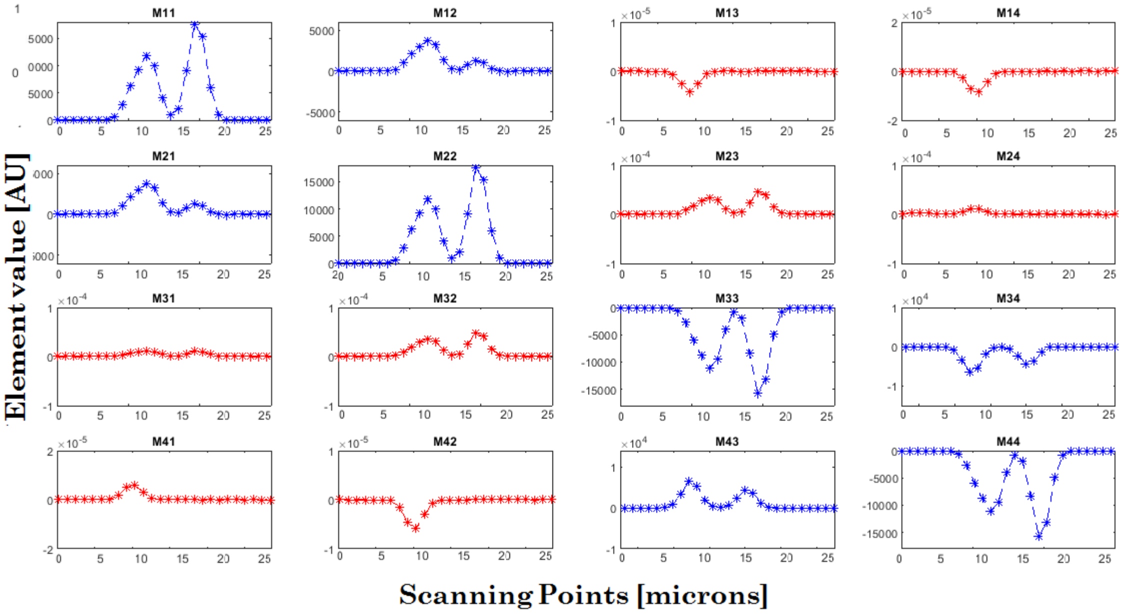

Figure 6.13: Theoretical Mueller matrix elements using Kirchhoff Approximation for one rib of 15μm and a thin film of aluminium as a reflective material. The parameters introduced in the simulation are the same as the experimental parameters used in Fig. 6.14. The intensity in each of the MM elements is in arbitrary units (AU) because the elements in blue points in the graph have a larger scale in comparison with the elements in red points, and we want to show the changes in the polarization state for all elements.

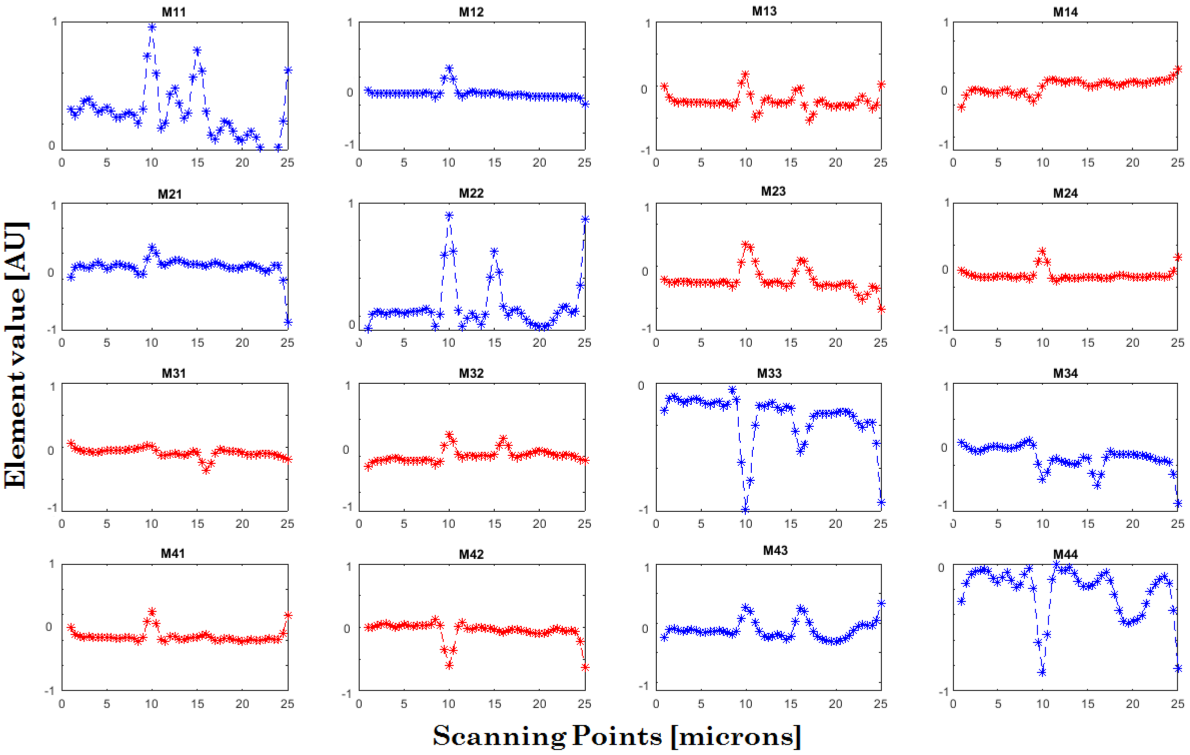

Figure 6.14: Mueller matrix elements for one rib of 15μm and a thin film of aluminium as a reflective material. The magnitude in each MM elements is in arbitrary units (AU) because the elements in blue points in the graph have a larger scale in comparison with the elements in red points, and we want to show the changes in the polarization state for all elements.

Using the polarimeter developed in this thesis, working in reflection mode, with the PSG illuminating normally to the surface, the PSA is at 45° as shown in Fig. 4.17b). With a spot-size of 5μm, a structured surface of one rib of ht =15μm and wd =15μm, with aluminium as a reflective material, we performed the measurement of the 16 MM elements, scanning point-to-point the beam on the surface with a resolution of one micrometer . The changes in the polarization state of the intensity of light scattered by the sample were measured and calculated using the calibration and data exaction proposed method in this work, obtaining the results presented in Fig. 6.13. and Fig. 6.14.

In Fig.6.13 the elements of the MM for a simple structure (one rib) with $ht =$ 15μm and wd = 15μm are presented. There is a strong symmetry in the matrix for the simulated case, however, this symmetry is not so good as expected for experimental structures (Fig. 6.14), showing the presence of inhomogeneities due to the manufacturing process of the sample. The matrix must contain all the polarimetric information available for the geometry studied and the wavelength used, however its study and use cannot be done in a direct way.

To start the analysis of the results obtained with the polarimeter developed in this thesis, we will begin by explaining the types of symmetry appearing in these matrices, which are the consequence of: a) the geometric symmetries of the samples, b) the symmetries in the Matrix sense between different elements, and c) the symmetry due to the angles of incidence and detection of the implemented system.

For example, for spectroscopic ellipsometry the Mueller matrix becomes symmetric and there are components in m11, m12, m21, m22, m33, m34, m43 and m44, in which there is no dependence on φ [77](as in our polarimeter), and then the matrix is corresponding to the matrix of an isotropic sample. This reduces the analysis of the Mueller matrix. In our system it is seen that the elements described above present the most significant changes and the rest of the elements, although they behave symmetrically, have a lower order of magnitude. The elements m13, m14, m23, m24, m31, m32, m41, and m42, (elements outside the diagonal) do not cancel each other and the Mueller matrices are different from zero.

The symmetry between different elements of the matrix will be analyzed in terms of the sign of the elements of MM, which is described by the matrix in Eq. 6.1. Where, for example elements in m11, m12, m21 and m22 have positive sign and the elements m33, m34, and m44 have negative sign, which was to be expected because we are working the system by reflection. On the other hand the elements m23 and m32 also have the same sign. It can be seen in the figures that elements m13 and m14 are anti-symmetrical with the elements m31 and m41, in the same way that m24 and m34 are with m42 and m43, respectively.

$$\begin{bmatrix} + & + & - & - \\ + & + & + & + \\ + & + & - & - \\ + & - & + & - \end{bmatrix} \tag{6.1}$$

For symmetry due to the symmetries of the sample studied we can see in Fig. 6.13 and Fig.6.14 that since this is a symmetric surface of $ht = 15\mu$m and w$d = 15\mu$m, then we find the maximum and minimum of intensity in the elements of the MM around the edges of the rib. The most representative relationship is attributed to the elements m11 and m22 with m33 and m44, which shows a clear anti-symmetry in sign and shape with respect to zero intensity. On the other hand the elements m12 and m21 present symmetry in form. In the same way at the edges of the structure the elements m34 and m43 present anti-symmetry with respect to the zero of intensity. The m23 and m32 elements show a shape symmetry around the same points of the surface, described before. The rest of the elements also present relationships of shape but to a lesser extent.

The analysis of symmetries is the first step to obtain information related to the geometry of the surface, from the study of the changes in polarization of the incident beam and scattered by the sample described in terms of the MM.

Discussion of results

In general terms, measurements of polarization were carried out through the Mueller matrix, for a micro-fabricated and previously characterized sample, and fixed angle of incidence, size of the spot of illumination and type of the reflective material to reduce the parameters. Varying the position of the surface a micrometric scan was made to obtain at each point, the 16 measurements of intensity that through our system of acquisition and calibration allowed us to obtain the Mueller matrix of the sample point to point in each part of the illuminated surface.

Based on the study of a structured surface, it was possible to analyze the symmetries due to: the shape of the surface, the angular parameters of the polarimeter and the relation of the elements of the Mueller matrix. The numerical and experimental results in Fig. 6.14 y Fig. 6.13 show in both cases the same symmetry of shape and angle and between the elements of the matrix, so it is possible to conclude that the experimental results are consistent with the theoretical case, validating our polarimeter system which uses variable liquid crystal retarders as generating elements of polarization states.

Although it is possible to carry out other types of polarimetric analysis which has been widely studied in the literature, for example, spectroscopic ellipsometry, reflectometry or analysis through the Polar Decomposition of the Mueller matrix [78], for now with the results presented, our system meets the objectives posed in this thesis, which consisted in the design, construction, calibration and extraction of data from a polarimeter using liquid crystal variable retarders, using a spot focused as an illuminating source of the measurement of previously characterized structured surfaces. The polarimeter compensates the information of the wavelength or the angular variation used in other similar systems, with the study of the changes in polarization state from one point to another of the surface, which allowed us to validate the correct performance of the system.

Chapter 7

Conclusions

The last two chapters presented the advantages of measuring the polarization effects in the scattering pattern from one point to another in a studied sample using focused illumination. The results presented constitute an experimental proof-of-concept when compared with numerical calculations results that allow us to validate the proposed method.

In this chapter, we shall give the final remarks about the results obtained and we present the perspective for the current instrument and its potential reach.

7.1 Polarimetry using LCVRs

Although there are different ways to measure the changes in the polarization state of light when it varies after interaction with an optical system, in this work we focused on the study of the measurement of these variations by Mueller matrix polarimetry.

The implementation of our polarimeter involve a controlled modulation of input polarization states. These states are modified during passage through the system, then analyzed, to extract the Mueller matrix of the sample studied from these measurements. Light polarization can be modulated and analyzed by a variety of approaches: rotating retardation plates, rotating compensator, Pockels cells, photoelastic modulators or liquid-crystal variable retarders, the last one used in this work. LCVRs have some limitations, in particular, the accessible spectral range, but also significant advantages, such as the absence of moving parts and high driving voltages.

We built a polarimeter choosing the retardance values given the values of the incident and detected polarization states required by the method of Bickel and Bailey to extract the sample Mueller matrix from the measured intensities. To change the condition number in the experiment, the number of independent polarization states was changed. So, with the same experimental system it was possible to change from an optimized system (36 intensity measurements) to a non-optimized system (16 intensity measurements). For the non-optimized case we used only four incident and four detected Stokes vectors.

The experimental device built in this thesis illuminates the sample with a spot size on the order of a few micrometers, and studies local effects in samples through a polarimetric analysis of the intensity measurements. The polarimeter was built to work by transmission (for calibrations process) and reflection (study of samples) mode, in both cases it was necessary to obtain the characterization of the optical components such as, polarizers, retarders, LCVRs, and lenses.

For the LCVR it was necessary to study its optical properties to improve results and estimate errors, as in any application using these devices. So, a set of experimental procedures to measure optical properties as a function of the voltage applied were implemented. In chapter 4.3, we presented the experimental characterization and phase unwrapping of the LCVR which showed good accuracy and good agreement with the expected results.

The polarimeter was automated using LabVIEW, which allowed us to systematically and with good accuracy control the LCVRs, the detector and the positioning plates simultaneously, and allowed us to develop an interface for the control of all parameters of the instrument.

In Chapter 4 the experimental procedure to perform the measurement of the experimental Mueller matrix was presented. We presented the experimental Mueller matrices obtained with our polarimetric device, which are known matrices of the known samples. These Mueller matrices were not exactly the expected matrices. The differences between the experimental matrices and the theoretical matrices were mainly due to errors in the angles of the fast axes of the retarders, errors in the values of the retardances used in the variable retarders to produce the required incident and detected Stokes vectors, and it may be that, to a lesser extent, the quality of each polarizing element.

These differences between the theoretical Mueller matrices and the measured Mueller matrices of known samples created the necessity of work in the precision of the polarimeter, because we obtained errors for known samples of up to 22%. Initially we tried to correct the errors with manual adjustments in the experiment, however there will always be systematic errors. Then, we developed a calibration and data extraction program that considers the errors present in the instrument in such a way that the accuracy of the instrument is improved.

7.2 Calibration and data extraction method

A fundamental contribution of this work is a method for calibration and data-extraction for non-optimized Mueller matrix polarimeters. The proposed method is very precise to estimate the Mueller matrix, and allows a reduction in measurement time to compensate the time used by our polarimeter which is a scanning polarimeter.

The calibration process requires the measurement of four known polarization devices. We used free-space transmission, a horizontal and a vertical linear polarizer, and a quarter-wave retarder with its fast axis at 30° to the horizontal. The method proposed here does not require exact optimization of the experimental system to reduce the condition number, and uses calibration samples to calculate the errors in the experimental system. Experimental data for a rotating quarter-wave retarder, half-wave retarder and a linear polarizer showed very good results. The results presented show that the RMS is even smaller for the case of a non-optimized system using our fitting method, than when an optimized polarimeter is implemented using the direct method of Bickel and Bailey to measure the Mueller matrix of the measured intensities. We found that the average reduction of the RMS when calibrating a polarimeter using our method was up to 77.08%, which was an extremely important result in this thesis because it allowed us to measure very accurately the Mueller matrix of a structured surface, and as the method gives good results for a non-optimized polarimeter then we could reduce the time used for the measurements of the Mueller matrix on a sample with a point-to-point scan.

The method proposed in this thesis for calibration and data extraction has more relevance because it is well known that in LCVR there is a dependence on temperature with optical retardation, especially for low voltages. When we repeated measurements on different days and climate conditions, the characterization curves of the LCVRs changed significantly, which produced an unreliable experimental system. After performing the calibration of the system with the method developed, the experimental results obtained showed good accuracy and good agreement with the results calculated using a numerical simulation based on the Kirchhoff Approximation.

7.3 Calculation of the scattered field using the Kirchhoff Approximation

Based on a simulation that implements the Kirchhoff approximation calculating the Mueller matrix from a specific area of the micro-structured surface, we found the most significant parameters in the developed polarimeter. For this, it was necessary to restrict the variables in the system.

The results presented in Chapter 6 allowed us to fix the angle of incidence and detection of the PSG and the PSA, respectively and the type of reflective material to reduce the parameters.

It was shown that by changing the properties of width, height and separation between the structures, considerable changes are presented in the elements of the MM.

The hypothesis was validated that when illuminating with a smaller spot-size (of the order of the structure dimensions) it is possible to observe more significant changes in the elements of the MM.

Therefore, the presented results allowed us to guarantee that the simulation is a good tool to limit the variables of our problem, which helped to establish the parameters in the experimental device.

7.4 Polarimetric studies of structured surfaces

Using the parameters defined by the numerical simulation and the instrument developed in this thesis, a polarimetric study was performed for a surface with only one step (rib) of height equal to 15μm and width equal to 15μm, with aluminium as a reflective material. The changes in the polarization state of the intensity of light scattered by the sample were measured and calculated using the calibration and data extraction method proposed in this work.

The structured surface used to make the comparison with the numerical simulation was micro-fabricated and characterized, showing very good agreement and consistency with the design parameters. Multiple surfaces with different sizes were manufactured, although we only present the case for a step of 15x15 micrometers because it is the easiest case to analyze. The geometric parameters of the ideal surface and the experimental surface showed a difference of less than 5%, guaranteeing a consistency in the theoretical-experimental comparison.

Numerical and experimental data were compared in Chapter 6 and showed good agreement. We found that the elements of the matrix presented symmetries due to: the shape of the surface, the angular parameters of the polarimeter and the relation of the elements of the Mueller matrix, showing good consistency.

In conclusion, the proposed polarimetric system, which uses variable liquid crystal retarders to perform the polarization state changes of the PSG and PSA, respectively, and that uses a focused illumination works according to the theory, and the experimental results are consistent with results of numerical calculation based on the Kirchhoff Approximation, demonstrating the validity of the proposed polarimeter and the calibration and data extraction method.

7.5 Future work

Once the validity of the proposed method was demonstrated, which included the design, construction, calibration and extraction of data from a polarimeter using LCVRs, using a focused spot as a source of illumination, we performed a polarimetric study of structured surfaces with defined parameters. The next step will be to implement more sophisticated techniques of polarimetric analysis. A viable option is to analyze the results using the Polar Decomposition of the Mueller matrix, which allows a quantitative interpretation of the matrix. Although in the present work it was demonstrated that the elements of the matrix have symmetries, it is not possible to relate these symmetries directly with the size and geometric structure of the studied surface.

After carrying out the polar decomposition process of the Mueller matrix for our system, it will be possible to analyze the changes due to the particular shape and the different materials on the study sample. Therefore, with the surfaces that were already micro-fabricated with different parameters, a quantitative polarization study will be carried out, to study the effects of the geometric changes of the sample.

Our polarimeter compensates the variation of the scatter pattern with the wavelength or the angular variation used in other systems, with the study of the changes in polarization state from one point to another of the surface, which allowed us to validate the correct performance of the system. However, it is very easy to add angular variations to our current system, so we will study these angular variations to obtain complementary information of the sample.

Finally, after carrying out the studies presented in this section, the system will be able to study unknown structured samples, so that we can implement our instrument for the study of scattering on rough or structured surfaces, which has diverse applications in scientific and technological areas, such as measurement of critical dimensions or testing of printed circuits. The system will be able to study unknown structured samples, so that we can implement our instrument for the study of remote sensing images and security validation of packages and documents.

Bibliography

[1] J.A. Ogilvy, *Theory of wave scattering from random rough surfaces*, Institute of Physics Publishing, Bristol, (1991).

[2] P. Beckmann y A. Spizzichino, *The Scattering of Electromagnetic Waves from Rough Surfaces*, Pergamon, New York, (1963).

[3] D.Goldstein, "*Polarized light*", 2^{nd} Edition, Marcel Dekker, New York, (2003)

[4] T.A. Germer, *Effect of line and trench profile variation on specular and diffuse reflectance from a periodic structure*, J. Opt. Soc. Am. A 24, 696-701, (2007).

[5] M. Rosete-Aguilar, N.C. Bruce y O.G. Rodriguez Herrera, *Optical design of a scatterometer with an ellipsoidal mirror*, Optical Engineering, 42, 1772-1777, (2003).

[6] O.G. Rodriguez-Herrera, M. Rosete-Aguilar y N.C. Bruce, *Scatterometer of visible light for 2D rough surfaces*, Review of Scientific Instruments, 75, 4820-4823, (2004).

[7] M. Rovira-Laparra, N.C. Bruce, O.G. Rodriguez-Herrera, J.G. Bañuelos-Muñeton, E.V. Basiuk J.M. Saniger-Blesa, *Characterisation of chemically etched Indium Phosphide surfaces with light scattering*, Waves in Random and Complex Media, 17, 221-231, (2007).

[8] [8] R.A. Depine and D.C. Skigin, *Scattering from metallic surfaces having a finite number of rectangular grooves*, J. Opt. Soc. Am. A 11, 2844-2850, (1994).

[9] Y-L Kok, *General solution to the multiple-metallic-grooves scattering problem: the fast polarization case*, Applied Optics 32, 2573-2581, (1993).

[10] M.G. Moharam. E.B. Grann and D.A. Pommet, *Formulation for stable and efficient implementation of the rigorous coupled-wave analysis of binary gratings*, J. Opt. Soc. Am. A 12, 1068-1076, (1995).

[11] Mendoza-Suárez and E. R. Méndez, *Light scattering by a reentrant fractal surface*, Applied Optics, 36, 3521–3531, (1997).

[12] D.E. Barrick, *Rough surface scattering based on the specular point theory*, I.E.E.E. Trans. Ant. Propag. 16, 449-454, (1968).

[13] K. Tang, R.A. Dimenna and R.O. Buckius, *Regions of validity of the geometric optics approximation for angular scattering from very rough surfaces*, Int. J. Heat Mass Transfer. 40, 49-59, (1997).

[14] Ishimaru and J.S. Chen, *Scattering from very rough metallic and dielectric surfaces: a theory based on the modified Kirchhoff approach*, Waves in Random Media 1, 21-34, (1991).

[15] C. Macaskill y B.J. Kachoyan, *Iterative approach for the numerical simulation of scattering from one- and twodimensional rough surfaces*, Applied Optics, 32, 2839-2847, (1993).

[16] N.C. Bruce, *Scattering from infinitely sloped surfaces by of the Kirchhoff approximation*, Applied Optics, 42, 2398-2406, (2007).

[17] N.C. Bruce, Control of the backscattered intensity in random rectangular-groove surfaces with variations in the groove depth", Applied Optics, 44, 784-791, (2005).

[18] N.C. Bruce, "Randomly rough rectangular-groove surfaces with predetermined backscatter intensities", Rev. Mex. Fis., 52, 246-254, (2006).

[19] K.A. ODonnell and M.E. Knotts, *Polarization dependence of scattering from one-dimensional rough surfaces*, J. Opt. Soc. Am. A 8, 1126-1131, (1991).

[20] T.R. Michel, M.E. Knotts and K.A. ODonnell, S*tokes matrix of a one-dimensional perfectly conducting rough surface*, J. Opt. Soc. Am. A 9, 585-596, (1992).

[21] J.L. Pezzanti and R.A. Chipman, *Mueller matrix scatter polarimetry of a diamond-turned mirror*, Opt. Eng. 34, 1593-1598, (1995).

[22] R.C. Thompson, J.R. Bottiger and E.S. Fry, Measurement of polarized light interactions via the Mueller matrix, App. Opt. 19, 1323-1332, (1980).

[23] N.C. Bruce, A.J. Sant y J.C. Dainty, The Mueller matrix for rough surface scattering using the Kirchhoff Approximation, Opt. Comm., 88, 471-484. (1992).

[24] F. Delplancke, Automated high-speed Mueller matrix scatterometer, App. Opt., 36, 5388-5395, (1997).

[25] G. Videen, W.S. Bickel, V.J. Iafelice and D. Abromson, Experimental light-scattering Mueller matrix for a fiber on a reflecting optical surface as a function of incident angle, J. Opt. Soc. Am. A 9, 312-315, (1992).

[26] R. Espinosa-Luna, S.E. Acosta-Ortiz and L.F. Zou, Mueller matrix for characterization of one-dimensional rough perfectly reflecting surfaces in a conical configuration, Opt. Lett. 23, 1075-1077, (1998).

[27] R. Espinosa-Luna, Scattering by rough surfaces in a conical configuration: experimental Mueller matrix, Opt. Lett. 27, 1510-1512, (2002).

[28] T.A. Germer and C.C. Asmail, Goniometric optical scatter instrument for out-of-plane ellipsometry measurements, Rev. Sci. Inst. 70, 3688-3695, (1999).

[29] Egon Marx and T.V. Voorburger, Direct and inverse problems for light scattered by rough surfaces, Applied Optics 25, 3613-3623 (1990).

[30] J. M. Sanz, F. Moreno(S), F. González, *The polar decomposition method in the polarimetric study of light scattered by deterministic profiles and dense media*, Opt. Pura Apl. 45 (2) 121-130 (2012).

[31] Ray J. Hoobler, Ebru Apak *Optical critical dimension (OCD) measurments for profile monitoring and control: applications for mask inspection and fabrication*, Proceedings of SPIE Vol. 5256 23rd Annual BACUS Symposium on Photomask Technology,SPIE, Bellingham, WA, (2003) .·

[32] D.G. Stavenga, H.L. Leertouwer, P. Pirih, and M.F. Wehling, Imaging scatterometry of butterfly wing scales, Optical Express, 17, 193-202, (2009).

[33] Xiuguo Chen, Honggang Gu, Hao Jiang, Chuanwei Zhang, and Shiyuan Liu, *Robust overlay metrology with differential Mueller matrix calculus*, OPTICS EXPRESS 8491, Vol. 25, No. 8, 17 Apr (2017).

[34] O. Rodríguez-Núñez, Neil C. Bruce, *Measurement of defects by measuring of light scattering from surfaces using focused illumination*, Proc. SPIE 9890, Optical Micro- and Nanometrology VI, 989012, (2016).

[35] N. C. Bruce, ”Vector-electromagnetic scattering from metal surfaces using the infinite-slope Kirchhoff approximation,” Proc. SPIE 8011, 22nd Congress of the International Commission for Optics: Light for the Development of the World, 80115T, (2011).

[36] Shiyuan Liu, Xiuguo Chen, and Chuanwei Zhang, *Mueller Matrix Polarimetry: A Powerful Tool for Nanostructure Metrology*, ECS Transactions, 60 (1) 237-242 (2014).

[37] R. M. A. Azzam, *Stokes-vector and Mueller-matrix polarimetry*, Journal of the Optical Society of America A, Vol. 33, No. 7, July (2016).

[38] Azzam, R. M. A. et Bashara, N. M., *Ellipsometry and Polarized Light*, North-Holland, New York, 1977.

[39] A. Röseler, *Infrared Spectroscopic Ellipsometry*, Akademie-Verlag, (1990).

[40] M. Schubert, *Infrared Ellipsometry on Semiconductor Layer Structures: Phonons, Plasmons, and Polaritons*, (Springer, 2004).

[41] H. G. Tompkins and E. A. Irene, eds., *Handbook of Ellipsometry*, William Andrews, (2005).

[42] H. Fujiwara, *Spectroscopic Ellipsometry: Principles and Applications*, Wiley, (2007).

[43] M. Losurdo and K. Hingerl, eds., *Ellipsometry at the Nanoscale*, Springer, (2013).

[44] K. Hinrichs and K.-J. Eichhorn, eds., *Ellipsometry of Functional Organic Surfaces and Films*, Springer, (2014).

[45] D. E. Aspnes, *Spectroscopic ellipsometry—past, present, and future*, Thin Solid Films 571, 334–344 (2014).

[46] . T. Gehrels, ed., *Planets, Stars, and Nebulae Studied with Photopolarimetry*, University of Arizona, (1974).

[47] . J. O. Stenflo, *Solar Magnetic Fields*, Kluwer, (1994).

[48] . K. N. Nagendra and J. Stenflo, eds., *Solar Polarization*, Springer, (1999).

[49] . J. Trujillo-Bueno, F. Morino-Insertis, and F. Sanchez, eds., *Astrophysical Spectropolarimetry*, Cambridge University, (2002).

[50] . J. Tinbergen, *Astronomical Polarimetry*, Cambridge University, (2005).

[51] . D. Clarke, *Stellar Polarimetry*, Wiley-VCH, (2010).

[52] . R. Bellazzini, E. Costa, G. Matt, and G. Tagliaferri, eds., *X-Ray Polarimetry: A New Window in Astrophysics*, Cambridge University, (2010).

[53] . L. Kolokolova, J. Hough, and L.-C. Levasseur-Regourd, eds., *Polarimetry of Stars and Planetary Systems*, Cambridge University, (2015).

[54] J. S. Tyo, D. L. Goldstein, D. B. Chenault, and J. A. Shaw, *Review of passive imaging polarimetry for remote sensing applications*, Appl. Opt. 45, 5453–5469 (2006).

[55] V. V. Tuchin, L. Wang, and D. A. Zimnyakov, *Optical Polarization in Biomedical Applications*, (Springer, 2006).

[56] N. Ghosh and I. A. Vitkin, *Tissue polarimetry: concepts, challenges, applications, and outlook*, J. Biomed. Opt. 16, 110801 (2011).

[57] P. S. Hauge, *Recent developments in instrumentation in ellipsometry*, Surf. Sci. 96, 108–140 (1980).

[58] Russel A. Chipman. *Polarimetry. In M. Bass, editor, Handbook of Optics*, volume 2, chapter 22, pages 22.1–22.37. McGraw-Hill, 1995.

[59] C. J. Raymond, M. R. Murnane1, S. L. Prins, S. Sohail, H. Naqvi, J. R. McNeil, and J. W. Hosch, J. Vac. Sci. Technol. B, 15(2), 361 (1997).

[60] . X. Niu, N. Jakatdar, J. Bao, and C. J. Spanos, IEEE Trans. Semicond. Manuf., 14(2), 97 (2001).

[61] . C. H. Ko and Y. S. Ku, Opt. Express 14(13), 6001 (2006).

[62] . T. Novikova, A. De Martino, P. Bulkin, Q. Nguyen, B. Drévillon, V. Popov, and A. Chumakov, Opt. Express, 15(5), 2033 (2007).

[63] . Y. N. Kim, J. S. Paek, S. Rabello, S. B. Lee, J. T. Hu, Z. Liu, T. D. Hao, and W. McGahan, Opt. Express, 17(23), 21336 (2009).

[64] . X. G. Chen, S. Y. Liu, C. W. Zhang, and H. Jiang, J. Micro/Nanolith. MEMS MOEMS, 12(3), 033013 (2013).

[65] M. Born and E. Wolf. *Principles of Optics.* Cambridge University Press, 7*th* edition, 1999.

[66] D.Goldstein, *Polarized light*, 2^{nd} Edition, Marcel Dekker, New York, (2003)

[67] Oscar G. Rodríguez-Herrera. *Far-field method for the characterisation of three-dimensional fields: vectorial polarimetry.* PhD thesis, National University of Ireland, Galway, London, 2009.

[68] R.W. and J.J Koh, J. Opt. Soc. Am. A 16, 1997 (1999).

[69] G.E. Jellison, Jr., and F.A. Modine, Appl. Opt. 36, 8184 (1997).

[70] E. Compain and B. Drévillon, Rev. Sci. Instrum. 69, 1574 (1998).

[71] J.S. Tyo and T.S. Turner, Jr., PRoc. SPIE 3753, 214 (1999).

[72] J.M. Bueno and P. Artal, Opt. Lett. 24, 64 (1999).

[73] N C Bruce, Alejandro Dominguez Báez, Tonatiuh Santana Sánchez, Xanat Téllez Díaz, Arturo Nogueira Jiménez and Rigoberto Nava Sandoval, *Design of a scanning polarimetric scatterometer for rough surface scattering measurements*, Journal of Physics: Conference Series 274,012135,(2011).

[74] John C. Stover, "*Optical Scattering, Measurement and Analysis*", 3rd Edition, SPIE, Bellingham, Washington, (2012)

[75] Eugene Hecht, *Optica*, Addisson Wesley Iberoamericana, Madrid (2000).

[76] Jeremy Vizet and Rasvigor Ossikovski, "*Symmetric decomposition of experimental depolarizing Mueller matrices in the degenerate case*"

[77] Sami Ben Hatit, *Polarimétrie de Mueller résolue en angle.* Physics. Ecole Polytecnique X, 2009. English.

[78] Lu, S.-Y. et Chipman, R. A., *Homogeneous and inhomogeneous Jones matrices*, J. Opt. Soc. Am. A 11 (1994) 766?773.

[79] Lu, S.-Y. et Chipman, R. A., *Interpretation of Mueller matrices based on polar decomposition*, J. Opt. Soc. Am. A 13 (1996) 11061113.

[80] G. Arfken and H. Weber, "*Mathematical Methods for Physicists*", 5th Edition, Academic Press, San Diego, (2001)

[81] Gil, J. J., Characteristic properties of Mueller matrices, J. Opt. Soc. Am. A 17 (2000) 328–334.

[82] Gil, J. J. et Bernabeu, E., A depolarization criterion in Mueller matrices, Opt. Acta 32 (1985) 259–261.

[83] Anderson, D. G. M. et Barakat, R., Necessary and sufficient conditions for a Mueller matrix to be derivable from a Jones matrix, J. Opt. Soc. Am. A 11 (1994) 2305–2319.

[84] Kostinski, A., Givens, C., et Kwiatkowski, J., Constraints on Mueller matrices of polarization optics, Appl. Opt. 32 (1993) 1646–1651.

[85] Kostinski, A., Depolarization criterion for incoherent scattering, Appl. Opt. 31 (1992) 3506–3508.

[86] Brosseau, C. et Kostinski, A., Generalized trace condition on the Mueller-Jones polarization matrix, J. Opt. Soc. Am. A 10 (1993) 2248–2251.

[87] William S. Bickel and Wilbur M. Bailey. *Stokes vectors, Mueller matrices, and polarized scattered light.* Am. J. Phys., 53(5):468-478, 1985.

[88] David Lara-Saucedo. *Three-dimensional Complete Polarisation Sensitive Imaging using a Confocal Mueller Matrix Polarimeter.* PhD thesis, Imperial College, London, 2005.

[89] O. Arteaga, J. Freudenthal, B. Wnag, and B. Kahr, Appl. Opt. 51, 6805 (2012).

[90] J.S Tyo, *Design of optimal polarimeters:maximization of signal to noise ratio and minimization of systematic errors*, Applied Optics, 41(4),619-630, 2012.

[91] Dhairya Dixit, Nick Keller, Yevgeny Lifshitz, Taher Kagalwala, Alexander Elia, Vinit Todia Jody Fronheiser and Alok Vaida, *Nonconventional applications of Mueller matrix-based scatterometry for advanced technology nodes*, J. Micro/Nanolith. MEMS MOEMS 17(3), 034001, (2018).

[92] Shiyuan Liu, Xiuguo Chen, and Chuanwei Zhang, *Mueller Matrix Polarimetry: A Powerful Tool for Nanostructure Metrology*, ECS Transactions, 60 (1) 237-242 (2014).

[93] T. Novikova, A. De Martino, R. Ossikovski, and B. Drévillon, *Metrological applications of Mueller polarimetry in conical difraction for overlay characterization in microelectronics*, Eur. Phys. J Appl Phys. 31, 63-69 (2005).

[94] Clément Fallet, Tatiana Novikova, Martin Foldyna, Sandeep Manhas, Bicher Haj Ibrahim, Antonello De Martinbo Cyril Vannuffel, Christophe Constancias, *Overlay measurments by Mueller polarimetry in back focal plane*, J. Micro/Nanolith. MEMs MOEMS 10(3), 033017 (2011).

[95] Maria Losurdo, Michael Bergmair, Giovanni Bruno, Denis Cattelan, Christoph Cobet, Antonello de Martino, Karsten Fleischer, Zorana Dohcei-Mitrovic, Norbert Esser, Melanine Galliet, Rados Gajic, Dusan Hemzal, Kurt Hingerl, Joseph Humlicek, Razvigo Ossikovski, Zoran V. Popovic and Ottilia Saxl. *Spectroscopic ellipsometry and polarimetry for materials and systems analysis at the nanometer scale: state-of-the-art, potential, and perspectives*, J. Nanopart Rev. 11:1521-1554 (2009).

[96] O. Rodríguez-Núñez, *Medición de luz esparcida en superficies rugosas utilizando iluminación enfocada*, Master thesis, Universidad Nacional Autónoma de México, CDMX, Mexico, 2014.

[97] Neil Bruce, *Application of the Kirchhoff Approximation to Scattering from Rough Surfaces*, PhD Tesis, Imperial College of London, (1992).

[98] A.H. Firester, M. E. Heller, and P. Sheng. *Knife-edge scanning measurements of subwavelength focused light beams.* Appl. Opt. 16, 7 (1977).

[99] Mario González-Cardel, Pedro Arguijo, and Rufino Díaz. *Gaussian beam radius measurement with a knife-edge: a polynomial approximation to the inverse error function.* Appl. Opt. 52, 16 (2013).

[100] THORLABS, TDC001 DC Servo Motor Driver (User Guide), HA0142T Rev 12 February (2011).

[101] THORLABS, PM320e DUAL CHANNEL OPTICAL POWER AND ENERTY METER and S12C Silico Photodiode.

[102] $https : //www.thorlabs.com/newgrouppage9.cfm?objectgroup_id = 6339pn = LCC1113 - A$

[103] J.M. Lopez-Tellez, *Development of optical polarimeters using liquid-crystal variable retarders*, PhD thesis, Universidad Nacional Autónoma de México, CDMX, México, 2016.

[104] D. C. Ghiglia and M. D. Pritt, *Two-Dimensional Phase Unwrapping: Theory, Algorithms, and Software*, John Willey Sons, New York, 1998.

[105] M. A. Shocfield and Y. Zhu, *Fast phase unwrapping algorithm for interferometric applications*, Opt. Lett. 28 (14), 1194-1196 (2003).

[106] Juan M. Bueno, *Polarimetry using liquid-crystal variable retarders: theory and calibration*, J. Opt. A Pure Appl. Opt. 2 8200).

[107] J. M. Lopez-Téllez and N. C. Bruce, *Mueller matrix polarimeter using analysis of the nonlinear voltage-retardance relationship for liquid-crystal variable retarders*, App. Opt. 53(24) 5359 (2014).

[108] W.H. Press, S.A. Teukolsky, W.T. Vetterling and B.P Flannery, *Numerical Recipes in C, The Art of Scientific Computing*, Second Edition, Cambridge University PRess, Cambridge, (1992), chapter 10.

[109] A. de Martino, Y-K- Kim, E. García-Caurel, B. Laude and B. Drévillon, *Optimized Mueller polarimeter with liquid crystals*, Optics Letters, 28(8), (2003), 616-618.

[110] G. Martinez-Ponce, C. Solano and C. Pérez. Barrios, Hybrid complete Mueller polarimeter based on phase modulators, Optics and Lasers in Engineering, 49, (2011), 723-728.

[111] Nesse W, *Introduction to Optical Mineralogy* 4th edn (New York: Oxford University Press), 2012.

[112] Wood E A, *Crystals and Light: Introduction to Optical Crystallography*, (New York: Dover), 1977.

[113] Inoué S and Sato H, *Arrangement of DNA in living sperm: a biophysical analysis Science*, 136 1122–4, 1962.

[114] Vrabioiu A M and Mitchison T J, *Structural insights into yeast septin organization from polarized fluorescence microscopy*, Nature 443 466–49,2006.

[115] Wang Y, He H, Chang J, He C, Liu S, Li M, Zeng N, Wu J and Hui Ma, *Mueller matrix microscope: a quantitative tool to facilitate detections and fibrosis scorings of liver cirrhosis and cancer tissues*, J. Biomed Opt. 21 071112, 2016.

[116] Serrels K A, Ramsay E, Warburton R J and Reid D T, *Nanoscale optical microscopy in the vectorial focusing regime*, Nat. Photon. 2 311–4, 2008.

[117] Zhang T, Ruan Y, Maire G, Sentenac D, Talneau A, Belkebir K, Chaunet P C and Sentenac A, *Full-polarized tomographic diffraction microscopy achieves a resolution about one-fourth of the wavelength*, Phys. Rev. Lett. 111 243904, 2013.

[118] Fallet C, Novikova T, Foldyna M, Manhas S, Ibrahim B H, De Martino A, Vannuffel C and Constancias C, *Overlay measurements by Mueller polarimetry in back focal plane*, J. Micro/Nanolith. MEMS MOEMS 10 033017, 2011.

[119] Tan Y, Chen C, Chen X, Du W, Gu H and Liu S, *Development of a tomographic Mueller-matrix scatterometer for nanostructure metrology*, Rev. Sci. Instrum. 89 073702, 2018.

[120] Chao Chen, Xiusugo Chen, Honggang Gu, Hao Jiang, Chuanwei Zhang ang Shiyuan Liu, *Calibration of polarization effect of a high-numerical-aperture objective lens with Mueller matrix polarimetry*, Meas. Sci. Technol.025201 (9pp), 30 (2019).

[121] G. Videen, W. S. Bickel, *Light-scattering Mueller matrix for a rough fiber*, Appl. Opt. 31, 3488-3492 (1992).

[122] S. N. Savenkov, L. T. Mishchenko, R. S. Muttiah, Y. A. Oberemok, I. A. Mishchenko, *Mueller polarimetry of virus-infected and healthy wheat under field and microgravity conditions*, J. Quant. Spectrosc. Ra. 88, 327-343 (2003).

[123] J. Foucher, Pargon, E., Martin, M., Reyne, S., et Dupréa, C., *Paving the way for multiple applications for the 3d-afm technique in the semiconductor industry, in Metrology*, Inspection and Process Control for Microlithography XXI, volume 6922 of Proc. SPIE, pages 69220F1–9, 2008.

[124] J. Foucher, R. Thérèse, Y Lee, S.-I. Park, S.-J. Cho, Introduction of next-generation D AFM for advanced process control, Proc. SPIE 8681, Metrology, Inspection, and Process Control for Microlithography XXVII, 868106, (2013).

[125] P.Russell, D. Batchelor, J. Thornton, SEM and AFM: Complementary Techniques for Hight Resolution Surface Investigations, Digital Instuments Manual. Veeco, Metrology Group.

[126] McGahan, W. A., Dusa, M. V., Kiers, T., Holden, T. J. M., et Giubotti, T., *Normal incidence spectroscopic ellipsometry and polarized reflectometry for measurement and control of photoresist critical dimension*, in Metrology, Inspection and Process Control for Microlithography XVI, volume 4689 of Proc. SPIE, pages 1110–1121, 2002.

[127] Huang, H.-T. et Jr, F. L. T., *Erratum to "spectroscopic ellipsometry and reflectometry from gratings (scatterometry) for critical dimension measurement and in situ*, realtime process monitoring" [thin solid films 455-456 (2004) 828-836], Thin Solid Films 468 (2004) 339–346.

[128] Sendelbach, M. et Archie, C. N., *Scatterometry measurement precision and accuracy below 70 nm, in Metrology*, Inspection, and Process Control for Microlithography XVII, volume 5038 of Proc. SPIE, pages 224–238, 2003.

[129] Koshy, J., Sendelbach, M., et Herrera, P., *Enabling gate etch process development using scatterometry, in Metrology*, Inspection, and Process Control for Microlithography XXI, volume 6518 of Proc. SPIE, 2007.

[130] Leray, P. et al., *Accurate and reliable optical cd of mugfet down to 10 nm, in Metrology*, Inspection, and Process Control for Microlithography XXI, volume 6518 of Proc. SPIE, 2007.

[131] Lensing, K. et al., *A comprehensive comparison of spectral scatterometry hardware, in Metrology*, Inspection, and Process Control for Microlithography XIX, volume 5752 of Proc. SPIE, pages 337–350, 2005.

[132] Soulan, S., Besacier, M., Leveder, T., et Schiavone, P., *Real-time profile shape reconstruction using dynamic scatterometry, in Metrology, Inspection, and Process Control for Microlithography XXI*, volume 6518 of Proc. SPIE, 2007.

[133] Ku, Y., Wang1, S., Shyu, D., et Smith, N., *Scatterometry-based metrology with feature region signatures matching*, Opt. Express 14 (2006) 8482–8491.

[134] Hettwer, A., Benesch, N., Schneider, C., Pfitzner, L., et Ryssel, H., *Phi-scatterometry for integrated linewidth and process control in dram manufacturing*, IEEE Trans. Semicond. Manuf. 15 (2002) 470–477.

[135] Petit, J. et al., *Improved cd and overlay metrology using an optical fourier transform instrument, in Metrology*, Inspection and Process Control for Microlithography XIX, volume 5752 of Proc. SPIE, pages 420–428, 2005.

[136] A. Ishimaru and J. S. Chen, *Scattering from very rough surfaces based on the modified second-order Kirchhoff approximation with angular and propagation shadowing*, J. Acoust. Soc. Am. 88, 1877–1883 (1990).

[137] . A. Ishimaru and J. S. Chen, *Scattering from very rough metallic and dielectric surfaces: a theory based on the modified Kirchhoff approach*, Waves Random Media 1, 21–34 (1991).

[138] E. I. Thorsos, *The validity of the Kirchhoff approximation for rough surface scattering using a Gaussian roughness spectrum*, J. Acoust. Soc. Am. 83, 78–92 (1988).

[139] D. L. Jaggard and X. Sun, *Scattering from fractally corrugated surfaces*, J. Opt. Soc. Am. A 7, 1131–1139 (1990).

[140] N. C. Bruce and J. C. Dainty, *Multiple scattering from rough dielectric and metal surfaces using the Kirchhoff approximation,* J. Mod. Opt. 38, 1471–1481 (1991).

[141] N. C. Bruce and A. J. Sant, *The Mueller matrix for rough surface scattering using the Kirchhoff approximation*, Opt. Commun. 88, 471–484 (1992).

[142] C. J. R. Sheppard, *Scattering by fractal surfaces with an outer scale*, Opt. Commun. 122, 178–188 (1996).

[143] $https : //www.photonics.com/Products/Photonic_Professional_GT/pr61179$

[144] Data Sheet nanoscribe

[145] Odian G, *Principles of polymerization*, 3rd edn. Wiley, New York, (1991).

[146] Shuhui Wu, Jesper Serin Min Gu, Two-photon polymerisation for three-dimensional micro-fabrication, Journal of Photochemestry and Photobiology A: Chemistry 181 (2016).

[147] Hong-Bo Sun, Satoshi Kawata, *Two-Photon Photopolymerization and 3D Lithographic Microfabrication*, Springle, New York, volume 170, (2006).

[148] Aaron Cruz and Matheiu Hatfeuille, *Reporte técnico fabricación ICAT*, LaNSBioDyt, Facultad de Ciencias, México, (2018).

[149] Joel Pérez Urquizo, *Microscopía THz de campo cercano con sondas tipo Bow Tie*, Mater Tesis, UNAM, (2015).

[150] Goodman Joseph W., *Introduction of Fourier Optics*, McGraw-Hill, (1968).

[151] $http : //www.edmundoptics.com/technical - resources - center/lasers/understanding - spatial - filters/? = LAcountry = 141$

Appendix A

Experimental details of the experiment

A.1 Spatial Filtering

A spatial filter is based on Fourier optics [150] to filter a coherent beam of light or other electromagnetic radiation. In the developed system, it is used to filter the output of a laser, suppressing intensity changes due to imperfections in optics. A converging lens is used to focus the beam that, because, of the additional structure on the beam will not focus to a single point, but in the focal plane it will create a point surrounded by the light from additional structure. This corresponds to the Fourier transform of the distribution of transverse energy intensity of the beam and the pupil of the lens. The center light corresponds to an almost perfect Gaussian wave in the plane of the transformation, the additional light is the contribution with a higher spatial frequency.

The spatial filter device used consists of a microscope objective with a focal length of $8mm$, which has a pinhole with a diameter of 15μm and a positioning mechanism [151]. The precision positioning mechanism has XY movements that center the pinhole on the focal point of the objective lens by passing the central beam through the pinhole. The size of this pinhole depends on the wavelength of the light and the focal length of the lens. An almost perfect Gaussian beam is obtained at the cost of reducing the intensity. The beam diameter can be calculated as shown in equation A.1

$$D_{beam} = \frac{\lambda * f}{r} \tag{A.1}$$

Where D_{beam} is the diameter of the central beam in μm, λ the laser wavelength in μm, f the focal length of the objective lens in mm and r is the input beam radius at the $1/e^2$ point, in mm.

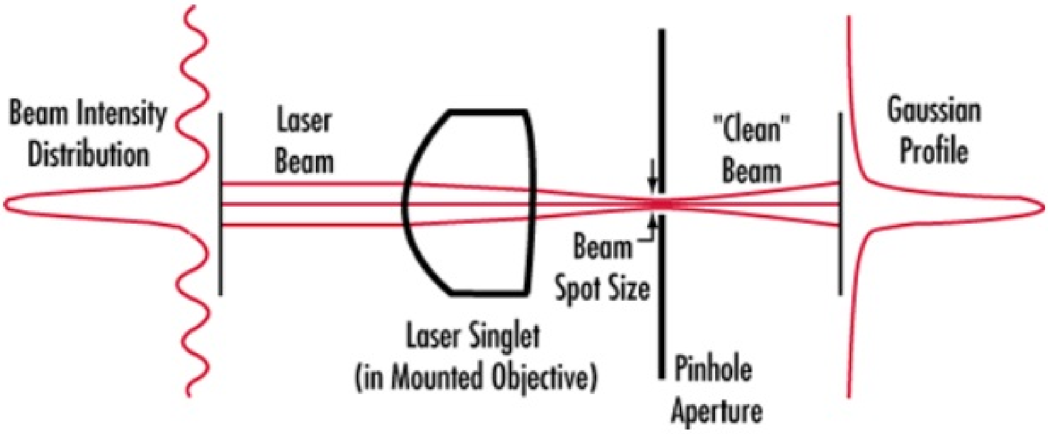

Figure A.1: Schematic representation to show how the spatial filtering works[151].

A.2 Aspheric Lens

Aspherical surfaces are those that are not spherical or flat. These surfaces are used in optical systems, so the importance of these surfaces is that with them it is possible to avoid the defects present in the images (aberrations) such as: spherical aberration, coma, astigmatism and barrel-type distortion, which are inevitable consequences of spherical surfaces. The ability of aspheric surfaces to produce well-corrected images (or without aberrations) allows optical systems to increase their field of view by reducing the number of optical elements.

The aspheric surfaces are divided into two groups: 1) surfaces of revolution with an axis of symmetry; 2) surfaces of revolution with two planes of symmetry.

The aspherical surfaces most used in optics, belong to the first group and among them are parabolas, ellipses and hyperbolas. These are the simplest aspherical shapes and are generated by the revolution of a conical section. To solve optical problems that do not have rotational symmetry, the surfaces of revolution are used with two planes of symmetry.

A.3 Results of the knife-edge test

We present in Table A.1 the values of the spot-size including the percent error, which is very small (lower than $\simeq 3\%$).The values of the spot-size are for the optical system, which consists of two aspheric lenses. With this system it is possible to reach a size of the focused beam of $3.70 \pm 1.89\mu$m, with an Image length $= 90mm$.

If we need another size of beam, we need only to move the focus position. For example, we have a spot-size = 10μm with an Image length = $210mm$ or the case with a single lens spot-size = 5μm with an Image length = $50mm$.

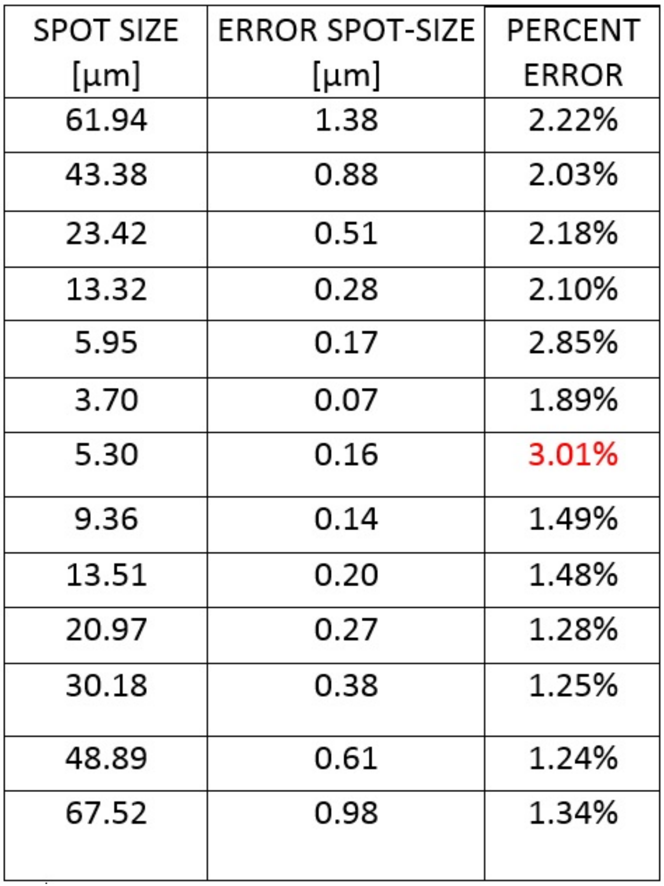

SPOT SIZE [µm]	ERROR SPOT-SIZE [µm]	PERCENT ERROR
61.94	1.38	2.22%
43.38	0.88	2.03%
23.42	0.51	2.18%
13.32	0.28	2.10%
5.95	0.17	2.85%
3.70	0.07	1.89%
5.30	0.16	3.01%
9.36	0.14	1.49%
13.51	0.20	1.48%
20.97	0.27	1.28%
30.18	0.38	1.25%
48.89	0.61	1.24%
67.52	0.98	1.34%

Table A.1: Knife-edge test for the beam used in this work to illuminate a structured surface.

A.4 Complete data of the transmittance

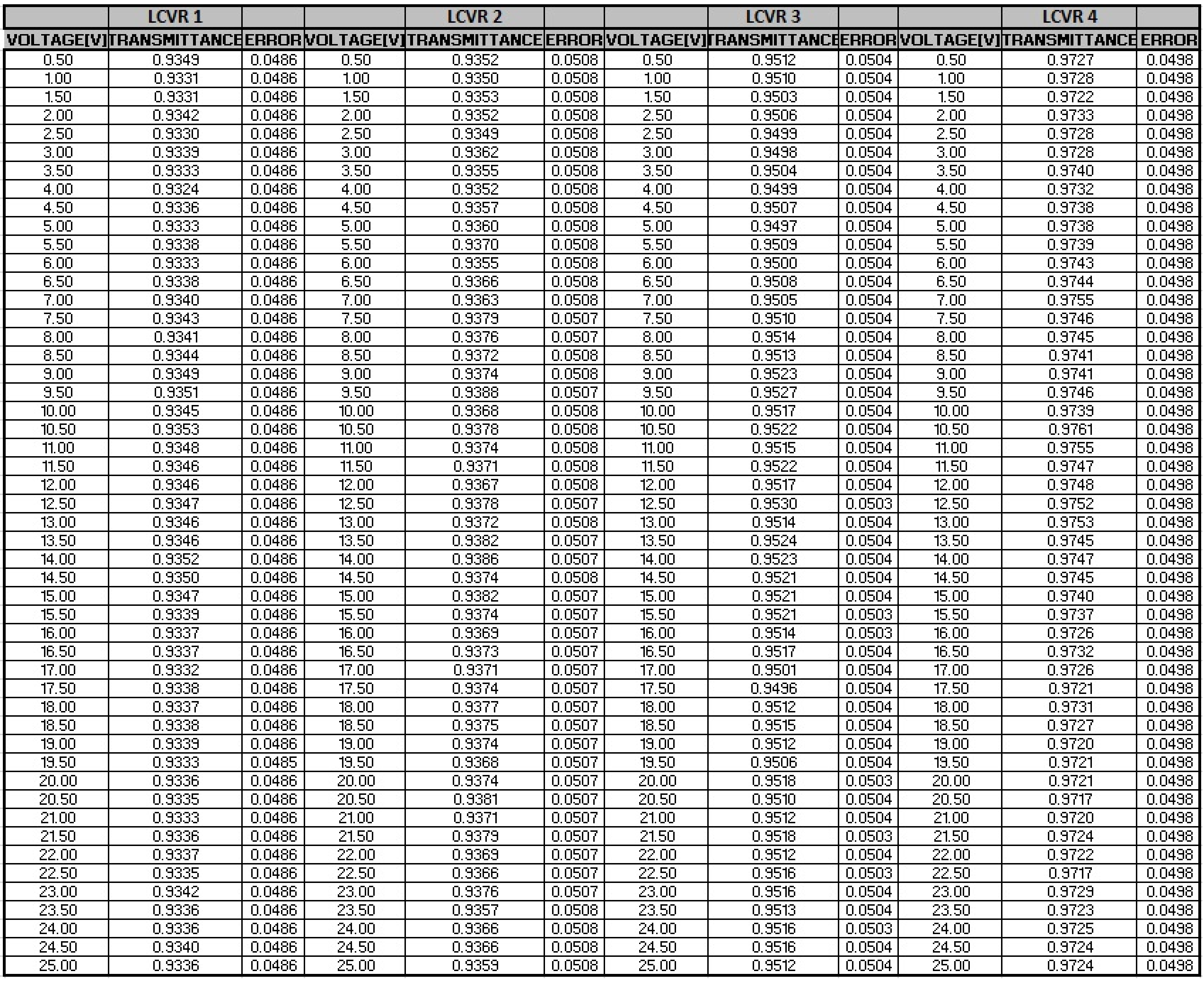

	LCVR 1			LCVR 2			LCVR 3			LCVR 4	
VOLTAGE[V]	TRANSMITTANCE	ERROR	VOLTAGE[V]	TRANSMITTANCE	ERROR	VOLTAGE[V]	TRANSMITTANCE	ERROR	VOLTAGE[V]	TRANSMITTANCE	ERROR
0.50	0.9349	0.0486	0.50	0.9352	0.0508	0.50	0.9512	0.0504	0.50	0.9727	0.0498
1.00	0.9331	0.0486	1.00	0.9350	0.0508	1.00	0.9510	0.0504	1.00	0.9728	0.0498
1.50	0.9331	0.0486	1.50	0.9353	0.0508	1.50	0.9503	0.0504	1.50	0.9722	0.0498
2.00	0.9342	0.0486	2.00	0.9352	0.0508	2.50	0.9506	0.0504	2.00	0.9733	0.0498
2.50	0.9330	0.0486	2.50	0.9349	0.0508	2.50	0.9499	0.0504	2.50	0.9728	0.0498
3.00	0.9339	0.0486	3.00	0.9362	0.0508	3.00	0.9498	0.0504	3.00	0.9728	0.0498
3.50	0.9333	0.0486	3.50	0.9355	0.0508	3.50	0.9504	0.0504	3.50	0.9740	0.0498
4.00	0.9324	0.0486	4.00	0.9352	0.0508	4.00	0.9499	0.0504	4.00	0.9732	0.0498
4.50	0.9336	0.0486	4.50	0.9357	0.0508	4.50	0.9507	0.0504	4.50	0.9738	0.0498
5.00	0.9333	0.0486	5.00	0.9360	0.0508	5.00	0.9497	0.0504	5.00	0.9738	0.0498
5.50	0.9338	0.0486	5.50	0.9370	0.0508	5.50	0.9509	0.0504	5.50	0.9739	0.0498
6.00	0.9333	0.0486	6.00	0.9355	0.0508	6.00	0.9500	0.0504	6.00	0.9743	0.0498
6.50	0.9338	0.0486	6.50	0.9366	0.0508	6.50	0.9508	0.0504	6.50	0.9744	0.0498
7.00	0.9340	0.0486	7.00	0.9363	0.0508	7.00	0.9505	0.0504	7.00	0.9755	0.0498
7.50	0.9343	0.0486	7.50	0.9379	0.0507	7.50	0.9510	0.0504	7.50	0.9746	0.0498
8.00	0.9341	0.0486	8.00	0.9376	0.0507	8.00	0.9514	0.0504	8.00	0.9745	0.0498
8.50	0.9344	0.0486	8.50	0.9372	0.0508	8.50	0.9513	0.0504	8.50	0.9741	0.0498
9.00	0.9349	0.0486	9.00	0.9374	0.0508	9.00	0.9523	0.0504	9.00	0.9741	0.0498
9.50	0.9351	0.0486	9.50	0.9388	0.0507	9.50	0.9527	0.0504	9.50	0.9746	0.0498
10.00	0.9345	0.0486	10.00	0.9368	0.0508	10.00	0.9517	0.0504	10.00	0.9739	0.0498
10.50	0.9353	0.0486	10.50	0.9378	0.0508	10.50	0.9522	0.0504	10.50	0.9761	0.0498
11.00	0.9348	0.0486	11.00	0.9374	0.0508	11.00	0.9515	0.0504	11.00	0.9755	0.0498
11.50	0.9346	0.0486	11.50	0.9371	0.0508	11.50	0.9522	0.0504	11.50	0.9747	0.0498
12.00	0.9346	0.0486	12.00	0.9367	0.0508	12.00	0.9517	0.0504	12.00	0.9748	0.0498
12.50	0.9347	0.0486	12.50	0.9378	0.0507	12.50	0.9530	0.0503	12.50	0.9752	0.0498
13.00	0.9346	0.0486	13.00	0.9372	0.0508	13.00	0.9514	0.0504	13.00	0.9753	0.0498
13.50	0.9346	0.0486	13.50	0.9382	0.0507	13.50	0.9524	0.0504	13.50	0.9745	0.0498
14.00	0.9352	0.0486	14.00	0.9386	0.0507	14.00	0.9523	0.0504	14.00	0.9747	0.0498
14.50	0.9350	0.0486	14.50	0.9374	0.0508	14.50	0.9521	0.0504	14.50	0.9745	0.0498
15.00	0.9347	0.0486	15.00	0.9382	0.0507	15.00	0.9521	0.0504	15.00	0.9740	0.0498
15.50	0.9339	0.0486	15.50	0.9374	0.0507	15.50	0.9521	0.0503	15.50	0.9737	0.0498
16.00	0.9337	0.0486	16.00	0.9369	0.0507	16.00	0.9514	0.0503	16.00	0.9726	0.0498
16.50	0.9337	0.0486	16.50	0.9373	0.0507	16.50	0.9517	0.0504	16.50	0.9732	0.0498
17.00	0.9332	0.0486	17.00	0.9371	0.0507	17.00	0.9501	0.0504	17.00	0.9726	0.0498
17.50	0.9338	0.0486	17.50	0.9374	0.0507	17.50	0.9496	0.0504	17.50	0.9721	0.0498
18.00	0.9337	0.0486	18.00	0.9377	0.0507	18.00	0.9512	0.0504	18.00	0.9731	0.0498
18.50	0.9338	0.0486	18.50	0.9375	0.0507	18.50	0.9515	0.0504	18.50	0.9727	0.0498
19.00	0.9339	0.0486	19.00	0.9374	0.0507	19.00	0.9512	0.0504	19.00	0.9720	0.0498
19.50	0.9333	0.0485	19.50	0.9368	0.0507	19.50	0.9506	0.0504	19.50	0.9721	0.0498
20.00	0.9336	0.0486	20.00	0.9374	0.0507	20.00	0.9518	0.0503	20.00	0.9721	0.0498
20.50	0.9335	0.0486	20.50	0.9381	0.0507	20.50	0.9510	0.0504	20.50	0.9717	0.0498
21.00	0.9333	0.0486	21.00	0.9371	0.0507	21.00	0.9512	0.0504	21.00	0.9720	0.0498
21.50	0.9336	0.0486	21.50	0.9379	0.0507	21.50	0.9518	0.0503	21.50	0.9724	0.0498
22.00	0.9337	0.0486	22.00	0.9369	0.0507	22.00	0.9512	0.0504	22.00	0.9722	0.0498
22.50	0.9335	0.0486	22.50	0.9366	0.0507	22.50	0.9516	0.0503	22.50	0.9717	0.0498
23.00	0.9342	0.0486	23.00	0.9376	0.0507	23.00	0.9516	0.0504	23.00	0.9729	0.0498
23.50	0.9336	0.0486	23.50	0.9357	0.0508	23.50	0.9513	0.0504	23.50	0.9723	0.0498
24.00	0.9336	0.0486	24.00	0.9366	0.0508	24.00	0.9516	0.0503	24.00	0.9725	0.0498
24.50	0.9340	0.0486	24.50	0.9366	0.0508	24.50	0.9516	0.0504	24.50	0.9724	0.0498
25.00	0.9336	0.0486	25.00	0.9359	0.0508	25.00	0.9512	0.0504	25.00	0.9724	0.0498

Figure A.2: We present the complete values of transmittance measurements of the liquid crystal variable retarders with the associated error.

Appendix B

Program to control the polarimeter

The interface with the user is presented in Fig. B.1. This interface was developed to be as friendly as possible for a more optimal manipulation of the system. As can be seen in Fig. B.1, we have controls to establish the position parameters of the study surface (horizontal-X and vertical-Y), we have set the step size of the rotating stage and the parameters of the detector. With the central part of the program it is possible to determine the section of surface to be scanned. In addition, you can monitor all the parameters with their corresponding display. Here we present a summary of the most important options in the main program and describe their functionalities.

B.1 Controls

1. **Retarder 1**. Define the set of retardances for the first LCVR, we need to introduce three parameters: start voltage, end voltage and the magnitude of the increment that we want for the voltage which produces a specific value of retardance. The set of the retardances is given by the values in Table 3.2 for polarimetric measurements.

2. **Retarder 2**. This control works in the same way as that for Retarder 1, only changing to LCVR2

3. **Retarder 3**. This control works in the same way as that for Retarder 1, only changing to LCVR3

4. **Retarder 4**. This control works in the same way as that for Retarder 1, only changing to LCVR4

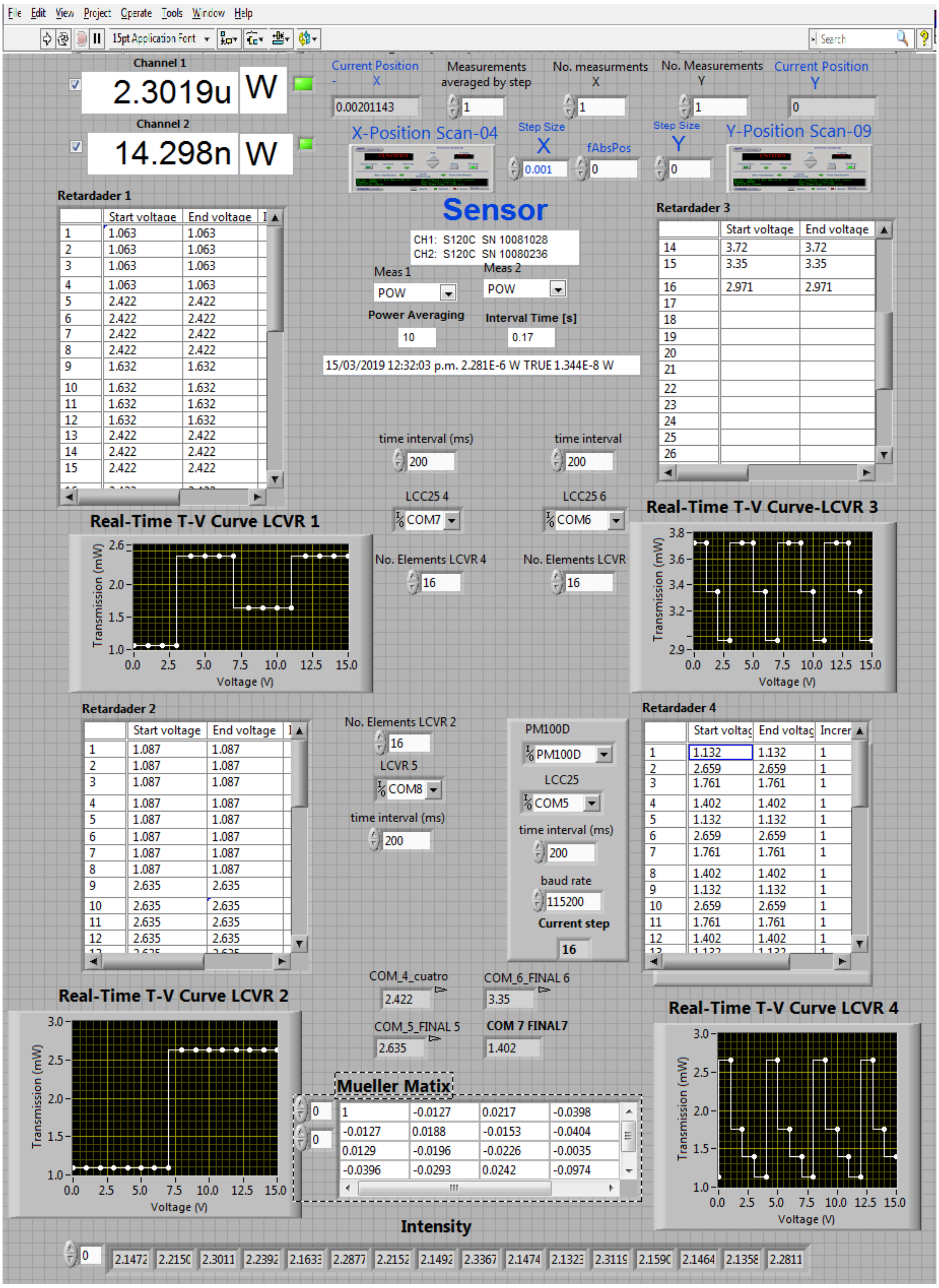

Channel 1
☑ 2.3019u W

Channel 2
☑ 14.298n W

Current Position - X: 0.00201143

Measurements averaged by step: 1

No. measurments X: 1

No. Measurements Y: 1

Current Position Y: 0

Step Size X: 0.001

fAbsPos: 0

Step Size Y: 0

Sensor

CH1: S120C SN 10081028
CH2: S120C SN 10080236

Meas 1: POW

Meas 2: POW

Power Averaging: 10

Interval Time [s]: 0.17

15/03/2019 12:32:03 p.m. 2.281E-6 W TRUE 1.344E-8 W

time interval (ms): 200

time interval: 200

LCC25 4: COM7

LCC25 6: COM6

No. Elements LCVR 4: 16

No. Elements LCVR: 16

Retardader 1

	Start voltage	End voltage
1	1.063	1.063
2	1.063	1.063
3	1.063	1.063
4	1.063	1.063
5	2.422	2.422
6	2.422	2.422
7	2.422	2.422
8	2.422	2.422
9	1.632	1.632
10	1.632	1.632
11	1.632	1.632
12	1.632	1.632
13	2.422	2.422
14	2.422	2.422
15	2.422	2.422

Retardader 3

	Start voltage	End voltage
14	3.72	3.72
15	3.35	3.35
16	2.971	2.971
17		
18		
19		
20		
21		
22		
23		
24		
25		
26		

Retardader 2

	Start voltage	End voltage
1	1.087	1.087
2	1.087	1.087
3	1.087	1.087
4	1.087	1.087
5	1.087	1.087
6	1.087	1.087
7	1.087	1.087
8	1.087	1.087
9	2.635	2.635
10	2.635	2.635
11	2.635	2.635
12	2.635	2.635

No. Elements LCVR 2: 16

LCVR 5: COM8

time interval (ms): 200

PM100D: PM100D

LCC25: COM5

time interval (ms): 200

baud rate: 115200

Current step: 16

Retardader 4

	Start voltag	End voltag	Increr
1	1.132	1.132	1
2	2.659	2.659	1
3	1.761	1.761	1
4	1.402	1.402	1
5	1.132	1.132	1
6	2.659	2.659	1
7	1.761	1.761	1
8	1.402	1.402	1
9	1.132	1.132	1
10	2.659	2.659	1
11	1.761	1.761	1
12	1.402	1.402	1

COM_4_cuatro: 2.422

COM_6_FINAL 6: 3.35

COM_5_FINAL 5: 2.635

COM 7 FINAL7: 1.402

Mueller Matix

0
0

1	-0.0127	0.0217	-0.0398
-0.0127	0.0188	-0.0153	-0.0404
0.0129	-0.0196	-0.0226	-0.0035
-0.0396	-0.0293	0.0242	-0.0974

Intensity

0 | 2.147 | 2.215 | 2.3011 | 2.239 | 2.163 | 2.2877 | 2.215 | 2.149 | 2.3367 | 2.1474 | 2.132 | 2.311 | 2.159 | 2.1464 | 2.135 | 2.2811

Figure B.1: LabVIEW program to control the experiment.

5. **Power Averaging.** Number of measurements averaged by the detector to reduce possible power variations. We typically use a value of 10.

6. **Time Interval.** Time that the detector takes to acquire the N averages of optical power defined by *Power Averaging.*

7. **Measurements averaged by step.** It is possible to repeat the measurement at each point of the sample, this control allows us to define how many averages of optical power we want to make. The number of required averages is saved separately in the text file.

8. **Number of measurements in X.** We define how many points in the horizontal direction we want to scan on the sample, this value is not limited, however it should be considered that the larger this value then the program will take more time.

9. **Number of measurements in Y.** With this function we define how many points we use in the vertical direction and we complete the bi-dimensional scan of the sample.

10. **Step size in X.** Typically we use a resolution of 1 micrometer for this parameter, however is possible extend the measurement up to 2500 micrometers, but again this will take more time. It is possible to change the resolution in multiples of a micrometer.

11. **Step size in Y.** Vertical movement has a resolution of 1 micrometer and we can synchronize the step size in both directions.

12. **Home position X.** Control to return the motor that moves the sample in the X-direction to the position defined as the initial setting or home. The motor returns to the start position when the program completes the entire cycle.

13. **LCC25 1.** Defines the connection port of the LCVR1 on the computer.

14. **LCC25 2.** Defines the connection port of the LCVR2 on the computer.

15. **LCC25 3.** Defines the connection port of the LCVR3 on the computer.

16. **LCC25 4.** Defines the connection port of the LCVR4 on the computer.

17. **Number of elements LCVR1.** Selects the number of measurements to be made by LCVR1. Typically there are 16 blocks of intensity, but with the methods presented in this work it is also possible to implement measurements of 36 blocks of intensity.

18. **Number of elements LCVR2.** Selects the number of measurements to be made by the LCVR2.
19. **Number of elements LCVR3.** Selects the number of measurements to be made by the LCV3.
20. **Number of elements LCVR4.** Selects the number of measurements to be made by the LCVR4.
21. **Dead Time LCVR1.** Sets the time needed by the molecules to produce the required retardation in the liquid crystal cell 1. It is important to synchronize the downtime of the 4 LCVRs.
22. **Dead Time LCVR2.** Sets the time needed by the molecules to produce the required retardation in the liquid crystal cell 2.
23. **Dead Time LCVR3.** Sets the time needed by the molecules to produce the required retardation in the liquid crystal cell 3.
24. **Dead Time LCVR4.** Sets the time needed by the molecules to produce the required retardation in the liquid crystal cell 4.

B.2 Indicators

1. **Sensor.** Systematized selection of the two detectors used to measure the optical power with the PM320 Power Meter.
2. **Channel 1.** Value of the optical power averaged for each measurement carried out by the detector 1. The units are in Watts $[W]$
3. **Channel 2.** Value of the optical power averaged for each measurement carried out by the detector 2, used to normalize and reduce the noise due to possible variations in the laser intensity.
4. **X-Position Scan.** Real value of the motor position in the horizontal direction, shown on the display.
5. **Y-Position Scan.** Real value of the motor position in the vertical direction, shown on the display.
6. **Set of retardances step by step.** Indicators with step-by-step voltage values, which produce the required in each block to produce and detect the polarization states required.

7. **Real Time Curve LCVR1.** Schematic curve with real time voltage values for 16 or 36 blocks of the LCVR1.
8. **Real Time Curve LCVR2.** Schematic curve with real time voltage values for 16 or 36 blocks of the LCVR2.
9. **Real Time Curve LCVR3.** Schematic curve with real time voltage values for 16 or 36 blocks of the LCVR2.
10. **Real Time Curve LCVR4.** Schematic curve with real time voltage values for 16 or 36 blocks of the LCVR3.
11. **Normalized Intensity.** Normalized and ordered intensity values in a 4x4 matrix. This data is also saved as a text file.
12. **Mueller matrix.** Experimental Mueller matrix obtained with the method proposed in this dissertation which implements the program described above.

Appendix C

Datasheet of optical devices

We present the data-sheets with the technical information about the optical compoents used in this word.

- Data sheet Liquid Crystal Variable Retarder.
- Power meter PM300E-Silicon Photodiode S120.
- Servo Linear Motor TDC001.
- JDS Uniphase Laser Source.
- Nanoparicle Linear Film Polarizer.
- Ghan Thompson Polarizer.
- Mounted Zero-Order Quarter Waveplate at 633nm.
- 1-3 Axis Motion Controller/Driver for Rotatory Stages.

1:2 ISOMETRIC VIEW
FOR REFERENCE ONLY

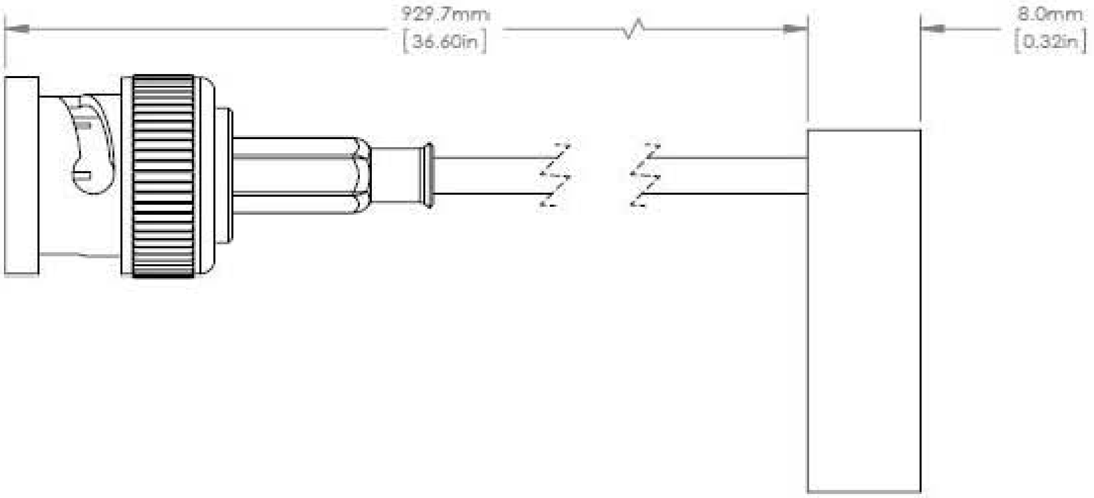

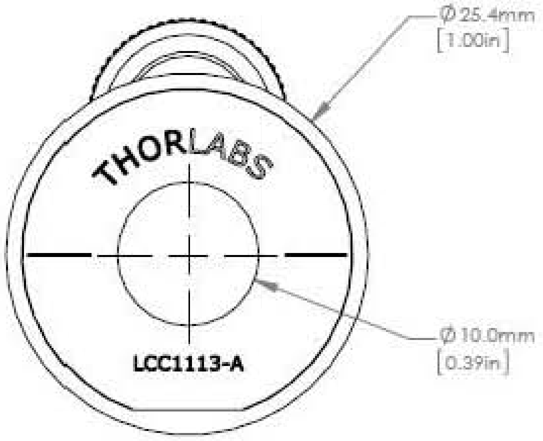

NOTES/SPECIFICATIONS:
1. MATERIAL: NEMATIC LIQUID CRYSTAL
2. RETARDANCE RANGE: ~30nm TO >1λ
3. CLEAR APERATURE: 10mm
4. SURFACE QUALITY: 40-20 SCRATCH-DIG
5. AR COATING: ON GLASS TO AIR INTERFACES
6. WAVELENGTH RANGE: 350-700nm

FOR INFORMATION ONLY
NOT FOR MANUFACTURING PURPOSES

DRAWING PROJECTION

	NAME	DATE
DRAWN	LZ	02/JUL/12
APPROVAL	SR	02/JUL/12

VALUES IN PARENTHESIS ARE CALCULATED AND MAY CONTAIN ROUNDOFF ERRORS

THORLABS
www.thorlabs.com

LIQUID CRYSTAL RETARDER

MATERIAL	REV
N/A	A

ITEM #	APPROX WEIGHT
LCC1113-A	0.05 kg

Full-Wave Liquid Crystal Variable Retarders / Wave Plates

- Nematic Liquid Crystal Full-Wave Variable Retarders
- Available with Ø10 mm or Ø20 mm Clear Aperture
- AR Coated for Visible, NIR, or MIR Light
- Compensated Models Achieve 0 nm Retardance

Related Items

Temperature Controller

Temperature-Controlled Lens Tubes

Rotation Mounts

Variable Retarders

https://www.tho

Overview | Specs | Performance | Switching Time | Applications | Damage Thresholds | LIDT Calculations | LC Controller | Custom Capabilities | Patterned Retarders | Feedback

Compensated Full-Wave LC Retarders

Item #		LCC1413-A	LCC1423-A	LCC1413-B	LCC1423-B	LCC1413-C	LCC1423-C
Wavelength Range		350 - 700 nm[a]		650 - 1050 nm		1050 - 1700 nm	
Retardance Range		0 nm to >λ					
Clear Aperture		Ø10 mm	Ø20 mm	Ø10 mm	Ø20 mm	Ø10 mm	Ø20 mm
Housing Outer Dimensions		Ø1"[b] (Ø25.4 mm)	Ø2.20"[c] (Ø55.8 mm)	Ø1"[b] (Ø25.4 mm)	Ø2.20"[c] (Ø55.8 mm)	Ø1"[b] (Ø25.4 mm)	Ø2.20"[c] (Ø55.8 mm)
Liquid Crystal Material		Nematic Liquid Crystal					
Surface Quality		60-40 Scratch-Dig					
Switching Speed (Rise/Fall, Typical)[d]		39.4 ms / 310 µs @ 25.6 °C		129 ms / 660 µs @ 25.6 °C		209 ms / 193 µs @ 25.6 °C	
Damage Threshold	Pulsed (ns)	2.04 J/cm^2 (532 nm, 10 Hz, 8 ns, Ø200 µm)		3.56 J/cm^2 (810 nm, 10 Hz, 7.6 ns, Ø234 µm)		2.5 J/cm^2 (1542 nm, 10 Hz, 10 ns, Ø458 µm)	
	Pulsed (fs)	0.024 J/cm^2 (532 nm, 100 Hz, 76 fs, Ø162 µm)		0.023 J/cm^2 (800 nm, 100 Hz, 36.4 fs, Ø189 µm)		0.161 J/cm^2 (1550 nm, 100 Hz, 70 fs, Ø145 µm)	
AR Coating		R_{avg} < 0.5%[e]					
Wavefront Distortion		≤λ/4 (@ 635 nm)					
Retardance Uniformity (RMS)[f]		<λ/20					
Housing Thickness		8.6 mm (0.34")	15.0 mm (0.59")	8.6 mm (0.34")	15.0 mm (0.59")	8.6 mm (0.34")	15.0 mm (0.59")
Storage Temperature		-30 to 70 °C					

Operation Temperature	-20 to 45 °C

Uncompensated Full-Wave LC Retarders

Item #		LCC1113-A	LCC1223-A	LCC1113-B	LCC1223-B	LCC1113-C	LCC1223-C	LCC1113-D	LCC1113-MIR
Wavelength Range		350 - 700 nm[a]		650 - 1050 nm		1050 - 1700 nm		1650 - 3000 nm	3600 - 5600 nm
Retardance Range		~30 nm to >λ							
Clear Aperture		Ø10 mm	Ø20 mm	Ø10 mm	Ø20 mm	Ø10 mm	Ø20 mm	Ø10 mm	Ø10 mm
Housing Outer Dimensions		Ø1"[b] (Ø25.4 mm)	Ø2"[g] (Ø50.8 mm)	Ø1"[b] (Ø25.4 mm)	Ø2"[g] (Ø50.8 mm)	Ø1"[b] (Ø25.4 mm)	Ø2"[g] (Ø50.8 mm)	Ø1"[b] (Ø25.4 mm)	Ø1"[b] (Ø25.4 mm)
Liquid Crystal Material		Nematic Liquid Crystal							
Surface Quality		40-20 Scratch-Dig						60-40 Scratch-Dig	
Switching Speed (Rise/Fall, Typical)[d]		12.7 ms / 310 µs @ 22 °C		15.0 ms / 356 µs @ 25.6 °C		23.6 ms / 489 µs @ 25.6 °C		596 ms / 7.0 µs @ 25.6 °C	4.4 s / 94 µs @ 25.6 °C
Damage Threshold	Pulsed (ns)	2.04 J/cm^2 (532 nm, 10 Hz, 8 ns, Ø200 µm)		3.56 J/cm^2 (810 nm, 10 Hz, 7.6 ns, Ø234 µm)		2.5 J/cm^2 (1542 nm, 10 Hz, 10 ns, Ø458 µm)		0.082 J/cm^2 (2000 nm, 10 Hz, 6.5 ns, Ø292 µm)	N/A
	Pulsed (fs)	0.024 J/cm^2 (532 nm, 100 Hz, 76 fs, Ø162 µm)		0.023 J/cm^2 (800 nm, 100 Hz, 36.4 fs, Ø189 µm)		0.161 J/cm^2 (1550 nm, 100 Hz, 70 fs, Ø145 µm)		0.05 J/cm^2 (2000 nm, 100 Hz, 100 fs, Ø220 µm)	N/A
AR Coating		R_{avg} < 0.5%[e]							R_{avg} < 1.0%[e]
Wavefront Distortion		≤λ/4 (@ 635 nm)						-	
Retardance Uniformity (RMS)[f]		<λ/50						<λ/10	

Item #	LCC1113-A	LCC1223-A	LCC1113-B	LCC1223-B	LCC1113-C	LCC1223-C	LCC1113-D	LCC1113-MIR
Housing Thickness	8.0 mm (0.32")							
Storage Temperature	-30 to 70 °C							
Operation Temperature	-20 to 45 °C							

a. Liquid crystal is more susceptible to damage when exposed to light sources close to UV wavelengths. Our tests show that the liquid crystal variable retarder can be deteriorated while exposed to a 395 nm, 6 W/cm^2 light source for four hours. With a 365 nm, 40 mW/cm^2 light source, the liquid crystal variable retarder can be damaged within 15 minutes. Therefore, it is recommended that the liquid crystal variable retarder be used with light sources of 400 nm or longer wavelength. If wavelengths of shorter than 400 nm are used, then the power must be lower along with a shorter exposure duration. The shorter the wavelength, the more susceptible the liquid crystal is to damage.

b. Recommended Mounts: RSP1 (RSP1/M), CRM1 (CRM1/M), CRM1P (CRM1P/M), KM100

c. Recommended Mounts: RSP2 (RSP2/M), LCRM2 (LCRM2/M), KM200T, SM2TC

d. Switching speed is highly dependent on several factors, including voltage change and cell temperature. See the *Switching Time* tab for more details.

e. At all air-to-glass surfaces for the specified wavelength range.

f. Specified Over the Entire Clear Aperture

g. Recommended Mounts: RSP2 (RSP2/M), LCRM2 (LCRM2/M), KM200

Specifications

Detector Type	Silicon Photodiode
Wavelength Range	400 - 1100 nm
Optical Power Working Range	50 nW - 50 mW
Max Average Power Density	20 W/cm²
Max Pulse Energy	20 µJ
Linearity	± 0.5%
Resolution [1]	1nW
Measurement Uncertainty [2]	±3% 440 - 980 nm ±5% 400 - 439 nm, ±7% 981 - 1100 nm
Typical Application	Low Power Lasers
Laser Types	Diode, Diode Arrays, He-Ne, Dye, Ion Lasers (Ar+, Kr+)
Coating /Diffuser [3]	Reflective ND (OD1)
Cooling	Convection
Head Temperature Measurement	NTC Thermistor 4.7kΩ
Console Compatibility	PM100D, PM100A, PM100USB, PM200, PM320E
Response Time	< 1 µs
Sensor Dimensions	Ø30.5 mm x 12.7 mm
Active Detector Area	9.7 mm x 9.7 mm
Input Aperture	Ø9.5 mm
Cable Length	1.5 m
Connector	Sub-D 9p male
Weight	0.07 kg
Post [3]	#8-32 & M4 thread
Aperture Thread	SM1, outer thread
Fiber Adapters (optional)	FC, SC, LC, SMA, ST

[1] Measured with PM100D console in bandwidth low setting.
[2] Beam diameter = 1mm
[3] This specification is valid for S120C devices from serial number 1203xxx. For older versions, please contact technical support.

Please note that the S120C power meter head is not compatible with the older Thorlabs power meter consoles (PM100, PM30, PM300, PM300E, S100).

Typical Response Graph

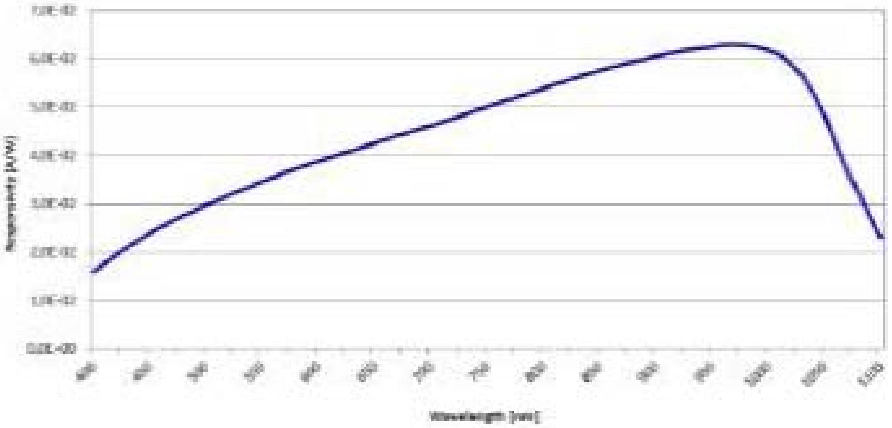

Drawings

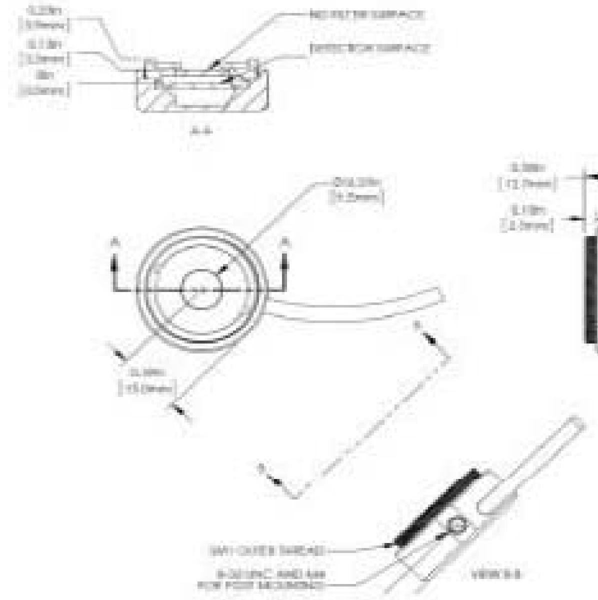

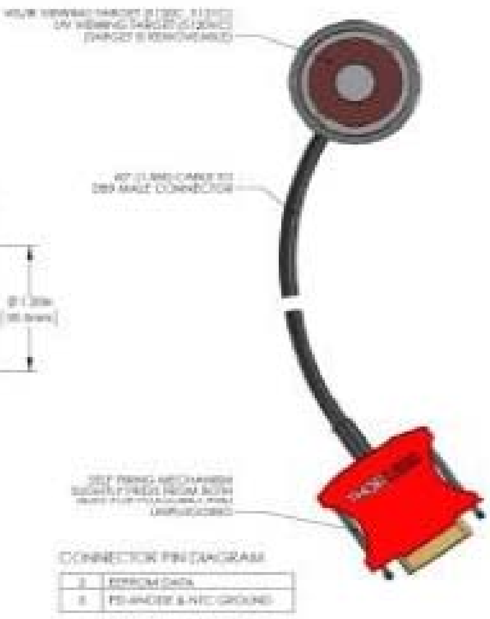

CONNECTOR PIN DIAGRAM

2	EEPROM DATA
3	PD ANODE & NTC GROUND

56 Sparta Avenue • Newton, New Jersey 07860
(973) 300-3000 Sales • (973) 300-3600 Fax
www.thorlabs.com

THORLABS

TDC001 - February 3, 2016

Item # TDC001 was discontinued on February 3, 2016. For informational purposes, this is a copy of the website content at that time and is valid only for the stated product.

T-CUBE DC SERVO MOTOR CONTROLLER

- Drives Brushed DC Servo Motors Up to 2.5 W
- Seamless Operation with Thorlabs Z8 Series Actuators
- Control via Local Panel or USB Computer Connection
- Optional USB Hub for Multi-Channel Applications

USB

TDC001
Power Supply
Sold Separately

Application Idea

TDC001
A TDC001 Controller can be Used to Drive a CR1-Z7 Rotation Stage (Sold Separately)

OVERVIEW

Features

- Compact Footprint 60 mm x 60 mm x 47 mm (2.4" x 2.4" x 1.8")
- Differential Encoder Feedback (QEP Inputs) for Closed Loop Positioning
- Auto-Configure Function for all Thorlabs Z8 Equipped Stages/Actuators
- Range of PSU Options Available Separately
- USB Plug-and-Play - Multi-axis Expansion
- Easy to Use Manual Controls with Velocity Slider and Jog Buttons
- Full Software Control Suite Supplied
- Extensive ActiveX® Programming Interfaces
- Fully Software Integrated with Other APT™ Family Controllers

T-Cube Motion Control Modules
Brushed DC Servo Motor Controller
Brushless DC Servo Motor Controller
Stepper Motor Controller
Single-Channel Piezo Controller
Single-Channel Strain Gauge Reader
Dual-Channel NanoTrak Auto-Aligner
Quadrant Detector
Solenoid Controller

Click to Enlarge
Back View of the TDC001 T-Cube (See the *Pin Diagrams* Tab for More Information)

The T-Cube APT^{TM} USB DC Driver (TDC001) is a very compact single channel DC servo controller/driver for easy manual and automatic control of DC Servo motors. This driver has been designed to operate with a variety of lower powered DC brushed motors (up to 15 V/2.5 W operation) equipped with encoder feedback. The TDC001 has been optimized for 'out of the box' operation with the Thorlabs range of Z8 series DC motor equipped opto-mechanical products.

Please note that older units will require a firmware upgrade before they can be used with the Z8 series motors. An upgrade is included with the latest APT software, which can be downloaded here. The highly flexible software settings and closed loop tuning also supports operation with a wide range of third party

56 Sparta Avenue • Newton, New Jersey 07860
(973) 300-3000 Sales • (973) 300-3600 Fax
www.thorlabs.com

THORLABS

TDC001 - February 3, 2016

Item # TDC001 was discontinued on February 3, 2016. For informational purposes, this is a copy of the website content at that time and is valid only for the stated product.

T-CUBE DC SERVO MOTOR CONTROLLER

- Drives Brushed DC Servo Motors Up to 2.5 W
- Seamless Operation with Thorlabs Z8 Series Actuators
- Control via Local Panel or USB Computer Connection
- Optional USB Hub for Multi-Channel Applications

TDC001
Power Supply
Sold Separately

Application Idea

TDC001
A TDC001 Controller can be Used to Drive a CR1-Z7 Rotation Stage (Sold Separately)

OVERVIEW

Features

- Compact Footprint 60 mm x 60 mm x 47 mm (2.4" x 2.4" x 1.8")
- Differential Encoder Feedback (QEP Inputs) for Closed Loop Positioning
- Auto-Configure Function for all Thorlabs Z8 Equipped Stages/Actuators
- Range of PSU Options Available Separately
- USB Plug-and-Play - Multi-axis Expansion
- Easy to Use Manual Controls with Velocity Slider and Jog Buttons
- Full Software Control Suite Supplied
- Extensive ActiveX® Programming Interfaces
- Fully Software Integrated with Other APT™ Family Controllers

T-Cube Motion Control Modules
Brushed DC Servo Motor Controller
Brushless DC Servo Motor Controller
Stepper Motor Controller
Single-Channel Piezo Controller
Single-Channel Strain Gauge Reader
Dual-Channel NanoTrak Auto-Aligner
Quadrant Detector
Solenoid Controller

Click to Enlarge
Back View of the TDC001 T-Cube (See the *Pin Diagrams* Tab for More Information)

The T-Cube APT^{TM} USB DC Driver (TDC001) is a very compact single channel DC servo controler/driver for easy manual and automatic control of DC Servo motors. This driver has been designed to operate with a variety of lower powered DC brushed motors (up to 15 V/2.5 W operation) equipped with encoder feedback. The TDC001 has been optimized for 'out of the box' operation with the Thorlabs range of Z8 series DC motor equipped opto-mechanical products.

Please note that older units will require a firmware upgrade before they can be used with the Z8 series motors. An upgrade is included with the latest APT software, which can be downloaded here. The highly flexible software settings and closed loop tuning also supports operation with a wide range of third party

Compatible Motor Specifications

Motor Type	Brushed DC Servo
Peak Power	2.5 W
Rated Current	10 - 200 mA (Nominal)
Motor Type	Brushed DC
Coil Resistance (nominal)	5 to 50 Ω
Coil Inductance	250 to 1500 µH
Postition Control	Incremental Encoder
Resolution	Encoder Specific

PIN DIAGRAMS

Motor Control Connector
D-type Female

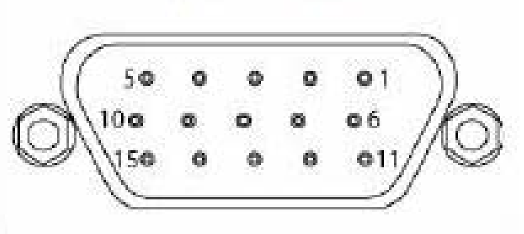

Pin	Description	Pin	Description
1	Ground	9	Ident
2	Forward Limit Switch	10	5 V Encoder Supply
3	Reverse Limit Switch	11	Encoder Channel A
4	Not Connected	12	Not Connected
5	Motor -	13	Encoder Channel B
6	Not Connected	14	Not Connected
7	Motor +	15	Not Connected
8	Not Connected		

Computer Connection
USB Mini-B*

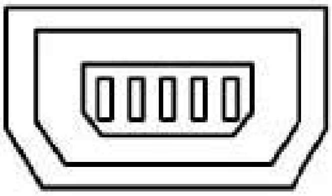

*USB type Mini-B to type A Included

FURTHER INFO

Introduction

The T-Cube DC Servo Controller (TDC001) is a very compact single channel USB controller/driver, designed to operate with a variety of 12-15 V DC brushed motors up to 2.5 W operation and equipped with encoder feedback - it is ideally suited for driving the Z8 motor series offered by Thorlabs (see Related Items tab). The unit contains a full embedded controller and driver circuit that can be operated with and without a PC. Although compact in footprint, the T-Cube DC Servo controller offers a fully featured motion control capability including veocity profile settings, limit switch handling, "on the fly" changes in motor speed and direction for more advanced operation, control over the closed loop PID parameters and adjustment of settings such as lead screw pitch and gearbox ratio allowing support for many different actuator configurations. When used with the extensive range of Thorlabs Z8 motorized opto-mechanical products, many of these parameters are automatically set to allow immediate "out of the box" operation with no further tuning required.

Specifications

Parameter	1101/P	1103/P	1107/P	1108/P	1122/P	1125/P	1135/P	1137/P	1144/P	1145/P	Unit
Optical											
Min. output power (TEM_{00})	1.5	2.0	0.8	0.5	2.0	5.0	10.0	7.0	15.0	22.5/21.0	mW
Wavelength	632.8	632.8	632.8	632.8	632.8	632.8	632.8	632.8	632.8	632.8	nm
Mode purity (TEM_{00})	>95	>95	>95	>95	>95	>95	>95	>95	>95	>95	%
Beam diameter (1/e2 points, ±3%, TEM_{00})	0.63	0.63	0.48	0.48	0.63	0.81	0.68	0.81	0.70	0.70	mm
Beam divergence (TEM_{00}, ±3%, mrad- full angle)	1.3	1.3	1.7	1.8	1.3	1.0	1.2	1.0	1.15	1.15	mrad
Polarization ratio (minimum, P versions)	N/A /500:1	N/A /500:1	N/A /500:1	N/A /500:1	N/A /500:1	N/A /500:1	N/A /500:1	N/A /500:1	N/A /500:1	N/A /500:1	-
Longitudinal mode spacing (nominal)	730	730	1090	1090	730	435	320	435	257	257	MHz
Maximum noise (rms, 30 Hz to 10 MHz)	0.1	0.1	0.1	0.1	0.1	0.2	1.0	0.2	0.5	0.5	%
Max. drift (mean power measured over 8 hours)	±2.5	±2.5	±2.5	±2.5	±2.5	±2.5	±3.0	±2.5	±2.0	±2.0	%
Max. mode sweeping contribution	3	3	10	20	3	2	2	2	1	1	%
Max. warm-up time (minutes to 95% power)	10	10	10	10	10	10	15	10	20	20	min.
Beam pointing stability (from cold start, 25 °C)	N/A	N/A	N/A	N/A	<0.10	<0.10	<0.10	<0.10	<0.20	<0.20	mrad
Beam pointing stability (after 15 minutes warm-up)	N/A	N/A	N/A	N/A	<0.10	<0.10	<0.02	<0.02	<0.03	<0.03	mrad
Operating voltage (V DC ±100)	1700	1700	1250	1250	1800	2300	3100	2300	3800	3800	V DC
Operating current (±0.1 mA)	4.9	4.9	4.0	4.0	6.5	6.0	6.5	6.0	6.5	6.5	mA
Dimensions											
L-overall length	9.50	9.50	7.00	7.00	10.71	15.79	19.13	15.79	25.00	25.00	inches
D-mounting diameter (±0.005 inches)	1.245	1.245	1.245	1.245	1.740	1.740	1.740	1.740	1.740	1.740	inches
B-distance: cable end to mounting surface	1.00	1.00	0.75	0.75	1.50	3.00	4.00	3.00	5.00	5.00	inches
A-distance: output end to mounting surface	0.75	0.75	0.50	0.50	1.50	3.00	4.00	3.00	5.00	5.00	inches
CDRH class (head & 1200 Series power supply)	IIIa	IIIa	IIIa	II	IIIa	IIIb	IIIb	IIIb	IIIb	IIIb	-

Specifications — Continued

Parameter	1101/P	1103/P	1107/P	1108/P	1122/P	1125/P	1135/P	1137/P	1144/P	1145/P
General										
Maximum starting voltage	10 kV DC									
Mode purity	>95%									
Storage lifetime	Indefinite (hard-sealed)									
Static alignment	Center to outer cylinder within ±0.01 inch. Parallel to outer cylinder within ±1 mR.									
Environmental										
Temperature	-40 to 70 °C (operating), -40 to 150 °C (non-operating)									
Atitude	0 to 10,000 feet (operating), 0 to 70,000 feet (non-operating)									
Relative humidity (no condensation)	0 to 100%									
Shock	25 g for 11 ms, 100 g for 1 ms									
Physical										
Shipping weight	5 lb. (1100 Series heads); 10 lb. (1100 Series head and 1200 Series power supply)									

Ordering Information

For more information on this or other products and their availability, please contact your local JDS Uniphase account manager or JDS Uniphase directly at 1-800-254-3684 in North America and +800-5378-JDSU worldwide or via e-mail at sales@jdsu.com.

Sample: 1122P

56 Sparta Avenue • Newton, New Jersey 07860
(973) 300-3000 Sales • (973) 300-3600 Fax
www.thorlabs.com

THORLABS

NANOPARTICLE LINEAR FILM POLARIZER

LPVISB050-MP2 - Dec. 15, 2016

Item # LPVISB050-MP2 was discontinued on Dec. 15, 2016. For informational purposes, this is a copy of the website content at that time and is valid only for the stated product.

- UV, Visible, NIR, and IR Spectral Ranges
- Unmounted and Mounted Versions
- Extinction Ratios up to 100 000:1
- Laser Damage Thresholds up to 25 W/cm^2

Unmounted Linear Polarizers

LPVIS100
(Ø25.0 mm)

LPUV050
(Ø12.5 mm)

LPVISB050-MP2
(SM05 Compatible)

LPMIR100-MP2
(SM1 Compatible)

Mounted Linear Polarizer in RSP1X15 Indexed Rotation Mount

OVERVIEW

Features

- High Extinction Ratio and Laser Damage Threshold (See Tables Below)
- Two Polarizer Sizes: Ø12.5 mm and Ø25.0 mm
- Unmounted or Mounted in SM-Threaded Housing
- Unmounted Versions Have Protective Glass Substrate (Except LPNIRA & LPMIR)
- Resistant to UV Radiation and Chemicals

Linear Polarizer Selection Guide	
Item # Prefix	Wavelength Range
LPUV	365 - 395 nm
LPVISA	480 - 550 nm
LPVISB	500 - 720 nm
LPVISC	510 - 800 nm
LPVIS	550 nm - 1.5 µm
LPNIR	650 nm - 2.0 µm
LPNIRA	1.0 - 3.0 µm
LPMIR	1.5 - 5.0 µm

These Nanoparticle Linear Film Polarizers consist of spherical ellipsoid nanoparticles that have been embedded in sodium-silicate glass. They offer superior performance compared to conventional polymer-based polarizers. While both conventional and nanoparticle polarizers absorb the light that is polarized perpendicular to the transmission axis, the nanoparticles have a significantly higher damage threshold and a dramatically better extinction ratio. The polarizer's transmission axis is indicated by two black marks on the edge of every unmounted polarizer except the LPMIR050 and LPMIR100. On the mounted polarizers, the polarization axis is indicated by engraved white lines on the housing.

The unmounted polarizers shown below (except for the LPNIRA and LPMIR) consist of a thin layer of sodium-silicate polarizer laminated between two pieces of index-matched Schott glass (B270) for additional strength. The mounted polarizers, as well as LPNIRA and LPMIR unmounted polarizers, are not laminated, allowing for a higher laser damage threshold. They only consist of the thin sodium-silicate polarizer, which is between 0.20 mm and 0.28 mm thick; as a result, they are more delicate to handle. However, they may still be cleaned using standard optics cleaning methods and solvents.

Please note that the mounted polarizers cannot be separated from their housings. Due to their thickness and precise alignment, they are bounded by a retaining ring and epoxy.

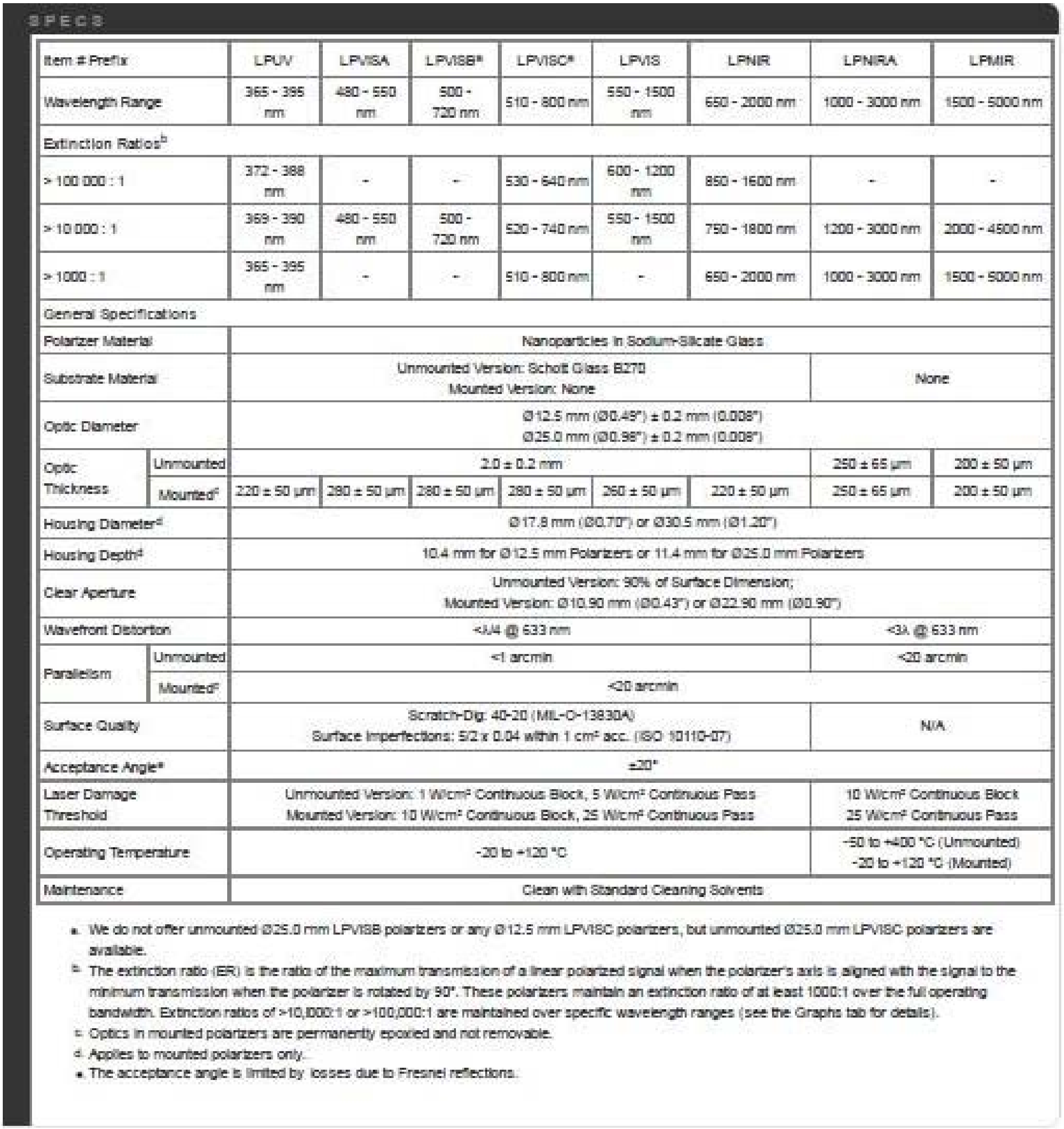

SPECS

Item # Prefix		LPUV	LPVISA	LPVISB[a]	LPVISC[a]	LPVIS	LPNIR	LPNIRA	LPMIR
Wavelength Range		365 - 395 nm	480 - 550 nm	500 - 720 nm	510 - 800 nm	550 - 1500 nm	650 - 2000 nm	1000 - 3000 nm	1500 - 5000 nm
Extinction Ratios[b]									
> 100 000 : 1		372 - 388 nm	-	-	530 - 640 nm	600 - 1200 nm	850 - 1600 nm	-	-
> 10 000 : 1		369 - 390 nm	480 - 550 nm	500 - 720 nm	520 - 740 nm	550 - 1500 nm	750 - 1800 nm	1200 - 3000 nm	2000 - 4500 nm
> 1000 : 1		365 - 395 nm	-	-	510 - 800 nm	-	650 - 2000 nm	1000 - 3000 nm	1500 - 5000 nm
General Specifications									
Polarizer Material		Nanoparticles in Sodium-Silicate Glass							
Substrate Material		Unmounted Version: Schott Glass B270 Mounted Version: None						None	
Optic Diameter		Ø12.5 mm (Ø0.49") ± 0.2 mm (0.008") Ø25.0 mm (Ø0.98") ± 0.2 mm (0.008")							
Optic Thickness	Unmounted	2.0 ± 0.2 mm						250 ± 65 µm	200 ± 50 µm
	Mounted[c]	220 ± 50 µm	280 ± 50 µm	280 ± 50 µm	280 ± 50 µm	260 ± 50 µm	220 ± 50 µm	250 ± 65 µm	200 ± 50 µm
Housing Diameter[d]		Ø17.8 mm (Ø0.70") or Ø30.5 mm (Ø1.20")							
Housing Depth[d]		10.4 mm for Ø12.5 mm Polarizers or 11.4 mm for Ø25.0 mm Polarizers							
Clear Aperture		Unmounted Version: 90% of Surface Dimension; Mounted Version: Ø10.90 mm (Ø0.43") or Ø22.90 mm (Ø0.90")							
Wavefront Distortion		<λ/4 @ 633 nm						<3λ @ 633 nm	
Parallelism	Unmounted	<1 arcmin						<20 arcmin	
	Mounted[c]	<20 arcmin							
Surface Quality		Scratch-Dig: 40-20 (MIL-O-13830A) Surface Imperfections: 5/2 x 0.04 within 1 cm^2 acc. (ISO 10110-07)						N/A	
Acceptance Angle[e]		±20°							
Laser Damage Threshold		Unmounted Version: 1 W/cm^2 Continuous Block, 5 W/cm^2 Continuous Pass Mounted Version: 10 W/cm^2 Continuous Block, 25 W/cm^2 Continuous Pass						10 W/cm^2 Continuous Block 25 W/cm^2 Continuous Pass	
Operating Temperature		-20 to +120 °C						-50 to +400 °C (Unmounted) -20 to +120 °C (Mounted)	
Maintenance		Clean with Standard Cleaning Solvents							

[a] We do not offer unmounted Ø25.0 mm LPVISB polarizers or any Ø12.5 mm LPVISC polarizers, but unmounted Ø25.0 mm LPVISC polarizers are available.

[b] The extinction ratio (ER) is the ratio of the maximum transmission of a linear polarized signal when the polarizer's axis is aligned with the signal to the minimum transmission when the polarizer is rotated by 90°. These polarizers maintain an extinction ratio of at least 1000:1 over the full operating bandwidth. Extinction ratios of >10,000:1 or >100,000:1 are maintained over specific wavelength ranges (see the Graphs tab for details).

[c] Optics in mounted polarizers are permanently epoxied and not removable.

[d] Applies to mounted polarizers only.

[e] The acceptance angle is limited by losses due to Fresnel reflections.

GRAPHS

The plots below show the measured transmission as a function of wavelength (blue lines) and the theoretically calculated extinction ratio (ER) as a function of wavelength (red lines) for each linear polarizer when the light is normally incident. For measured extinction ratio values which are guaranteed, please see the Specs tab. The percenttransmission is the percentage of light with a linear state of polarization (SOP) aligned with the transmission axis that is transmitted through the linear polarizer. This number is less than 100% because of surface reflections and internal absorption. The ER is the ratio of the transmitted intensity of a linearly polarized beam of light with the orientation of the SOP parallel to the transmission axis to the transmitted intensity of the same linearly polarized beam of light with the orientation of the SOP perpendicular to the transmission axis. For reference, an ER of 1×10^5 is typical of a top-of-the-line Glan-Laser Calcite Polarizer, although a cacite polarizer has a significantly higher damage threshold.

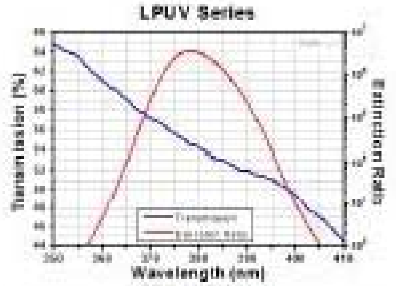

Click to Enlarge
Click to Download LPUV Series Transmission Data

Click to Enlarge
Click to Download LPVISA Series Transmission Data

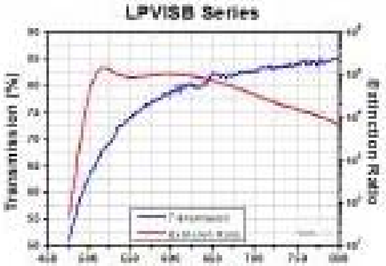

Click to Enlarge
Click to Download LPVISB Series Transmission Data

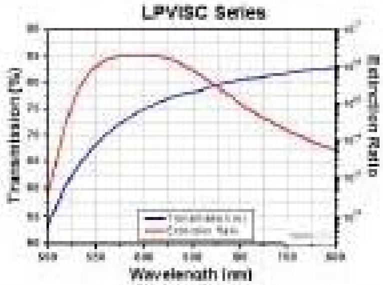

Click to Enlarge
Click to Download LPVISC Series Transmission Data

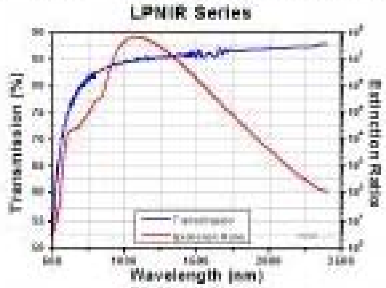

Click to Enlarge
Click to Download LPNIR Transmission Data

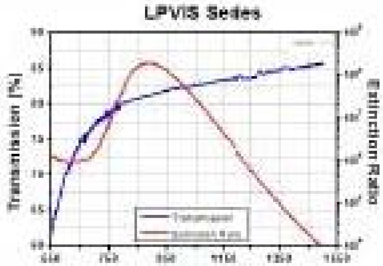

Click to Enlarge
Click to Download LPVIS Series Transmission Data

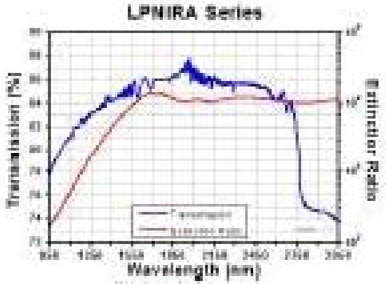

Click to Enlarge
Click to Download LPNIRA Transmission Data

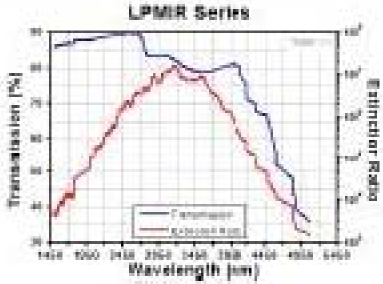

Click to Enlarge
Click to Download LPMIR Transmission Data

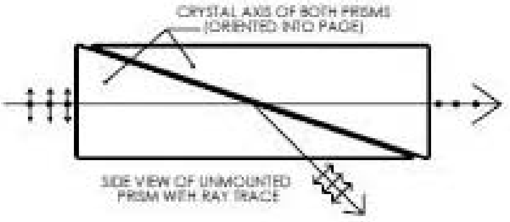

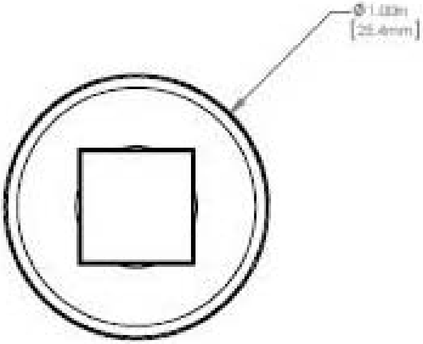

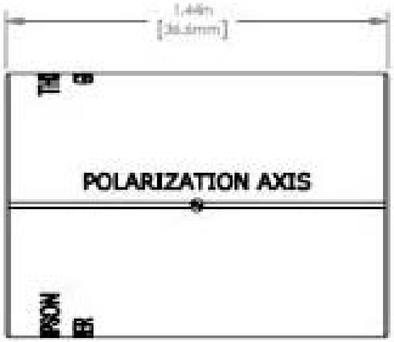

NOTES/SPECIFICATIONS:

1. EXTINCTION RATIO: 100,000:1
2. WAVEFRONT DISTORTION: ≤λ/4 @ 632.8nm
3. CLEAR APERTURE: 10.0mm x 10.0mm
4. SURFACE QUALITY (INPUT & OUTPUT FACES): 20-10 SCRATCH-DIG
5. COATED SURFACES: ENTRANCE AND EXIT WINDOWS
6. MATERIAL:
   1. OPTICS: OPTICAL GRADE CALCITE
   2. HOUSING: BLACK ANODIZED 6061-T6 ALUMINUM

FOR INFORMATION ONLY
NOT FOR MANUFACTURING PURPOSES

DRAWING PROJECTION			THORLABS www.thorlabs.com
	NAME	DATE	GLAN THOMPSON POLARIZER
DRAWN	SS	06/SEP/2011	MATERIAL SEE NOTES
APPROVAL	MG	20/SEP/11	REV B
COPYRIGHT © 2011 BY THORLABS			ITEM # GTH10M
VALUES IN PARENTHESES ARE CALCULATED AND MAY CONTAIN ROUND OFF ERRORS			APPROX WEIGHT 0.15 kg

ORDER OF ASSEMBLY		
ORDER	ITEM NUMBER	MATERIAL
①	ENGRAVED HOUSING	ALUMINUM
②	O-RING	NEOPRENE
③	633nm WAVEPLATE	CRYSTAL QUARTZ
④	SM05RR	ALUMINUM

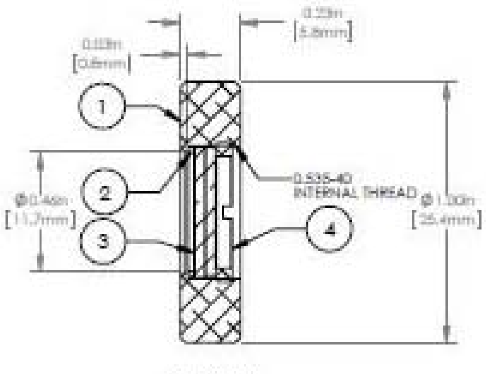

SECTION A-A

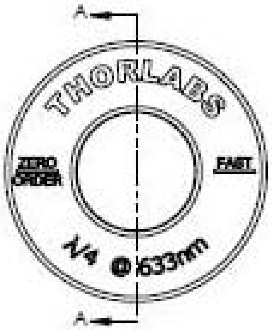

NOTES/SPECIFICATIONS:

1. UNMOUNTED DIAMETER: 0.50" ±0.004 [12.7mm ±0.1]
2. BEAM DEVIATION: <10 arcsec
3. RETARDANCE ACCURACY (TYP): <λ/300
4. TRANSMITTED WAVEFRONT ERROR: λ/8 AT 633nm
5. SURFACE QUALITY: 20-10 SCRATCH-DIG
6. CLEAR APERTURE: Ø0.39" (Ø10.0mm)
7. COATING: V-AR AT 633nm, R<0.25%, 0° AOI/PER SURFACE

FOR INFORMATION ONLY
NOT FOR MANUFACTURING PURPOSES

DRAWING PROJECTION			THORLABS www.thorlabs.com	
	NAME	DATE	MOUNTED ZERO-ORDER QUARTER WAVEPLATE AT 633nm	
DRAWN	EMT	23/JAN/13	MATERIAL SEE TABLE	REV D
APPROVAL	MQ	12/FEB/13		
COPYRIGHT © 2013 BY THORLABS			ITEM # WPQ05M-633	APPROX WEIGHT 4.0 g
VALUES IN PARENTHESES ARE CALCULATED AND MAY CONTAIN ROUNDOFF ERRORS				

ESP300
1–3 Axis Motion Controller/Driver

Key Features

- *1–3 axes universal motion controller/driver*
- *Uses one driver module for stepper, DC open-loop and closed-loop motors at 3 A (max.) per axis*
- *ESP Stage compatible for "plug and play" capability*
- *1000x programmable micro-step resolution for ultra-smooth low speed stepper positioning*
- *Synchronized circular/linear interpolation and continuous path contouring for complex motion profiling*
- *RS232-C communications link for easy computer interfacing*
- *Optional front panel, joystick, trackball, hand-held keypad, IEEE-488 interface, and rack mount*

The ESP300 motion control platform offers excellent functionality at an affordable price. The ESP300 is an integrated controller and driver in one chassis which simplifies system hookup and provides improved reliability. The ESP300 can drive and control up to three axes of motion using any combination of DC and/or stepper motors. Each driver module will drive 2- or 4- phase stepper and brush DC servo motors at 3 A (max.) per axis. This capability will allow you to drive a large selection of stages and actuators.

Technology

The ESP300 uses a 32-bit, floating point, DSP processor for high precision synchronized control. A digital PID-FF (feed-forward) servo loop ensures precise velocity profile tracking and accurate positioning. A 1000x programmable micro-step resolution provides ultra-smooth low-speed stepper positioning capability, and 18-bit DC motor command output ensures improved stability for precision applications.

Motion

The ESP300 provides several modes of positioning including synchronized and non-synchronized point-to-point, jogging, linear or circular interpolation, and continuous path contouring. With electronic gearing, any axis of the ESP300 can be "slaved" to any other axis, even if they have different motor/gearhead ratios or lead screw pitches. Other sophisticated motion features include on-the-fly position, velocity, or trajectory changes for complex motion and alignment routines. Software limits can be set to improve systems safety. An advanced origin search routine includes encoder index pulse consideration for precision homing. Backlash and linear error compensation eliminate repeatable system errors.

Inputs/Outputs

16 bi-directional digital I/O can be user programmed as either inputs or outputs for internal or external event synchronization. When configured as inputs, they

The alphanumeric keypad ESP-K allows the user to access the full command set without the use of a host computer. The digital joystick and trackball provide convenient manual jog control.

ESP300 Compatible Rotary Stages

RV Series
page 973

Except V6 versions

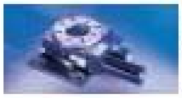

URM Series
page 985

Except V6 versions

URS Series
page 981

SR50 Series
page 990

PR50 Series
page 992

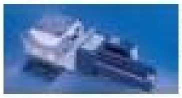

BGM Series
page 995

Except V6 versions

Accessories

Model	Description
ESP300-R	19 in. Rack Mount Brackets
ESP-K	Hand-held Keypad
ESP300-J	Joystick (digital switchstick)
ESP300-T	Trackball (digital)
ESP300-CMACC	Cable Adaptor for CMACC

How to Order

The ESP300 is configured by first specifying driver options for each axis. Next, options are chosen for the front panel, communications interface, and power supply. The example here specifies a ESP300 configured with a front panel display, drivers for 2 axes, and a 350 W power supply. No other options are selected.

A passthrough board is available to connect to an external amplifier. If interested, please contact our technical support group.

NOTE: Please refer to the max. motor driver power consumption table ([T-727475]) when configuring your system. The total power consumption of all stages must be smaller than the available drive power of the ESP300 (150 W or 350 W) in order to operate all stages simultaneously and at maximum speed.

Specifications

Number of Axes	1–3 axes of any combination of stepper and DC motors
Computing Power	400 µs servo cycle up to 3 axes
	32 Bit, 60 MHz DSP processor
	Digital PID servo loop with velocity and acceleration feed forward
Motion	Trapezoidal and s-curve velocity profile
	Synchronized and non-synchronized point-to-point
	Jogging, Continuous moves
	3D Linear interpolation, 2D Circular interpolation
	Master-slave, Electronic gearing
	On-the-fly trajectory modification, changes of target position, speed, acceleration, PID
Contouring	2D Contouring with continuous buffer loading
External Event Synchronization	Program execution depending on TTL I/O status
Operating Modes	Real-time command execution via computer interfaces
	Stand-alone execution of stored programs
	Front panel manual motion command execution (optional)
	Digital joystick, trackball, hand-held keypad (all optional)
Programming	100+ intuitive, 2 letter ASCII commands
	Command set includes: User defined units, software limits, home search (with and w/o top zero), linear error and backlash compensation, etc.
Software Drivers	Communication DLL for Windows 95/98/2000/NT/ME/XP
	Drivers for LabView 6i
	Software development tools compatible with Windows 95/98/2000/NT/ME: Setup, PID tuning program, Motion Wizard (used to configure non-ESP compatible stages)
Computer Interfaces	RS-232-C, IEEE-488-1 (optional)
I/O	16 user programmable TTL I/O (programmed in groups of 8)
	"Watchdog" timer and remote interlock
Memory	64 kB Flash non-volatile user program memory (last for approx. 6,000 commands)
	512 kB Flash non-volatile firmware memory
Front Panel Display (Optional)	Backlit LCD display, 4 lines x 20 characters, 21 mm x 70 mm
DC Motor Control	DC brush motors at 48 V, 3 A max.
	Open- or closed-loop operation
	16-bit DAC resolution
	5 MHz max. encoder input frequency
Stepper Motor Control	2 or 4-phase stepper motors at 48 V, 3 A max.
	Open- or closed-loop operation
	10 kHz commutation rate
	1000x max. (programmable) micro-step resolution
Total Available Motor Power	150 W or 350 W, 48 V, 3 A max per axis
Power Requirements	115/230 V, 50/60 Hz auto-select, 400 W (max.)
Dimensions (W x D x H)	16.5 x 12 x 3.25 in. (+0.5 in. bottom clearance) (419 x 305 x 83 mm) for 150 W power supply option; 16.5 x 13.5 x 3.25 in. (+0.5 in. bottom clearance) (419 x 343 x 83 mm) for 400 W power supply option
Weight	6 kg max for 150 W power supply option 8 kg max for 350 W power supply option